Université du Québec
Institut National de la Recherche Scientifique
Centre Énergie Matériaux Télécommunications

Printed Memory, Battery, and Sensors for Autonomous Systems

Par

Johannes Jehn

Thèse présentée pour l'obtention du grade de
Philosophiae doctor (Ph.D.)
en sciences de l'énergie et des matériaux

14 Juin 2022

Jury d'évaluation

Président du jury et examinateur interne	Professeur Emanuele Orgiu Institut National de la Recherche Scientifique Centre Énergie Matériaux Télécommunications
Examinateur externe	Professeur Marty Gregg Queen's University Belfast School of Mathematics and Physics
Examinateur externe	Professeur Damien Deleruyelle Institut National des Sciences Appliquées de Lyon Institut des Nanotechnologies de Lyon
Co-directrice de recherche	Professeur Christina Schindler Munich University of Applied Sciences Laboratory for Microsystems Technology
Directeur de recherche	Professeur Andreas Ruediger Institut National de la Recherche Scientifique Centre Énergie Matériaux Télécommunications

Résumé

L'électronique imprimée offre un énorme potentiel pour les processus de fabrication personnalisés et à faible coût sur des substrats flexibles en vue de la réalisation de l'Internet des objets (IoT). Les techniques d'impression permettent un dépôt précis d'encres fonctionnelles sur une variété de substrats tels que des feuilles, du tissu ou du papier tout en conservant leurs propriétés flexibles. Les éléments constitutifs de l'IdO sont les interconnexions imprimables, les entrées/sorties, la logique, les cellules de mémoire, les capteurs et le stockage d'énergie. Même si la recherche sur les composants entièrement imprimés a rapidement progressé ces dernières années, la compatibilité, la facilité de fabrication et la compréhension détaillée sont toujours limités pour de nombreux composants. Divers matériaux et processus doivent être ajustés pour permettre une fabrication parfaite, tandis que l'interaction entre les composants est cruciale pour toute application ; tout cela nécessite une compréhension microscopique des mécanismes. Cette thèse vise l'intégration de multiples constituants imprimés afin de réaliser un système autonome. Les mécanismes de transport de courant, les structures et l'intégration des mémoires, des capteurs et des batteries sont analysés par des méthodes microscopiques et électriques.

Les cellules de mémoire résistive consistent en une structure à trois couches, où un matériau isolant est pris en sandwich entre deux électrodes conductrices. La configuration la plus simple la rend particulièrement adaptée aux processus d'impression. Un filament métallique peut être formé et dissous par l'application de différentes tensions et, par conséquent, la modification de la résistance entre les électrodes est utilisée pour stocker des informations. Des approches d'impression complète ou hybride sont utilisées pour créer des cellules de mémoire en Ag/Spin-on-Glass/Ag ainsi qu'en Cu/CuxS/C. Elles présentent une très faible consommation d'énergie (1pJ par commutation) et permettent d'ingénier la formation du filament pour stocker plus d'un bit dans chaque cellule en contrôlant le filament par la conformité du courant. Pour alimenter la mémoire, une batterie planaire Zn/MnO2 sérigraphiée sur du PET flexible est fabriquée et présente des performances de pointe. Il est démontré que la batterie partage une électrode avec la mémoire et peut commuter l'état logique avec une longue rétention. Cette conception spécifique réduit le nombre d'étapes d'impression nécessaires ainsi que le matériel.

Différents capteurs entièrement imprimés par jet d'encre sont présentés pour surveiller les changements de contrainte, de température et d'humidité relative. Une approche d'impression en deux étapes de nanotubes de carbone (CNT) et de PDMS permet une lecture piézo-résistive des régimes de déformation en tension et en compression. Les développements à long terme sur des milliers de cycles de flexion révèlent des mécanismes complexes de réorientation des CNT qui aideront au développement de futures applications basées sur les CNT. L'impression et le frittage de nanoparticules (NPs) de Cu par lumière pulsée intense (IPL) sont determinés pour la réalisation d'un capteur de température semi-conducteur CuxS. La transformation ultérieure de Cu en CuxS est réalisée par un dépôt local de Na2S et les changements structurels au cours de ces processus sont étudiés par microscopie électronique à balayage confocale et (faisceau ionique focalisé). Le CuxS

semi-conducteur présente un coefficient de température de résistance négatif et est également utilisé pour la couche isolante des cellules de mémoire. Les structures Cu-NP frittées sont ensuite utilisées comme électrodes pour un capteur d'humidité imprimé. Ici, les NPs de WO3 sont déposées sur le Cu en forme de peigne entrelacés et la réponse résistive exponentielle aux changements d'humidité relative est présentée.

Les différents composants sont finalement intégrés dans un seul dispositif afin de stocker les informations de température dans la mémoire. Ceci est réalisé en limitant le courant fourni par la batterie à la cellule de mémoire par la tension d'un capteur de température. La résistance élevée (faible) du capteur à basse (haute) température réduit (augmente) le flux de courant à travers la mémoire, ce qui entraîne un filament plus fin (plus épais), déterminant l'état logique résistif de celui-ci.

En conclusion, dans le cadre de cette thèse, des composants entièrement imprimés sont présentés qui ouvrent la voie à des dispositifs personnalisés à faible coût pour des appareils flexibles et intelligents qui sont essentiels pour l'IdO.

Mots-clés : Électronique imprimée; impression jet d'encre; commutation résistive; batteries imprimées; capteur de contrainte; capteur d'humidité; capteur de température; systèmes autonomes.

Abstract

Printed electronics offer tremendous potential for customizable, low-cost fabrication processes on flexible substrates contributing to the realization of the Internet of Things (IoT). Printing techniques allow for the precise deposition of functional inks on various substrates such as foils, fabric, or paper while maintaining their flexible properties. Building blocks towards IoT are printable interconnections, input/output, logic, memory cells, sensors, and energy storage. Even though the research towards fully printed components has rapidly progressed within the last years, compatibility, facile fabrication, and detailed understanding are still missing for many components. Various materials and processes need to be adjusted to allow seamless fabrication. The interplay between components is crucial for any application, all of which require a microscopic understanding of the underlying mechanisms. This thesis aims to integrate multiple printed constituents to achieve an autonomous system. Microscopic and electrical methods analyze the underlying mechanisms, structures, and integration of memories, sensors, and batteries.

Resistive memory cells consist of a three-layered structure, where an insulating material is sandwiched between two conductive electrodes. The simplest setup makes it particularly suitable for printing processes. A metallic filament can be formed and dissolved by applying different voltages, and hence, the change in resistance between the electrodes stores the information. Fully or hybrid printing approaches use Ag/Spin-on-Glass/Ag and Cu/Cu_xS/C setups to create memory cells. They exhibit very low power consumption (1 pJ per switching) and allow engineering the filament formation to store more than one bit within each cell by controlling the filament size through the compliance current. A planar screen-printed Zn/MnO_2 battery on flexible PET is fabricated to power the memory and exhibits state-of-the-art performance. It is shown that the battery shares one electrode with the memory and can switch the logical state with long retention. This specific design reduces the number of necessary printing steps and materials.

Different fully inkjet-printed sensors are presented to monitor strain, temperature, and relative humidity changes. A two-step printing approach of carbon nanotubes (CNTs) and PDMS allows for piezoresistive read-out of tensile and compressive strain regimes. Long-term developments over thousands of bending cycles reveal complex reorientation mechanisms of CNTs that will aid the development of future CNT-based applications. Printing and sintering of Cu-nanoparticles (NPs) by intense pulsed light (IPL) is achieved to create a semiconducting Cu_xS temperature sensor. The subsequent transformation of Cu to Cu_xS is realized by local deposition of $Na_2S_{(aq)}$, and structural changes during these processes are investigated through confocal and (focused ion beam) scanning electron microscopy. The semiconducting Cu_xS exhibits a negative temperature coefficient of resistance and is also used for the insulating layer of the memory cells. Sintered Cu-NP structures are further utilized as electrodes for a printed humidity sensor. Here, WO_3-NPs are deposited on interlacing comb-shaped Cu fingers, and the exponential resistive response to changes in relative humidity is presented.

The different components are eventually integrated into one device to store temperature infor-

mation in the memory. This is achieved by limiting the current provided by the battery to the memory cell through a temperature sensor. The high (low) resistance of the sensor at low (high) temperatures reduces (increases) the current flow through the memory, resulting in a thinner (thicker) filament, determining its resistive logical state.

In conclusion, this thesis presents fully printed components that pave the way for customizable low-cost devices for flexible and smart devices critical for IoT.

Keywords: Printed Electronics; Inkjet Printing; Resistive Switching; Printed Batteries; Strain Sensor; Humidity Sensor; Temperature Sensor; Autonomous Systems

Acknowledgment

The preparation and submission of this work is the final step towards successfully completing the Ph.D. program at the INRS, which was mainly carried out at the University of Applied Sciences Munich. With the end of this journey, I would like to thank my supervisor, Prof. Andreas Ruediger, and co-supervisor, Prof. Christina Schindler, for their continuous support. The hospitality and opportunities during my time at the INRS through Prof. Ruediger and his whole team will accompany me for a long time. The mentoring and scientific guidance of Prof. Schindler was essential for accomplishing various goals. I am grateful for the challenging and encouraging time in our small lab, which offered tremendous possibilities and freedom.

Many thanks go to Prof. Ulrich Moosheimer for supporting anything related to printing technology. I also thank Michael Kaiser not only for countless pieces of advice on technical questions but also for the pleasant and enjoyable time in the lab. Further, I am indebted to my predecessor Bernhard Mittermeier for building expertise and sharing his experiences with me during my first months.

The presented results and further investigations were often supported by students' works in our laboratory for microsystems technology. Thanks to Sebastian Heeg, Alexander Dirndorfer, Marinus Werber, Vijay Kumar, Patrick Schildwächter, Trung Duong, Stephan Preiwisch, Stefan Marxen, Magdalena Eder, Mario Maz Courrau, Peter Saad Naguib, Johanna Stoib, Jonas Kubitschek, and Luis Huber. The collaboration and enriching conversations made the work more diverse.

Further, I would like to thank Dr. Constanze Eulenkamp for her time and patience in obtaining impressive SEM images. To emphasize my gratitude to a few colleagues, without claim for completeness, I thank Patrick Oser for our collaboration and good times at the printer, Yoandris Gonzales for measurements and hospitality, Azza Youssef for assistance with *questions française*, Dr. Andreas Dörfler for his work on the simulation, Prof. Korbinian Heil for assistance for reverse titration, Werner Geitner for the microtome cuts, and all other people who helped me on numerous accounts. Comments on the style and presentation of this work by Yannik Gleichmann, Constantin Jehn, Kilian Rolle, Cornelius Weis, and Tobias Nienke greatly improved the final form.

Finally, I am deeply grateful for my family and Irina's unconditional support and understanding. Without you, this work would not have been possible.

Contents

List of Figures

List of Tables

List of Abbreviations

AE ..... Active Electrode
C ..... Capacity
CE ..... Counter Electrode
CNN ..... Conductive Carbon Nanotube Network
DoD ..... Drop-on-Demand
DS ..... Drop space
EDX ..... Energy Dispersive X-Ray Spectroscopy
ECM ..... Electrochemical Metallization Memory
FIB ..... Focused Ion Beam
GF ..... Gauge Factor
HRS ..... High Resistive State
IDT ..... Interdigital Transducer
IoT ..... Internet of Things
IPL ..... Intense Pulsed Light
LRS ..... Low Resistive State
MWCNT ..... Multi-Walled Carbon Nanotubes
NP ..... Nanoparticle
NTC ..... Negative Temperature Coefficient
PCB ..... Printed Circuit Board
PE ..... Printed Electronics
PEDOT:PSS ..... Poly(3,4-Ethylenedioxythiophene) Polystyrene Sulfonate
PEN ..... Polyethylennaphthalat
PET ..... Polyethylenterephthalat
PI ..... Polyimide (Kapton)
PDMS ..... Polydimethylsiloxane
PVP ..... Polyvinylpyrrolidone
RH ..... Relative Humidity
RRAM ..... Resistive Random Access Memory
RS ..... Resistive Switching
SEM ..... Scanning Electron Microscopy
SMU ..... Source Measure Unit
SoG ..... Spin-on-Glass

Let's unwrite these pages
and replace them
with our own words.

- Tim McIlrath

Chapter 1

Introduction

Printing techniques have always contributed to the progress and evolution of electronic devices. Printed circuit boards (PCBs) were an early step in addressing challenges in this field. PCBs support and electrically connect different electronic components using conductive tracks, pads, and other features etched from copper sheets laminated onto a non-conductive substrate [1]. It is fabricated using a semi-additive process, where copper is structured through lithography. The etch-resistant pattern in this process is applied using screen printing, as it provides thicker layers of resist to protect the covered areas fully [2]. This approach represents the opportunities of printed electronics (PE): scalability, fast manufacturing, and low-cost materials leading to variable and cost-effective production. Already now, the market for printed, flexible, and organic electronics is US$ 41 billion (2020) and is expected to grow to US$ 74 billion in 2030 [3]. Here, displays contribute the largest share, e.g. inkjet-printed 31.5 ” 4K OLED displays [4]. Still, it demonstrates the potential for other applications to embrace printed solutions as viable alternatives to conventional fabrication processes.

However, printing is not limited to decorative or protective patterns but enables the partial or complete fabrication of electronic devices using functional inks on various substrates. Flexible polymer foils could be used for large-scale roll-to-roll fabrication of components such as memories [5] or batteries [6] for the Internet of Things (IoT). This term describes a network made up of decentralized, autonomous smart objects with the capabilities of sensing, processing, and communicating [7, 8]. One promising approach to achieve these goals is flexible hybrid electronics (FHE): conventional semiconductor components are mounted on flexible or bendable substrates and can be customized by printing technology. Traditionally, highly integrated systems are fabricated by sophisticated and technologically demanding techniques such as vacuum and photolithography processes in a cleanroom. The necessary laboratory environment, as well as the advanced equipment, lead to immense fabrication costs and energy consumption. Due to the required purity and structure size, these processes are unavoidable for chip integration on the nanometer scale, but many applications do not have these demands. While many PE devices exhibit tremendous potential for novel applications, their efficacy is not competitive with conventional processes [9]. FHE aims to combine the advantages of small, available, and inexpensive standard components with the opportunities of printing technology. To achieve this, research focuses on new materials, advanced manufacturing technologies and utilizing them for emerging applications such as bio-integrated systems e.g. for pharmacological delivery [10].

Temperature-sensitive processes such as bonding or sintering pose a challenge for this unification. Low-temperature sintering processes by electric current, plasma, light, or microwave are investigated to enable FHE [11]. It is further explored as to how interconnections between com-

ponents can be realized at room temperature to preserve sensitive functional inks and substrates [12, 13]. After integration, sensor data could be wirelessly transmitted from simple, battery-less tags using Radio Frequency Identification (RFID) [14]. For continuous measurements, printed flexible and rechargeable batteries could provide power to do so [15]. Special attention is also given to printed diodes that have been successfully incorporated for rectification, energy harvesting, or displays. Even though these displays are unlikely to outperform peers in lifespan or overall performance, they possess a significant chance of becoming competitive within the next decade of development by virtue of far more accessible cost [16]. Memory cells are shown to be flexible but often require physical lift-off [17], vacuum processes [18], or traditional microstructuring [19]. But transparent, sinter-free cells have also been demonstrated [20]. As an alternative to foils, Si-wafers are considered flexible with good mechanical stability for thinned wafers below 50 µm and can currently be thinned down to 10 µm [21].

Bonding or pick-and-place solutions offer the chances for cross-fertilization between different research areas towards next-generation devices. However, FHE cannot preserve all advantages of fully printed fabrication, such as bending properties or low technological requirements. Individual components for PE have already been demonstrated, e.g. solar cells [22], transistors [23, 24], memories [25], sensors [26], and batteries [27]. However, the integration of different devices requires a plethora of various inks and non-compatible processing steps, thus partly diminishing the original advantages. Fewer inks also lead to fewer required print heads and, therefore, to fewer expenses, alignment, and calibration.

The presented work investigates opportunities to pave the way for integrating different printed components into a system that uses common inks and compatible substrates. Thus, we pursue a fully printed autonomous system consisting of a memory cell, battery, and sensor to reduce the number of fabrication and sinter steps. Applications for such a system are event detection or smart tags for logistics where ample spaces on packages are available [28]. Larger footprints come with PE but are compatible as parcels for logistics easily provide more than (10x10) cm^2 to attach a printed smart label. Therefore, the advantages of PE can be exploited for more efficient electronic solutions in terms of time, energy, and resource demands. We regard this novel approach for holistic integration to provide the most significant merit towards printed autonomous systems.

Chapter 2

Fundamentals

This thesis aims to investigate fully printed electrical components such as batteries, sensory devices, and logical memory cells. It aims to open pathways for integrating single devices into a stand-alone solution for e.g. smart and flexible tags for IoT. In this chapter, the fundamentals of the memory technology resistive random-access memories (RRAM) are explained, and considerations for integrating multiple components into one device are discussed. Material combinations and potential applications of the same material for different device elements are elaborated. This holistic approach is used to determine the advantages of different fabrication techniques and materials in order to preserve the benefits of simple additive processes.

Two printing techniques will be used in this thesis: screen printing for larger areas where more volume is required, e.g. to provide sufficient material for a battery; and inkjet printing which is ideal for rapid prototyping and depositing sub-micron thin layers necessary for memory applications and mechanically flexible components. Both approaches can print directly on flexible, transparent substrates such as PEN (polyethylennaphthalat), PET (polyethylenterephthalat), and PI (polyimide). Substrates are chosen depending on the requirements for thermal stability, wettability, and cost. Materials for deposition or processing are nm–µm sized particles of metallic (Ag, Cu), semi-conducting (Carbon Nanotubes, Cu_xS), and insulating (Spin-on-Glass, WO_3) materials. Metallic components are the backbone for conductive tracks, such as current collectors in batteries or as active electrodes in memory cells. The non-conductive materials are utilized as an insulating layer for resistive memory cells or as sensing layers for humidity or temperature sensors. The overall selection of substrates and materials is governed by the vision to utilize the same material for different applications and ensure compatibility between components and processes.

2.1 Sensor Principles

Sensors are used to detect chemical and physical changes in a system. An excerpt of physical sensor categories is:

- Environmental: Temperature, relative humidity, gasses
- Physical: Strain, vibration, magnetic
- Control: Leaks, flow, position.

The change is measured through the modification of an electrical property such as voltage, resistance, or impedance. To monitor the state of an autonomous system, the most relevant examples

of sensors are strain, temperature, and humidity. In general, a sensor needs to be chosen in accordance with the whole setup. Low initial resistance is beneficial for applications with minimal power consumption. In contrast, higher initial resistance facilitates the read-out due to lower technological demands for the same measurement accuracy. A relative sensitivity of e.g. 1 % results in a larger absolute change for a larger initial value. The demands and functionality will be discussed in the following.

2.1.1 Strain Sensing

Resistive strain sensors exhibit a change of electrical resistance due to a change in geometry. The resistance R of a conducting line is defined as

$$R = \rho \cdot L/A, \tag{2.1}$$

where ρ is the material's resistivity, L the length, and A the cross section. For tensile (compressive) strain, L is increasing (decreasing) while A is decreasing (increasing) since the volume remains constant. This leads to a rise of R for tensile and a reduction of R for compressive strain. The description holds true for metals but becomes more intricate with semiconductors, as strain changes the crystal structure and thus also the band structure, which defines the specific resistance. The amount of strain $\epsilon(t)$ at a given time t can be described as

$$\epsilon(t) = \frac{L(t) - L_0}{L_0}, \tag{2.2}$$

where $L(t)$ and L_0 are the length at time t and in relaxed position, respectively. The relationship between the different parameters is summarized in Table 2.1. To comparatively quantify the

Table 2.1: Changes for tensile and compressive strain for strain ($\Delta\epsilon$), length (ΔL), cross section (ΔA), and resistance (ΔR).

	$\Delta\epsilon$	ΔL	ΔA	ΔR
Tensile	>0	>0	<0	>0
Compressive	<0	<0	>0	<0

sensitivity of a strain sensor, the gauge factor (GF)

$$GF = \frac{\Delta R}{R_0} \cdot \frac{1}{\epsilon} \tag{2.3}$$

is used. It quantifies the change in resistance ΔR with respect to the initial value R_0 for any given strain. Commercial strain gauges are specified with GF of ca. 2 [29].

Based on these primary considerations, an appropriate starting point for sensor design and material can be chosen for a given application. Long-term effects such as fatigue due to crack formation or intrinsic material changes must be studied for a more detailed approach. A further prerequisite for printed strain sensors is a flexible substrate.

2.1.2 Humidity Sensing

Temperature and relative humidity are the two most critical environmental parameters to monitor during shipment or quality control. Humidity sensors are capable of determining the relative humidity (RH) of the environment, which is defined as the ratio of the amount of moisture content

of air to the maximum (saturated) moisture level that the air can hold at a given temperature and pressure [30]. The working principle of such sensors is the change in physical or electrical properties of the sensing layers with variation in relative humidity. The most common types of humidity sensors are resistive or capacitive: for the former, water vapor alters the electrical resistivity of the sensory layer, while it changes the dielectric constant and hence its capacitance for the latter. This hygroscopic response relies on adsorption and desorption of water molecules. In general, humidity sensitivity increases with porosity due to the expanded surface area. This plays a pivotal role in low RH conditions, while at high RH, the mesopore volume and capillary condensation become more important [31]. The resistive sensor type will be used in this work, where the sensing mechanism is the electronic-ionic type. For low RH levels, electron donations from water molecules are responsible for changes in the conduction. At high RH levels, ionic conduction based on proton hopping between water molecules will be the dominant mechanism [30]. The resistance response will be described by the exponential relationship $R(RH) = A \cdot \exp[k \cdot RH]$, with the coefficient A and k, which can be regarded as a resistive humidity coefficient.

2.1.3 Temperature Sensing

The electrical resistance depends on the temperature differently for metals and insulators. The change of electrical resistance R with temperature T is given by the temperature coefficient α as $dR/dT = \alpha\, R$, leading to the relationship

$$R(T) = R_0 \exp(\alpha(T - T_0)). \tag{2.4}$$

For conductors, the first-order Taylor series approximation for resistance R_c around T_0 yields the known linear relationship with $\alpha > 0$ (positive temperature coefficient, PTC):

$$R_c(T) = R_0(1 + \alpha(T - T_0)). \tag{2.5}$$

Semiconductors exhibit a strong non-linear relation between resistance R_c and T due to the exponential excitement of charge carriers from the valence to the conduction band. The excited carriers lead to enhanced conduction and, therefore, to a negative temperature coefficient (NTC). One of the first NTCs was reported by Michael Faraday. In 1833, he reported for silver sulfide

> "I have lately met with an extraordinary case [...] which is in direct contrast with the influence of heat upon metallic bodies [...] On applying a lamp [...] the conducting power rose rapidly with the heat [...] On removing the lamp and allowing the heat to fall, the effects were reversed." [32]

One way to describe this behavior is via the single parameter $\beta_{T_0/T}$, of unit K. This empiric approach is used for commercial sensors and characterizes the temperature behavior between the base temperature T_0 to the end of the fitting range T:

$$R_s(T) = R_0 \exp\left(\beta\left(\frac{1}{T} - \frac{1}{T_0}\right)\right). \tag{2.6}$$

Common NTC materials exhibit a range from $\beta = 2000 - 5000\,\mathrm{K}$. The values for β are given for a specific temperature range, e.g. the company TDK gives values of $\beta_{25/100} = 1483\,\mathrm{K}$, $\beta_{25/85} = 1780\,\mathrm{K}$, and $\beta_{25/50} = 3854\,\mathrm{K}$ for the same material [33]. Therefore, experimental calibration is required to specify the thermal response for a given range. For more detailed and universal characterizations, the Steinhart-Hart equation can be used [34]. However, it will not be used in

this thesis as it is also an empirical description, but the parameters lack physical meaning and are not transformation invariant [35].

2.1.4 State-of-the-Art of Printed Sensors

Printing technology is already well established to fabricate many groups of electrical devices. Temperature sensing is one of the most fundamental sensing applications, as virtually any material exhibits thermoresistive behavior, making it accessible to many researchers. Additionally, most devices need to account for this behavior to compensate for cross-sensitivity. One possible application for printed temperature sensors is to aid healthcare monitoring. Here, wearable sensors have undergone rapid growth due to their unique properties such as mechanical flexibility, lightweight, and potential bio-compatibility [36]. Organic-inorganic hybrid and nano-composite materials are deposited on flexible substrates by various printing technologies. For example, a fully printed and passivated PEDOT:PSS-based temperature sensor on PET has been demonstrated to exhibit excellent stability in humid environments [37]. Carbon nanotube-based thermistors are promising as the negative resistance response distinguishes it from the contributions of metal electrodes. Screen printing can be utilized to fabricate a thermistor capable of measuring temperatures from -40–100 °C [38]. Furthermore, inkjet printing of Ag-NPs and PEDOT:PSS on paper can be used as a multiparametric sensor array for temperature as well as mechanical stress, and humidity [39]. The temperature coefficient of resistance for printed sensors based on conducting materials is around 0.3 %/°C for inkjet-printed Ag meanders, and -0.77 %/°C for PEDOT:PSS [36, 37].

One intriguing property of printed pressure or strain sensors is the application for on-skin electronics. These can be used for human-machine interfaces, sports performance monitoring, or healthcare. A recent review from Li *et al.* pointed out that a variety of printing techniques, e.g. screen printing, inkjet printing and direct ink writing are employed for this application [40]. The most common sensing mechanism is resistive and capacitive [41], where the first will also be investigated in this thesis. Metal- and carbon-based materials are used in the form of metal nanowires [42] or nanoparticles [43], as well as carbon nanotubes [44] or carbon black [45]. Challenges that must be addressed are long-term stability, cross-sensitivity between different strain directions, and reliable printing results. Different printing techniques have their respective advantages that need to be evaluated for sensor properties as well as roll-to-roll processing to achieve large-scale production [40]. The sensitivity is described by the gauge factor (GF, s. Eq. 2.3) and is reported e.g. around 6–60 for screen-printed Ag-NPs in a PDMS matrix and ca. 20 for non-contact printing techniques [40].

Humidity is a critical parameter for environmental analysis, as it is associated with the stability of materials and equipment [46]. Mattana *et al.* presented a study comparing resistive temperature and capacitive humidity sensors fabricated by photolithography (Cr/Au) and inkjet printing (Ag-NPs) [47]. Both techniques delivered a temperature sensor with linear response and comparable sensitivity, and both were able to detect humidity variations but with long response times. In a hybrid approach, screen-printed TiO_2 nanoparticles are shown to exhibit high sensitivity in the range of 24–90 %rH [48]. Zhang *et al.* showed that gravure-printed CNTs on polyimide can also be utilized for resistive humidity monitoring [49]. The performance is evaluated by the accessible humidity range as well as the response time, which can be as wide as 11–95 %rH and response times as low as 5 s [30].

Overall, printed sensors are intensely investigated on a lab-scale and utilized for the integration on complex surfaces for commercial applications. These can already be found in control panels in the automotive industry [50], in smart tags for cold chain monitoring in the food industry [51], or

active health monitoring for patients [52].

2.2 Battery

A battery is an electrochemical cell that consists of a positive and a negative electrode separated by an electrolyte which can conduct ions between the electrodes but acts as an electrical insulator [53]. A zinc-carbon battery is used within this work, where the positive mass consists of MnO_2 and the negative mass of Zn. This is the same combination as in one of the first batteries, the Leclanché element, where NH_4Cl was used as electrolyte [54]. Zn-MnO_2 batteries are well established due to their low cost, high safety, and simple manufacturing. The facile fabrication and recycling potential provides advantages for environmental and economic considerations [55].
Batteries can be divided into two categories: primary batteries are cells intended to be used until exhausted and then discarded (non-rechargeable); secondary batteries (or accumulators) are cells where the original charged condition can be restored after usage by an opposite flow of current (rechargeable) [56]. Even though the principle behind this cell was developed 150 years ago, researchers pursue to create rechargeable Zn-MnO_2 cells [57, 58] and to obtain screen-printed, planar micro-batteries [27].

The layout of the screen-printed battery can be seen in Figure 2.1 a). The planar design facilitates the printing procedure and achieving thinner batteries, which is beneficial for bending properties. Additionally, it requires no separator to minimize the influence of short-circuit issues caused by dendrite growth [59] with electrode distances on the millimeter scale. It also optimizes ion transport dynamics in the two-dimensional direction even under bending stress [60]. The disadvantage of this approach is that the active area is limited compared to a stacked setup. The planar design contains several fingers to maximize the area where the active materials face each other to overcome this issue. The number of fingers can be increased to gain a higher capacity. Figure 2.1 b) shows the cross section of a battery along the orange dashed line in a). The step-by-step printing process becomes apparent from this figure: first, a Ag current collector is printed. Then, highly conductive carbon is applied to cover it. This is necessary because Ag is also electrochemically active and must be protected from contact with any of the other active materials. In the next step, Zn is printed on the inner branch, and MnO_2 is added on the outer branch. By applying the electrolyte, the cell is activated and can supply an initial open-circuit voltage V_{OC} of ca. 1.35 V [57]. This value is taken across the terminals when no external current flows. The anode (-) reaction usually occurs at lower electrode potentials than at the cathode (+). For the discharge in a Zn-MnO_2 battery, Zn acts as the anode, where the oxidative chemical reaction releases electrons; MnO_2 is the cathode, where the reductive reactions gain electrons from the circuit [56].
The description of the reaction mechanism is complex due to the variety of different crystal structures of MnO_2 [55]. For the example of α-MnO_2, the reactions can be summarized as [55, 61]:

$$\begin{aligned} &\text{Anode :} && \mathrm{Zn^{2+} + 2e^- \longleftrightarrow Zn} \\ &\text{Cathode :} && \mathrm{MnO_2 + H^+ + e^- \longleftrightarrow MnOOH} \\ &\text{Cathode :} && \mathrm{2MnO_2 + Zn^{2+} + 2e^- \longleftrightarrow ZnMn_2O_4.} \end{aligned}$$

The parameters to assess the performance of a battery for printed devices are the open-circuit voltage V_{OC}, internal resistance R_i, and rated capacity C. V_{OC} is the voltage across the terminals of a cell when no external current flows. For non-ideal power sources, R_i summarizes contributions in resistance from the different components of the battery, resulting in internal losses. It can be determined by measuring V_{OC}, and V_s over a series load resistance R_s in series. This acts as a

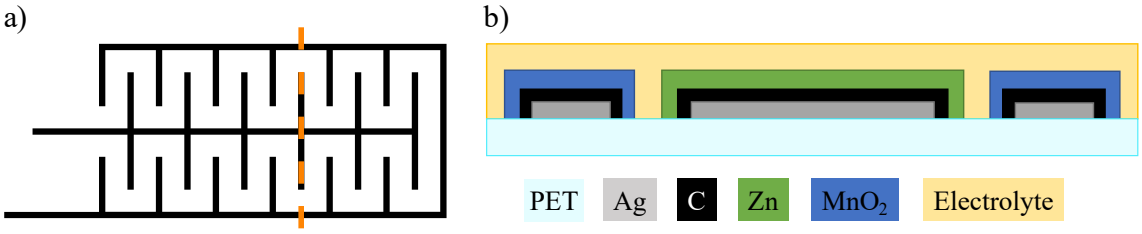

Figure 2.1: a) Planar layout of screen-printed battery. b) Cross section through the battery on PET substrate along the dashed line in a): the current collector (Ag) is protected by conductive carbon paste (C) to prevent it from reacting with the electrochemical electrodes (Zn, MnO_2) that are connected via an electrolyte.

voltage divider, and R_i is given by

$$R_i = \frac{V_{OC} - V_s}{V_s} \cdot R_s. \tag{2.7}$$

C is the total amount of electricity produced by the cell reaction and is most relevant to design the size and geometry of the battery to ensure sufficient current [56, 62]. Ideally, it is obtained from a new, conditioned battery subjected to a constant-current discharge at room temperature. The gradually decreasing voltage during this process is measured, and a threshold voltage V_{th} is defined where the battery is considered empty (s. Fig. 2.2). When V_{th} is reached, C is calculated as

$$C = \int_0^{t(V_{th})} I_{dis} dt \overset{I=const.}{=} I_{dis} \cdot t(V_{th}), \tag{2.8}$$

for constant discharge current I_{dis}. To compare capacities for different batteries, the rated capacity or C-rate is introduced. A x C-rating means that the battery takes $1/x$ hours for a full discharge. For example, an ideal battery with $C = 100\,\text{mAh}$ provides 100 mA for 1 h at 1 C, 200 mA for 1/2 h at 2 C, or 20 mA for 5 h at 0.2 C. Due to R_i, low discharging will yield higher values for C because less self-heating occurs. Finally, analogous to capacitors, individual battery cells can be combined in series or parallel. Serial connection leads to the summation of individual voltages, while parallel connection results in higher current or capacity, respectively.

Within this work, screen-printed single-cell Zn-MnO_2 primary batteries are used. The required materials are commercially available or obtained from a small cooperative company specializing in printed batteries. The advantages of Zn-MnO_2 compared to Li-ions are safety and environmental standpoints. For non-printed batteries, Li-ion systems use flammable electrolytes, making them hazardous and requiring sophisticated safety and thermal management components [63]. The abundance of raw materials for Zn-MnO_2-based systems makes this setup ideal for cost-efficient and practical solutions. Furthermore, the system provides sufficient voltage and current to power a possible memory cell and sensor combination. The screen-printed current collector made from Ag could also be used to create large-scale, flexible circuits and might be utilized as a common material for a memory cell.

2.3 Resistive Switching

This section will illustrate the fundamentals of resistive switching (RS). Here, information is stored as logical states ”0” and ”1” in the resistance of a memory cell. RS can be found under the labels Electrochemical Metallization Memory (ECM), programmable metallization cell or conductive bridging random-access memory (CBRAM) [64]. The mechanism for RRAM used throughout this

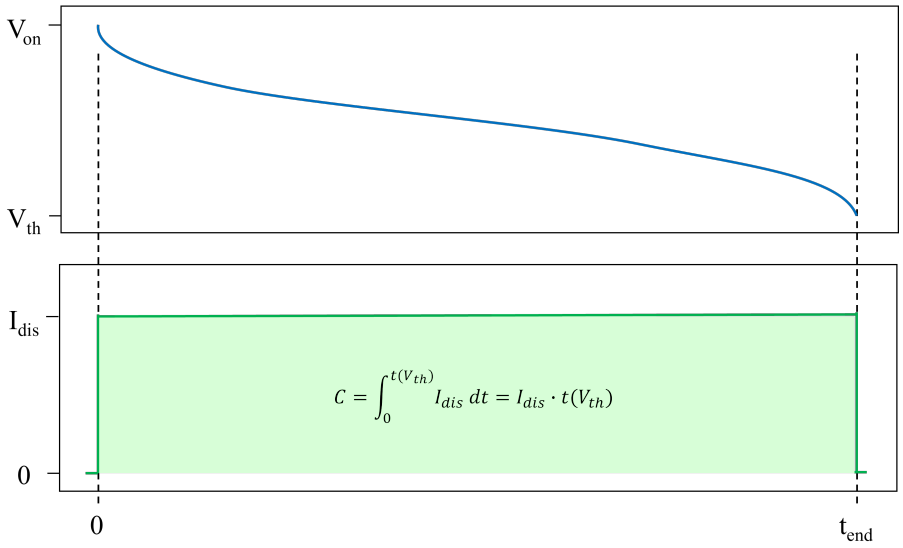

Figure 2.2: Schematic galvanostatic discharge curve for a battery. The upper curve shows the decrease of voltage over time with a constant discharge current I_{dis}. The measurement stops at threshold voltage V_{th} and capacity C is calculated by the given formula (s. Eq. 2.8).

work will be described as Electrochemical Metallization Memory (ECM).

It consists of a tri-layered conductor-insulator-conductor structure. In general, the initial high resistive state (HRS) measured between both electrodes is determined by the resistance of the insulating or dielectric layer. A conductive filament can bridge this barrier by applying a voltage across the electrodes. This filament gives the resistance of the resulting low resistive state (LRS). The technology itself has been known for around 60 years since the demonstration of resistive switching phenomena in different oxide materials [65, 66]. One of the first demonstrations of this non-volatile memory that spurred new interest in this technology was presented in 2004 with silver and copper layers combined with different solid electrolytes and an inert electrode [67]. The same mechanism was used to demonstrate a quantized conductance atomic switch in Ag_2S [68]. More and more ideas and applications have developed over time to e.g. enable neuromorphic computing [69, 70, 71]. The advancement of this technology is not limited to fundamental research anymore but can be found in commercial products. One example is the company NEC which uses its NanoBridge-series to provide power-efficient and radiation-tolerant field programmable gate arrays [72, 73].

In the following, fundamental electrochemical reactions and mechanisms of formation and rupture of the metallic filament will be discussed, and how it can be utilized for memory applications.

2.3.1 Switching Mechanism of Electrochemical Metallization Cells

The description and explanation of the switching mechanism of ECMs will be given based on the model of a modulating tunneling gap [74] and a varying filament size [75]. Considerations regarding switching kinetics are based on [76] and more elaborate or detailed information concerning RS can be found in [77]. The basis for the different descriptions of the switching mechanism and analytical modeling relies on the same assumptions. The ECM cell is switching between the (pristine) HRS and LRS through the formation and rupture of a metallic filament (Fig. 2.3 A–D).

Distinct resistive states can store information in logical states: 1 for LRS or 0 for HRS. The filament is created by applying a positive bias V to the active electrode (AE), usually consisting of Ag or Cu, while the inert counter-electrode (CE) is grounded. The occurring redox reaction [79]

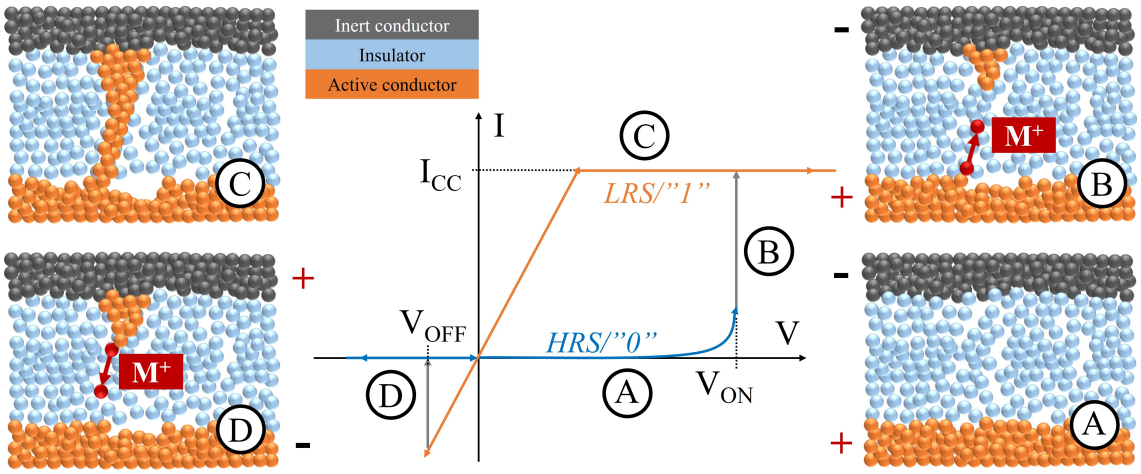

Figure 2.3: Switching mechanism of an ECM. A) High resistive state (HRS); B) Ions migrate towards the counter electrode (SET process); C) Filament is formed and low resistive state (LRS) is set by compliance current (I_{cc}); D) Filament is dissolved to return to HRS under reversed voltage. Adapted from [78].

consists of two parts: The bias oxidizes the metal (M) and leads to ion formation:

$$M \rightarrow M^+ + e^-. \tag{2.9}$$

A local electrical field $E = V/d$ is induced as in a capacitor by V over the insulating layer with thickness d. The ions are accelerated along the electrical field E towards the CE, where they are reduced:

$$M^+ + e^- \rightarrow M. \tag{2.10}$$

During the filament growth from CE towards AE, E is further increased due to the reduced separating distance d. It is assumed that different, parallel filaments start to form during this process. However, the dynamic growth leads to a self-accelerated process and results in a *the-winner-takes-it-all* scenario [80]. The smallest gap experiences the highest electric field and, therefore, the fastest growth until the SET process stops, as it bridges the insulating layer and the electrical field collapses. Defects and nano-pores within this layer facilitate the ion migration [81] and can even confine metal filaments locally in a defined channel based on engineered dislocations [82]. For RESET, filament atoms oxidize at random positions depending on the potential drop between filament and electrolyte and are removed from the filament. At the same time, Joule heating plays a minor role [80].

During operation, the ON state can be tuned by the current compliance. The diameter of the created filament, and hence R_{LRS}, can be controlled by limiting the allowed current as $R_{LRS} \propto I_{Set}^{-1}$. This is a prerequisite for the RESET process, where the filament gets partially dissolved. An uncontrolled SET process would lead to an irreversible filament, unsuitable for repeated writing and erasing cycles. The RESET current is proportional to the SET current ($I_{Reset} \propto I_{Set}$) and usually smaller ($I_{Reset} < I_{Set}$). In a descriptive model, higher I_{Set} creates thicker filament (Φ in Fig. 2.4) and therefore allows control of LRS. This controllable formation allows the storage of more than two logical states per cell. Dividing the OFF/ON range into four distinct states, namely the OFF-state and three different ON-states, enables multi-bit storage ("00", "01", "10", "11") which increases the potential storage density [74]. The data shown in Figure 2.5 illustrates this more

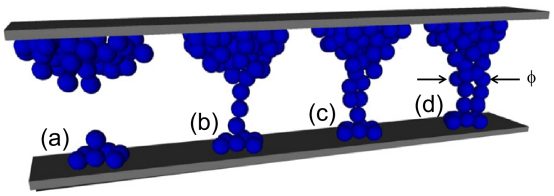

Figure 2.4: Filament growth model for the SET process in RRAM switching. A positive bias is applied to the top electrode, leading to the migration and nucleation of ions towards the bottom electrode, causing the formation of the conductive filament. Initially, no bridging filament is present (a), but higher I_{cc} leads to thicker filaments with diameter Φ (b–d) and decrease in R_{LRS} [77].

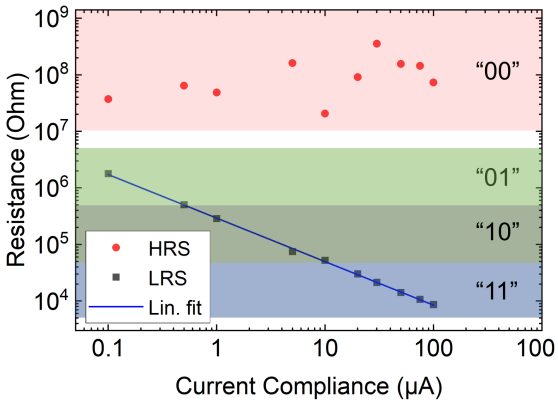

Figure 2.5: Experimental resistance values for HRS and LRS in an ECM consisting of Cu/Cu_xS/W with different current compliances. Assigning several logical states to the accessible range enables the storage of more than 1 bit per memory cell. The ranges are at least one decade in the logarithmic scaling, allowing for facile read-out and tolerating device variations. (Cf. [74])

graphically. The logical state "00" is assigned to the HRS for values larger than $10^7\,\Omega$. By choosing a current compliance below $0.5\,\mu A$, the LRS is in the range between $5 \cdot 10^5\,\Omega - 5 \cdot 10^6\,\Omega$, i.e. the logical state "10". Altering I_{cc} leads to a different LRS and hence to the other logical states. One decade in resistance per state facilitates the read-out and allows for some variation in the switching behavior. The read-out occurs with a voltage far below the switching threshold to preserve the state.

The modulation of the filament size itself does not fully explain the vast range of OFF/ON ratios of $> 10^6$ for small currents. One analytical model attributes this behavior to the modulation of a tunneling gap x between the filament and the active electrode. In this case, no galvanic contact is formed, and the strong non-linear kinetics is described by the exponential current dependency of the Simmons tunneling current on x.

There are still ongoing discussions about the best physical representation of the SET process [83]. Instead of the filament growing from CE towards AE, it can also be assumed that atoms from the active electrode are accelerated to an existing local protrusion and deposited there. This leads to the growth of this protrusion towards the CE and eventually stops once it reaches it [84]. In both cases, the filament growth rate is controlled by E and strongly dependent on the gap size.

However, the filament can spontaneously break, even though ECMs are non-volatile memories. This is due to the large surface-to-volume ratio of the filament and thus being susceptible to self-diffusion and Ostwald ripening [85]. Ostwald ripening describes the dissolution of small crystals and the redeposition of the dissolved species on the surfaces of larger crystals. The process occurs because smaller particles have higher surface energy, hence higher total Gibbs energy, than larger

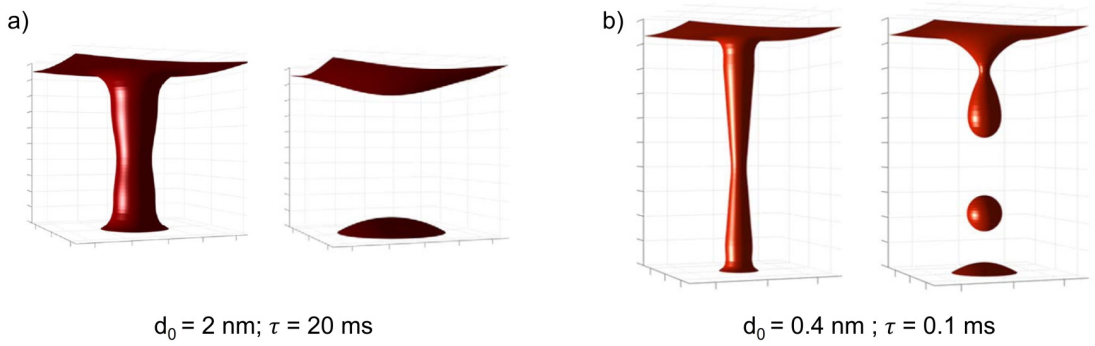

Figure 2.6: Simulation of filament rupture due to self-diffusion. a) Ag filament with an initial diameter $d_0 = 2\,\text{nm}$ has a lifetime $\tau = 20\,\text{ms}$, b) while a thinner filament with $d_0 = 0.4\,\text{nm}$ only exhibits $\tau = 0.13\,\text{ms}$. Adapted from [85, 91].

particles [86, 87] Figure 2.6 shows the morphological changes induced by surface diffusion for conductive Ag filaments with initial diameters (a) $d_0 = 2\,\text{nm}$ and (b) $d_0 = 0.4\,\text{nm}$, respectively. The lifetime of the filament decreases from around 20 ms (a) to about 0.13 ms (b) [85]. This spontaneous dissolution has also been experimentally observed and assigned to Ostwald ripening [88]. For inkjet-printed ECM cells, it was demonstrated that for small compliance currents of 10 µA, the weak filament comprised of nanoclusters is readily ruptured by thermal agitation once the electric field is removed [89]. Furthermore, Ostwald ripening can also be utilized for sinter-free printing of conductive films, where Ag-NPs of 15 nm are sintered by spontaneous coalescence driven by minimizing the surface-to-volume energy [90].

2.3.2 Requirements for Materials

This subsection introduces the foundation to assess the feasibility of materials for RS applications and describes the materials used. The three different layers, active electrode (AE), insulator, and counter electrode (CE) differ in the variety of investigated materials. In most cases, the AE is made of Ag or Cu due to their low oxidation potential $E^0(\text{Ag}^+/\text{Ag}) = 0.80\,\text{V}$, $E^0(\text{Cu}^{2+}/\text{Cu}) = 0.34\,\text{V}$, $E^0(\text{Cu}^{2+}/\text{Cu}^+) = 0.16\,\text{V}$, and $E^0(\text{Cu}^+/\text{Cu}) = 0.52\,\text{V}$ (at 25 °C, half-reaction relative to the standard hydrogen electrode) [92]. One of the requirements for the insulator is that the dissolved ions need to be easily conducted through it. A vast number of materials fulfill this condition, from the prototypical Ag conductors As_xS_y and related chalcogenides to oxides such as SiO_2. These oxides can also conduct ions due to very thin layers, decreasing the travel distance for ions [78]. Also, metal cations' migration benefits from defects in the insulating layer. It was shown that Ag cations have a higher diffusivity in sputtered defective SiO_2 than in the densely packed clusters of PECVD-grown SiO_2 [93, 94]. Additionally, ions should only be reduced at the CE and not already within the insulator. The Gibbs free energy of formation of oxides $\Delta_f\text{G}^\circ(\text{Ag}_2\text{O}) = -11.2\,\text{kJ/mol}$ and $\Delta_f\text{G}^\circ(\text{CuO}) = -129.7\,\text{kJ/mol}$ are relatively small and consequently only show weak interaction with anions from the electrolyte [92, 95]. The CE material should not release ions during the operation, therefore metals with higher oxidation potentials such as Pt or Au are commonly used: $E^0(\text{Pt}^{2+}/\text{Pt}) = 1.12\,\text{V}$, $E^0(\text{Au}^+/\text{Au}) = 1.83\,\text{V}$ [92].

Finally, practical, application-related aspects need to be considered as well. For comparison, Cu cations have lower mobility compared to Ag cations in chalcogenides. Yet, it is desirable to understand and develop Cu-based RRAM cells due to the lower costs and possible CMOS compatibility [96]. While both, Ag^+ as well as Cu^+ ions have high solubility and mobility in

Ag_xS or Cu_xS, respectively, these solid electrolytes have low glass transition temperatures [97] limiting their back-end-of-line usage. This disadvantage however could become insignificant for low temperature, additive printing techniques. The following subsection will describe further benefits and potential for printed memory cells.

2.3.3 Advantages of Printed Memory Cells

The active electrodes used within this work consist of Ag or Cu in the form of printed and sintered nanoparticles (NPs) or as a thin thermally deposited layer on a Si substrate. Some initial experiments will be carried out for feasibility studies and reference measurements on wafers. The goal is to achieve a fully printed memory cell or even a fully printed autonomous device consisting of energy supply, sensors, and memory. As described above, RS memory cells exhibit many promising features such as non-volatility, low energy consumption, and a simple three-layer setup. These properties are also accessible using printing technology.

Printed memory cells are characterized by larger feature-sizes than cells from thin-film technology in the nm-range, as the latter allows for atomic precision. But it offers opportunities for customized designs, inexpensive materials, and decentralized fabrication due to the relatively low technology demands compared to traditional clean-room technologies. Feature-size is of secondary importance, when the substrate for smart health monitoring or intelligent packaging offers many cm^2 that can be used. Inhomogeneities during the printing process could reduce the amount of switching cycles, sufficient for applications requiring only 100–1000 cycles, such as disposable smart labels. Overall, printing approaches can complement instead of competing with existing clean-room fabrication and extend resistive switching to large-scale applications with less sophisticated requirements.

2.3.4 State-of-the-Art of Printed Memories

A recent and extensive review of progress in solution-based RRAM devices and printed devices in general can be found by Carlos, *et al.* [98]. In their overview, they show that only 6 % of the publications on solution-based RRAM devices are done via printing techniques, and about 65 % are processed using high thermal annealing processes above 200 °C which is not suitable for most flexible substrates such as PEN or PET. The development from processes including spin coating and high-temperature post-treatment steps to less demanding printing technology is essential for the transition towards high-throughput fabrication to take advantage of the benefits as stated in the previous section.

The first printed RRAM device was presented in 2012 by Rahman *et al.* [99], using a symmetric $Ag/TiO_2/Ag$ structure and electrohydrodynamic printing, which is a more complex and demanding form of inkjet printing. They demonstrated flexibility and a stable performance even after hundreds of bending tests. In combination with a low curing temperature of 150 °C, they proved the potential to utilize printing techniques for memory applications. Nau *et al.* demonstrated the first fully inkjet-printed RRAM cell in 2015 with symmetric Ag/poly(methylmethacrylate)/Ag cells [100]. They suffered still from low yield of $< 20\%$ but the evolution towards better performance and printability is obvious. Noticeably, Huber *et al.* presented in 2017 a fully inkjet-printed flexible RRAM cell based on asymmetric Ag/spin-on-glass/PEDOT:PSS cells where the transparent, conductive polymer PEDOT:PSS acts as CE. The authors showed low switching voltages, low write currents, high OFF/ON ratio, and yield over 70 % in cooperation between Prof. Ruediger's group at the INRS and the Munich University of Applied Sciences. More and more focus is put on (partially) printed cells, as can be seen from recent publications in 2021 from Hu *et al.* showing

RS devices based on Ag/ZnO/Au, where the Au electrode is thermally evaporated [101]. Or by new materials becoming usable via inkjet printing such as the multiferroic $BiFeO_3$ [102], which has promising features such as controllable leakage current.

A next step towards high volume production of fast and cost-effective RRAM devices was presented in 2021 by Strutwolf *et al.* [5]. They use flexographic roll-to-roll printing technology to fabricate Ag/PMMA(PVA)/ITO cells, where the insulating layer consists of poly(methyl methacrylate) (PMMA) with a surplus of poly(vinyl alcohol) (PVA) and indium tin oxide (ITO) as the inert electrode. Even though this system relies on brittle and pricey ITO and Ag electrodes are fabricated using stencil printing, the PMMA(PVA) layer can be applied with a printing speed of 30 m/min, proving the scaling possibilities. In a different approach, Ramon *et al.* demonstrated in 2021 the scaling of WORM (Write-Once-Read-Many) memory which is not considered an RRAM device and cannot be rewritten and therefore only used in simpler applications [103]. However, the transition from the lab-scale Dimatix Materials Printer DMP2831, which is used within this thesis, to the large-scale inkjet printer DMP3000 encourages the vision for the potential of large quantity inkjet-printed electronic devices.

In general, for characterization and assessment of resistive memory cells, different aspects need to be considered [104, 105]. A threshold for the ratio OFF/ON has to be defined to distinguish different logical states. A larger difference facilitates the read-out and allows for some cell-to-cell variation for a functioning device. A ratio of 5 can be sufficient for some applications, a smaller ratio might suffice for proof-of-principle works, while the demands are higher for commercial implementations. Quasi-static voltage sweeps often obtain the switching voltages but these findings may differ for practical applications with voltage pulses. Therefore, the acquired characteristic values for an ECM are valuable results to improve the performance, but they need to be considered with certain limitations.

2.4 Integrated Multi-Component Systems

To illustrate the interaction and co-dependencies of different components, the virtual journey of the current can be traced, originating from the power source, altered by the sensor, and changing the logical state of the memory.

The first fundamental property to acknowledge is that no ideal power source exists, where the output voltage to a load would be independent of the load resistance. A counterexample can validate this: For an infinite resistance in an open circuit, no current flows and the ideal power source provides no power. The voltage remains constant for any load resistance R_L while more current flows for smaller loads. This leads to a diverging current for a vanishing load resistance in the case of a short circuit. As there cannot be an infinite power supply, ideal power sources do not exist. For commercial batteries, the internal resistance R_i of a battery is usually in the order of 0.1–1 Ω [106]. Therefore, in circuits where $R_i \ll R_L$, batteries can still be treated as an ideal power source, as the voltage V drops proportionally to the resistance R. Furthermore, Joule heating during the discharge does not affect low-rate applications [56]. For printed Zn-MnO_2 batteries, R_i is reported to be in a wider range in the order of 0.1–10 Ω [107, 61], due to contributions from the electrolyte and larger structures. So, a printed battery may bring a higher R_i and therefore is more suitable to power high resistance applications, where it still can be treated as an ideal power source.

This is in accordance with the resistance range of RRAM cells with $R_{OFF} >$ MΩ and tuneable ON state. Usually, the ON state is controlled during the characterization via an active current limiter of a source measure unit. One solution in a fully printed, autonomous system is a series

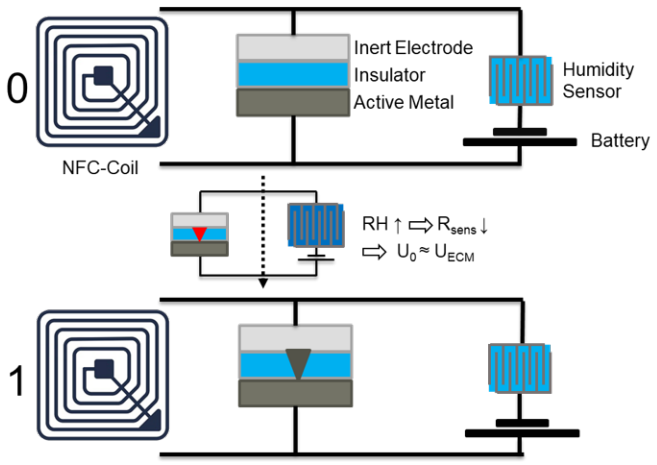

Figure 2.7: Scheme of components for fully printed event detection system. Originally, the memory cell is in the HRS in series with the NFC coil circuit. When the resistance of the humidity sensor decreases, there is sufficient voltage in the battery so that the memory cell changes to the ON state. Now this change can be read out contact-less by the closed NFC coil.

resistor R_S for passive current limitation. It needs to be in the same order of magnitude as R_{ECM}, to enable voltage-induced switching. For a practical example, a battery providing at least $V = 1.0\,\mathrm{V}$ and a short-circuit current of $10\,\mathrm{mA}$. To achieve a current compliance I_{cc} of $0.5\,\mathrm{mA}$ leading to an ON resistance of the ECM $R_{ON} \approx 250\,\Omega$, R_s should be about $1.75\,\mathrm{k}\Omega$ ($R_s = V/I_{cc} - R_{ON}$). However, this must be taken only as a first estimate since the series resistor also alters the voltage applied at the ECM.

Instead of a simple resistor, a resistive sensor could be used to realize event-detection systems as in Figure 2.7. This sensor would be similar to R_S as described above but changes its resistance $R_{Sen}(RH, T)$ with environmental conditions like relative humidity (RH) or temperature (T). A memory cell could be implemented in the coil of an NFC (near field communication) unit for this purpose ($R_{NFC} = R_{Coil} + R_{ECM}$). The coil cannot be read out since the cell has a very high resistance. At the same time, the cell is connected in series to a sensor and battery. The humidity sensor has a higher resistance and therefore a higher voltage load than the cell ($R_{Coil} \ll R_{ECM} < R_{Sen}$). In this configuration, V_{ECM} is not sufficient to switch the logical state of the cell. At higher relative humidity (RH), the system changes to $R_{ECM} \approx R_{Sen}$, so that a higher voltage is now applied to the cell, triggering the SET process. This non-volatile state change is maintained; thus, the NFC unit can be read out. As a result, the high humidity event is permanently stored and can be read out without contact.

In conclusion, the different components need to be characterized individually to assess their performance. But more importantly, they must be compatible on different levels. Firstly, they are ideally printed on the same substrate and consist of a minimum of different inks to preserve the advantage of simplicity. Secondly, printing techniques need to be chosen accordingly: the screen-printed battery requires more active material to obtain sufficient capacity to power the device. The ECM on the other hand demands a sufficiently thin insulating layer for functioning, which can only be achieved using inkjet printing. Lastly, the physical parameters need to fulfill specific requirements. The battery's voltage output needs to provide sufficient voltage to alter the logical state of the ECM. This needs to be valid even when a sensor is integrated and therefore reduces the voltage drop at the memory cell. At the same time, a current limiter needs to be in the appropriate order of resistance to limit the current to prevent an irreversible SET process.

2.5 Potential of Components

Material Costs

One way to compare screen- and inkjet-printed electronics is the production cost of consumables. Table 2.2 presents the dimensions and estimated material costs to print a $l = 5\,\text{cm}$ long conductive track of Ag. The necessary wet ink volume $V(\text{ink})$ to print this track is calculated by

$$V(\text{ink}) = (w\,h\,l)/c(\text{Ag}), \tag{2.11}$$

where w and h are the width and height of the dried and cured structures, respectively. Importantly, inkjet-printed lines are significantly smaller than the screen-printed pendants. The volume is adjusted to the Ag content $c(\text{Ag})$, as the required wet ink should be compared. Inkjet printing ink requires lower viscosity, as its rheological properties must obey certain restrictions (s. Sec. 3.1.3). The ink contains more solvents and less solid contents, and thus relatively more ink is used by inkjet printing compared to screen printing. Following these considerations, the required ink volume for inkjet is still lower by a factor of 50. On the other hand, Ag-based screen printing ink is less technologically demanding and already established for large scale fabrication. This results in screen printing ink prices around US$ 500 for 1 l, while inkjet ink is not manufactured in the same quantities and costs ca. US$ 10,000 for 1 l. However, the overall cost for a 5 mm long printed Ag electrode is 2.5 times lower for inkjet printing (s. Tab. 2.2).

Table 2.2: Cost analysis for 5 mm long conductive Ag electrode printed with inkjet or screen printing. Width w, height h, and length l are typical values for the dried lines. The Ag content is given to compensate for lower Ag load in inkjet inks for required wet ink volume. The cost is given by the applied ink and price per ml. The screen-printed line is 2.5 times more expensive than by inkjet printing.

	w [mm]	h [µm]	l [mm]	Ag cont. [%]	V(ink) [ml]	[US$/ml]	Cost [ct]
Inkjet	0.2	0.2	50	25	$8{\cdot}10^{-6}$	10	0.008
Screen	1.0	5	50	62	$4{\cdot}10^{-4}$	0.5	0.020

This calculation should only be regarded as a crude estimation of one aspect of the printing process. A more detailed investigation becomes arbitrarily complicated by including initial acquisition costs, fabrication and lifetime of screens, printing speed, or suitability for large scale applications. Still, the cost is a pivotal factor for the establishment of different techniques for printed electronics and shows that inkjet printing has the potential to challenge established processes such as screen printing. Another advantage of inkjet printing is the digital process making it attractive for small print runs because no individual screens are required.
Printing technology already facilitates the fabrication of organic photovoltaic (OPV) to compete with established technologies. The low-cost mass-production adopted from printing processes leads to cost reduction. With further improvements to their efficiency and lifetime, as well as cheaper material costs due to commercial scaling, OPV modules are expected to become more viable than Si-based panels [108].

Power Consumption

Another aspect is to evaluate whether the different components can be operated autonomously without an external power source, e.g. plugged into a wall outlet. Planar, screen-printed batteries require a larger footprint but are easier to fabricate and therefore more likely to be integrated into

roll-to-roll processes. A potential application for a printed battery in a device is to store information about an event in an ECM. One switching event for an ideal memory cell consumes ca. 1 pJ of energy [104]. Thin-film batteries deliver a volumetric energy density of around 10 mWh/cm^3, or 36 J/cm^3 [27, 61]. A planar battery with half the size of a business card (5×5) cm^2 and thickness of 0.01 cm possesses available energy of 9 J. This means that it could provide sufficient energy to theoretically switch a memory 10^{13} times, or 1 kb of memory for 10^{10} times. These crude approximations neglect many important aspects such as self-discharge and energy consumption of the logic and other components. However, it demonstrates that even a small printed battery has the potential to switch a memory cell multiple times. Thus, it is perfectly suitable for event detection or smart labeling applications, where only a few kB of memory and a limited amount of writing cycles are necessary.

Chapter 3

Materials and Methods

This work explores the possibilities of individual components for printed electronics and their combination for integrated systems. In the following, an overview of different printing methods is presented, and the requirements for the used inks are discussed. These methods and materials are then assessed for their capabilities to realize components such as sensors, batteries, and memory cells. Key factors are the possible feature size, compatibility with different substrates, and critical dimensions such as layer thickness. The content of this section was partially published by me as first author in cooperation with different co-authors [109, 110, 111]. As I did the main part of the written compilation of the contributions, excerpts from these publications will be used verbatim or paraphrased.

3.1 Printing Technology

3.1.1 Requirements for Printed Electronics

The possibilities and requirements for printed electronics differ vastly from conventional electronics. As discussed in Subsection 2.3.3 regarding advantages of printed memories compared to thin-film technology, both approaches have their respective strengths and weaknesses. Correspondingly, printed and conventional electronics have different application areas, therefore not rivaling but complementing each other. Thin-film technology offers high precision and accuracy down to the nm-scale in lateral and sub-nm-scale for vertical dimensions using techniques such as physical vapor deposition (PVD), magnetron sputtering, or thermal evaporation combined with lithography for structuring and patterning. The requirements for printed electronics differ on several levels:

- **Inks:** Materials or compounds are transferred as particles or precursors in solvents or as polymers
- **Substrates:** Substrate materials determine applications by their ink compatibility, wetting properties, and thermal stability
- **Feature size:** Printing technologies offer different ranges in printing resolution and speed
- **Variability:** Due to non-cleanroopm processes, more variability needs to be expected and accounted for in the design

These considerations will be discussed in the following for screen and inkjet printing that are used within this thesis. The demands for respective inks, and potential electronic components (battery, sensor, memory cell) are presented. Key parameters for the two printing techniques are

Table 3.1: Performance of inkjet and screen printing in terms of dynamic ink viscosity, critical linewidth, film thickness, minimum feature size, and printing speed for applications. Viscosity is given in the equal units mPa·s or cP [114, 115].

	Viscosity [mPa·s]	Linewidth [µm]	Thickness [µm]	Feature [µm]	Speed [m/s]
Inkjet	5–50	30–70	0.1–1	20–50	0.01–0.1
Screen	500–10,000	50–150	5–100	50–100	0.1–1

given in Table 3.1. These values are for commercial setups, while more sophisticated approach can achieve higher resolutions such as screen printing of conductive Ag tracks with 22 µm line width [112], or inkjet printing of line arrays below 5 µm [113].

3.1.2 Screen Printing

Screen printing is an established printing technique based on a stencil process that is traditionally used for media prints from large-scale billboards to small format T-shirts [116]. But it is also used for conductive or insulating patterns for printed flexible electronics [117] or printed circuit boards [2]. It is used to achieve high layer thickness but with a lower resolution. The principle of this technique is shown in Figure 3.1. The pattern on the screen is created via a UV-sensitive emulsion and a lithography step. The mesh itself is made of interlaced threads out of polymers or stainless steel in the range of 10–400 threads/cm, where a higher thread count provides a better print quality and lower printing thickness. The uncovered mesh area, thread count, and thread thickness determine the transferred volume and resolution. An appropriate mesh must be chosen to obtain the desired layer thickness, usually in the micron range. The squeegee transfers the ink and controls the spread of ink across the screen and removes excess ink from the mesh. Varying the pressure is used to control the thickness of the structure [116]. Inks used for screen printing have a viscosity in the range of 500–10,000 mPa s under no shear stress (cf. honey ca. 2,000–10,000 mPa· s [118]). This value decreases to ca. 1,000–3,000 mPa s during the printing process under shear stress, allowing the ink to flow through the fine mesh [114, 115]. Printing steps can also be repeated to increase the thickness. After printing, the structure usually requires a drying step eliminating residual solvents or UV exposure to cross-link polymers.

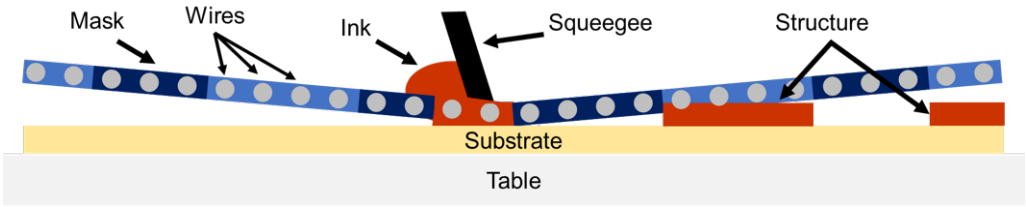

Figure 3.1: Schematic visualization of screen printing process. The mesh is made of interlaced wires that are partially covered by a mask. The squeegee transfers the ink through the openings onto the substrate to create the structure.

In the early laboratory phase, flatbed screen printing (FSP) offers decent quantity output by sheet-to-sheet (S2S) production. Here, individual planar sheets (or wafers) are getting printed on and taken out or moved on before printing to the next sheet. This process reaches the technical limitations for further increase in throughput. But the printing parameters from research efforts can directly be transferred to large-scale operations. One example is a rotary screen printing (RSP) prototype for solar cell metallization: In RSP, a rotating mesh-based cylinder continuously transfers ink onto a moving substrate. This principle was used to decrease the printing duration for a wafer

from over 1 s in a state-of-the-art FSP system down to 0.45 s [119]. This example of enhancement of more than 100 % printing speed motivates the research into small quantity fabrication that can be scaled up in the future.

3.1.3 Inkjet Printing

This section will explain the basic principles of drop-on-demand (DoD) inkjet printing, and possible applications in printed electronics.

Since the 1980s, inkjet printing has shown an impressive evolution in technology as well as areas of application. Starting from its first commercial uses in marking and coding, it became widespread as a home or office tool in the 2000s and is now established as an additive manufacturing method for printed electronics [120]. One of the main advantages that have driven this development is the digital, customizable design of printed images or structures. Instead of costly, time-consuming, and plate-making processes in traditional printing techniques such as screen or offset printing, a digital pattern is directly fabricated by inkjet arrays. While this method is also used on an industrial scale, rapid prototyping in additive manufacturing is a key benefit. It describes processes for rapidly creating a system or part representation before final release or commercialization [121].

The two main droplet formation technologies for inkjet printing are continuous mode and DoD mode. In the first mode, a steady stream of electrically charged ink droplets is ejected from the fluid reservoir and deflected by an electric field to the desired destination. The second mode (DoD) is used throughout the fabrication in this thesis and will be explained in detail: Here, individual drops are directly formed on-demand from the nozzle and deposited on the substrate. The ejection can occur via thermal or piezoelectric actuators. The principle of drop formation by piezo-actuator is depicted in Figure 3.2. An applied voltage leads to the deformation of the piezo element. At the beginning of each cycle, the biased actuator (0) is relaxed by bringing the voltage to zero (I), which pulls new ink into the chamber. Then, the chamber is compressed by a higher voltage (II) as initialization for the drop ejection. In the recovery phase (III), the chamber is refilled by returning to the initial bias [122]. This waveform is repeated with a frequency of up to 20 kHz [121].

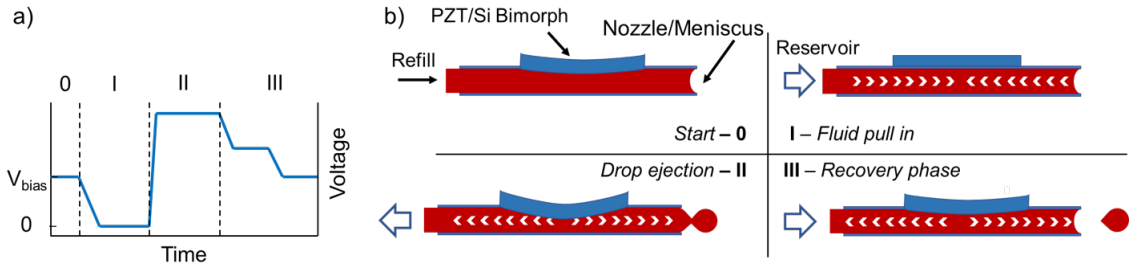

Figure 3.2: Stages of drop formation for piezo-driven drop-on-demand inkjet printer. a) Voltage waveform applied to piezo element at the nozzle. b) Illustration of chamber deformation and ink flow during different stages of drop ejection. Adapted from [122].

The waveform needs to be adjusted for each ink because the rheological properties and hence the jetting conditions vary significantly with density ρ, dynamic viscosity η, and surface tension γ. Different dimensionless groupings of these physical constants are used to describe the drop behavior, Reynolds (Re), Weber (We), and Ohnesorge (Oh) number:

$$Re = \frac{v\rho L}{\eta}, \tag{3.1}$$

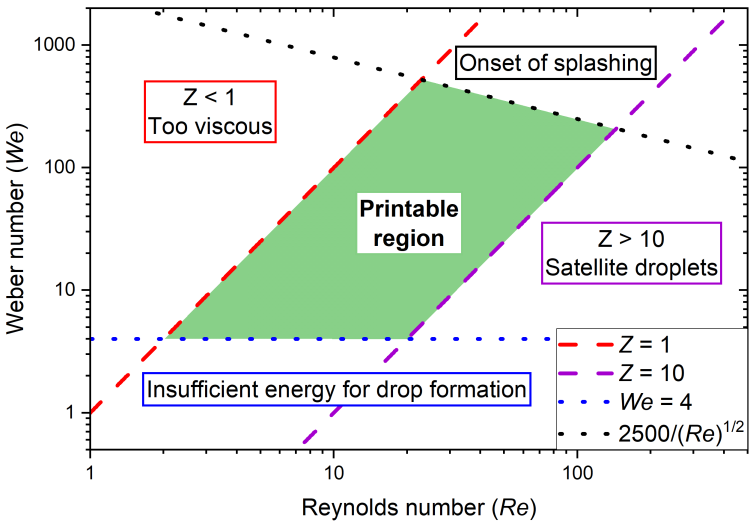

Figure 3.3: Parameter space describing regions of stable printing. The dimensionless Z number can be expressed through We and Re. Adapted from [126].

$$We = \frac{v^2 \rho L}{\gamma}, \tag{3.2}$$

$$Oh = \frac{\sqrt{We}}{Re} = \frac{\eta}{\sqrt{\gamma \rho L}}, \tag{3.3}$$

where v is droplet velocity and L a characteristic length, which is the nozzle diameter for inkjet printing [123]. The most common single parameter to describe the printability of an ink is the Z number:

$$Z = 1/Oh = \frac{\sqrt{\gamma \rho L}}{\eta}, \tag{3.4}$$

which eliminates the value for v from Equations 3.1 and 3.2. For Z < 1, the ink is too viscous for ejection, which corresponds to a large η, and could be further inhibited by low ρ, γ, and small L. For Z > 10, satellite droplets form, which are additional drops that do not follow the trajectory of the initial drop and lead to deposition at random positions. Low η, or large values for ρ, γ, and L favor this behavior. It is empirically found that particle-containing inks can generally be printed for the range $1 < Z < 10$ (Fig. 3.3). A minimum velocity gives two further limitations to overcome the surface tension of the nozzle ($We > 4$ [124]) and a maximum velocity before splashing occurs upon impacting on the substrate ($We \approx 2500/\sqrt{Re}$ [125]) [126]. The different constraints and regimes can be seen in Figure 3.3. These values are obtained by taking certain assumptions and approximations, providing a good indication for printability but not an explicit constraint. To this day, the behavior of e.g. inkjet-printed picoliter drops is still subject to research, emphasizing the complex dynamics in its description [127, 128, 129]. The physical properties and printing parameters of inkjet inks at room temperature used within this thesis are given in Table 3.2 and the corresponding waveforms in Appendix Figure A.2. It lists density ρ, surface tension σ, dynamic viscosity η, and Z number for $L = 21\,\mu m$. These rheological values are all temperature dependent, as can be seen for water in the range from 20–60 °C in Appendix Section A.1. Controlling the cartridge's temperature can therefore help to achieve steady printing conditions.

Inkjet printing is performed with the Dimatix DMP 2831, allowing precise deposition regarding spatial accuracy and applied volume. A key parameter for the fabricating inkjet-printed structures is the dropspace DS, defined as the lateral distance between the deposition of two adjacent drops.

Table 3.2: Physical properties and printing properties of inkjet inks at room temperature: density ρ, surface tension σ, dynamic viscosity η, and Z number for $L = 21\,\mu m$, as well as voltage V and speed v during ejection. The values for H_2O are given for $Na_2S_{(aq)}$, and the rheological properties of CNT and PDMS were not evaluated.

	ρ [g/cm^3]	σ [mN/m]	η [mPa·s]	Z	V [V]	v [m/s]
SoG (T11)	0.90	21.9	1.7	12.0	40	2–3
WO_3	0.80	20.2	2.5	7.4	40	6–8
PEDOT:PSS	1.00	24.8	22.5	1.0	36	8–9
Cu-NP	1.17	32.0	29.5	1.0	20	5–8
H_2O ($Na_2S_{(aq)}$)	1.00	72.8	1	39	26	3–4
CNT	-	-	-	-	40	9
PDMS	-	-	-	-	40	7

Choosing it too large results in disjoint beads where the drops do not coalesce. If DS is too small, bulging occurs where excessive ink spreads over the ideal parallel-sided line [123]. The DS is controlled by the printhead traverse speed v_T: a constant jetting frequency $f = 5\,kHz$ and $DS = 25\,\mu m$ gives $v_T = DS \cdot f = 25 \cdot 10^{-6}\,m \cdot 5 \cdot 10^3\,1/s = 12.5\,cm/s$. Deposited volume V for a printed line of length l is given by:

$$V = V_{drop} \cdot \frac{l \cdot N}{DS}, \tag{3.5}$$

where N is the number of layers. For example, a 5 mm line of $V_{drop} = 10\,pl$, $l = 5000\,\mu m$, $N = 5$, and $DS = 10\,\mu m$ results in a total print volume of $V = 25,000\,pl$ (cf. Fig. 3.4).

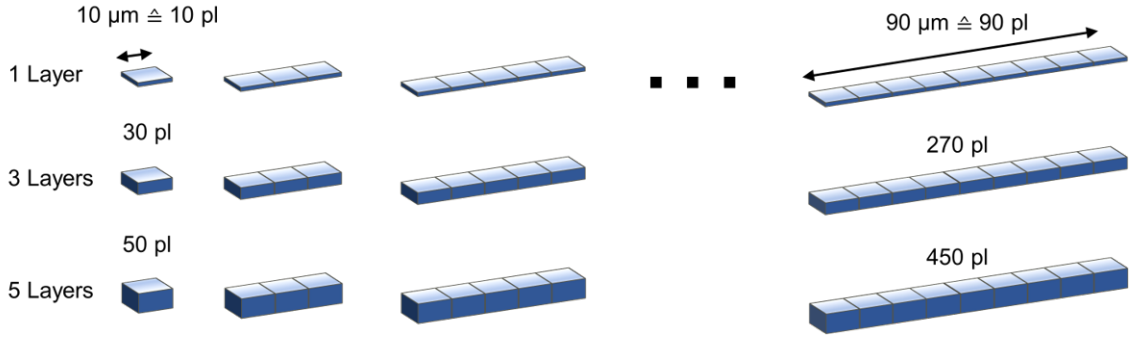

Figure 3.4: Visualization of inkjet-printed volumes with 10 pl drop volume for dropspacing of 10 µm and different number of layers.

Another aspect to consider is the so-called coffee-stain (or coffee-ring) effect is almost inevitable for inkjet-printed structures and needs to be considered. It describes the capillary flow from drying liquid drops towards the fringes, enhancing material deposition. The original model from Deegan *et al.* [130] assumes that the drop contains a dispersed material within a solvent and the contact line of the drop stays pinned while the solvent evaporates. The evaporation flux is greater at the rim, causing outward fluid flow to compensate for losses (s. Fig. 3.5). A detailed description of the coffee-stain effect is still under ongoing discussion [131]. This behavior affects printing results, as the elevated regions could cause short circuits in RRAM cells or affect the ink flow of subsequent layers. It also offers opportunities to either suppress its formation by an appropriate substrate or drying choice or its utilization for, e.g. biochemical analysis through convection induced assembly [132].

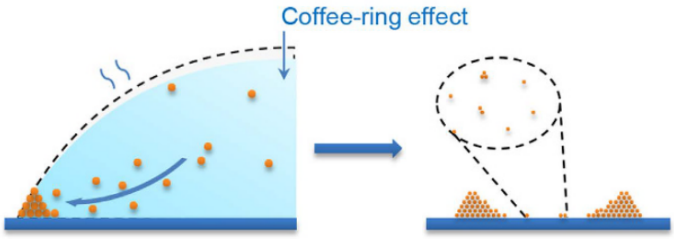

Figure 3.5: Capillary outflow during evaporation process results in enhanced deposition of dispersed material at the edges, causing the coffee-stain effect [133].

3.2 Inks and Sintering

3.2.1 Materials and Requirements for Printed Inks

Inks contain particles or precursors suspended in solvents to achieve the desired printing properties. As described in Subsections 3.1.2 and 3.1.3 for screen and inkjet printing, respectively, inks need to be within certain physical boundaries concerning their rheological properties. This section introduces and motivates the usage of the individual inks in this work. One crucial aspect is the potential use of the same ink for different purposes, such as Cu for conductive track and active electrode or a dielectric material as an insulator and sensor material. This reduces the number of required inks for a device, leading to fewer compatibility issues, simpler technology demands, and hence to more time- and cost-effective fabrication.

3.2.1.1 Screen Paste

The first important material for screen printing is highly conductive silver ink LOCTITE ECI 1010 E&C. It acts as current collector for the screen-printed battery but could also be used as active electrode material for resistive switching. This material is industry-established and provides high conductivity with good mechanical strength and flexibility. It is designed to be used on the inexpensive substrate polyethylenterephthalat (PET) and requires a low curing temperature of 120 °C. Using a shared screen-printed Ag electrode provides a reliable and cost-effective fabrication. This is partly due to lower technological requirements than Ag-based inks for inkjet printing requiring nm-sized Ag particles. While Ag is more expensive, Cu-based inks capable of screen printing are subject to research [134] and are offered as commercially available products with relatively low sintering temperatures of 180–300 °C [135]. Screen printing offers a faster printing speed compared to inkjet printing (s. Tab. 3.1) and better large-area scalability.

3.2.1.2 Inkjet Nanoparticles

For inkjet printing, the primary material used for conductive tracks within this work are Cu-NPs (Metalon CI-004). It is ca. 50% less expensive than Ag-based ink with similar conductivity from the same manufacturer (Metalon JS-A102A). The size of Cu-NPs is given as 100 nm (number averaged) or 160 nm (Z-averaged), measured and calculated by Novacentrix using a Zeta Sizer by Malvern Instruments. The values differ, as the number average gives equal weights to particles of different sized, while Z-average considers the intensity-weighted average where larger particles contribute more to the signal. The particle size is two orders of magnitude smaller than the nozzle diameter of 21.5 µm making it suitable for inkjetting. Still, smaller NPs are more desirable in terms of stable printing, as even small particles can cause nozzle clogging by aggregation or coagulation in the microchannels [128]. One of the most essential aspects of Cu-NP inks is the possibility for photonic

Table 3.3: Weight and volumetric percentages of constituents of WO_{3-x} (Avantama) suspension of 16 nm NPs in water and 2-propanol.

	WO_3	H_2O	2-propanol
wt %	2.5	1.0	96.5
vol %	0.28	0.80	98.9

sintering (s. Sec. 3.2.2.2). It allows for rapid sintering within milliseconds and in-line processing of roll-to-roll fabrication. This reduces the time and energy consumption massively compared to e.g. printed Ag tracks that are sintered at 200 °C for 10 min under nitrogen atmosphere [25].

As an insulating material, WO_{3-x} NPs (Avantama P-10) from Sigma-Aldrich are used. It is a colloidal suspension of 16 nm (mean size) tungsten oxide NPs with a concentration of 2.5 wt % in 2-propanol and water (s. Tab. 3.3). Due to reduced clogging, the small particle size makes it ideal for inkjet printing. The azeotropic solvent 2-propanol possesses a low boiling point of 80 °C [92], thus no post-treatment is necessary due to fast evaporation. At the same time, this property needs to be considered to avoid dried nozzles. This material also offers significant benefits for multi-use applications of the same ink. It is already established as a hole extraction layer for solar cells [136], printed gas sensors [137], or as a promising for non-volatile RS applications [20, 138, 139, 140].

3.2.1.3 Inkjet Solutions

Spin-on-Glass (SoG) is a material class that is well established in the semiconductor industry and has been used in optics and microelectronics for doping applications, planarization, or for insulating layers [141]. Honeywell Accuglass T-11 is used as an insulating material due to its high electrical resistance for thin layers and planarization capabilities. It is usually spin-coated on wafers and consists of silicon-oxide compounds that form SiO_x structures upon thermal post-treatment. It is based on methyl-siloxane polymers and has proven to have excellent crack resistance and the capability to form relatively thick films [142]. These are the prerequisites to completely cover the active electrode for RRAM cells and prevent short circuits. The manufacturer recommends sintering temperatures of 425 °C to obtain the best insulation properties by outgassing organic components. However, it has been shown that switching voltages for RRAM applications do not depend on the SoG sintering temperature in the temperature range 100–400 °C [25]. Therefore, SoG becomes a suitable material even for temperature-sensitive substrates such as polymer foils.

Transformation is another way to fabricate an insulating layer on Ag or Cu structures. $Na_2S_{(aq)}$ is utilized to locally apply thin layers of e.g. Cu_xS on the Cu surface. It will be labeled as ink throughout this thesis, even though it is strictly speaking no ink, as it does not contain the compound material to be deposited. The advantage is that no particles or polymers can clog the nozzles. The downside is that ink residues need to be rinsed off with DI water afterwards and emerging H_2S vapor is potentially harmful to the operator or other sensitive materials. The low quantities used are in the µl-range and well below safety concerns. The motivation to deal with these difficulties is that Ag_xS and Cu_xS are semiconductors with potential applications as sensing materials and especially excellent switching behavior in RRAM cells [68, 143, 144, 145].

3.2.1.4 Inkjet Nanotubes

Multi-walled carbon nanotubes (MWCNTs) are used as a promising material in the form of a spaghetti-like conductive network. Since their discovery in 1991 [146], CNTs have found many applications due to their high electrical conductivity and strong mechanical stability. A two-

step printing process of MWCNTs and polydimethylsiloxane (PDMS) is employed, where PDMS provides a polymeric matrix for stability and adhesion to the substrate. It has been synthesized by a collaborative researcher in a joint effort to fabricate inkjet-printed fiber-optic photoacoustic generators [147, 148]. The conductive network has potential as inert electrodes for RRAM cells or as strain sensors. The individual MWCNTs have an outer diameter of 6–9 nm and lengths around 5 µm. Inkjet printing works due to flow-induced alignment despite the CNTs' length being in the same order of magnitude as the nozzles [149]. It can be visualized as tree trunks in a river aligning with the flow direction and therefore no clogging occurs.

3.2.2 Sintering

One way to process materials in the context of additive manufacturing is powder bed fusion. Here, one or more thermal sources induce fusion between powder particles to control powder fusion to a prescribed region [150]. This method will not be used within this thesis but will help to understand the mechanisms and possible advantages of the technique used. Usually, lasers are utilized which can be specialized to sinter polymers or metals. The platform holding the substrate and powder bed can be heated.

> This preheating of powder and maintenance of an elevated, uniform temperature within the build platform is necessary to minimize the laser power requirements of the process (with preheating, less laser energy is required for fusion) and to prevent warping of the part during the build due to non-uniform thermal expansion and contraction (resulting in curling). [150, p. 108]

The most relevant fusion mechanisms within the scope of this thesis are solid-state sintering and complete melting. Sintering indicates the fusion of (powder) particles without melting at elevated temperatures T ($0.5 \cdot T_{melt} < T < T_{melt}$). The driving force is minimizing particles' total free energy E_s, leading to diffusion between particles. It is proportional to total particle surface area S_A, through the equation $E_S = \gamma_S \cdot S_A$, where γ_S is the surface energy unit area for a particular material, atmosphere, and temperature. For elevated temperatures, particles fuse to minimize S_A, leading to neck-formation and pore-shrinkage (s. Fig. 3.6).

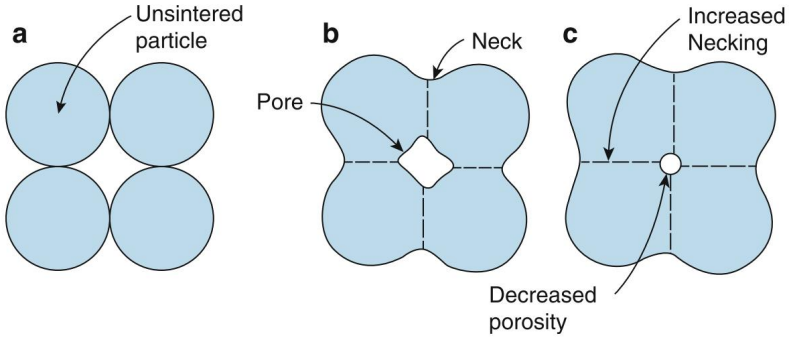

Figure 3.6: Solid-state sintering. (a) Initial state of unsintered particles. (b) Particles start to agglomerate around $0.5 \cdot T_{melt} < T$ to minimize their free energy. (c) To further decrease the surface area, neck size increases and pore size decreases. [150]

As sintering progresses, the total surface area decreases, slowing the sintering rate. Therefore, long sintering times or high sintering temperatures are required to achieve low porosity levels. Smaller particles have a larger surface-to-volume ratio since the surface is proportional to the square of the radius r^2, while the volume scales as r^3. Thus, smaller particles experience a greater

driving force for necking and consolidation, making sintering more rapid and possible at lower temperatures than larger particles. Sintering becomes exponentially more rapid as temperatures approach T_{melt}, but is still diffusion-limited and is typically longer than for fusion by melting [150].

The phenomenon of dropping melting temperature with decreasing particle size is also known as *melting-point depression*. It was already described in 1909 by Pawlow [151] that the melting point of smaller grains should be lower than the melting point for large grains. Experimental results verified this development: copper nanoparticles (NPs) of 50 nm show a melting point of 700 K embedded in a silica matrix [152] and 720 K for NPs separated only by an organic shell [153]. This equals a melting-point depression of 655 K and 635 K compared to the bulk melting point (1355 K), respectively. Similarly, for thin films of Ag-NPs, melting occurs at 780 K, equivalent to a depression of 455 K compared to bulk at 1235 K [154].

The method of laser sintering has the advantage to precisely sinter regions of loose material or powder that is easy to provide. On the other hand, the laser beam spot of typically 300 µm is rastering over the surface which is time-consuming. This property becomes a problem for larger areas, complex structures, or parallel processing. Therefore, large-scale fabrications require other sintering techniques discussed in the following.

3.2.2.1 Thermal Sintering

The most common method for thermal post-treatment is oven-processing. Different temperature profiles or an inert gas atmosphere allow for various sintering conditions. Conveyor belt ovens offer the possibility to integrate these processes into large-scale industrial operations. The main advantages are defined, homogeneous thermal conditions, solving issues with poor heat conduction for polymer substrates on hot plates. Inert gases can further prevent oxidation of the layers during this process. Disadvantages are the high demand for energy and time and the limitations to substrates that can withstand this thermal stress.

3.2.2.2 Photonic Sintering and Porosity

One possible solution for large-scale sinter operations that facilitates industrial printed electronics applications is photonic sintering or intense pulsed light (IPL).

The principle of the IPL technique was patented in 2005 [155] and is a millisecond short, white light pulse from a Xe-flash lamp to heat a thin film of material, e.g. printed Ag-, or Cu-NPs on a low-temperature substrate without damaging it [156]. The main idea is that metallic NPs are locally heated due to surface plasmon resonance causing melting, while most polymer substrates only absorb in the UV region [157]. The short pulse length and low thermal conductivity, as well as the high heat capacity of the substrate, enable sintering of metallic NPs without damaging the substrate. Simulations with a 300 µs pulse (1 J/cm^2) of a 1 µm Ag film on 150 µm PET shows surface temperatures above 1000 °C while the backside of the substrate is not heated appreciably during the pulse. The substrate at the interface at the top side will be exposed to temperatures above its working temperature. However, this period is not long enough to significantly change its properties [156]. The fast process makes it suitable for in-line processing of printed electronic structures.
The conditions for photonic curing are [156]:

1. Very thin film compared to the substrate as the thermal mass of the substrate is required to cool the thin film via conduction

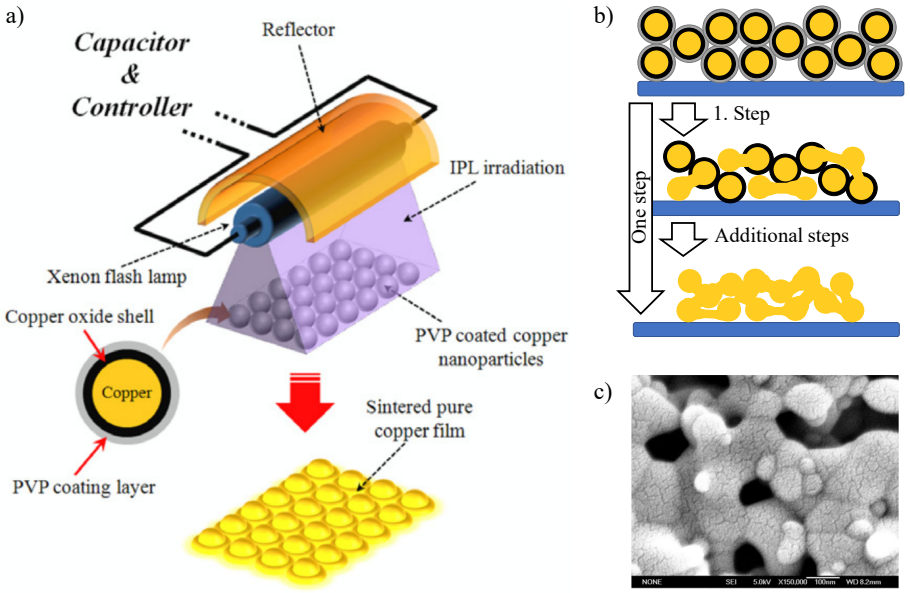

Figure 3.7: a) Photonic sintering system containing the Xe-flash lamp to sinter a thin Cu film [162]. b) Schematic steps of single- or multi-step process during sintering, where the PVP shell of the Cu-NPs facilitates the reduction of copper oxide. c) SEM cross section showing the porous structure of a sintered Cu film using IPL [159].

2. Heating is completed before the substrate is in thermal equilibrium to maintain thermal gradient for film cooling

3. High threshold energy for sintering requires increasingly short pulse lengths with high power to fulfill the other conditions.

The sintering of printed Cu-NPs poses additional challenges but also opportunities. The fast oxidation of Cu makes it impractical to use conventional thermal sintering as it would require e.g. formic acid to prevent oxidation [158]. To utilize the more economical alternative to Ag, Cu-NPs are usually covered with a native oxide shell and a photo-reactive polyvinylpyrrolidone (PVP) layer (s. Fig. 3.7). Ryu *et al.* explained the reactive IPL sintering process of copper oxide reduction through intermediate products during photo-degradation of PVP, resulting in conductive, pure copper films [159]. A single millisecond-pulse can be used to obtain conductive Cu-NP structures, while multiple steps (Fig. 3.7 b)) can also be utilized to reduce substrate warping [160] or achieve a lower porosity [161].

Porosity is a crucial parameter as it strongly affects mechanical, thermal, and electrical properties. The electrical conductivity is reduced in the presence of pores, or other non-conductive inclusions [163]. For equal spheres, the highest possible packing fraction is 74 %, and for more amorphous packings, it is only 64 %, meaning a porosity of 26 % and 36 %, respectively [164]. The experimentally observed upper limit of porosity (Θ_M) for powders of µm-sized particles is the so-called tap porosity, which is the equilibrium reached by moderate vibration. For metallic powders, this value is in the range 43–83 % [165]. To describe the porosity-dependent conductivity $\sigma(\Theta)$, an empirical equation that is related to findings in the field of percolation can be used [163]

$$\sigma = \sigma_0 \left(1 - \Theta/\Theta_M\right)^n , \tag{3.6}$$

where σ_0 is the conductivity of the pore-free bulk material, Θ_M the maximum porosity, and n is a fitting parameter. This equation satisfies the boundary conditions $\sigma \to \sigma_0$ as $\Theta \to 0$, and $\sigma \to 0$

as $\Theta \rightarrow \Theta_M$. In Section 4.3, the sintering results will be discussed based on electrical conductance and porosity determinations from FIB-SEM images. The values for Θ_M can be estimated as an upper bound to be 60 %, as found for spherical shaped particles [165] and the exponent n is found to be in the range from 1 to 1.44 [163].

To understand and experimentally probe the sintering process, a built-in bolometer can be used to determine the absorption coefficient α. This value does not include spectral information about absorption but provides a precise value for the used sintering setup. In bolometry, the power of a light source can be calculated from the temperature increase of an absorber for a broadband pulse. First, the radiant exposure of the light source I_0 is measured. Next, different substrates are characterized by the bolometer to obtain the attenuated intensity I to quantify their absorption coefficients α_{Sub}. In a final step, an identical substrate with a partially transparent thin film with thickness t of Cu-NPs is placed on the bolometer to obtain α_{CuNP}.

The attenuation of light is given by the simplest form of the Lambert-Beer law as [166]:

$$I = I_0 \cdot \exp(-\alpha \cdot t) \qquad \longrightarrow \qquad \alpha = -ln(I/I_0)/t. \tag{3.7}$$

For the scenario of a semitransparent thin film of Cu on a substrate, α_{Cu} can be calculated through

$$I = I_0 \cdot \exp(-\alpha_{Cu} \cdot t_{Cu}) \cdot \exp(-\alpha_{Sub} \cdot t_{Sub}) = I_0' \cdot \exp(-\alpha_{Cu} \cdot t_{Cu}), \tag{3.8}$$

where I_0' is the attenuated intensity through the substrate, to be

$$\alpha_{Cu} = -ln(I/I_0')/t_{Cu}. \tag{3.9}$$

3.3 Surface Transformation to Cu_xS by $Na_2S_{(aq)}$

It is well known that exposure to sulfur-containing gases leads to tarnishing of noble metals such as Ag or Cu [167]. While this phenomenon is best known for silverware, the sulfidation rate of copper is at least an order of magnitude larger than for silver [168]. The humidity in air is sufficient to promote the reaction for both metals with the standard electrode potentials $E^0_{Ag} = 0.80\,\mathrm{V}$ ($Ag^+ + e^- \rightarrow Ag$) and $E^0_{Cu} = 0.34\,\mathrm{V}$ ($Cu^{2+} + 2e^- \rightarrow Cu$) [92]. This is one of the reasons why sulfur is avoided as a species for electronic circuits. Printed circuit boards (PCBs) are made of Cu and are industry standard to provide conductive paths. Here, environments high in reduced sulfur gasses lead to frequent failures in the PCB technology where corrosion is prominent inside via holes [169]. Sulfides also accelerate corrosion of copper pipes, where it forms thick, black scales [170]. The resulting corroded layer and corrosion rate increases with Cu content in alloys, temperature, pH, and sulfide ion concentration [171]. The main product found here is Cu_2S [172].

However, the reactivity of Cu with sulfides can be taken advantage of to fabricate semiconducting Cu_xS, which can function as a sensory material [173] or as an insulating layer for memory cells [143, 145]. Further applications for CuS are investigated as hydrophobic protection layer [174] or as a cathode material for use in Li-ion batteries due to its high specific capacity and the use of low-cost and abundant materials [173, 175]. Copper sulfides are usually described as $Cu_{2-x}S$ and one of the most complicated binary compounds to describe their crystal phase [173]. Numerous non-stoichiometric compositions differ in sulfur content and crystal structure, e.g. CuS (Covellite), $Cu_{1.8}S$ (Dignenite), and Cu_2S (Calcocite), but most exhibit p-type electronic character [173]. Due to the variety of compounds and the low-tech approach for fabrication in this thesis, the material will be labeled as Cu_xS and regarded as a poly-crystalline system including different compositions.

The transformation mechanism is explained by the following steps [171, 176]. The cathodic reduction of the aerated electrolyte medium occurs as follows:

$$O_2 + 2H_2O + 4e^- \longrightarrow 4OH^-. \tag{3.10}$$

Hydrosulfide ions (HS^-) originate from the dissociation of Na_2S in water

$$Na_2S + H_2O \longrightarrow 2Na^+ + HS^-_{aq} + OH^-. \tag{3.11}$$

It is worth mentioning that the presence of sulfide ions $S^{2-}_{(aq)}$ (pKa$\geq$ 17) occurs only in negligibly low concentrations [177, 178]. If S^{2-} would be present, it would attract a proton from the autoprotolysis of water.
Then, HS^- will adsorb to the copper surface as precursor of the oxidation reaction:

$$Cu + HS^- \longrightarrow Cu(HS^-)_{ads}, \tag{3.12}$$

before the anodic dissolution of copper may take place:

$$Cu(HS^-) \longrightarrow Cu(HS) + e^-, \tag{3.13}$$

followed by the dissociation and the recombination processes:

$$Cu(HS) \longrightarrow Cu^+ + HS^-_{aq}, \tag{3.14}$$

$$2Cu^+ + HS^- + OH^- \longrightarrow Cu_2S \downarrow + H_2O. \tag{3.15}$$

The overall reaction can be expressed as

$$4Cu + 2HS^-_{aq} + 2O_2 + 2H_2O \longrightarrow 2Cu_2S \downarrow + 6OH^-. \tag{3.16}$$

The effectiveness of protective cuprous oxide (Cu_2O) film is prevented by the presence of Cu_2S [176].

Pitting corrosion also needs to be considered for small, applied volumes or drops of $Na_2S_{(aq)}$ on a metal surface. Here, oxygen from the environment is diffusing more rapidly into the solution at the edges of the drop [62, p. 243]. The increased oxygen concentration could lead to an enhanced reduction rate (s. Eq. 3.10) and thus to more reaction products in the shape of concentric circles [179]. This phenomenon, as well as the coffee-stain effect (s. Fig. 3.5), need to be considered for possible elevated features at the circumference of deposited drops.

In this work, concentrations c of $Na_2S_{(aq)}$ are around 0.1 M which results in a basic solution with pH $\approx$13. To yield 100 ml of 0.1 M solution, 2.40 g Na_2S get dissolved in 98.38 ml of DI water [180]. The precise concentration is determined via reverse (indirect) titration and is shown in Appendix A.7 in Figure A.10. It is important to consider the basic nature of the solution to be compatible with sensitive substrates or materials such as photoresists.

3.4 Sensor Fabrication

Sensors are used to translate conditions and changes in their environment into physically quantifiable outputs such as voltage or impedance. Sensory solutions for measuring strain, humidity, and temperature will be explained in the following.

3.4.1 Strain (MWCTNs)

As discussed in Subsection 2.1.1, strain sensors convert mechanical deformations (Fig. 3.8) into an electrical signal and are characterized by their stretchabilities, gauge factor, hysteresis, and response time. The electrical signal can originate from e.g. capacitive, piezoelectric, or resistive changes [181].

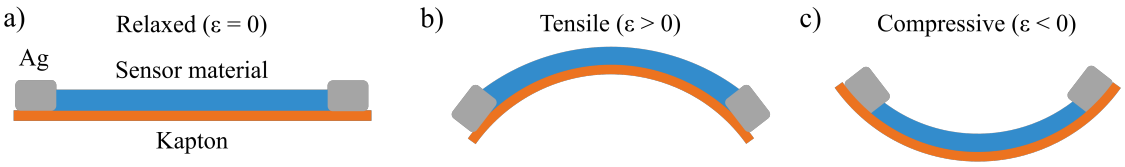

Figure 3.8: Schematic visualization of printed sensor material such as Cu or carbon nanotubes on a flexible Kapton substrate. The Ag contacts facilitate the read-out. The resistance of the relaxed position (a) changes depending on tensile (b, $\epsilon > 0$) and compressive (c, $\epsilon < 0$) strain.

Capacitive sensors can be advantageous in terms of better hysteresis performances [45, 182] and piezoelectric ones exhibit extraordinary gauge factors [183] but often lack facile fabrication via printing. Piezo-resistive sensors are used for easy read-out, printability, and potential for integration into a fully printed device. Traditionally, resistive strain sensors of meander-shaped metal lines were fabricated on a flexible substrate using lithographic processes. The design allows engineering the resistance to the desired range. Commercial strain gauges consist e.g. of meander tracks made of 5 µm copper-nickel alloys on a 50 µm polyimide (Kapton) substrate with a nominal resistance of 120–350 Ω and a gauge factor (GF) of approximately 2 [29].

The resistance of the fabricated strain sensor is designed to exhibit resistance in the order of kΩ–MΩ. Here, the absolute change in resistance will be higher and therefore allowing for more facile read-out. For this reason, inkjet-printed carbon nanotubes (CNTs, cf. 3.2.1.4) are utilized embedded in polydimethylsiloxane (PDMS) for stability and adhesion. Especially multi-walled carbon nanotubes (MWCNTs) as sensitive material have drawn research attention and will be used within this work. One of the first facile fabrications of CNT as a flexible sensor was achieved by disposing CNT powder between adhesive tapes [184]. From there, controlled growth of CNTs enables creating conductive networks [185, 186] via screen printing [187, 188], or even inkjet printing [189] for CNT-based applications. Towards recyclable printed electronics, carbon-based electronics exhibit enormous potential with a recovery yield of 95 % [190]. A recent review article provides a comprehensive and detailed overview of recent progress on piezoresistive strain sensors in general [41]. Uniformly distributed MWCNTs within PDMS have been found to enable strain sensors with an almost linear piezoresistive response for applications with up to 40 % strain [44]. Novel design and scopes are accessible, as the bio-compatibility of PDMS allows its use for health monitoring due to the bio-compatibility [191].

The synthesis of the inks used for inkjet printing in this work is based on recent research projects realizing an inkjet-printed fiber-optic photoacoustic generator using MWCNTs and PDMS [147, 148]. The fabrication consists of two steps to facilitate the printing process and extend the shelf-life of the inks: the first ink contains MWCNTs and PDMS, and the second ink contains PDMS and curing agent (CA). The MWCNTs have an outer diameter of 6–9 nm, lengths around 5 µm, and are purchased from Sigma Aldrich (724769-100G), while PDMS and CA are available from Dow Corning (Sylgard 184). The first inkjet ink (MWCNT/PDMS) is a water-based MWCNT-PDMS ink where Triton-X-100 (polyethylene glycol phenyl ether) is used to dissolve MWCNTs in water and mediate MWCNTs and PDMS in the solution. The constituents MWCNTs and PDMS

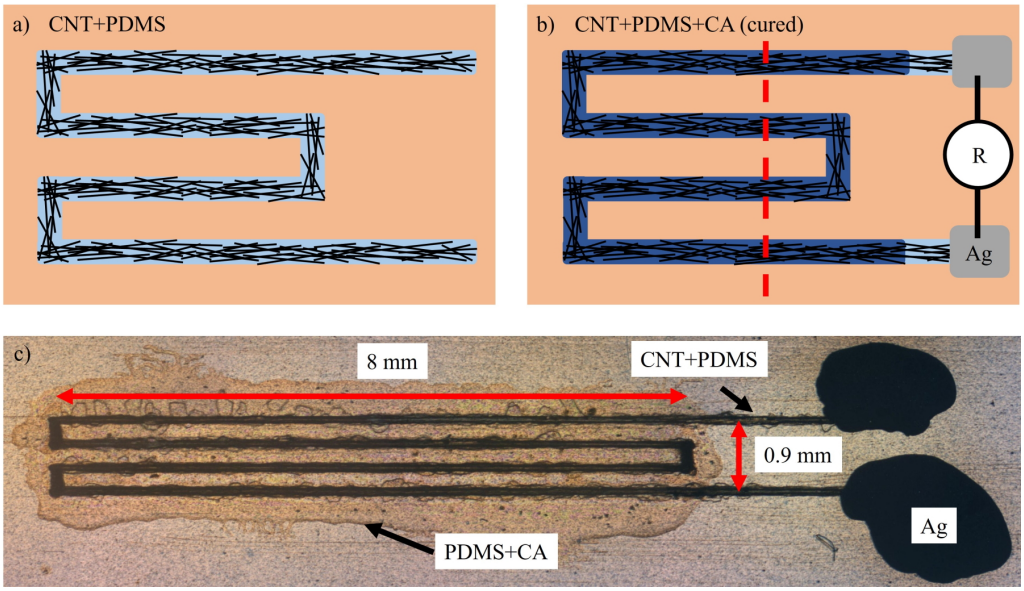

Figure 3.9: The printing process on polyimide substrate includes a) application of the CNT/PDMS structure and after drying (100 °C, 10 min) follows b) printing of PDMS/CA and curing step (250 °C, 30 minutes), and Ag paste for contacting. The resistance is measured between the two contacts for the characterization and the red, dashed line indicates the bending axis. c) Stitched optical microscope image of final structure. [110] © 2022 IEEE

are present in the ratio 1:3, therefore, the first ink contains 25 wt% of MWCNT. The untreated components are homogenized for 30 minutes using a 130 W ultrasonic homogenizer. In preceding works, solubility of 1 mg/ml of PDMS in 0.1 % Triton-X-100 based on deionized water was found [147]. Additional short-chain PDMS molecules act as a solvent within the second component (PDMS/CA). Undissolved parts of PDMS/CA are homogenized for 2 minutes using the ultrasonic homogenizer [148]. Excess PDMS in the first ink benefits the homogeneous distribution of CNTs within the PDMS matrix, promoting stability by reducing distances between CNT and PDMS. It further promotes stability and adhesion to the substrate of the printed structures.

The sensors are fabricated by a two-step inkjet printing process using the Dimatix DMP 2831 inkjet printer. Polyimide (Kapton 500 HN, 125 µm) is utilized as a flexible substrate and cleaned with 2-propanol for a particle-free surface. In the first step, the DMP 2831 is depositing the sensor pattern using CNT/PDMS ink with drop spacing of 25 µm (Fig. 3.9 a). The printing procedure is repeated multiple times to achieve resistance in the desired range from 100 kΩ to 10 MΩ. Subsequent layers merge into each other as the evaporation time of the solvent is much longer than the application duration of multiple layers. After printing several layers, the structure is placed on a hotplate at 100 °C for 10 minutes to remove residual solvents.

For the second fabrication step, the meander is covered with PDMS/CA ink, using a drop spacing of 25 µm (Fig. 3.9 b)). The areas at the two ends of the structure are not covered to allow contacting with Ag paste (Acheson 1415). The number of layers in the second step is adjusted to the CNT/PDMS volume from before for a fixed ratio of PDMS and CA, as more (less) CA leads to a stiffer (softer) cured PDMS matrix. Complete polymerization of PDMS can be assumed for the final sensor, as similar amounts of PDMS and CA were used by Naserifar *et al.* [192]. Curing on a hotplate at 250 °C for 30 minutes accomplishes complete polymerization of PDMS. Characterization of piezoresistive properties of the final CNT-based sensor is carried out using a lab-built rotate-to-bend apparatus [193], which is discussed in Subsection 3.7.2.

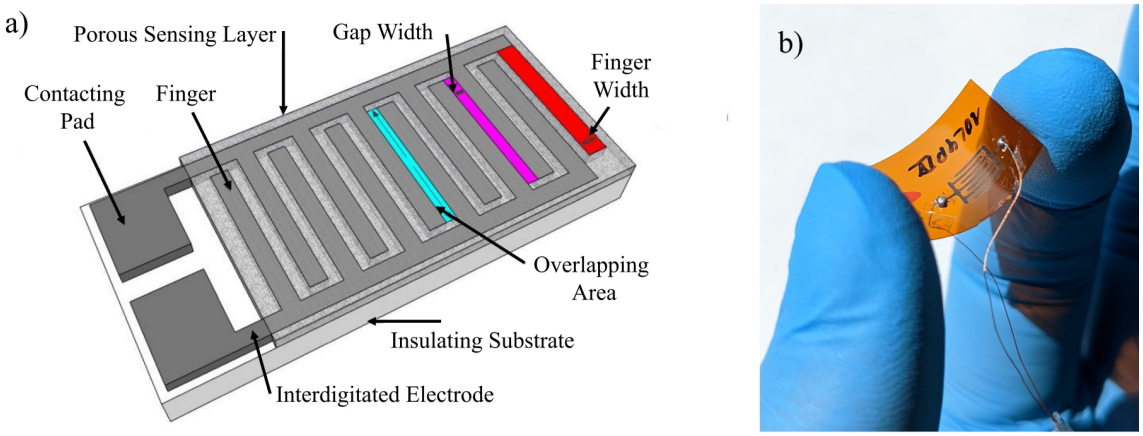

Figure 3.10: a) Schematic design of planar humidity sensor based on resistive response of the porous sensing layer due to ad- and desorption of water vapor (adapted from [30]). b) Flexible humidity sensor based on Cu and WO_3. The fabrication steps are shown in Figure 3.11.

3.4.2 Humidity (WO_3)

Similarly to strain sensors, types of relative humidity (RH) sensors include capacitive [194], piezoelectric [195], and resistive [39, 48]. Essential factors in evaluating the potential of a humidity sensor are sensitivity to RH, humidity range, and response time [181]. As for the strain sensors, resistive sensors are employed due to their easy read-out, printability, and potential for integration.

A schematic design of a possible flexible humidity sensor, as well as the realization, are shown in Figure 3.10 a) and b). It includes an insulating substrate with interdigitated (IDT) electrodes covered by a porous sensing layer. The IDT structure consists of two sets of parallel fingers with variable gap width. The resistance can be approximated by $R(RH) = \rho_{sens}(RH) \cdot d/(l \cdot h)$, where $\rho_{sens}(RH)$ is the humidity-dependent resistivity of the sensing layer, d the gap width, and $l \cdot h$ as the length l of the overlapping area and height h of the electrodes, i.e. the effective area. Thus, more fingers or smaller gap widths decrease the resistance R.

Figure 3.11 displays fabrication steps of Cu structures in general, and in particular for Cu-IDTs covered by WO_3-NPs for a humidity sensor. The first panel (a) shows the digital design for Cu-IDT structures. Here, every black pixel represents the application of a 10 pl drop with drop spacing of 25 µm. The printing process occurs row-wise, i.e. every structure is broken down into horizontal lines. To cover a larger printing area, up to 16 parallel jets are available for vertical deposition of up to 375 µm in one run. However, if one jet is clogged or unsteady, the final structure will be incomplete and thus not usable. Therefore, relying on less required jets leads to shorter calibration and faster process tuning efforts.

This is done in Figure 3.11 a), where horizontal lines are a single pixel wide, i.e. only one jet is required. Also, vertical structures would consist of a single pixel, but inkjet printing is prone to *first-drop-inaccuracy* (cf. Fig. 4.6). The jetting mechanism with an ejection rate of e.g. 1 kHz takes a few milliseconds to stabilize, leading to systematic inaccuracies for the first drops. While this is not problematic for millimeter-sized horizontal structures, it becomes an issue for a single drop for vertical structures. Short and parallel horizontal lines circumvent this problem: the vertical spacing is small enough for the ink to merge vertically, and the horizontal extent is sufficiently long to provide a stable deposition. Additionally, it lowers the necessary runs to print the whole structure since fewer horizontal prints must be printed. Repeating this process for additional layers enables further control of the structure. This design allows rapid prototyping as only one stable inkjet nozzle is required for larger printed structures. The layout parameters are given in Table

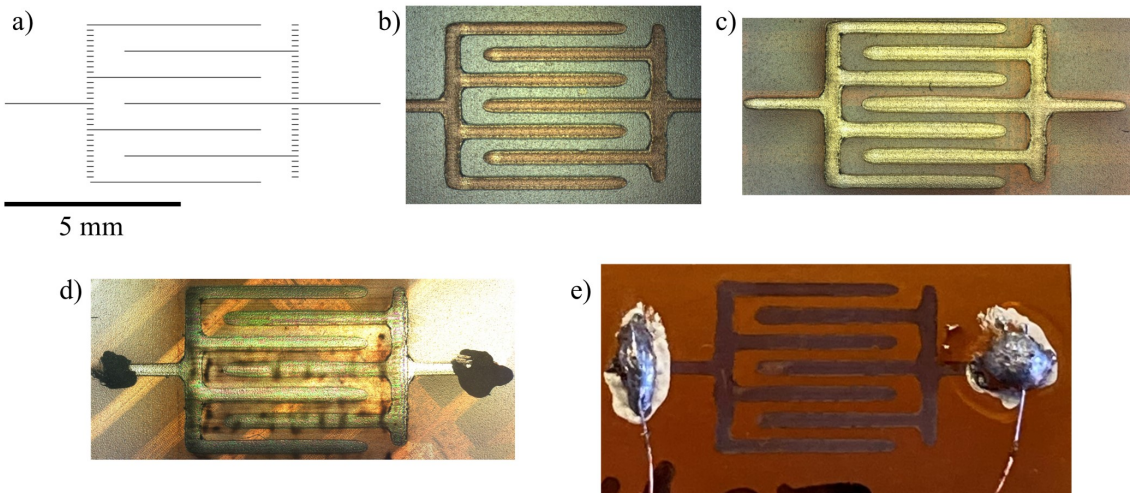

Figure 3.11: a) Digital layout for inkjet printing of Cu-IDT on Kapton of (6.0×4.5) mm^2 effective area and additional lines for contacting. Microscopic images of b) the dried Cu-IDT after printing, c) the structure after photonic sintering, and d) after applying the humidity sensitive WO_3 layer and Ag paste to facilitate contacting. e) Optical image of the final structure with soldered copper wires for measurements in the climate chamber. The scale bar applies to all images.

3.4 and consider the spreading of the ink of ca. ±200 µm. The overlapping length is given by the finger length and gap width.

Figure 3.11 b) depicts the printed structure with six layers after drying for 10 min on a 100 °C hotplate to remove residual solvents. In Figure 3.11 c) the samples have been photonically sintered by a series of eight broadband pulses in the visible spectrum of 0.625 ms with 0.625 ms delay and a total energy of 5.97 J/cm^2 (Novacentrix 1300 Pulseforge), as investigated in Figure 4.14 b). This step is accompanied by a change in color from brown to metallic orange, and the lines exhibit a resistivity of $\rho = (21.8 \pm 1.3)\,\mu\Omega$·cm, which is ca. 13·$\rho_{Cu,bulk}$ ($\rho_{Cu,bulk} = 1.7\,\mu\Omega$·cm). After extensive investigations, the parameters for printing and sintering were chosen to achieve a good combination of printing homogeneity and conductivity. The width of the sintered horizontal lines is 500 µm, reducing the effective gap width to 250 µm.

Figure 3.11 d) shows the final sensor after the application of the humidity sensitive WO_3-layer and Ag paste to facilitate contacting. Similar to the design of Cu-IDTs (Fig. 3.11 a)), the whole active area is covered by printing five layers of merging parallel lines with $DS = 5$ µm and vertical spacing of 150 µm. To ensure full coverage, the printing pattern with (5.2×6.5) mm^2 is slightly larger than the IDT area. The optical image in Figure 3.11 e) presents the structure after soldering Cu wires for measurements in the climate chamber.

Table 3.4: Print and design parameters for IDT shown in Figure 3.11. The gap width is given as the distance between fingers and the vertical spacing as distance for single lines to form vertical connections. The overlapping length is calculated by finger length and gap width.

Dropspace	Gap Width	Vertical Spacing	Finger Length	Overlapping Length
25 µm	750 µm	100 µm	4.5 mm	31.5 mm

After investigating the sensory potential for humidity sensing, a vapor barrier will be introduced. A pouch made of sealed metalized laminates as packaging also protects the components from mechanical damage, dust particles, and UV light. The potential of a vapor barrier is investigated by comparing the response of printed WO_3-based humidity sensors that are within a sealed composite foil package to unprotected sensors. The foil consists of 12 µm PET substrate, metalized with

pinhole-free 9 µm Al, and 40 µm PE-LD (low-density polyethylene) sealable top layer. Heat sealing pliers are used to melt LD-PE of two foils together, while the PET substrate withstands the sealing process of ca. 200 ° C, 20 N/cm^2, and ca. 5 s. Furthermore, packaging will be relevant for practical applications, as the performance of resistive memory cells [196] and batteries with (water-based) electrolytes are influenced by humidity [197].

3.4.3 Temperature (Cu$_x$S)

There are plenty of material choices for resistive temperature sensors as most systems exhibit a temperature-dependent resistance. For various applications, different regions of resistance are necessary. It should be in the order of 10^3–$10^6\,\Omega$ for the use as the current limiter for memory cells. This would require a length of 0.5 m to achieve $10^3\,\Omega$ for printed Cu lines as described above. Therefore, materials with larger resistivity values are more suitable for these application-oriented solutions. As semiconductors exhibit a negative temperature response, they are especially suitable for discriminating their change from metals' positive responses.
The MWCNT-based strain sensor described in subsection 3.4.1 is expected to be in the MΩ range and will be investigated for the thermal sensor properties as well. It is crucial for any practical application to determine the system's response to environmental changes. Depending on the application, the device could be used as a temperature sensor, or the cross-sensitivity during strain-sensing needs to be compensated.

The second probed material will be Cu$_x$S. Here, sulfurization using $Na_2S_{(aq)}$ transforms the inkjet-printed Cu-based structure into a Cu$_x$S-based thermistor (s. Subsec. 3.3). Inkjet printing allows precise application to cover designated areas and create local Cu$_x$S structures. Photonically sintered Cu structures exhibit a porous volume structure (s. Sec. 3.2.2.2), supporting the chemical conversion due to larger surface area and more diffusion paths for $Na_2S_{(aq)}$. Hence, the porous Cu material may impair the resistivity but facilitates speed and in-depth conversion from Cu to Cu$_x$S. Semiconducting Cu$_x$S is a promising material for thermistors, as the large expected TCR simplifies the read-out. The thermistor preparation consists of printing two layers of Na_2S_{aq} (0.1 M) with $DS = 10\,\mu m$ over $l = 5\,mm$ and rinsing with DI water after two minutes to remove ink residues.

3.5 Screen-Printed Zn/MnO$_2$ Battery

In Section 2.2 key parameters such as open circuit voltage V_{OC}, internal resistance R_i, and capacity C were introduced. The choice of anode, cathode, and electrolyte material determines V_{OC}, while the geometric properties control C.

For possible operation of an electrochemical metallization cell (ECM) by a screen-printed battery, the provided voltage must exceed the switching threshold V_{th} of the memory cell. Zn-based batteries exhibit a nominal voltage of 1.2–1.6 V, while it is around 3.0 V for Li-based systems [56]. As ECMs typically posses $V_{th} < 0.5\,V$, both materials suffice for switching operations [77]. Therefore, Zn/MnO$_2$ batteries are used to fulfill the requirements while benefiting from established processes, less environmental impact, and lower costs. Several battery cells could be connected in series to achieve multiples of the single-cell voltage.

The planar layout allows fabrication without additional steps for a separator to avoid direct contact between anode and cathode layer or manual folding for assembly [198]. The capacity can be adjusted by customizing the active area through a larger area, more fingers, or using multiple cells in parallel. While a small battery footprint is sufficient to trigger a low number of incidents during event detection, larger areas may be desired for e.g. powering an indicator LED. The layout

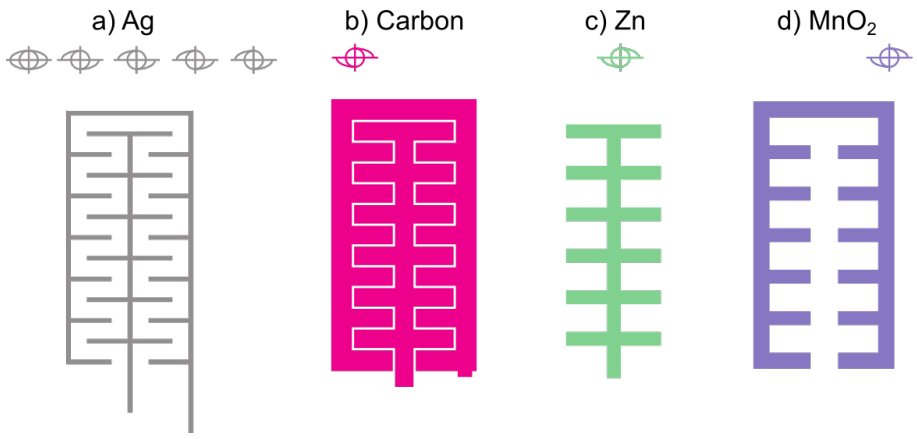

Figure 3.12: Digital design of different layers of screen-printed Zn/MnO_2 battery with fiducial markers for alignment during the multi-step printing. The Ag current collector (a) is fully covered by conductive carbon (b), and the inner and outer combs are made from the active materials Zn and MnO_2, respectively.

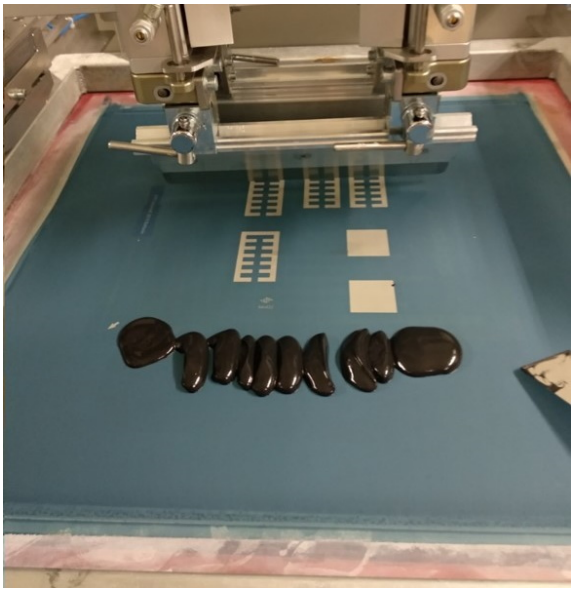

Figure 3.13: Screen printing step: MnO_2 ink (black, in front) before being transferred by the squeegee through the patterned screen onto the substrate.

of the screen-printed, interdigitated zinc-carbon micro-battery (MB) is shown in Figure 3.12. For the in-house fabrication, a state-of-the-art screen-printing, semi-automatic shuttle table machine Thieme 1000 transfers ink with a squeegee through a patterned mesh onto the substrate (s. Fig. 3.13). The mesh of PET is partially covered with UV-hardened emulsion. It is characterized by mesh count MC (wires/cm) and thread width TW and determines the thickness of the printed structure. A planar layout is chosen to facilitate the printing process and achieve thinner devices which is beneficial for bending properties (Fig. 3.14 a)).

Pre-shrunk 100 µm PET foils serve as a substrate for MBs. After printing Ag as the current collector (LOCTITE ECI 1010 E&C, $MC = 150$, $TW = 31$), the dried layer is covered by a highly conductive carbon layer (Zincell conductor paste C1001, $MC = 150$, $TW = 31$) that prevents it from reacting with the active masses. The latter consist of non-toxic and well established materials MnO_2 (Zincell cathode paste M802001, $MC = 43$, $TW = 80$) and Zn (Zincell anode paste Z604001, $MC = 43$, $TW = 80$), which act as positive, oxidizing and negative, reducing

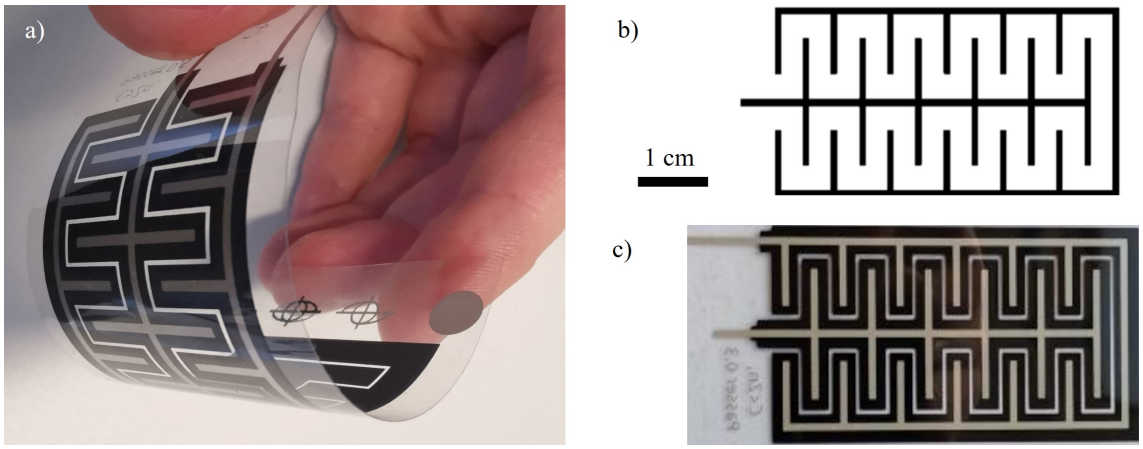

Figure 3.14: a) Screen-printed Zn/MnO_2 battery in bent state. b) Interdigitated design for the battery. c) Optical image through the transparent PET substrate revealing the Ag current collector, MnO_2 on the outer branch, and Zn on the inner branch.

electrodes, respectively. Drying each layer in a furnace at 120 °C for 10 minutes removes residual solvents. The electrolyte (Zincell electrolyte paste EC1020) is manually applied to activate the battery and does not require further treatment. The electrolyte is a water-based gel with metal salts and adjusted to pH = 4. Figure 3.14 c) presents an optical image through the transparent substrate of the bottom side of the MB with the Ag current collectors and the active electrodes MnO_2 and Zn (outer and inner comb, respectively).

One benefit of using shared, screen-printed Ag electrodes with e.g. memory cells is the well-established and more cost-efficient fabrication. This is due to higher technological requirements for inkjet inks that require nanometer-sized Ag particles to avoid nozzle clogging. However, larger Ag flakes in the screen printing paste lead to significant surface roughness. While inkjet-printed Ag lines with a height of 200 nm show low roughness of ca. 20–30 nm (RMS), screen-printed exhibit rougher surfaces of ca. 100–200 nm (RMS) at a thickness of 3–5 µm. This makes obtaining a pinhole-free, insulating coverage more challenging to avoid short circuits between bottom and top electrode, as it is in the same range as the inkjet-printed insulating layer. The roughness needs to be considered for fabrication but also for the electrical characterization of the memory cell. It has been reported for ECMs that roughness of the active electrode reduces the SET voltages and RESET currents, while it might decrease switching variability and endurance [199]. Overall, multi-use of inks streamlines the prototyping process, as the previously screen-printed electrode can be used further, reducing the necessary manufacturing steps and the number of individual inks.

3.6 Memory Cell Setup

Two different setups for ECM memory cells will be discussed, where both aim to reduce the number of necessary inks towards the integration of different printed electronic components. The first consists of a symmetric design of Ag/Spin-on-Glass/Ag and takes advantage of the screen-printed Ag electrode, which can be used as the current collector for the battery but also as the active electrode for ECM cells. The second explores the opportunities to utilize emerging Cu-based components in printed electronics for a Cu/Cu_xS/W cell. Scientific and technological advancements enable the replacement of Ag-based conductive tracks by Cu [134] and even make them commercially available [135].

3.6.1 Ag/SoG/Ag

To complement the thick-film technology required for the batteries, the insulating layer is inkjet-printed, ejecting drops with volume of 10 pl. This method allows the precise deposition of a thin layer of ca. 100 nm, which is essential for the initial switching process that is controlled by the electric field within this layer [64]. Inkjet printing is a non-contact technique and allows the usage of the existing screen-printed Ag structure without impairment. Spin-on-Glass (SoG, Honeywell Accuglass 111) provides an electronically insulating layer that acts as a matrix allowing metallic filament growth. Sintering of SoG for 1 h at 200 °C has been shown to create highly insulting layers, allowing resistive switching ratios of 10^4 [25]. Defects and nanometer-sized pores within the amorphous glass layer facilitate ion migration [81]. After this step, the electrode is partly covered with an insulating, adhesive tape to facilitate the application of the top electrode. This step can also be integrated for large-scale fabrication since the battery requires encapsulation for any application. The top electrode is applied manually to complete the Ag/SoG/Ag cell and consists of conductive paste based on 8 µm small Ag flakes (ACHESON 1415).

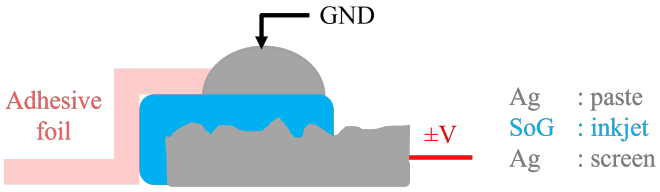

Figure 3.15: Schematic setup of printed Ag/Spin-on-Glass/Ag ECM cell. The screen-printed Ag bottom electrode also functions as current collector for the battery. Inkjet printing is used to deposit the thin insulating layer of Spin-on-Glass (SoG). An adhesive foil functions as a packaging template and the top electrode consists of Ag paste.

3.6.2 Cu/Cu$_x$S

Copper as a base material for Cu/Cu$_x$S-based ECMs is either thermally evaporated on Si-wafers or inkjet-printed on Kapton substrate. The first approach is more technologically demanding and requires clean-room environment. However, more defined conditions enable proof-of-concept investigations before transferring the process to a fully printed design. Furthermore, the wafer will be lithographically structured (s. Fig. 3.16) to observe the transformation from Cu to Cu$_x$S in a defined area and provide a separation layer for contacting. The second approach uses inkjet-printed Cu lines sintered using IPL to demonstrate the potential for a fully printed memory cell.

Cu - Wafer

The structuring begins with evaporating 250 nm of Cu onto a 4” Si/SiO$_2$(100 nm) wafer under vacuum conditions. Next, photoresist (PR) is applied and lithographically structured. For positive resists, unexposed areas remain insoluble to the basic developing solution. Therefore, positive PRs are not feasible due to inkjet printing of $Na_2S_{(aq)}$ outside the cleanroom. Here, natural UV light develops the PR, thus the basic Na_2S ink (pH(0.1 M Na_2S) = 12.93) dissolves the PR buffer. This can be overcome by using a negative PR which functions as a robust spacer (micro resist technology, maN415). Spin-coating applies the PR onto the substrate after applying a Ti-primer (5,000 rpm) as adhesion promoter. The spin-coating speed of 10,000 rpm deposits the negative PR layer with a homogeneous thickness d of 1100 nm.

The spacer thickness must be similar to the deposited dielectric material to enable areal contacting. Further, resistive switching benefits from thinner dielectric layers since the electric field E increases with $E \propto 1/d$, driving ionic migration. Additionally, shorter filaments are more robust against disturbances and require less energy during filament formation [200, 201]. Well performing storage cells possess d in the range of 100 nm [25] but can be smaller than 5 nm by using thin-film deposition techniques [202]. Due to these considerations and the thin dielectric material Cu_xS in the following steps, partial development (micro resist technology, maD332s) reduces d(PR) down to 150 nm before exposure (s. Fig 3.17). Reflectometry probes the resulting thickness non-destructively to confirm the result. This method allows precise determination of the extent of the semi-transparent PR layer without exposing it. After spin coating, the PR displays an average thickness of (1141±23) nm, where the inaccuracy is determined from the minimum and maximum film thickness. The partial development is performed in several steps, continuing development after measurement. As seen in Figure 3.17, at 60 s the wafer fully developed in some areas (i.e. $d = 0$ nm), while the thickest part is still 180 nm. The inhomogeneity can be explained by the manual process of swiveling the beaker and rinsing it with DI water. After partial development is complete, an appropriate area is chosen, where PR functions as insulating material and allows areal contacting with e.g. conductive carbon tape. The linear decrease of d with partial development time t in Figure 3.17 yields $d(t) = 1141\,\text{nm} - 16\,(\text{nm/s})\cdot t$. The partial development is stopped at 55 s, using DI water and yielding $d = 150$ nm. For lithography, the sample is exposed through a shadow mask that exhibits holes of 86 µm in diameter or trenches between 20–40 µm . The openings are used to create Cu_xS through inkjet application of $Na_2S_{(aq)}$. The dimensions of these structures are confirmed via profilometry.
For switching characterization, the top electrode is either the W-tip of the micromanipulator or adhesive conductive carbon tape (DuploCOLL 28930) consisting of conductive acrylic fabric with a thickness of 110 µm.

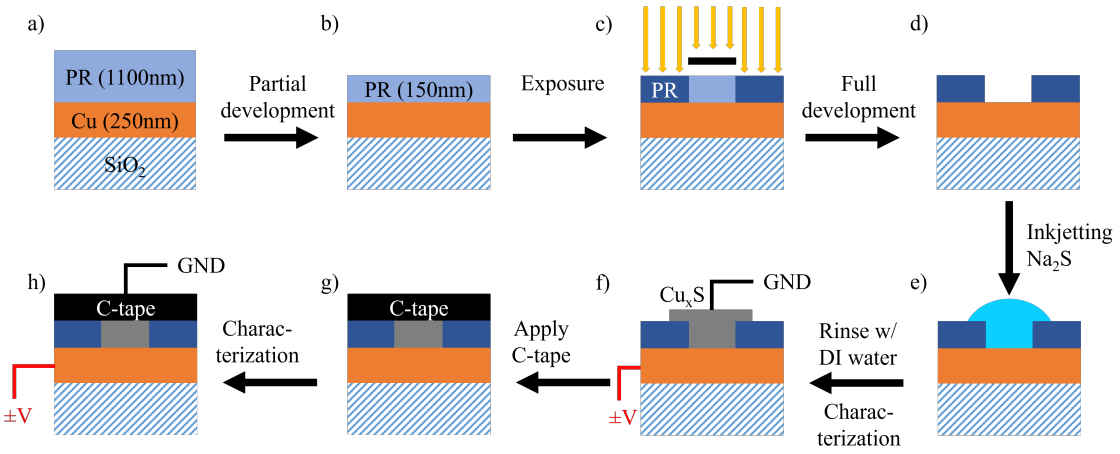

Figure 3.16: Steps for sample preparation and contacting of Cu/Cu_xS/C resistive memory cells. A 250 nm layer of Cu is thermally evaporated onto a Si/SiO_2 wafer (a) and 1100 nm of negative photoresist (PR) is deposited and thinned by partial development (b). After exposure (dark blue PR) and development (c,d), $Na_2S_{(aq)}$ is applied via inkjet printing (e). The fabricated Cu_xS layer is either directly contacted for characterization via W-tip (f) or after the application of a conductive carbon (C) tape (g,h). [111] © 2022 IOP Publishing

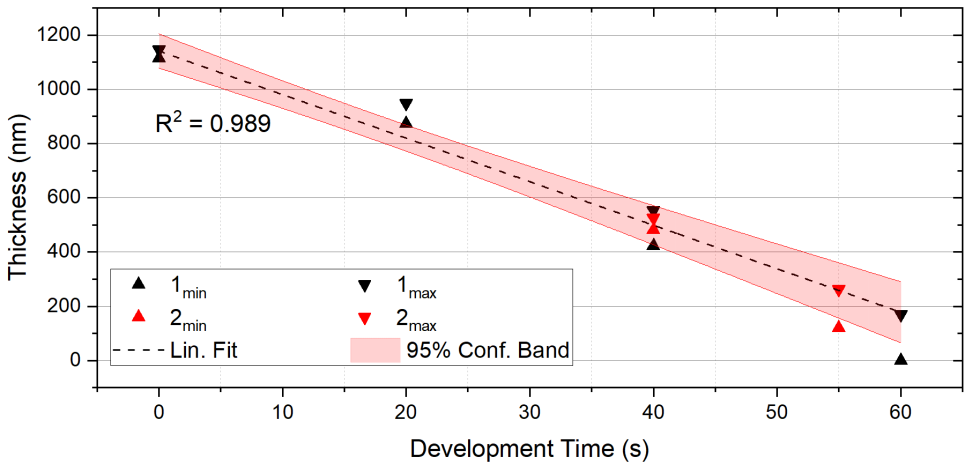

Figure 3.17: Thickness obtained via reflectometry of the photoresist for different partial development times. The inaccuracy is determined from the minimum and maximum of the film thickness. Fitting PR thickness d with partial development time t yields $d(t) = 1141\,\text{nm} - 16\,(\text{nm/s})\cdot t$.

Cu - Inkjet

Inkjet-printed and photonically sintered Cu structures will be used for fully printed memory cells. The fabrication of Cu-NP lines is as described in Section 3.4.2 for the electrodes of the humidity sensor. Furthermore, pads of Cu-NP are prepared as an areal base material for surface transformation and also to investigate the photonic sintering process (s. Fig. 4.13). The spacing of the individual lines d with dropspace DS is chosen appropriately so that the deposited ink merges into a homogeneous layer. The sintered surface is then locally transformed into Cu_xS via inkjet printing using $Na_2S_{(aq)}(0.1\,\text{M})$. Small volumes of 250–750 pl $Na_2S_{(aq)}$ are applied with $DS = 10$ and 5 layers.

3.7 Analysis

3.7.1 Electrical Characterization

The electrical characterization is an essential tool to evaluate the response from different sensors, determine the performance of batteries, and describe the switching behavior of memory cells. The source measure unit Keithley 2400 provides current sourcing and measurement capabilities that can be controlled via a Labview interface. To characterize ECM cells, two tungsten tips are placed on the electrodes via micromanipulators inside an electromagnetically shielded probing station. It can set the compliance current I_{CC} between 1 nA to 1 A within 80 ns for precise control of the SET process. For the highest current sensitivity, the measurement accuracy is ca. ±300 pA [203], which enables reliable measurements in the sub-nA range. Triangular quasi-static sweeps between V_{max} and V_{min} in steps of ΔV and Δt provide information about the switching voltages V_{SET} and V_{RESET} (s. Fig. 3.18). Values for increments in V and t are $\Delta V = 10\,\text{mV}$ and $\Delta t = 80\,\text{ms}$, respectively.

3.7.2 Mechanical Characterization

For investigating the piezoresistive properties of e.g. CNT-based sensor presented in subsection 2.1.1, a lab-built rotate-to-bend apparatus is used (s. Fig. 3.19) [193]. It allows customized sequences of tensile and compressive bending operations by a stepping motor. The latter has to be

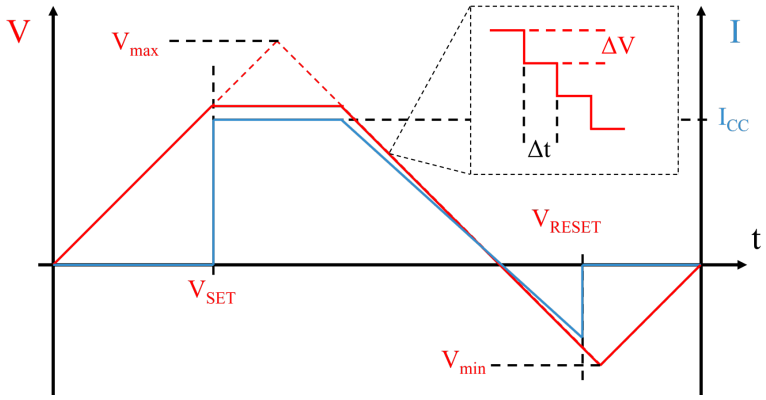

Figure 3.18: Scheme of quasi-static triangular voltage sweep between V_{max} and V_{min} in steps of ΔV and Δt. At V_{SET}, the ECM switches into the ON state and is controlled by the compliance current I_{CC}, therefore the voltage does not reach V_{max}. The Ohmic behavior breaks at V_{RESET} where the filament is dissolved.

emphasized as many publications only report on tensile stress due to the difficulty of compressing a flexible substrate in a controlled fashion. This can be overcome by utilizing our rotate-to-bend setup where the curvature during the rotation can be converted to a bending radius r [193]:

$$r(\beta) = L/\left(2\pi\sqrt{\left(1-\sin\left(\frac{180°-|\beta|}{2}\right)\right)-\frac{\pi^2 d^2}{12\cdot L^2}}\right), \tag{3.17}$$

where β is the bending angle with respect to the neutral position, which is positive for tensile and negative for compressive deformation (s. Fig. 3.19), d is the thickness of the substrate, and L is the spacing between the clamps holding the sample. The tensile or compressive strain ϵ is closely related to r by the formula $\epsilon = \pm d/(2r)$ [204].

The piezoresistive response to bending can be characterized in two ways: during a static bending measurement, the sample is bent stepwise and measurements are performed at defined bending angles. For fatigue tests, the samples perform complete bending cycles (tensile, compressive, or both) with a certain maximum bending radius and are characterized at the neutral, unstrained position. This allows fast and reliable evaluation of change in resistance during or after strain exposures. To comparatively quantify the sensitivity of devices, the gauge factor (GF) is given by

$$GF = \frac{\Delta R}{R_i}\cdot\frac{1}{\epsilon}, \tag{3.18}$$

where $\Delta R = R_f - R_i$ is the difference between the final and initial resistance, respectively.

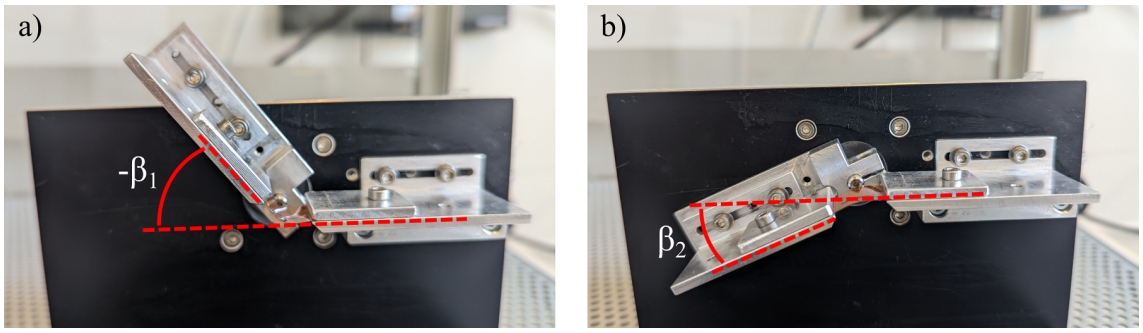

Figure 3.19: Strain regimes for structures on the topside of flexible substrate. Compressive (a) and tensile (b) strain with bending angles $-\beta_1$ and β_2, respectively.

3.7.3 Temperature and Humidity Environment

At the probing station, a thermal chuck (WaferTherm SP 53 A) provides controlled conditions for measuring thermo-resistive changes. It is actively heated or cooled to the set point controlled by a lab-built LabView program to investigate changes in R with varying temperature steps of ΔT in the range between 20 °C–100 °C and an accuracy of 1 °C. If necessary, samples are glued via thermal conductive paste (Gelid GC-2) on a Si-wafer for homogeneous temperature distribution and easier handling. Vacuum suction holds the wafer in contact with the thermal chuck for better thermal contact. A Keithley 2400 sourcemeter measures R (s. Sec. 3.7.1) with a variable waiting time of usually 5 s after the thermal chuck has reached its designated value to avoid thermal fluctuations.

A climate chamber (ESPEC, SH-242) offers active temperature and humidity control via the BTHC system (balanced temperature and humidity control). A low heat-capacity heater and humidifier as well as a high heat-capacity cooler (dehumidifier) control the desired temperature and humidity in real-time. The humidity is determined utilizing the psychrometric principle of two identical thermometers where one is covered by a wet-bulb wick. The dry one measures the current temperature while the wet one (100 % relative humidity, RH) is cooled by evaporation. The RH is calculated from the resulting temperature difference. Without humidity control, the chamber's temperature range is from -40 °C to +150 °C, while the control range using the BTHC system extends from 15 °C to 85 °C and 30 % to 95 % RH (s. Fig. A.9, Appendix) [205].

3.7.4 Profilometry

Contact stylus profilometry (Veeco Dektak 150) probes the geometrical outline of different printed structures in a line scan and can provide vertical sub-nm resolution on a scan length of 55 mm [206]. The probing needle with a tip radius of 12.5 µm is in contact with the specimen and converts the vertical deflections to topographic information. It is a fast and reliable method to determine the surface roughness and lateral and vertical dimensions of samples on rigid as well as flexible substrates. The instrument possesses a maximum vertical range of 524 µm and a vertical step height repeatability of 5 Å at 6.55 µm z-range.

3.7.5 Confocal Microscopy

An optical imaging profiler (Sensofar PLµ 2300) provides information on the three-dimensional micro- and nano-geometry of surfaces. Confocal profiling allows the measurement of smooth to rough surfaces as it vertically scans in steps so that every point on the surface passes through the focus. The interferometric mode requires smooth surfaces where the sample is already in focus. The interference patterns between the reflection and a reference beam provide sub-nanometer vertical resolution for shape features on the nanometer scale [207].

3.7.6 Focused Ion Beam Scanning Electron Microscopy

A scanning electron microscope (SEM) is a versatile instrument to probe the surface by rastering a focused electron beam and gathering the reflected or scattered electrons. A high-voltage anode accelerates electrons focused by electromagnetic lenses onto the sample in an evacuated chamber. Different detectors provide 3D information with nanometer resolution about the interaction of the electrons with the material. The SEM images are acquired using in-beam secondary electron (SE) and in-beam backscattered electron (BSE) detectors. The BSE image is more sensitive to elements with higher Z-numbers, while the SE displays more surface features. An X-ray detector enables energy-dispersive X-ray spectroscopy (EDX) to characterize the sample's chemical composition.

This technique is ideally suitable to investigate structural properties of sintered nanoparticle films or microscopic changes for surface transformation after sulfurization. Additionally, a focused ion beam (FIB) allows to directly probe the cross section of a sample. Here, Ga-ions are accelerated perpendicular onto the surface to sputter the sample in a defined region. This milling exposes the cross section and makes it accessible to SEM imaging. Vertical artifacts (curtaining) may occur for heterogeneous structures or porous materials. The spatial variation of the sputter rate causes forward scattering of the ions, thereby modulating the milling speed and resulting in vertical stripes [208, 209]. To avoid this, a thick and uniform cap of Pt is applied before milling to smoothen the surface. The model 'Tescan Lyra3' will be utilized to investigate stacked layers or probe the active printed battery components. Continuous magnification from 1–1,000,000 x makes this instrument ideal to understand the samples on a large as well as on a small scale [210].

Chapter 4

Results and Discussion

This chapter presents results and discussion of the individual printed electronic components and the first steps towards their integration. The content of this section was partially published by me as first author in cooperation with different co-authors [109, 110, 111]. As I did the main part of the written compilation of the contributions, excerpts from these publications will be used verbatim or paraphrased.

4.1 Screen-Printed Battery

The screen-printed Zn/MnO_2 battery will be characterized through profilometry and FIB-SEM for geometrical dimensions and structural properties. Then, the recharging capabilities and capacity of the activated battery are presented.

4.1.1 Geometrical and Microscopical Characterization

In order to characterize single layers of the battery stack, separate sheets with the respective materials are printed. Each layer shown in Figure 3.12 is printed on clean, pre-shrunk PET substrates and dried. This approach allows weighing individual materials and probing the average height via profilometry.

Multiple clean foils are weighed as a reference in an air-protected and temperature-stable environment. This weight is subtracted from the measurement after printing and drying to give the values in Table 4.1. The significant errors associated with the thin Ag layer originate because it is only slightly heavier than variations of the reference foils. The 50 µm wide alignment registers are used as a defined printed structure to determine the thickness of individual layers. This avoids uncertainties with substrate warping for larger profilometry scan lengths but could differ from areal print. The uncertainties for the average height in Table 4.1 are given by variations between different samples and the roughness of the surface. Finally, the density ρ is calculated from mass m and volume V given by multiplying the height with the printed area known from the digital layout.

Comparing experimental densities to their respective literature values exhibits significant differences of factors 2–5. However, the references are given for crystalline materials (Ag, Zn, MnO_2) or are not well defined for conductive carbon, which consists of microscopic carbon powder. Also, the height measurement does not account for porosity within the materials, reducing the effective densities and the proprietary inks of active electrodes Zn and MnO_2 are mixed with carbon.

A complete printed battery without electrolyte is investigated via scanning electron microscopy

Table 4.1: Weight, average height, and density ρ of individual Zn/MnO_2-battery components compared to its literature values.

	Ag	C	Zn	MnO_2
Weight [g]	0.06 ± 0.02	0.14 ± 0.01	0.34 ± 0.03	0.34 ± 0.01
Height [µm]	3.2 ± 0.8	9.3 ± 2.2	24.9 ± 5.4	35.3 ± 7.5
ρ [g/cm^3]	4.33 ± 1.82	1.12 ± 0.24	3.76 ± 0.48	0.91 ± 0.21
ρ_{Lit} [g/cm^3] [92]	10.5	ca. 1.0	7.1	5.1

(SEM) and focused ion beam (FIB) sputtering for closer examination. Figure 4.1 shows the surfaces of the MnO_2-electrode (a) and the Zn-electrode (b), respectively. The MnO_2-electrode possesses a porous micro-crystalline structure, while the Zn-electrode displays spherical features covered by a continuous material. In c), the cross section of the area in b) is sputtered and polished via FIB to expose the different layers. At the bottom, the flake-based Ag current collector with a thickness of 3 µm is followed by 6 µm of conductive carbon. The main part of the cross section is the 17 µm thick Zn-electrode consisting of Zn particles ranging from 1.0–6.8 µm embedded in conductive carbon. The boundary between the protective carbon layer and Zn-electrode can be determined from the transition of a granular structure at the bottom to the smoother structure with large pores. In d), the central area from the Ag-layer in c) is magnified to show the microscopic structure and the dense and smooth substrate. These SEM images make it clear that the active electrodes are either very porous (MnO_2) or mainly filled with conductive carbon (Zn). This most likely explains the lower experimentally obtained value of ρ compared to literature values. Furthermore, dimensions of the individual layers by SEM are smaller than found via profilometry (e.g. Zn, 17 to 25 µm, Tab. 4.1). Thus, profilometry is a fast and facile way to estimate the physical dimensions of the components but may overestimate the actual values.

4.1.2 Electrical Characterization

Critical parameters for characterizing batteries are capacity C and recharging capabilities, as these factors determine the purposes and fields of application. For determining C, a Labview program controls the SMU for a galvanostatic discharge of the battery. Here, a constant current is drawn from the battery, and the state-of-charge (SoC) is given by the ratio of initial to threshold voltage. The capacity is given by integrating current over time until the voltage has reached the threshold (s. Sec. 2.2). The battery starts at 100 % charge with ca. 1.35 V and is considered empty when the voltage falls below 1.00 V or 0.90 V. The current is reversed after the battery is empty for recharging tests until the voltage has reached 1.70 V.

Figure 4.2 shows the development of capacity and efficiency for 15 repeated discharging and charging cycles at a constant current of 200 µA with $V_{thresh} = 1.0$ V. Initially, the battery exhibits a capacity of ca. 1 mAh but degrades drastically over the first cycles, as seen from the semi-logarithmic plot. The Coulombic efficiency is given by the ratio of introduced and drawn charges from the battery during charging and discharging, respectively. Even though the efficiency increases from below 80 % to over 95 %, it cannot outweigh the poor capacity; a capacity of 0.1 mAh equals a (dis-)charge duration of 0.5 h at 200 µA. It rather approaches the characteristics of a capacitor with a high time constant and possibly considerable self-discharging. Therefore, the screen-printed Zn/MnO_2 battery is not suitable for rechargeable applications. This behavior could be expected as dendrite growth often prohibits the recharge possibility [59], but the manufacturer of the inks claims otherwise, and recent advances have shown solutions to this issue [63, 211].

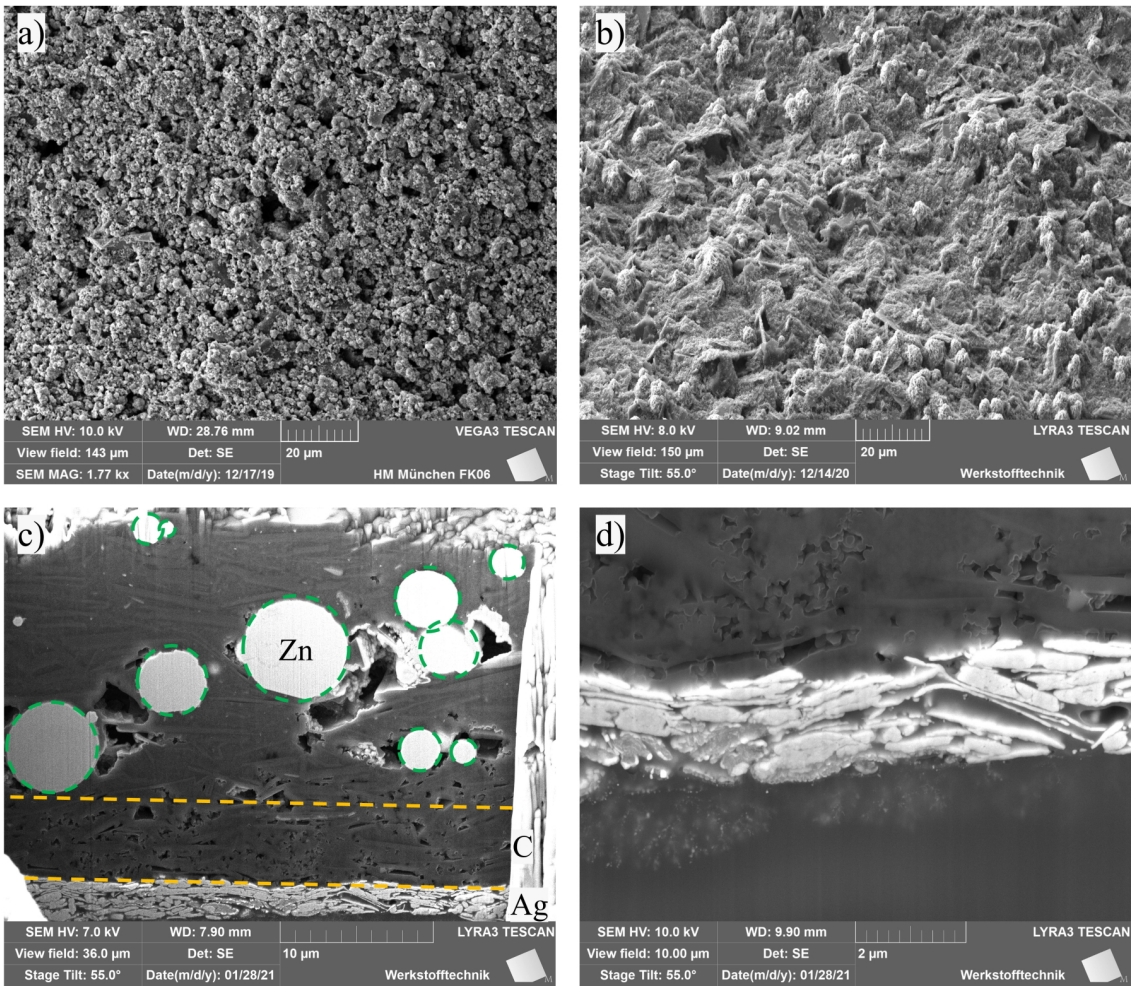

Figure 4.1: Scanning electron microscopy (SEM) images of a) surface of MnO_2-electrode, b) Zn-electrode, c) cross section uncovered by *in-situ* focused ion beam (FIB) sputtering. It shows the flake-based Ag layer (3 µm), conductive carbon (6 µm), and Zn particles (green dashed circles) ranging from 1.0–6.8 µm embedded in conductive carbon (17 µm). In d) the central area of the Ag layer is magnified.

Macroscopic dendrite growth was observed for repeated (dis-)charge cycles. The battery is (dis-)charged at 100 µA over ca. 5 days (115 h) and stored in a styrofoam box to avoid temperature fluctuations and dry the electrolyte. Figure 4.3 shows the optical image of the battery after the experiment. The planar gap between the inner Zn and outer MnO_2 branch is 0.5 mm wide, and many individual needle-like structures have formed starting from Zn. At the highest magnification, these Zn dendrites are highlighted with a length of up to 0.4 mm. The formation of Zn dendrites is especially severe in alkaline electrolytes due to high electrochemical activity, and high solubility of Zn in alkaline media [59]. At the end of a discharge cycle, zincates in the electrolyte are reduced on the surface of the anode to plate out metal zinc. The resulting inhomogeneity in the surface morphology facilitates further growth of dendrites [59]. Even though the electrolyte used here is mildly acidic (pH = 4), which should enable rechargeable aqueous Zn/MnO_2 batteries [58, 57]. Dendrite growth cannot be suppressed, rendering the system unsuitable for long-term applications requiring recharging.

However, the more critical characteristics of tags or labels in intelligent packaging are capacity, facile fabrication, and environmental compatibility. The activated battery is sealed into a polyethylene (PE) pouch for single capacity measurements to maintain humidity in the aqueous electrolyte.

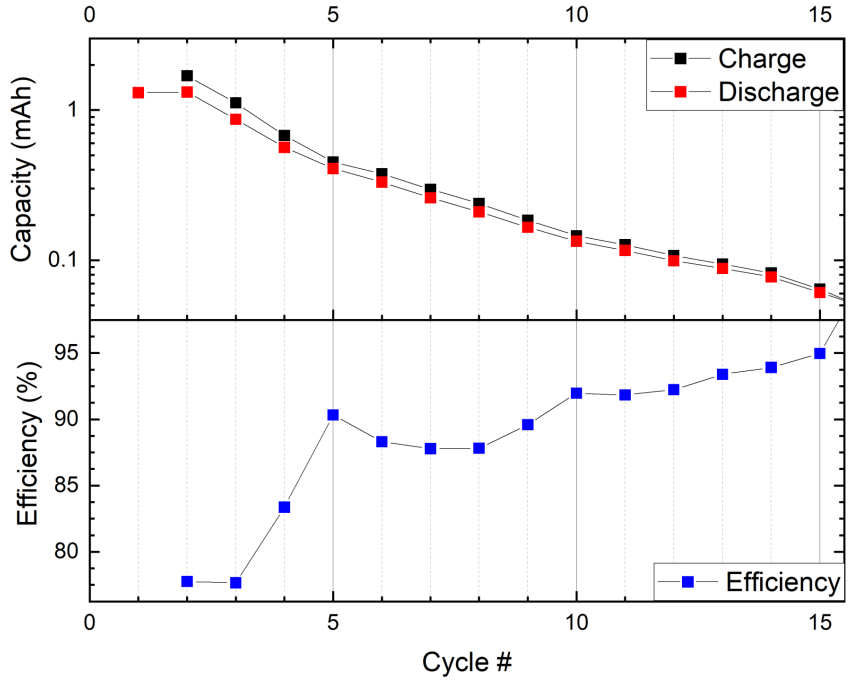

Figure 4.2: Development of capacity for repeated discharge and charging cycle under constant current of 200 μA. The efficiency is given by the ratio of discharge and previous charge.

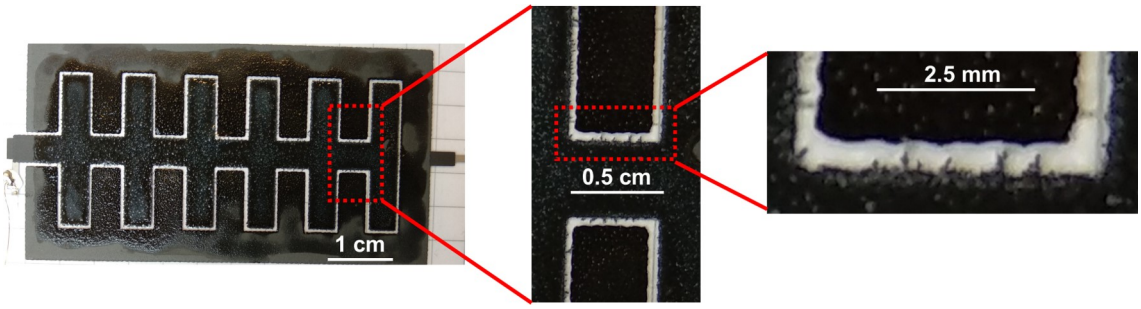

Figure 4.3: Screen-printed, planar Zn/MnO_2 battery after three (dis-)charge cycles with 100 µm over 5 days (115 h). The subsequent zoom-ins highlight the up to 0.4 mm long Zn dendrites towards the MnO_2 electrode across the 0.5 mm gap.

Figure 4.4 shows a discharge curve under constant current of 200 µA over a duration of 52.2 h until it reaches $V_{th} = 0.90$ V. This yields a capacity of 10.4 mAh, and energy of 40.4 J. The internal resistance is determined according to Equation 2.7 and yields $R_i = (91 \pm 11)\,\Omega$ for $R_s = 10\,\text{k}\Omega$ after $t = 0.35$ s. This is considerably larger than for commercial batters ($< 1\,\Omega$) and can be explained by the relatively large distance between the active electrodes. However, it is suitable to operate resistive memory cells, as their required switching voltage (0.2–0.3 V) and maximum compliance currents (1 mA) are still well below what the battery provides.

To compare the battery performance to reported values in literature, the weight needs to be accounted for. To do so, gravimetric capacity is calculated by relating C to the total mass of the battery, excluding the substrate (s. Sec. 4.1.1). This yields 130 mAh/g, which is comparable to traditionally fabricated Zn/Mn-based batteries (100–410 mAh/g [61]). It can be further improved by improving the thickness of individual layers or the composition of active electrodes. Thus, reducing the weight of the battery and maintaining C can increase the gravimetric capacity. Another relevant property of the battery is the short circuit current. It gives the peak current the energy source can provide over a short duration while being directly connected to a load such as a memory

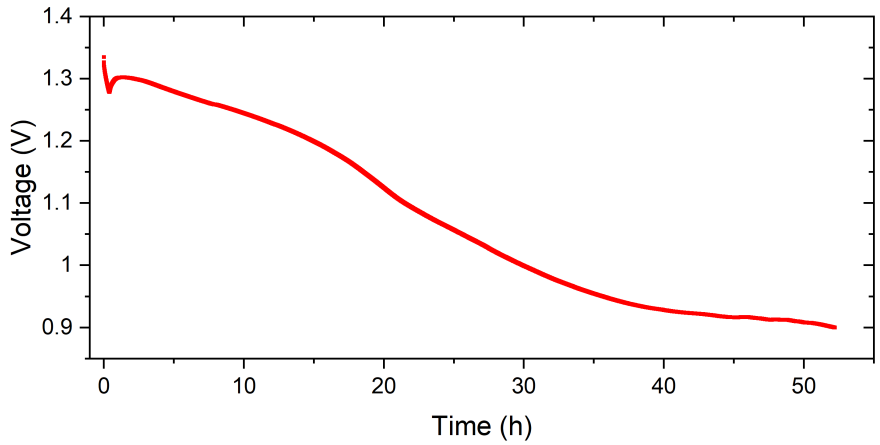

Figure 4.4: Discharge curve under constant current of 200 µA for 52.2 h until it reaches $V_{th} = 0.90$ V. The capacity and energy are calculated to be 10.4 mAh and 40.4 J, respectively. [109]

cell. The inner resistance and the geometric properties of the battery define it as a larger active area, and smaller spacing between the electrodes can provide more current. Different resistors are connected in series while the current is measured for 3 s and the value after 1 s is given in Table 4.2.

Table 4.2: Short circuit current I_{sc} of the screen-printed battery for different series resistors R_s after 1 s of discharge.

R_s [Ω]	1	100	1,000	10,000
I_{sc} [mA]	23.27	6.59	1.17	0.13

4.2 CNT-based Strain Sensor

In the following, CNT-based strain sensors will be presented that are printed in meander or square shape (s. Sec. 3.4.1). Cured and uncured samples are tested to investigate the influence of the curing process on the electrical and bending properties of the sensing MWCNT layer. For the electrical characterization, meanders and squares of (8×8) mm^2 are printed and measured before and after application and curing using the curing agent. The design for the squares is chosen to detect possible realignments of the CNTs by measuring the resistance between opposite edges of the square during bending operations. Initially, some degree of alignment of CNTs can be expected along the horizontal printing direction. The deposited MWCNTs experience a radial force towards the periphery, leading to agglomeration at the fringes. This phenomenon is related to the coffee-stain effect discussed in Section 3.1.3. The solvent flux during evaporation causes outward flow of the MWCNTs, and van-der-Waals interactions cause parallel alignment to the printing direction (s. Fig. 4.5 a)) [212]. Bending perpendicular to the printing direction could induce reorientation of the CNTs along this axis. This could be observable as change in resistance along the horizontal or vertical direction, R_{hor} or R_{ver}, respectively, in printed squares (s. Fig. 4.5 b,d). The reorientation could result in two different scenarios: a higher degree of alignment of the deposited CNTs should result in a smaller resistance due to a lower number of contact resistances between individual tubes [212]. Contrary, alignment in a conductive carbon nanotube network (CNN) results in less random orientation, leading to minimized interconnection and thus to increased electrical resistivity due

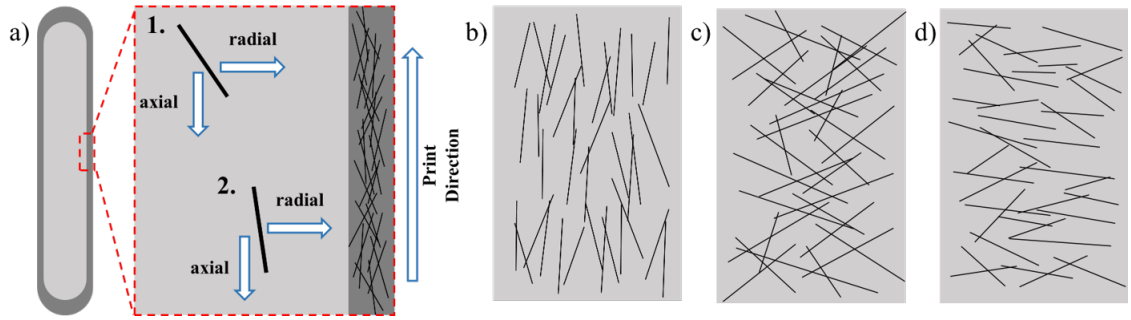

Figure 4.5: Schematic visualization of possible CNT orientations. a) Flow-induced alignment of CNTs in the edge-accumulated coffee-stain region, anti-parallel to the printing direction (adapted from [212, 149]). Orientations of a CNN with b) preferred vertical, c) random and d) horizontal orientation (adapted from [213]). [110] © 2022 IEEE

to higher tunneling distances [149, 213].

Another benefit of the square design is to probe the sheet resistance R_s via four-probe measurement. The probing needles are brought into contact with the sample in a light-shielded hood and pierce through the cured PDMS layer. Hence, changes of R_s due to the curing process can also be evaluated.

4.2.1 Morphology of Printed Structures

An interesting observation in the printing behavior of the CNT-based ink is a very brief settling phase in the beginning. By increasing the dropspace to 100 µm, individual droplets can be created on the substrate (Fig. 4.6 a)). In Figure 4.6 b), the initially applied drops show higher opacity before they become ring-shaped after a few hundred microns (Fig. 4.6 c)). The first drops have a diameter of ca. 44–49 µm with dark CNTs covering the main area. After the settlement phase, drops become slightly larger with diameters d of 48–51 µm and the width w of the rings of ca. 3.4 µm. This implies that the first drops have a higher CNT concentration. Reasons for this could be slight sedimentation after a resting period of the print head or a loss of solvent in the proximity to the ejection nozzles. Both explanations would lead to an increased CNT concentration of the first applied drops.

A similar trend is reported by Dinh *et al.* [212], where they described a remarkable widening at the starting position of the lines and agglomeration of MWCNTs. They interpret this as a sign of strong transportation against the printing direction due to an enhanced evaporation flux along the printed line to compensate for the solvent loss at the contact line [212]. While this is an elegant way to explain the line shape and the phenomenon of CNT agglomeration, a higher density of CNTs in the first printed drops is not addressed. In our case, the material flux cannot be the reason, as no continuous line is present. This behavior should not affect any properties of the device as it occurs only in the first few drops. Similarly, Kao *et al.* [214] report an agglomeration of CNTs at the printing origin due to edge-enhanced evaporation and an overall decrease of CNT density along the printed lines. Such an extended trend is not observed for the printed structures within this thesis.

To conclude, the printed sensor's physical characterization, adhesion, and stability are investigated. Self-adhesive tape tests are successfully conducted, where a strip of adhesive tape (tesafilm transparent, ca. 50 µm) is applied and smoothed onto a cured sample line. After the tape is pulled off, the only visible change is that the Ag paste has been partially removed. A slight increase in resistance of ca. 1 % is observed after removing the tape, which is within the measurement error

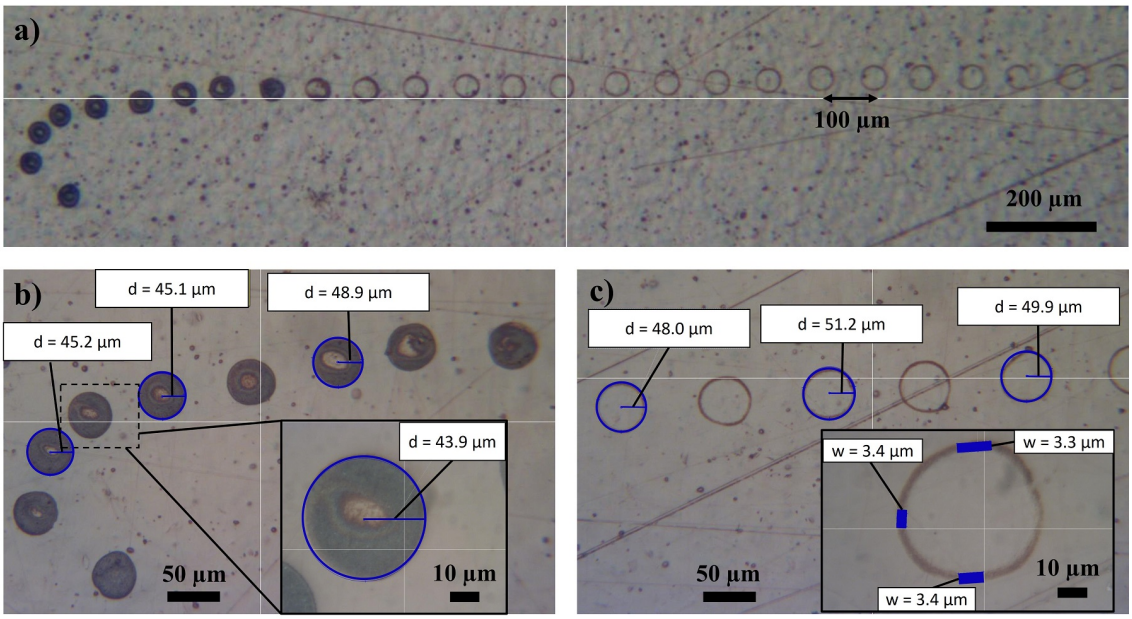

Figure 4.6: a) Optical image of single drops of the CNT-based inks printed on Kapton substrate, designed as a horizontal line with a dropspace of 100 µm. b) Close-up of the first drops with diameter d that are misaligned to the horizontal design due to first drop inaccuracy. c) Single, ring-shaped drops after the printing process have stabilized with width w.

of the multimeter (UT61B, ±1 %). The same procedure leads to the complete removal of the structure if it is performed before the curing step. This confirms that the PDMS content of the ink in the first printing step is not cross-linked to a significant degree and, therefore, cannot provide stability to the CNN structure before it is cured in the second step. It is noteworthy that even though the uncured sample is not resilient against external physical stresses, it exhibits no visible degradation or loss of adhesion during handling or bending operations.

4.2.2 Conductivity of CNT-Network

Conductive polymer composites (CPC) consist of an insulating matrix and conductive filler material, and their conductivity can be described via percolation theory. However, percolation begins at a far lower loading for high aspect ratio conductive fillers (e.g. CNTs) than for spheres. The basic mechanism is similar as there must be a complete path for the electrical current to flow across the structure. More existing paths lower the net resistance, whereas contact points of CNTs contribute the most to the overall resistance [215]. Above the percolation threshold, the conductivity is less influenced by smaller strain, as the impact of stress-induced deformation of nanomaterials is negligible compared to the macroscale composite strain upon stretching since the overall stress is poorly transferred to it [41]. Close to percolation threshold, composite strain sensor materials exhibit non-linear responses as the small number of conductive pathways is more likely to break apart, and thus the conductivity is dominated by the tunneling effect [216].

The length l of the sensor is determined by the print design, yielding a total length of 34.6 mm. Electric measurements are performed using a Keithley 2400. To calculate the resistivity $\rho_1 = R{\cdot}A/l$, (R: electrical resistance; A: cross section), A of the printed lines is measured by profilometry before curing (Veeco 150, 12.5 μm tip radius). The evaluation of A is a significant challenge due to the natural bending of the substrate. Even though the bending dimension is only in the range of μm, it is significant compared to the expected thickness of ca. 200–300 nm of the printed structure.

Table 4.3: Cross section A, resistance R, and resistivity ρ of CNT-based meanders for different number of printed layers. The uncertainty in R is negligible compared to the other values.

Nr. of Layers	A [10^{-11} m^2]	R [MΩ]	ρ [10^4 $\mu\Omega$ cm]
5	1.26 ± 0.52	3.28	12.0 ± 5.2
10	1.85 ± 0.76	1.86	10.0 ± 4.3
15	2.17 ± 1.27	1.12	7.0 ± 4.2
20	2.57 ± 1.32	0.56	4.2 ± 2.2

However, since the lines have a width of $< 200\,\mu$m , this effect is taken care of by subtracting a linear background and characterizing more than ten samples for a statistically significant value for A. As a secondary approach, the sheet resistance R_s of a fully printed CNT/PDMS square is measured using a four-point probe setup (Veeco FPP-100) to compare the influence of the curing process on R_s. Here, the thickness t is also measured by profilometry, where the bending of the substrate can be fitted and subtracted. For CNNs, the overall resistance is attributed to the summation of intrinsic resistance R_{CNT}, contact resistance R_C and tunneling resistance R_T [217].

To better understand the nature of the CNNs, sensors with different thicknesses are printed by increasing the layer count. Additional layers add more ink to the lines, resulting in a larger cross section A. For conventional conductive materials such as Cu or Ag, this decreases total resistance R, while the intrinsic material property resistivity ρ stays constant. In the case of CNNs, additional CNTs may contribute to the increase of A and create a denser CNN that enhances the number of contact points between individual tubes. Unfortunately, neither the density nor degree of networking of the CNTs is experimentally accessible, as profilometry only probes the outline. The cross section is calculated as $A = w \cdot t$, where w and t are the width and average thickness of the structure, respectively. The change in ρ with an increased number of layers and subsequent growth of A is shown in Table 4.3. As expected, more applied material leads to a growth of A and a decrease of R. However, ρ exhibits a clear downward trend. This does not imply that individual CNTs become more conductive but that the CNN might develop into a denser mesh. The values for ρ are given in units of $\mu\Omega$ cm to compare them to conventional conductors in the range of 1.5–10 $\mu\Omega$ cm.

The large error values in Table 4.3 are mainly induced by the uncertainties in the determination of t. Also, since the size of the probe is considerably larger than the roughness of the sample caused by the CNTs, the acquired result for A entails the convolution of the probe and the surface profile. This effect is well known for scanning force microscopy. It will lead to an increase of the experimentally observed size of A, where the convolution error is enhanced for narrow objects [218]. The profilometry results are not actively compensated for this effect because it is negligible compared to the impact of the substrate bending or its roughness.

Comparing the presented results to values found in literature is difficult because ρ is often not given in publications, or MWCNTs are mixed with other components such as epoxy or no binding material at all. As a point of reference, Bouhamed *et al.* reported the resistance of a screen-printed, CNT/epoxy sensor (2×0.5) cm^2 to be in the range of $10^7\,\Omega$ [219]. Unfortunately, the thickness was not given but assuming a thin screen-printed layer of 1 µm , $\rho \approx 2.5 \cdot 10^8\,\mu\Omega$ cm can be calculated, which is four orders of magnitude larger than the value found in this work. Yan *et al.* [220] used solution-casting to fabricate a MWCNT/PDMS based electric heating element. The authors have measured ρ as a function of MWCNT content (wt%) and found a dramatic decrease from ca. $10^{13}\,\mu\Omega$ cm for neat PDMS to ca. $10^6\,\mu\Omega$ cm for a 10 wt% composition of MWCNTs. This is highly relevant, as Yan *et al.* used the same material composition as within this work. Since the above-

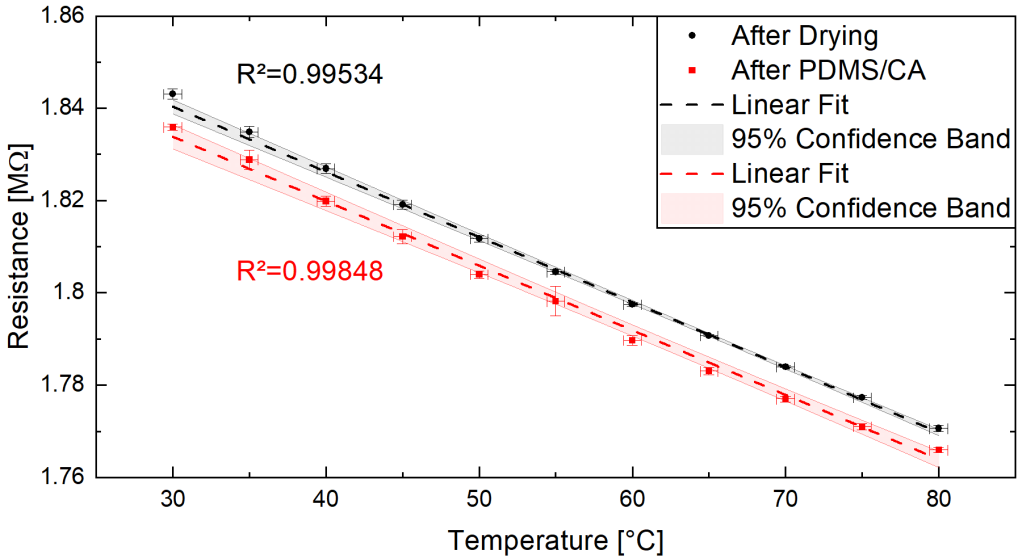

Figure 4.7: Thermoresistive behavior of a CNT/PDMS sensor after drying at 100 °C and after application of PDMS/CA and curing at 250 °C. The linear fits are shown with the corresponding 95 % confidence band. [110] © 2022 IEEE

reported resistivity is still at least one order of magnitude smaller, it can be concluded that the further increase of MWCNT content in the presented inkjet-printed sensors (25 wt% compared to 10 wt%) results in lower resistivity and agrees well with the detailed investigation by Yan *et al.*. Another reference value is found in the work of Kao *et al.* [214] where they used a commercially available CNT ink (CNT-22, lab311, Korea) for a fully inkjet-printed strain sensor. Unfortunately, the exact composition of the ink was not disclosed, and the thickness for a series of samples with a different number of passes printed was not given. But it was demonstrated that the sheet resistance decreases with the number of printed layers. Based on this observation, the authors claimed that the "increase in the CNTs density [shows that] the sheet resistance decreased with the number of passes" [214]. However, using the given sheet resistance and extrapolating the layer thickness from values given before in the paper, an almost constant resistivity of $\rho = (1.60 \pm 0.20) \cdot 10^5$ $\mu\Omega\,\mathrm{cm}$ can be calculated. Therefore, the claim of a denser CNN is questionable as they did not consider the increasing layer thickness. This is in the same range but still significantly higher than our reported values. To conclude, the values reported for resistivity are among the lowest for printed CNT-based structures, and indications of densification of the CNN is observed.

4.2.3 Thermal Cross-Sensitivity

The thermoresistive response of CNT/PMDS is measured as described in Section 3.7.3 to determine the temperature sensitivity. Figure 4.7 shows the change in resistance for a temperature range between 30–80 °C. The first curve is taken after the first printing step, where the sample was dried at 100 °C on a hotplate to remove residual solvents. The second curve is taken after application of the second layer with PDMS and CA and curing at 250 °C. Both curves exhibit almost identical initial resistances of 1.84 MΩ and TCR of -0.076 %/°C (s. Tab. 4.4). The instrumental inaccuracy for the resistance measurement is negligible and is taken as ±1°C for the measured temperature. The error bars are calculated as standard deviation from three individual, consecutive measurements. The TCR is obtained by linear fitting of the thermoresistive behavior with respect to the initial resistance at $T = 30\,°\mathrm{C}$. This value is in the same order of magnitude as reported TCRs of CNT-based thermistors in the literature that span from -0.036 %/°C (Expoxy/MWCNTs) [221] to

-0.400 %/°C (CNT) [38]. For established, metal-based, bonded strain gauges, the TCR is in the order of +0.001 %/°C [29].

Table 4.4: Parameters for linear fitting of data shown in Figure 4.7 with offset R_i and slope k. The temperature coefficient of resistance (TCR) is given with respect to $R(30\,°C)$.

Sample	R_i [MΩ]	k [Ω/°C]	TCR_{30} [%/°C]
After drying	1.876 ± 0.002	-1399 ± 32	-0.076 ± 0.002
After PDMS	1.883 ± 0.001	-1412 ± 18	-0.077 ± 0.001

4.2.4 Strain Sensitivity

Tensile and Compressive

To determine the piezoresistive response of the CNT sensor and the long-term stability, the gauge factor (GF) is calculated, and fatigue measurements are performed. Figure 4.8 shows a representative piezoresistive curve for static bending of a CNT/PDMS sensor. The values of resistance at the neutral position are taken at the beginning (R_0), after tensile bending (R_1), and at the end after compressive bending (R_2), respectively. Initial tensile bending towards a maximum strain of $\epsilon = 0.72\,\%$ and the return to the neutral position demonstrates a quasi-linear, hysteresis-free ($R_0 \approx R_1$) response with GF ≈ 1.4. For comparison, metal-based strain gauges have a GF of approximately 2 and a nominal resistance of ca. 100 Ω [29]. A higher initial resistance results in a larger absolute change in R, facilitating the read-out.

More complex behavior is becoming apparent by mirroring this strain to the compressive regime $\epsilon = -0.72\,\%$. Unlike conventional metallic strain gauges, the resistance does not decrease further. At $\epsilon \approx -0.2\,\%$ a sudden raise in R occurs, resulting in an increase preserved in the neutral position at R_2. According to the Poisson effect, compression leads to transversal elongation resulting in a greater cross section $A' > A$. The shortened length $l' < l$ and expanded $A' > A$ should result in a lower absolute resistance R. However, this simplistic model holds only true for bulk materials. As described above, the strain sensing properties of CNNs are attributed to the summation of intrinsic resistance R_{CNT}, contact resistance R_C, and tunneling resistance R_T thus. Changes in the resistive properties are associated with modifications of contact arrangements and tunneling distances between CNTs [217]. One explanation is that CNTs gradually change their alignment within the polymer matrix, especially during the compressive strain. It has been observed that an aligned network might increase the resistivity level as the orientation of CNTs becomes less random, reducing interconnections [149].

In the following, the two bending regimes are characterized individually. The sample is bent step-by-step to a maximum strain of $\epsilon = \pm 1.0\,\%$ and returned to the original position. This is repeated several times for the same strain regime before switching to the opposite side (s. Fig. 4.9). This approach investigates whether the peculiar behavior for the compressive region observed in Figure 4.8 is an effect originating from previously applied strain. In Figure 4.9 a), the tensile strain exhibits a quasi-linear response with a vanishing hysteresis after the third cycle. This demonstrates that this sensor could be used without concerns for tensile strain measurements after initializing bending cycles. The relative changes after each cycle in Figure 4.9 c) are calculated with respect to the initial resistance of R_0 for each individual curve for tensile (R_1) and compressive (R_2) strains. At the same time, the trend of R_0 is given for the change to the initial value. It becomes apparent that some degree of relaxation occurs after each measurement because the final resistance $R_{1,2}$ is always bigger than the initial resistance for the following measurement of R_0. Similar observations

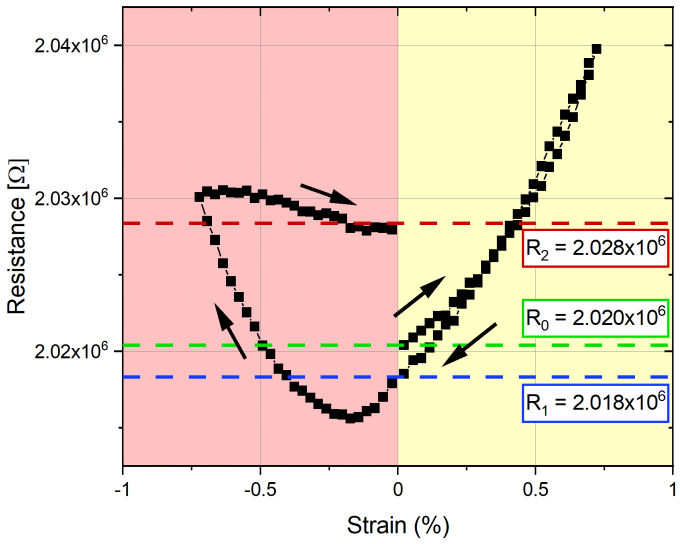

Figure 4.8: Piezoresistive behavior for static bending of cured CNT/PDMS sensor. The initial tensile strain ($\epsilon > 0$) causes a quasi-linear, hysteresis-free ($R_0 \approx R_1$) response with GF = 1.40. The subsequent compressive ($\epsilon < 0$) strain exhibits a more complicated behavior, resulting in a permanent increase of R, with respect to the initial value ($R_2 > R_0$). [110] © 2022 IEEE

were reported for CNT-bases CPCs [222, 223]. Increasing strain amplitudes led to a not fully recoverable increase in resistance. It is explained as perpetual damage to the conductive network and the microstructure of the viscoelastic polymer matrix.

For Figure 4.9 b), subsequent compressive bending cycles exhibit a similar trend with a fading hysteresis effect, visible as the decline in the relative change of R_2 in Figure 4.9 c). However, the characteristic rise at a particular strain level is always present, only shifting in its beginning from $\epsilon \approx -0.3\,\%$ for the first run to $\epsilon \approx -0.6\,\%$ for the fourth run. To conclude, this general behavior is not caused by previous tensile bending but is an intrinsic property of the CNT/PDMS network.

Fatigue

The longevity of the sensor is investigated by measuring the resistance in a neutral position after a repeated number of complete tensile-compressive bending cycles N. It is characterized after the first printing step where the ink only has been dried and with a different sample after the application of PDMS/CA and subsequent curing. As seen in Figure 4.10, the degree of maximum strain to the system is given as the bending radius and in absolute strain percentage, calculated according to Equation 3.17. The resistance R is measured every 10 cycles, and the strain level is altered every 5000 runs. For lower strain amplitudes ($< 2\,\%$) the fatigue testing can be regarded as 'high-cycle fatigue' [224].

Figure 4.10 shows several interesting trends that both curves have in common. Firstly, R for $\epsilon \geq 0.72\,\%$ increases significantly with repeated cycles. The increase exhibits a faster initial and larger absolute rise with growing strain levels, i.e. decreasing bending radii. Secondly, lowering absolute strain ($N > 20000$) exhibits an overall decreasing trend for resistance. This is especially remarkable as $\epsilon = 1.07\,\%$ initially led to a sharp increase in R ($10000 < N < 20000$) while now it displays an overall decrease in R ($20000 < N < 25000$). That is an indicator that the origin of the overall increase is not only a result of device deterioration but could be caused by reorientation of CNTs in the PDMS matrix. In the case of crack evolution, further load should accumulate device damage, leading to further increase in overall resistance. In the basic linear damage concept (Miner's rule), the degree of damage to a sample is given by the ratio of work absorption per cycle

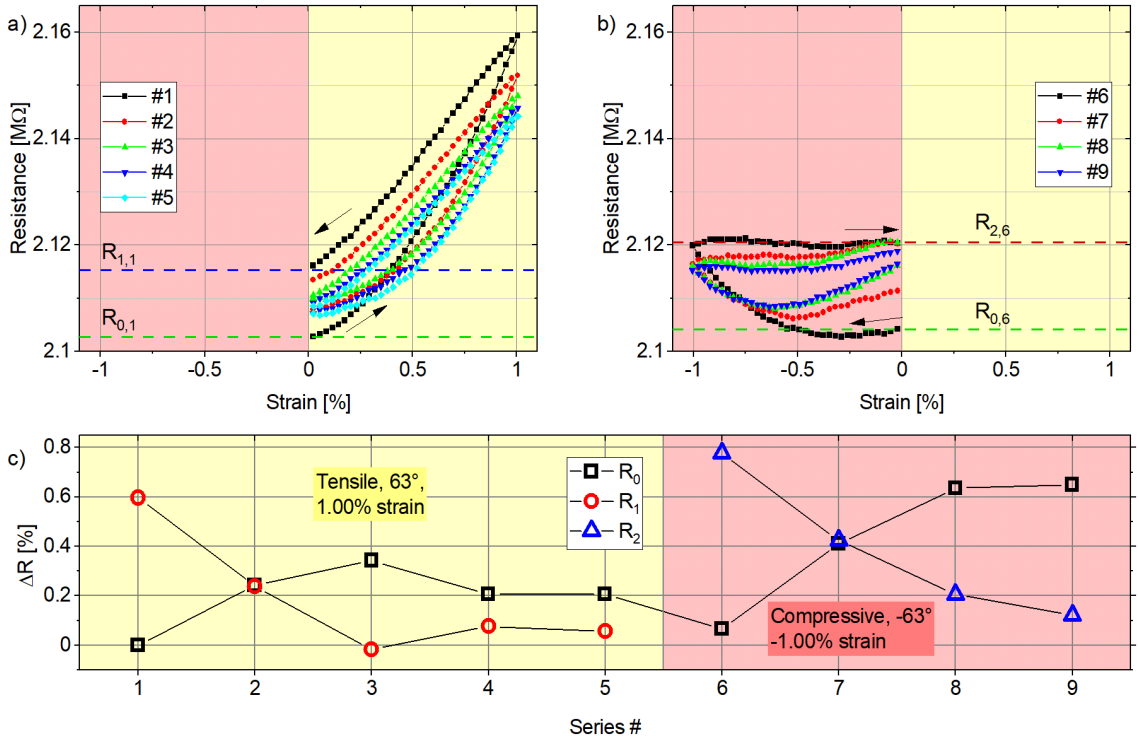

Figure 4.9: Piezoresistive behavior of cured sensor for repeated tensile strain (a), compressive strain (b) and relative variation (c) of resistance after tensile and compressive strain (R_1 and R_2) with regard to the initial resistance of each measurement R_0. The arrows in a) and b) indicate the direction of change and the dashed lines correspond to values used in c). Adapted from [110] © 2022 IEEE.

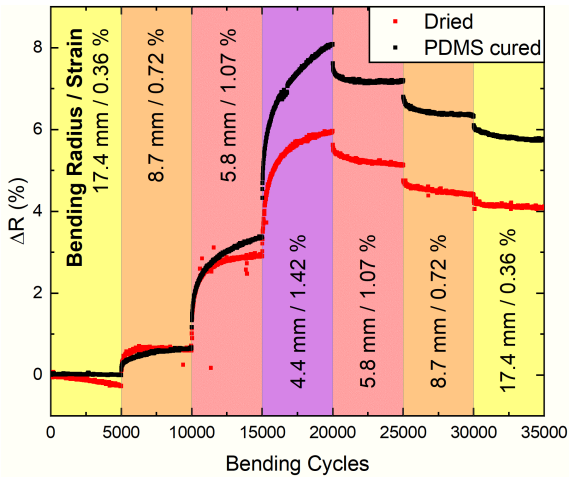

Figure 4.10: Endurance or fatigue measurement of CNT/PDMS sensor after the first printing step (dried) and after curing of PDMS (cured). The resistance is measured every 10 cycles in the neutral position after N complete tensile-compressive bending cycles under a certain bending radius and strain. The strain is changed every 5000 cycles. [110] © 2022 IEEE

Table 4.5: Sheet resistance $R_{s,L}$ for a CNT square of $(8\times8)\,\mathrm{mm}^2$ of various layers L after the first and second processing step. The first step contains printing of different layers of CNT/PDMS and drying at 100 °C for 10 min, the second step includes printing of PDMS/CA and curing at 250 °C for 30 min.

Printing step	$R_{s,5}$ [kΩ/sq.]	$R_{s,10}$ [kΩ/sq.]	$R_{s,15}$ [kΩ/sq.]
After drying	6.76 ± 0.98	3.00 ± 0.40	1.89 ± 0.20
After PDMS	7.37 ± 1.12	2.88 ± 0.21	1.96 ± 0.24

and a characteristic amount of work absorbed at failure [225]. Therefore, each load cycle is linearly added to the total damage and would result in a strictly monotonous resistance increase, which is not observed here. A related phenomenon was reported by Zhang *et al.*, where continuous (tensile) cycling with varying strain levels showed good recoverability after stabilization by cyclic loading. They also observed that lowering the strain level again led to recovery or even a decrease below the initial resistance. They concluded that this recovery is not only caused by the decrease in strain but also a time-dependent process. In our case, time-dependency cannot be excluded, but the overall increase of R suggests a permanent change in the sensor.

A similar trend is visible in Figure 4.10 for $\epsilon = 0.72\,\%$, where R exhibits an increase for low-to-high loading sequence ($5000 < N < 10000$) but a reduction for a high-to-low loading sequence ($25000 < N < 30000$). These observations suggest that CNNs can compensate for or heal deterioration over time which might be caused by the reorientation of CNTs. Hence, mobility and movement of CNTs induced by the high-to-low sequence enable energetically favorable CNT configurations, leading to a lower absolute resistance. For the lowest amount of strain (0.36 %), an initial slight decrease is visible for $0 < N < 5000$, indicating that the sample has been exposed to a higher load before this fatigue test. Finally, the region $30000 < N < 35000$ displays no notable change but an overall increase compared to $N = 0$ of $\Delta R_{fat}(N) = 100 \cdot (R(35000) - R(0))/R(0) = 4.1\,\%$ demonstrates that the sample has persistently changed.

However, the absolute change of R differs significantly between the two printing steps. The final cured sensor exhibits a more substantial increase, especially for the highest strain of 1.42 %. This rise is the main reason for the overall increase in R of 5.8 % for the cured sample with respect to the initial value. The cured sensor exhibits the same trends as the dried one but less recovery for high-to-low stresses. The origin and effects of the cured PDMS layer will be discussed in the next section.

4.2.5 Effects of PDMS Layer and Reorientation During Fatigue Stress

To investigate the direct influence of the curing process on the resistance of the CNN, sheet resistance R_s is measured at six different positions on CNT squares with 5, 10, and 15 printed layers after both printing and curing steps. In Table 4.5, R_s is given for the averaged measurement results before and after curing. It is remarkable that R_s agrees well within the uncertainty boundary and therefore stays virtually unaffected by the curing process. This demonstrates that neither the cross-linking process nor the high-temperature step causes a macroscopic change in the network of CNTs. This result is not self-evident as the transition from uncured, gooey PDMS to cured and solid PDMS might have come with significant changes within the CNN connections.

Finally, an additional fatigue test is performed to evaluate the different responses between CNTs embedded in uncured and cured PDMS. It is conducted similar to the one described in Section 4.2.4. Complete tensile and compressive bending cycles along the vertical axis are conducted with CNT-based squares. This time, additionally to the measurement of R_{hor} as before, the resistance

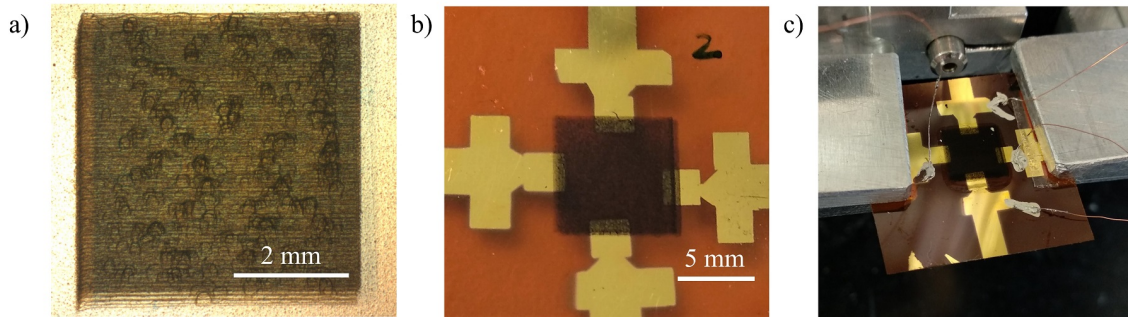

Figure 4.11: Optical image of inkjet-printed MWCNT squares on polyimide substrates. a) $(5\times5)\,\mathrm{mm}^2$ square. b) $(8\times8)\,\mathrm{mm}^2$ on thermally deposited Au contacts. c) Structure from b) in bending setup with connected Cu wires.

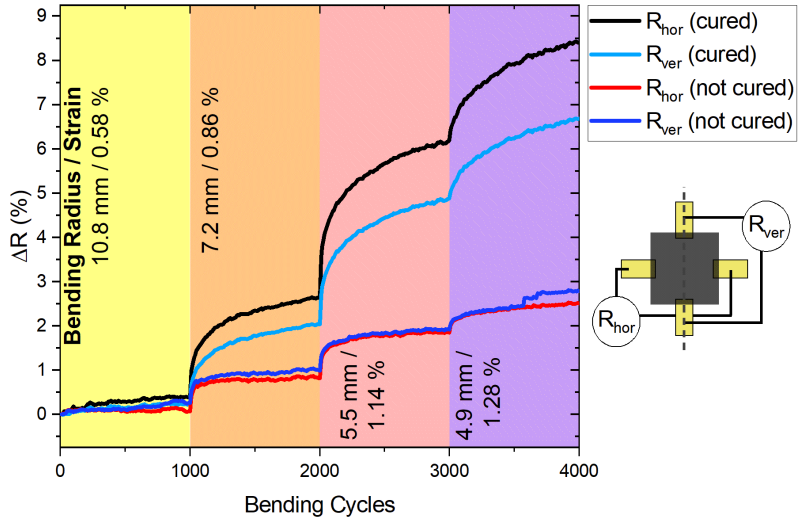

Figure 4.12: Fatigue measurement of CNT-based sensor within uncured and cured PDMS matrix. The resistance is measured after every 10 compressive-tensile cycles in the neutral position along the bending axis R_{ver} and perpendicular to it R_{hor}. The strain is changed every 1000 cycles. The inset shows the measurement configuration, and the grey, dashed line indicates the bending axis. [110] © 2022 IEEE

along the bending axis R_{ver} is determined every ten cycles. Every 1000 cycles, the strain is progressively increased. The square is printed on top of Au contacts of 200 nm that have been thermally deposited on the substrate to avoid contacting problems (s. Fig. 4.11). The contacts are positioned at the center of all four edges of the CNT-square with an overlap in width of ca. 2 mm and depth of ca. 0.5 mm.

Figure 4.12 shows a similar trend as Figure 4.10, where increased strain causes a steeper growth in overall resistance. It shows the relative change of R over several complete bending cycles in the neutral position ($\Delta R = (R - R_0)/R_0$). The comparison between changes in R_{ver} and R_{hor} exhibit important differences in the uncured and cured state. As given in Table 4.6, R_{ver} is significantly higher than R_{hor}, indicating some alignment along the horizontal printing direction. The vertical bending axis is perpendicular to the assumed alignment direction. Therefore, reorientation could occur along the vertical axis, lowering R_{ver} but increasing R_{hor}. Shown in Figure 4.12, the uncured device exhibits a change of 2–3 % in R after the complete procedure, while R of the cured device rises ca. 7–8 % for the same treatment. This could be caused by a difference between the soft, uncured PDMS matrix and the firm, cured matrix. The possible formation of micro-cracks or cavities might lead to a permanent increase in R. These effects will not occur in the uncured case

Table 4.6: Initial resistances of printed CNT square before and after curing of PDMS along the horizontal and vertical direction, as seen in the inset of Figure 4.12.

	R_{hor} [kΩ]	R_{ver} [kΩ]
Uncured	1.535	1.746
Cured	1.778	1.876

due to the missing intrinsic stability. Reorientation can not be excluded but plays a minor role compared to crack formation.

The micro-crack hypothesis is supported by the variance of R_{ver} and R_{hor} for the different PDMS states. The measurements for the uncured sample display the same development with increasing number of bending cycles and strain. However, for the cured structure, R_{hor} rises significantly more than R_{ver}. In the case of crack formation, defects would arise along the bending axis. These cracks would affect R_{ver} less than R_{hor} as they form along instead of perpendicular to the electric pathways. Therefore, the difference between R_{ver} and R_{hor} suggests the formation of cracks along the bending direction.

For future investigations, the cross section A of the sensors could ideally be measured using atomic force microscopy. Dinh *et al.* [212] used this approach for observing the coffee-stain effect of CNNs without PDMS. Also, orientation and possible realignment of CNTs due to bending were only probed indirectly via R. A more direct way could be taken using scanning electron microscopy, which enables the observation of the orientation of CNTs after different treatments. Furthermore, an accelerated process was used for the longevity estimation of the sensor. In applications with sporadic but enduring utilization, resting periods and changes in the environment such as temperature and humidity need to be tested as well. One possibility to compensate for differences in vertical and horizontal bending is to change the printing direction in between layers to achieve a more homogeneous structure [214]. Finally, it might be possible to investigate the effect of different curing levels of PDMS on the sensor performance. This could be achieved by varying the amount or content of the curing agent in the second processing step.

4.3 Photonic Sintering of Copper Nanoparticles

Printed Cu can be utilized as a cost-effective electrode material through photonic sintering. To understand the sintering process, structures of copper nanoparticles (Cu-NPs, Metallon CI-004) on polyimide (Kapton 500 HN) and microscopic glass slides are fabricated via inkjet printing. Two different substrates are selected to distinguish contributions to absorption from substrates and Cu-NPs. The digital design and images of the quadratic Cu structures with side length $l = 15\,\text{mm}$ are shown in Figure 4.13. The spacing of the individual lines $d = 100\,\mu\text{m}$ with dropspace $10\,\mu\text{m}$ is chosen appropriately so that the deposited ink merges into a homogeneous layer. After drying on a hotplate, the structures are sintered using Pulseforge 1300 photonic curing system (Novacentrix). Profilometry provides information about the thickness of the Cu-NP structure on the glass slide, where the smooth glass surface allows precise measurements over the entire region. In the following, results from simulations are discussed, and the sintering process is characterized via FIB-SEM and electrical conductivity measurements.

4.3.1 Absorption and Simulation

For a reliable simulation of the sintering process of inkjet-printed Cu-NPs, the emission spectrum of the sintering lamp, sinter profile, and transmission and reflectance are investigated.

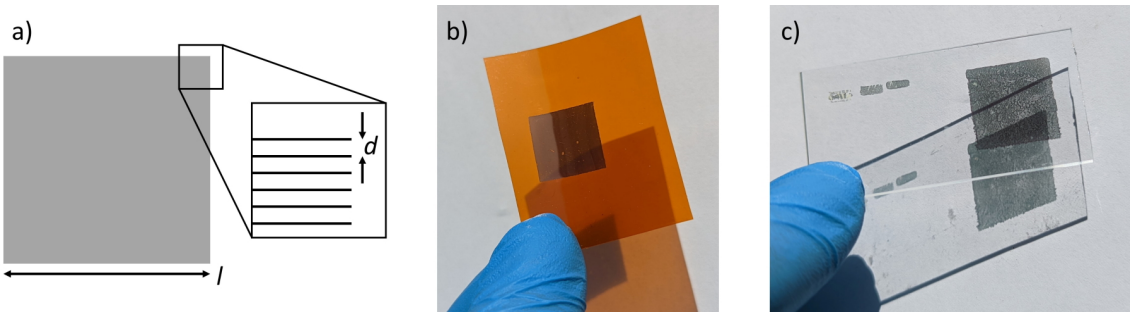

Figure 4.13: Design (a) and photos of unsintered inkjet-printed Cu-NPs pads on 125 µm Kapton (B) and 1100 µm glass slide (c) with side length $l = 15\,\text{mm}$ and $d = 100\,\mu\text{m}$ vertical spacing of individual lines. The lines merge into one homogeneous layer after printing.

Figure 4.14 a) shows the broadband emission of the Xe-flash lamp from ca. 300–950 nm. Higher driving voltages lead to higher discharge intensities. The main intensity ranges from 400–700 nm and shifts towards shorter wavelengths with increasing voltage [226]. In b), the sintering profile during the emission presents the radiant power at a voltage of 370 V with 8 pulses of equal length in an envelope of 10 ms. The software calculates the total power to be $6.2\,\text{J/cm}^2$. The power of the individual 625 µs pulses decreases during the discharge of the capacitor banks. Figures 4.14 c) and d) present transmittance (T, Shimadzu UV-2600) and reflectance (R, Ocean Optics S2000) measurements for 125 µm Kapton and 1100 µm microscopic glass slide, respectively. The absorption A is calculated using $A + R + T = 100\,\%$, and the accessible wavelength region is determined for small wavelengths by the range of the reflectometer. For Kapton, absorption occurs for wavelengths shorter than 600 nm, explaining the orange color and indicating that the flash lamp's intensity gets significantly absorbed. For plain microscopic glass slides, absorption is negligible and could therefore be used as reference substrate material to determine the absorption of thin layers of Cu-NPs. Even though the actual sintering for application will be done on Kapton.

As the spectral intensity for the sinter profile in Figure 4.14 b) is not precisely known, a built-in bolometer is used to determine the absorption coefficient α (s. Eq. 3.9). This value does not give spectral information on the absorption but provides a precise value for the sintering setup. Table 4.7 gives the results for bolometry based on the initial and attenuated intensities. The initial intensity I_0 is measured without any substrate to be $6.20\,\text{J/cm}^2$. For the results in Table 4.7, the reflectance of glass (Kapton) of 8 % (10 %) (s. Fig. 4.14 c), d)) is considered to reduce I_0 to the corrected value of $5.70\,\text{J/cm}^2$ ($5.58\,\text{J/cm}^2$). For Cu-NPs, reflectance is measured to be 15 %, reducing the maximum transmission to $5.27\,\text{J/cm}^2$.

Multiple profilometry scans over the full range of the unsintered Cu-NP structure on glass (s. Fig. 4.13 c)) yield an average height of $(293 \pm 40)\,\text{nm}$. The absorption results for the substrates $\alpha_{\text{Gla}} = 81\,\text{m}^{-1}$ and $\alpha_{\text{Kap}} = 3.7 \cdot 10^3\,\text{m}^{-1}$ are reasonable as window glass is in the range from 4–$32\,\text{m}^{-1}$ [166] and the optical absorption of Kapton 500 HN at 600 nm is $2.5 \cdot 10^3\,\text{m}^{-1}$ [227]. The experimentally obtained absorption for Cu-NPs of ca. $1.0 \cdot 10^7\,\text{m}^{-1}$ is significantly lower than for pure Cu ($\alpha_{Cu} = 6.2 \cdot 10^7\,\text{m}^{-1}$), which can be calculated from literature as $\alpha = 4\pi k/\lambda$ from the extinction coefficient k at 600 nm [228]. However, it agrees well with the value for thin films of Cu_2O and CuO mixtures of $\alpha_{\text{Cu2O+CuO}} = 9.4 \cdot 10^6\,\text{m}^{-1}$ [229], as the unsintered Cu-NPs are also oxidized. Systematic discrepancies could arise from a non-homogeneous film thickness t, which is

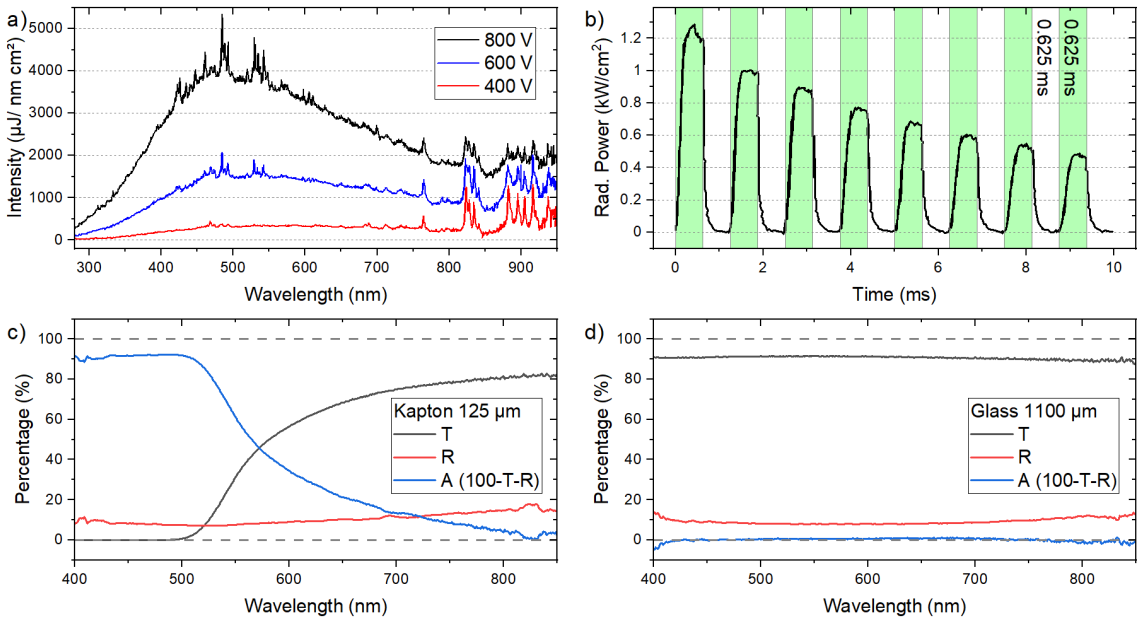

Figure 4.14: a) Emission spectra for 200 µs pulses at different voltages. The main intensity ranges from 400–700 nm and shifts towards shorter wavelengths with increasing driving voltage (adapted from [226]). b) Radiant power and pulseform of sinter profile at a voltage of 370 V with 8 pulses of equal length in an envelope of 10 ms. The total power is calculated from the software (SimPulse) to be 6.2 J/cm^2. c), d) Spectral transmittance (T) and reflectance (R) measurements and absorption (A) equals 100-T-R for 125 µm Kapton and 1100 µm microscopic glass slide, respectively.

Table 4.7: Bolometry results to determine the absorption coefficient α for the initial intensity I_0 and after attenuation I. Literature values α_{Lit} are given for comparison. The samples consist of a blank glass slide, and two thin films of Cu-NPs of different thickness t.

	I_0 [J/cm^2]	I [J/cm^2]	t [µm]	α [1/m]	α_{Lit} [1/m]
Kapton	5.58	3.51	125	$3.7{\cdot}10^3$	$2.5{\cdot}10^3$ [227]
Glass	5.70	5.22	1100	81	4–32 [166]
+Cu-NPs 1	5.27	1.44	0.10	$1.0{\cdot}10^7$	$6.2{\cdot}10^7$ [228]
+Cu-NPs 2	5.27	0.40	0.25	$1.3{\cdot}10^7$	

taken for the calculation, and pinholes in the film due to insufficient wetting. Furthermore, the measurement via bolometry at different energies might partially sinter the Cu-NP layer. Still, this facile measurement of α for different materials works remarkably well as it is in the same order of magnitude as more elaborate approaches.

The photonic sintering machine Pulseforge 1300 comes with the proprietary thermal stack simulation tool SimPulse (v. 3.0.0.3008) to model the time-dependent temperature development during exposure. Figure 4.15 shows the temperature development in steps of $\Delta t = 0.612$ ms on the surface of a new Kapton substrate (125 µm) and for a uniform Cu layer (1 µm) on top of it. For the simulation in SimPulse, values for absorption of 37.1 % and 53.1 %, respectively, are taken by the previous bolometry measurements considering the corresponding reflectivity. The inset of Figure 4.15 emphasizes the first 20 ms where the samples reach their highest temperatures at the end of the 10 ms radiant exposure (s. Fig. 4.14 b)). It is noteworthy that the simulation yields virtually the same results for a 1 µm layer of CuO or Cu_2O on the same substrate (not shown). Also, in the case of the stack Cu/Kapton, the temperature at the interface between Cu and Kapton is identical to the surface due to the high thermal conductivity of Cu. The simulation demonstrates the stark difference between the bare substrate and with Cu layer. With a thin film of Cu, the

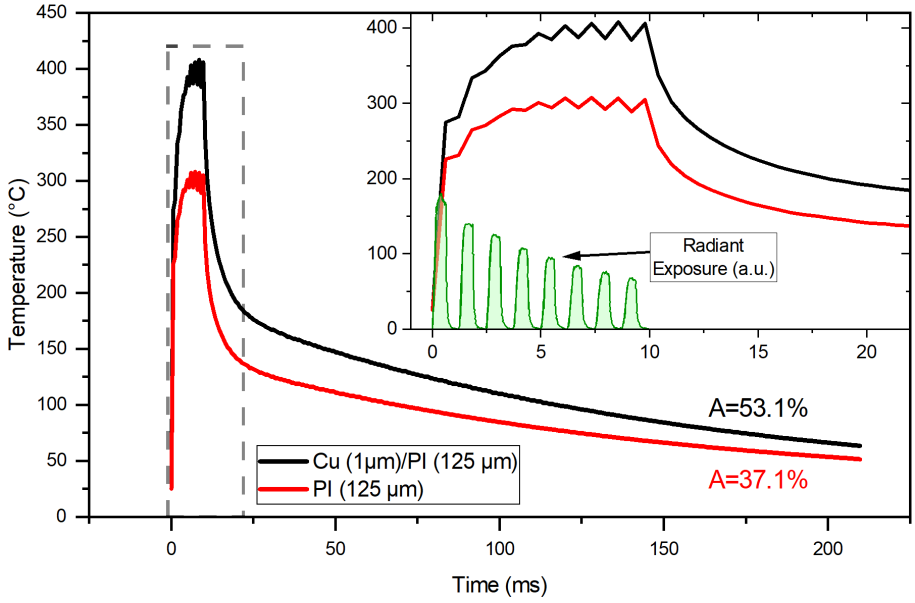

Figure 4.15: Simulation of the surface temperature for pristine Kapton (PI) substrate (125 µm) and for a uniform Cu layer (1 µm) on top of it. The simulation tool Simpulse utilizes the value for absorption of 37.1 % and 53.1 %, respectively. The inset shows the initial temperature rise during the radiant exposure of the sintering pulse (s. Fig. 4.14 b)).

glass transition temperature of Kapton (T_g = 400 °C) is surpassed for a few milliseconds, which could lead to deformations of the substrate. The surface temperature of Cu with 400 °C is far below the melting point of 1085 °C. However, nanoparticles have a high surface to volume ratio, leading to melting point depression due to the considerable influence of the surface energy on the structure of small particles [152, 153] (s. Sec. 3.2.2.2). For 50 nm Cu-NPs, differential scanning calorimetry was used to demonstrate a melting point of only 450 °C [153]. The following sections show the successful sintering process and that a conductive structure can be achieved. Thus, the simulation and literature references provide a first estimation and indicate the potential of the actual sintering process of Cu-NPs. To further validate and understand the sintering process, Appendix A.5 presents a Comsol simulation for temperature development for the boundary region and non-uniform profiles.

4.3.2 Scanning Electron Microscopy

Figure 4.16 shows the SEM images for inkjet-printed Cu-NPs on polyimide substrate after photonic sintering. The overview in a) exhibits the surface structure at the edge of the printed line as well as the milling area with the Ti cap that is applied *in-situ* before milling to prevent curtaining (cp. Section 3.7.6). The warping of the substrate is due to local deformations of the substrate during the sintering process. Figure 4.16 provides a closer look at the right end of the cross section. The backscattered electron (BSE) image highlights the material contrast between polyimide (PI) substrate, Cu-NPs with an average thickness of 370 nm, and the Ti capping layer. It also makes the porosity visible resulting from the necking of spherical Cu-NPs (cp. Fig. 3.6). To quantify the porosity, the area corresponding to Cu is marked, and it yields for the area of (2.50×0.45) µm^2 a filling of 54.5 % or porosity of 45.5 %, respectively. Further determinations at different locations lead to an average porosity of (49.7±4.1) %.

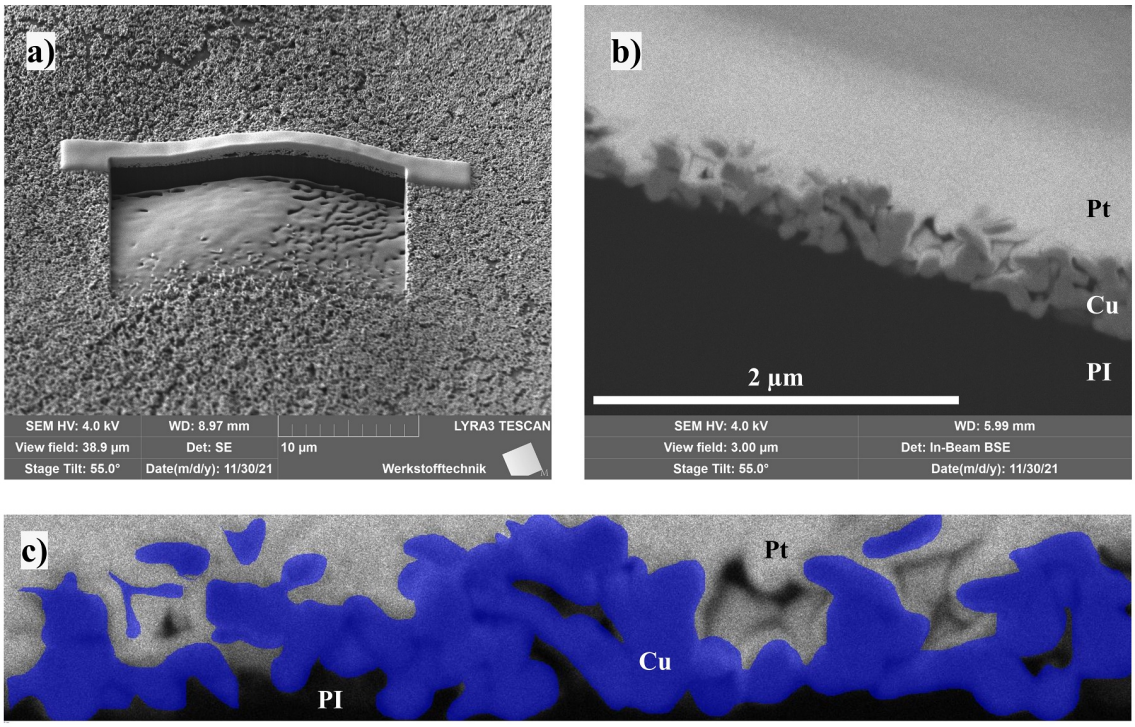

Figure 4.16: SEM images of FIB cross section of sintered Cu-NPs on PI. a) shows the overview with the uniform Ti cap to prevent curtaining. b) exhibits the cross section in detail and highlights the melted Cu-NP. The backscattered electron (BSE) image highlights the difference between the PI substrate and metallic components. In c) Cu areas are highlighted in blue, yielding a porosity of 45.5 %.

4.3.3 Conductivity

The resistivity of the Cu lines is calculated from the resistance and physical dimensions of inkjet-printed lines. They exhibit a smooth surface in the central plateau area of ca. 200 nm with a root mean square (RMS) roughness of RMS = 34 nm, narrow width distribution of the full line (320 ± 13) µm , but also an apparent coffee-stain effect resulting in 600–800 nm high and ca. 30 µm wide elevated edges. This yields a value for $\rho = (21.8 \pm 1.3)\,\mu\Omega{\cdot}\text{cm}$, which is ca. $13{\cdot}\rho_{\text{Cu,bulk}}$ ($\rho_{\text{Cu,bulk}} = 1.7\,\mu\Omega{\cdot}\text{cm}$) or 7.8 % of the bulk conductivity. Four-point probe measurements (Veeco FPP-100) confirm this value ($\rho_{\text{4PP}} = (22.2 \pm 2.6)\,\mu\Omega{\cdot}\text{cm}$) on a printed and sintered $(15{\times}15)\,\text{mm}^2$ Cu-NPs square. The elevated resistivity compared to bulk Cu is due to porosity in the sintered material. Instead of forming a crystalline, dense structure, Cu-NPs retain their spherical shape but connect via necking to create conductive pathways [159, 161]. However, the experimental value for ρ is calculated from the outline of the structure (cross section A) and does not consider the porosity. This overestimates the actual value for A, leading to an overestimated value for the resistivity due to $\rho \propto A$.

The porosity-dependent conductivity was introduced in Equation 3.6 as $\sigma = \sigma_0\,(1 - \Theta/\Theta_M)^n$. Different models are engaged to evaluate if the conductivity of the sintered layer $\sigma_{\text{CuNP}} = 7.8\,\%{\cdot}\,\sigma_{\text{Cu}}$ can be explained by porosity alone. Figure 4.17 depicts the relative electrical conductivity $\sigma_{\text{rel}} = \sigma/\sigma_0$ versus porosity Θ for different fitting parameters n and maximum porosity Θ_M. For the experimentally determined porosity of the sintered Cu-NPs $(49.7{\pm}4.1)\,\%$ and a maximum porosity $\Theta_M = 0.60$, the minimum value for $\sigma_{\text{rel}} = 3.8\,\%$ is obtained for $n = 1$, and the maximum to be $\sigma_{\text{rel}} = 24.0\,\%$ for $n = 1.44$. The wide range for σ_{rel} and the fact that σ_{exp} is on the lower end of this span indicates that porosity could be the main reason for the reduced conductivity, but other

factors have to be considered as well. One reason is the oversimplification of a constant thickness of the sintered structure. Also, the porosity model assumes pure copper, while possibly not all Cu-NPs have been reduced during sintering. Additionally, the sample possesses a large natural oxide layer on its surface due to porosity.

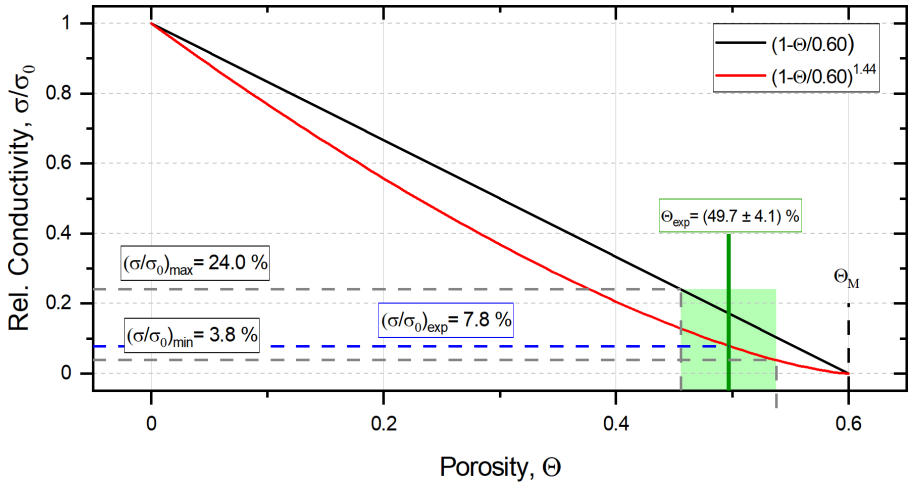

Figure 4.17: Relative electrical conductivity versus porosity for different fitting parameters $n = 1$, $n = 1.44$ and maximum porosity $\Theta_M = 0.60$. For the experimentally determined porosity of the sintered Cu-NPs of (49.7±4.1) %, the minimum and maximum relative conductivity is 3.8 % and 24.0 %, respectively.

Figure 4.16 reveals that the sintered structure is closer to individual spherical NPs than homogeneous bulk material. In literature, lower values for porosity in the range of 10 % are reported. Ryu *et al.* manually applied Cu-NP ink on PI substrate followed by drying and photonic sintering [159]. They demonstrated a porosity of 13.9 % but obtained it from a surface SEM image. This vastly underestimates the value, representing only the projection from the volume to the surface. Furthermore, they use this value to calculate the resistivity to be 5.2 µΩ·cm based on a model for "high porosity materials having three-dimensional reticulated structure" [230]. Chan *et al.* presented a more reliable comparison for inkjet-printed Cu-NP on PI [161]. Here, a 1 µm thick layer is printed and progressively photonically sintered to reduce the porosity from initially 38.3 % to 6.3 % but it also increases cracks in the material. The resistivity is found in the range of 7–15 µΩ·cm and demonstrates the potential for further improvement of the sintering process.

4.4 WO_3-based Humidity Sensor

In the following, inkjet-printed humidity sensors consisting of Cu interdigital transducers (IDTs), covered by WO_3-NPs are investigated. First, the printing result is geometrically characterized by profilometry, and confocal microscopy, followed by discussing the resistive response of the sensor to changes in a controlled environmental chamber. A vapor barrier made from composite PET/Al/PE film is evaluated for moisture insulation.

4.4.1 Geometrical Characterization

Geometrical characterization is carried out after sintering of the Cu-IDTs and after application of WO_3 (fabrication steps, s. Fig. 3.11). Figure 4.18 shows confocal microscopy images of two different Cu-IDT (a), c)) and after the application of WO_3 (b), d)). In a) white, dashed lines trace the Cu lines, and the black, dashed box in b) represents the outline of the WO_3-covered area.

Due to substrate warping and artifacts, a quadratic background was subtracted, and defects were removed by selected interpolation. The IDT fingers in a) and c) are designed to be 750 µm apart and exhibit a well-defined structure with finger widths of 450–520 µm, leaving gaps of 300–230 µm in between. After the application of WO_3 (b), d)), the area becomes more diffuse, indicating that the entire area has been covered.

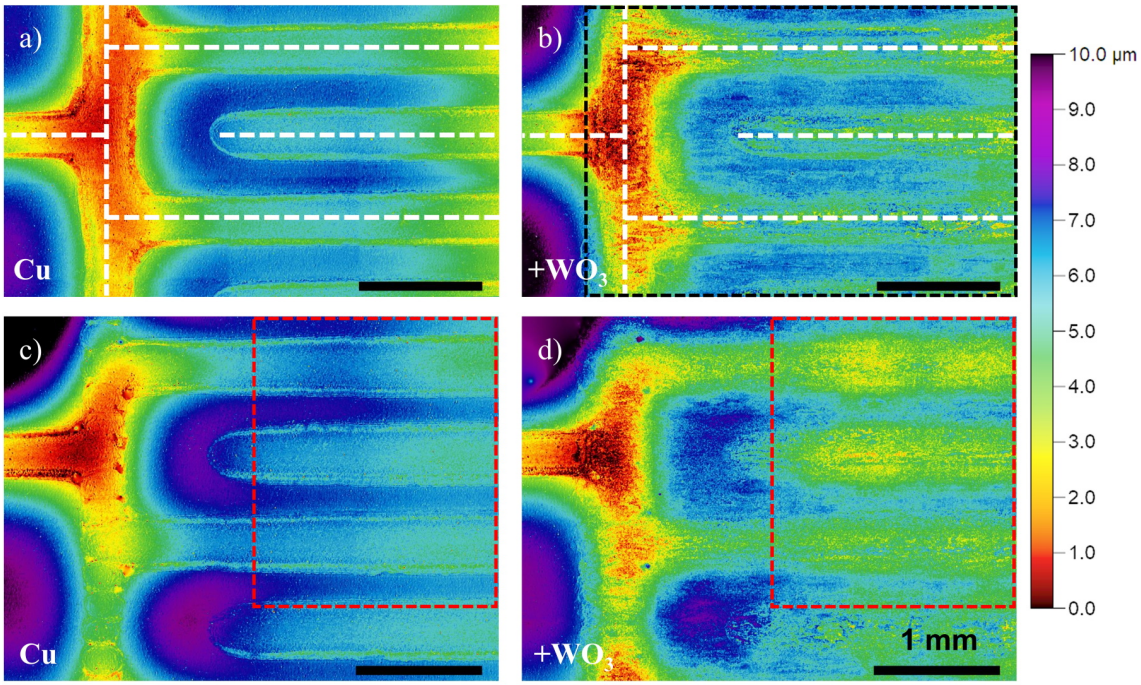

Figure 4.18: Stitched confocal microscopy of the left central area of the Cu-IDTs after background subtraction. a), c) show two different Cu-IDTs, and b), d) show the same area after the application of WO_3. White, dashed lines trace the Cu lines, and the black, dashed box represents the outline of the WO_3-covered area. The red, dashed boxes in c) and d) mark the region for the profiles taken in Figure 4.19. The corresponding image pairs are adjusted to show the same area and the same vertical scale. The scale bar is 1 mm in all images.

Figure 4.19 shows the vertical profiles of 2.55 mm from the confocal images in Figure 4.18, averaged over 2 mm. In a) different regions are labeled as Cu or polyimide (PI) for a more straightforward interpretation. As observed for photonic sintering of single lines (Sec. 4.3), the plateau of the IDTs sinks ca. 1 µm into the substrate. The sharp trenches visible in the Cu profiles mark the transition from the substrate to the slope of the Cu lines. The profiles after the application of WO_3 follow the same trend but with less sharp features. In b), the WO_3 profile was shifted vertically by 1.5 µm to allow for a better comparison. This step clarifies that confocal measurements provide valuable insights into the dimensions and surface structure, but it is not suitable for observing quantitative changes. The substrate warping requires post-processing to subtract the background for comparing different fabrication steps, but this also alters the relative position of the features.

Hence, to determine the thickness of the WO_3 layer, different volumes of ink are applied on a glass slide using two different approaches. The ratio of deposited ink volume to the volume of remaining particles after solvent evaporation allows for an estimation of WO_3 thickness on the sensor. First, different amounts of WO_3 ink are inkjet printed to allow for a precise volume determination to compare it to the measured volume via confocal microscopy. Then, to account for large area effects and to verify the method, a drop of WO_3 is manually applied and weighed to calculate the initial volume from the known density. The outline is probed via profilometry, and the final volume of the radially symmetric drop can be calculated through integration (Appendix

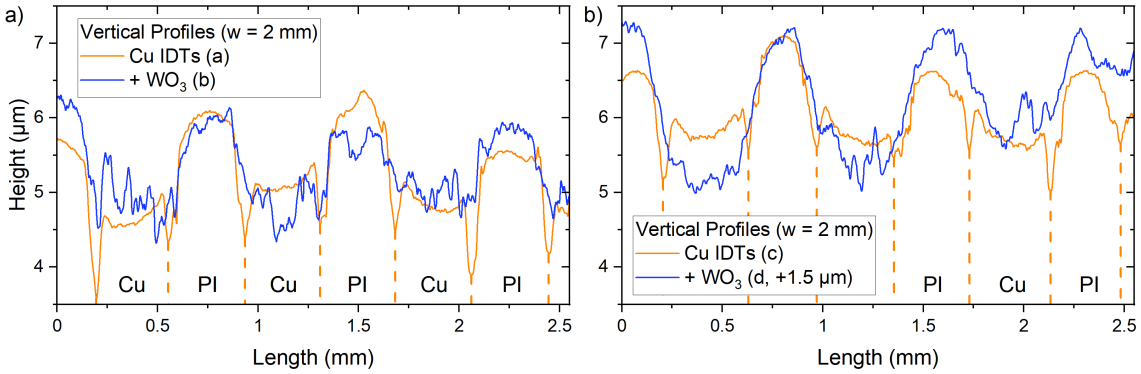

Figure 4.19: Averaged vertical profiles obtained via confocal microscopy of sintered Cu-IDT fingers before and after application of WO_3 (s. Fig. 4.18). The vertical dashed lines of the Cu profile mark the different regions of Cu or polyimide (PI) substrate.

A.4). Both approaches yield a volumetric fraction of ca. 0.8–1 % when comparing the applied ink to the volume of the deposited NPs. This is within the expected range, as the WO_3 ink consists of 2.5 wt% WO_3 NPs, 1 % water, and isopropanol (s. Tab. 3.3).

With these results, the thickness of the inkjet-printed WO_3 layer for the sensor can be well estimated to be 109–136 nm for an applied volume of 0.468 µL, which covers an area of (6.5×5.3) mm^2. The profiles in Figure 4.19 confirm that the WO_3 layer smoothens the surface. Furthermore, the material covers the entire area, as seen from the more diffuse surface in Figure 4.18 b) and d). The horizontal features of the printing process also suggest that the ink is not accumulating in deeper regions but dries shortly after application. All these observations conclude that complete coverage of the Cu-IDT structure is achieved.

4.4.2 (Cross-)Sensitivity to Temperature and Humidity

The sensor characteristic is investigated for different environmental conditions within a climate chamber. Of particular interest is the resistive response to changes in the relative humidity (RH). The humidity will be changed in steps of 5 or 10 %rh in the range 40–90 %rh at different temperatures T_i; the accessible $T - RH$ range is shown in the Appendix (Fig. A.9). Every step is held for at least one hour to allow the chamber to reach stable conditions and observe potential resistance drift under stable conditions.

The first goal is to demonstrate the sensor's sensitivity and disentangle variations within the

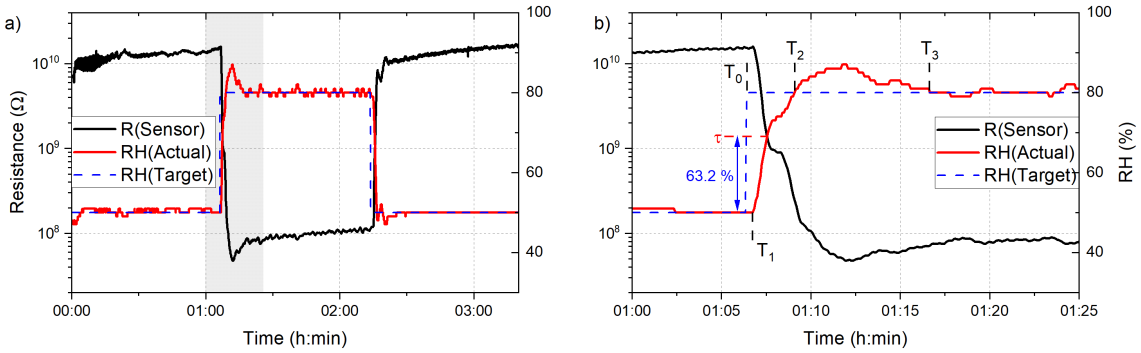

Figure 4.20: Sample 1: a) Resistive response on semi-logarithmic scale for WO_3-based humidity sensor over time, as well as actual and target values for a step in RH of 30 % at 30 °C. b) Close-up for the step from 50 to 80 %rh with different times T_i and τ for the actual and target humidity.

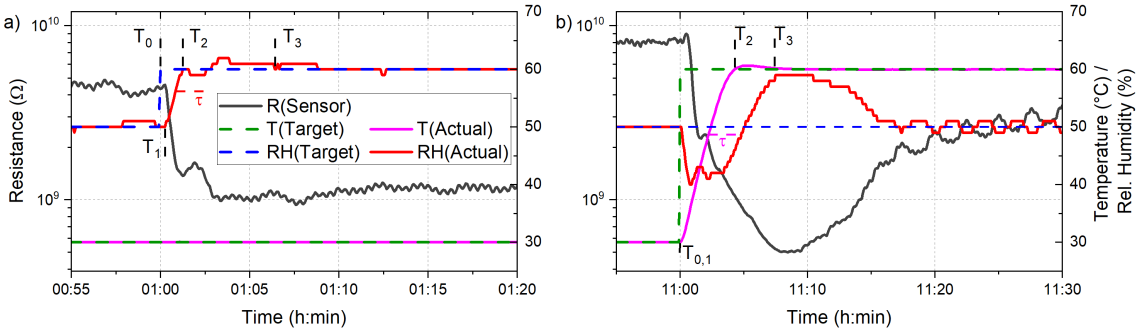

Figure 4.21: Sample 2: Response times of climate chamber for change in humidity (a) and temperature (b), taken from Figure 4.24. a) Resistive response on semi-logarithmic scale for WO_3-based humidity sensor over time, for a humidity step of $\Delta RH_{10} = 10\,\%$rh at 30 °C. b) Response time and change in humidity for a temperature step of $\Delta T_{30} = 30\,°C$ at 50 %rh. Different times T_i and τ are labeled for the actual and target values.

chamber during operation. For the sensors described in the following, the humidity sensitive WO_3-layer is manually applied and has a thickness of ca. 0.5 µm (s. App. Tab. A.1). Figure 4.20 shows the resistive response for two distinct RH levels at 50 %rh and 80 %rh at 30 °C. In a) the semi-logarithmic scale shows the drastic change in R of the sensor from $10^{10}\,\Omega$ to $10^{8}\,\Omega$ and back to the initial resistance value. Different times T_i are labeled in b) to quantify the response time of the climate chamber. The values are given in Table 4.8 and show that the climate chamber takes $T_1 - T_0 = 25\,$s between changing the target value and reacting to it. The time constant $\tau = 48\,$s is given by the time where the actual value reaches $1 - 1/e = 63.2\,\%$ of the goal. After $T_2 = 2{:}20\,$min the chamber surpasses the target value before it can be considered stable after $T_3 = 9{:}55\,$min. These values are affected by incremental errors, as the values are taken every 5 s and RH is given as one significant digit. However, it exemplifies that after 10 min the conditions within the humidity chamber are constant and thus should not affect the resistive response of the humidity sensor. The exponential response of the resistance can be clearly seen with the linear change in RH. An immediate correspondence of $R(RH)$ can e.g. be seen at the overshoot of the actual RH value in the chamber at ca. 1:09 h, where the resistance mirrors this trend.

After the characterization of the response time of the climate chamber and functioning of the sensor, smaller increments in RH and a change in temperature for the sensor are investigated. Figure 4.21 provides details of a step in humidity (a), and temperature (b) for a full sensor characterization, that will be discussed below (s. Fig. 4.24). In a), an excerpt of a longer measurement analogous to Figure 4.20 b) demonstrates that the climate chamber achieves stable conditions after a step of $\Delta RH_{10} = 10\,\%$rh significantly faster than for $\Delta RH_{30} = 30\,\%$rh (s. Tab. 4.8). This was expected but also shows that less oscillation is present in RH while the temperature stays constant. In b), the change in T is more intricate, as it corresponds to a variation in RH as well. The increase in T happens without delay and surpasses 63.2 % (τ) of the desired change

Table 4.8: Response times of climate chamber with respect to T_1 for changes in relative humidity of 10 and 30 %, as well as in temperature of 30 °C, as labeled in Figure 4.20 b) and Figure 4.21.

	Time [mm:ss]				
	T_0	T_1	τ	T_2	T_3
ΔRH_{30}	-00:20	00:00	00:48	02:20	09:55
ΔRH_{10}	-00:15	00:00	00:35	01:00	06:10
ΔT_{30}	00:00	00:00	02:15	04:20	07:25

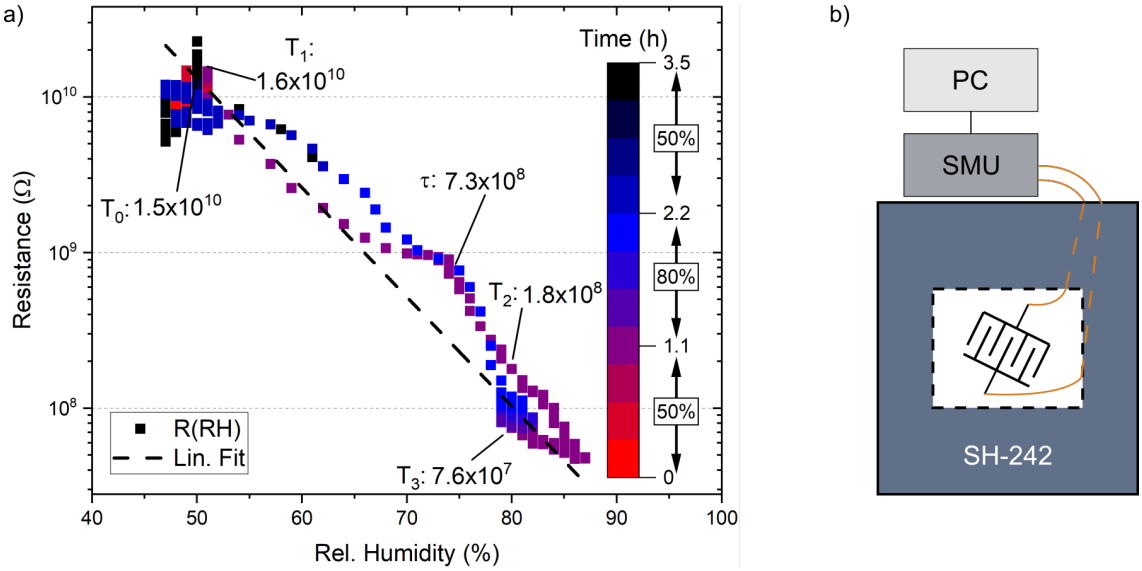

Figure 4.22: a) Sample 1: $R(RH)$ for data presented in Figure 4.20 a), including marked times T_i. The color scale represents the development over time and the three different target values for RH. The values 1.1 and 2.2 h correspond to the target changes in the climate chamber. The linear fit yields $R(RH) = 4.3\,10^{13} \cdot \exp(-0.16\,RH)\,\Omega$. b) Measurement setup of sensor in climate chamber SH-242, measured by SMU through PC.

after 2:15 min, and smoothly reaching the target after 4–7 min. At the same time, the humidity first drops before it gets overcompensated and surpasses the constant target value of 50 %rh by ca. 10 %rh. It takes almost 20 min to obtain stable conditions again, which will be considered for the temperature response analysis. Notably, the resistive change of the WO_3-based sensor closely follows the development of RH and even shows the corresponding answer to changes of only 1 %rh at e.g. 11:20–11:30 h. Thus, observations from the printed sensor that come with temperature changes are most likely due to accompanying changes in RH.

The characteristic $R(RH)$-curve of the sensor is presented in Figure 4.22 a) with the measurement setup in b). It includes the time steps labeled in Figure 4.20 and the development over time as colormap. The highest entry at 87 %rh corresponds to the overshoot within the climate chamber. The majority of the 2500 data points (3.5 h à 5 s) is centered at $R = 1 \cdot 10^{10}\,\Omega$ for $RH = 50\,\%$ and $R = 1 \cdot 10^{8}\,\Omega$ for $RH = 80\,\%$, respectively. This concentration and no hysteresis behavior, visible from the return to the initial resistance, demonstrates the potential for this sensor. Linear fitting of this linear trend in the semi-logarithmic plot yields $R(RH) = 4.3\,10^{13} \cdot \exp(-0.16\,RH)\,\Omega$.

As a next step, a different sensor is investigated in more detail with smaller RH steps. Figure 4.23 a) shows the development of R with different humidity steps within the climate chamber at 30 °C. The humidity range is chosen according to the sensor's sensitivity, and the maximum humidity considers the dewpoint temperature T_d. For 85 %rh at 30 °C, T_d is ca 27 °C [231], thus the temperature must not fall below it to avoid condensation. For the range 50–85 %rh, R spans between $2 \cdot 10^7 - 5 \cdot 10^9\,\Omega$. The resistance exhibits the same qualitative trend of stark decrease (increase) with rising (falling) humidity as seen in Figure 4.20. It also becomes apparent that the controlled humidity varies up to ±5 %, which can be seen for $RH(\text{Actual}) = 80\,\%$ and this noise directly translates into variations in R as well. Another systematic development is the slow but steady rise of R for most humidity plateaus which cannot be explained by the oscillatory deviations mentioned above. This climb is independent of the preceding direction of change in humidity and could suggest that humidity slowly desorbs from the sensor material over time. Another explanation could be found in the absorption and swelling of the polyimide substrate and

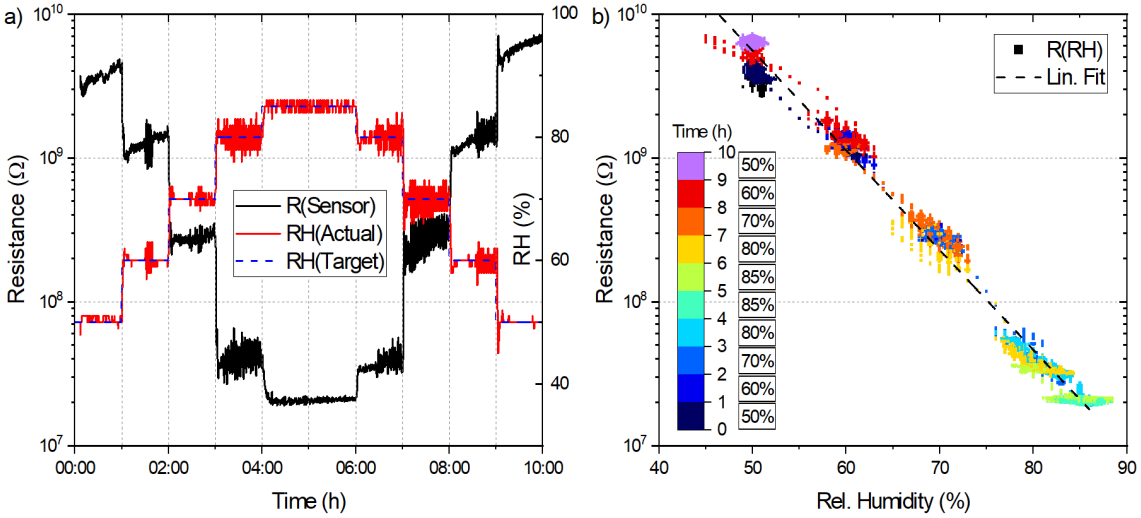

Figure 4.23: Sample 2: a) Resistive response on semi-logarithmic scale for WO_3-based humidity sensor over time, as well as actual and target values for RH at 30 °C. Humidity is swept in steps of at least one hour between 50 and 85 %rh. b) $R(RH)$ for data in a). The color scale represents the development over time and different target values for RH. Data points that overlap are arranged horizontally to make them visible. The linear fit yields $R(RH) = 1.6\,10^{13} \cdot \exp(-0.16\,RH)\,\Omega$.

thus changing the geometrical configuration and distances between the IDT fingers. However, this is unlikely as the rise of R is occurring for a long-term increase, as well as a decrease in humidity.

Figure 4.23 b) gives the $R(RH)$ relation, where the color scale indicates the development over time. Single data points between plateaus of RH trace the sensor's response. Data points that overlap are spread horizontally to make them visible, thus, humidity values are present beyond the maximum of 86 %. The visualization makes it apparent that the change to higher humidity levels (50 to 85 %) occurs faster, as seen from the fewer data points. For changes towards drier conditions (85 to 50 %), this trend is reversed, and it takes longer and exhibits larger values for R. This behavior can be interpreted as a faster response to rising compared to falling humidity levels or different responses of the climate chamber. The linear fit yields $R(RH) = 1.6\,10^{13} \cdot \exp(-0.16\,RH)\,\Omega$, and agrees well with the one found in Figure 4.22.

In order to expand the sensor characteristic, Figure 4.24 exhibits the continued measurement from Figure 4.23, which includes an increase of temperature from 30 °C to 60 °C. The spikes in RH associated with the temperature increase at 11:00 h were discussed along with Figure 4.21. As observed for $T = 30$ °C, the resistive response of the printed sensor is indirectly proportional to the change in humidity. Notably, the climate chamber provides more stable humidity control for elevated temperature, resulting in less signal noise for the resistance measurement. Again, this proves the direct correspondence of R and RH and reveals the rising trend for a constant humidity plateau. The behavior becomes apparent after decreasing RH and especially at 16:00 h, where the temperature returns to 30 °C and the humidity regulation undershoots to 30 %rh, leading to a jump in resistance. In Figure 4.24 b), $R(RH)(60\,°C)$ is depicted and the same trend as for 30 °C is observed. The color scale represents the development over time and is chosen to facilitate observing the course. The linear fit yields $R(RH) = 1.2 \cdot 10^{13} \cdot \exp(-0.16\,RH)\,\Omega$ and agrees well with the findings for the other humidity sweeps.

Table 4.9 states the highly reproducible fitting parameters for the analyzed data of Figures 4.22, 4.23, and 4.24. The values for the exponential relationship $R(RH) = A \cdot \exp[k \cdot RH]$ differ for the coefficient A but agree remarkably well for k, which can be regarded as a resistive humidity coefficient. For the measurements summarized in Table 4.9, k is found for different fits with high

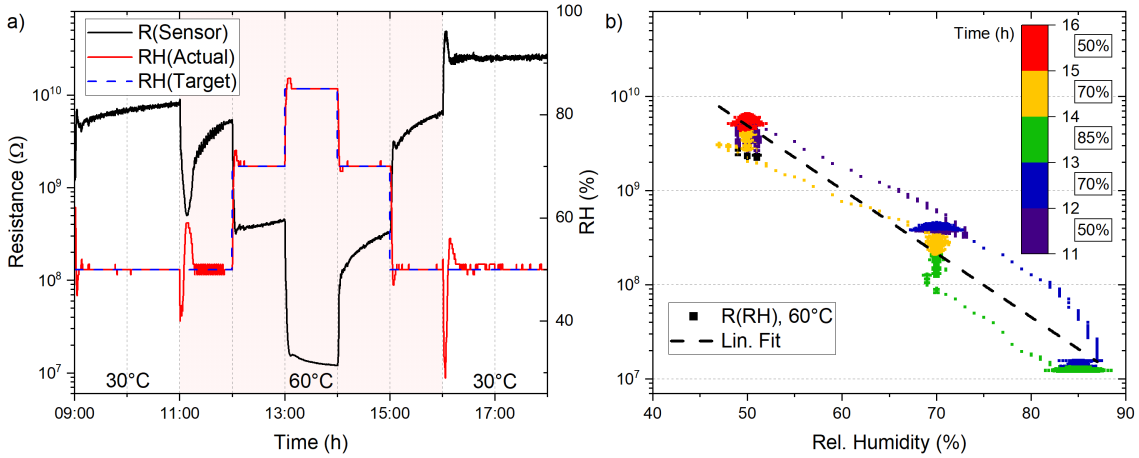

Figure 4.24: Sample 2: a) Resistive response on semi-logarithmic scale for WO_3-based humidity sensor continued from Figure 4.23 a),for RH at 30 °C and 60 °C. b) $R(RH)$ for data at 60 °C in a), starting from 11:20 h when the conditions are constant (cf. Fig. 4.21 b)). The color scale represents the development over time and the different target values for RH. Data points that overlap are arranged horizontally to make them visible. The linear fit yields $R(RH) = 1.2 \cdot 10^{13} \cdot \exp(-0.16\,RH)\,\Omega$.

Table 4.9: Summary of resistive humidity coefficients for WO_3-based sensors w/ and w/o vapor barrier and different WO_3 thicknesses, with $R(RH) = A \cdot \exp(k \cdot RH)$ and R^2-values at two different temperatures. The values are taken from the fits in Figures 4.22, 4.23, 4.24, and 4.26. The errors associated with the fitting are smaller than the given significant digits.

	Barrier	WO_3 [nm]	Temperature [°C]	A [$10^{13}\,\Omega$]	k [%rh^{-1}]	R^2
Sample 1	no	485	30	4.32	-0.162	0.990
Sample 2	no	485	30	1.63	-0.160	0.989
Sample 2	no	485	60	1.21	-0.156	0.954
Sample 3	no	109	30	0.41	-0.120	0.978
Sample 3	no	109	60	0.14	-0.113	0.978
Sample 4	yes	109	30	0.91	-0.077	0.695
Sample 4	yes	109	60	2.93^{-3}	-0.029	0.652

coefficients of determination ($R^2 > 95\,\%$) to be -0.16 (%rh)$^{-1}$.

4.4.3 Demonstration of Vapor Barrier

The following section moves on to describe the demonstration of a vapor barrier in greater detail. Such barrier can function as protection from humidity, particles, or mechanical damage and is used here to distinguish the influence of temperature and humidity on the sensors. This form of packaging could also be used for housing other printed components such as batteries or memory cells. Here, the used sensors were covered with a thinner humidity sensitive WO_3-layer of ca. 0.1 µm (s. Tab. A.1). The barrier consists of a 12 µm PET substrate, metallized with 9 µm Al, and 40 µm PE-LD (low-density polyethylene) sealable top layer (s. Sec. 3.4.2). A pouch is formed by folding and sealing laminate sheets before purging it with dry N_2 and sealing it shut. The Cu wires are embedded into the seal to contact the sensor to the measurement unit outside the climate chamber. Now, the potential of this vapor barrier is investigated by comparing the response of sealed, printed WO_3-based humidity sensors to unprotected sensors.

Figure 4.25 shows the resistive response of two different sensors and measurements along with

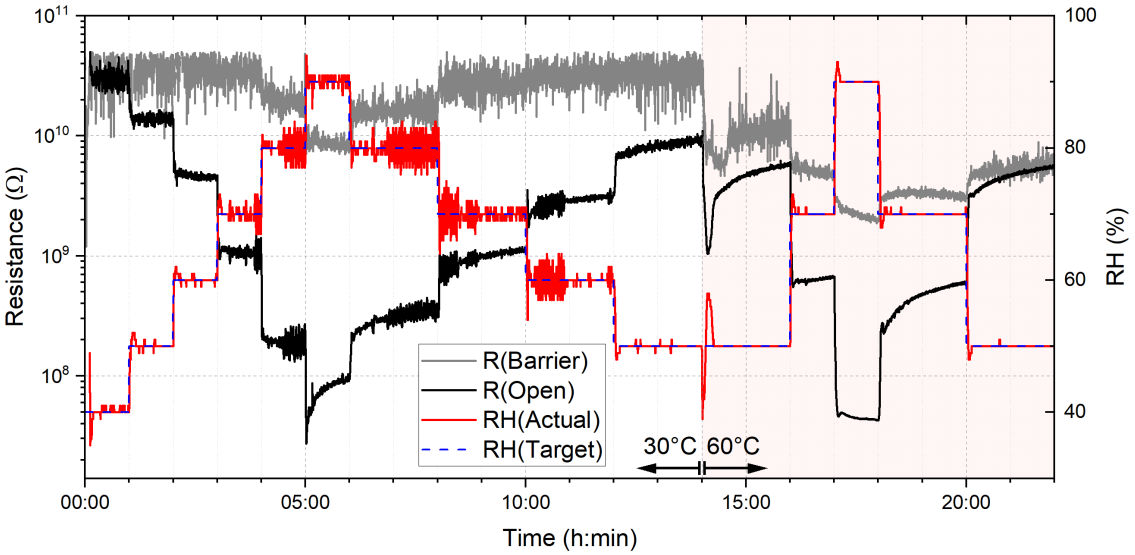

Figure 4.25: Sample 3 and 4: Resistive response on semi-logarithmic scale for WO_3-based humidity sensors, for samples with and without vapor barrier (grey and black, respectively). Humidity is swept in steps of at least one hour between 40–90 %rh. The vapor barrier holds well for 30 °C but is less effective at 60 °C.

environmental changes in RH and T. One sensor was prepared unprotected, i.e. open (black), while the other was inside the sealed vapor barrier (grey). The environmental profile was prolonged by increasing the time step after humidity reduction from one to two hours (cf. Fig. 4.23). The humidity range was increased from 50–85 %rh to 40–90 %rh to extend the probing range, but it entails a smaller temperature distance to the dew point of ca. 28 °C (at 30 °C, 90 %rh) and ca. 58 °C (at 60 °C, 90 %rh), respectively. The open sensor exhibits an analogous trend to the profiles shown in Figures 4.23 and 4.24. Variation in the humidity level inside the chamber leads to a noise-like response for the resistance measurement. The increase in temperature at 14:00 h leads to an abrupt change in RH and R. However, the initial value at 0:00 h is significantly higher than before, which could be caused by less acclimation time from the dry lab conditions ($RH \approx 20$ %rh).

The trend looks vastly different for the sensor within the barrier (Fig. 4.25, grey). Here, the sensor barely reacts even to the highest humidity levels of 80 and 90 %rh, where it decreases to $1{\cdot}10^{10}\,\Omega$. Resistance values greater than $5{\cdot}10^{10}\,\Omega$ are omitted as they are beyond the measurement range of the SMU. However, at the increase to 60 °C, the protection of the barrier becomes weaker. From 14:00 h on, the signal from R_{Barrier} follows every change in humidity but is attenuated by order of magnitude compared to R_{open}. The graph also exhibits more measurement noise (e.g. 15:00–16:00 h) for the protected sensor even though the humidity stays constant. At the last step of the humidity sweep, R_{Barrier} settles at a lower resistance value at 60 °C than for the whole humidity range in 30 °C. These observations conclude that the sensor also works encapsulated, but the vapor barrier becomes less effective for elevated temperatures.

Figure 4.26 examines the sensor characteristic for open and protected sensors at 30°C and 60°C, respectively. In a) the resistive response at 30°C of the open sensor closely follows RH, while the protected sensor only responds for $RH > 80$ %rh. Therefore, the full humidity range is considered for the fit of the open sensor, while only $RH > 77$ %rh is regarded for the protected one. The resistive humidity coefficient k is found to be $-0.12\,\%\mathrm{rh}^{-1}$ and $-0.08\,\%\mathrm{rh}^{-1}$ (Tab. 4.9), respectively, exhibiting lower sensitivity for the protected sensor. In b), the responses at 60 °C show that both sensors respond to the full humidity range but with significantly different values for $k_{\mathrm{open}} = -0.11\,\%\mathrm{rh}^{-1}$ and $k_{\mathrm{barrier}} = -0.03\,\%\mathrm{rh}^{-1}$, respectively. Additionally, at both

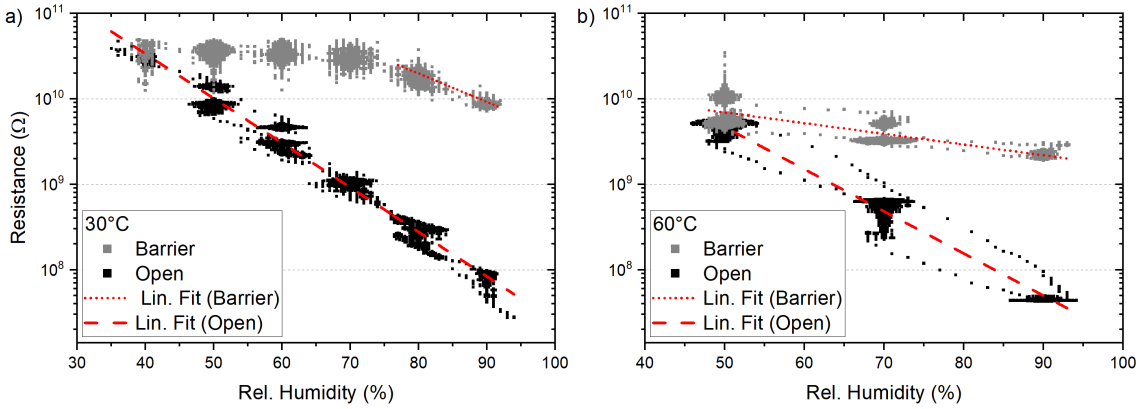

Figure 4.26: Sample 3 (black) and 4 (grey): $R(RH)$ for data presented in Figure 4.25. a) The different trends at 30 °C, where the open sensor shows a linear trend while the one protected by a vapor barrier only responds for $RH > 80$ %rh. b) At 60 °C, both sensors exhibit continuous trends but with different slopes. The linear fit results are given in Table 4.9. Data points that overlap are arranged horizontally to make them visible.

temperatures, the fit for the protected sensor has a R^2-value of below 0.7, while the open sensor shows $R^2 > 0.97$. Therefore, both scenarios can only be partially compared. The lower sensitivity could also be caused by the lag time through the barrier. This leads to a much slower steady-state vapor flux, and subsequently, a lower humidity level than expected [232]. On the other hand, this mechanism might lead to a hysteresis effect when returning to lower humidities. However, this is not observed, as seen at 6:00 h in Figure 4.25 at the transitions from 90 to 80 %rh at 30 °C.

Another noteworthy aspect is that the open sensors described in Section 4.4.2 exhibit $k \approx -0.16\,\%\mathrm{rh}^{-1}$, while the ones in this section are found to have $k \approx -0.12\,\%\mathrm{rh}^{-1}$. Both batches of sensors have been printed several months apart with the same Cu-IDT structure but were covered with different amounts of WO_3. Ideally, k would be a material-specific constant, independent of the thickness. Variations within inkjet printing, aging of inks, or other unknown factors could lead to variants of k.

Origins of the humidity permeation could be defects or pores in the Al layer, thermally activated diffusion mechanisms, or an imperfect seal due to particles or the embedded Cu wires. A pinhole-free Al foil of a few microns has negligible water vapor transmission [233]. This also holds for the thermally activated permeation of gas through solids, when the temperature increase of 30 °C leads to a 10-fold increase in water vapor transmission rate [234]. Thus, the seal is the most probable reason for the impaired humidity insulation, which is manually fabricated. The quality of the seal can be assessed through a microtome cut in combination with an optical microscope. Figure 4.27 provides the image of a 12 µm thick slab, sliced parallel to the sealing direction. The diagonal cuts visible in the PE-LD (low-density polyethylene) layer of 80 µm stem from the microtome cutting process. Polarized light shows the 100 µm Cu wire embedded in PE-LD and gaps of 20 µm surrounding the wire. Even though the seal is 2 cm wide and corrugated, these pores probably provide the path for water vapor. However, the measurement in Figure 4.25 showed that for low temperatures, even such a deficient seal provides effective humidity insulation. The Cu wires could be embedded without large gaps with lower sealing temperatures and longer sealing times, leading to an improved vapor barrier.

In summary, different WO_3-based humidity sensors were successfully fabricated via inkjet printing, and their resistive response to controlled changes in humidity and temperature were investigated. A vapor barrier was used as a demonstrator to protect an electrical component from humidity as well as mechanical damage, dust particles, and UV light. The failure mechanism of

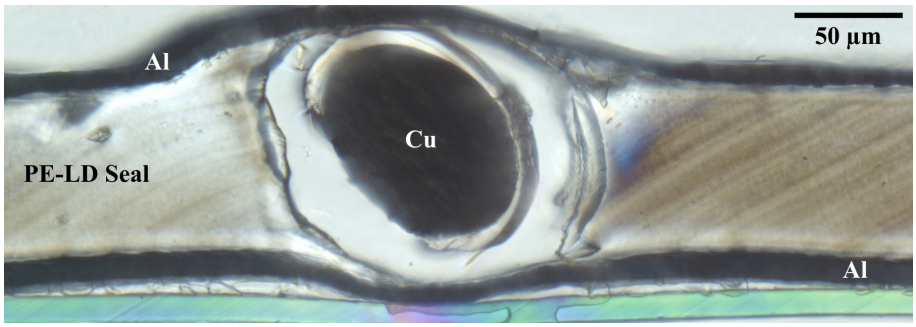

Figure 4.27: Optical microscopic image using polarized light of microtome cut (12 µm thickness) of sealed PET/Al/PE foil with embedded Cu wire. The heat-sealing pliers were pressed manually (ca. 20 N/cm^2) for 5 s at 220 °C.

the embedded Cu wires was discussed to improve this form of packaging in the future.

4.5 Cu_xS-based Temperature Sensor

4.5.1 Microscopic Analysis

To understand the transformation of Cu to Cu_xS, mediated by Na_2S_{aq} ink (pH(0.1 M Na_2S_{aq}) = 12.93), inkjet printing deposits drops of Na_2S_{aq} on a $Si/SiO_2/Cu(250\,nm)$ wafer. This method allows precise and defined application of 50 pl with different molar concentrations (0.0087, 0.087, 0.44) M. The printing parameters were found through systematic variation of dropspace and layer count (s. App. A.3).

Repeating each test structure ten times with 1, 3, and 5 layers allow for statistical validation. The structure-to-structure variability yields standard deviation shown in the error bars in Figure 4.28 c–e). Confocal microscopy (Sensofar PLµ2300) provides topographical information on the influence of molar concentration of the $Na_2S_{(aq)}$ solution on wettability, roughness, and volume of the transformed structure. Gwyddion [235] allows for grain analysis, shown exemplarily in Figure 4.28 a) and b). The phase shift interferometry (PSI) mode supports sub-nanometer vertical resolution for smooth surfaces, and nanometer-sized lateral features [207].

The mean square roughness (RMS) highlights surface topography changes with increasing molarity and layer count. The pristine Cu surface exhibits RMS < 1 nm (given as the averaged value of the focal spot) in a random area of ca. 10000 µm^2. Thus, the surface is almost atomically flat and no pores or inhomogeneities affect the spreading of the ink. Figure 4.28 c) illustrates that higher concentrations and more layers lead to a significant rise in roughness. The additional supply of HS^--ions leads to faster reaction and precipitation. The surface roughness of the different structures grows with molarity and additional layers in the range of 10–50 nm but it also increases the observed deviations. It is known from the interaction between Ag and Na_2S solutions that corrosion rate increases logarithmically with concentration and linearly with pH value [236]. As Cu exhibits similar electrochemical behavior as Ag, this can explain the observed trends.

Secondly, Figure 4.28 d) shows the radius of the transformed area as the radius for an assumed circle, which appears to be a valid approximation following Figures 4.28 a) and b). For low concentrations ($c \leq 0.0087$ M), the radius is constant with $r \approx 35$ µm but increases to over 100 µm for higher concentrations and layer counts. This trend is driven by the interaction between droplets and substrate and the evaporation process. For low concentrations, the wetting behavior is similar to pure water, where a single 70 pl droplet results in a radius of 25 μm on a silicon surface [127]. This is in good agreement with our measurements on the Cu surface of 30 μm, where the ink

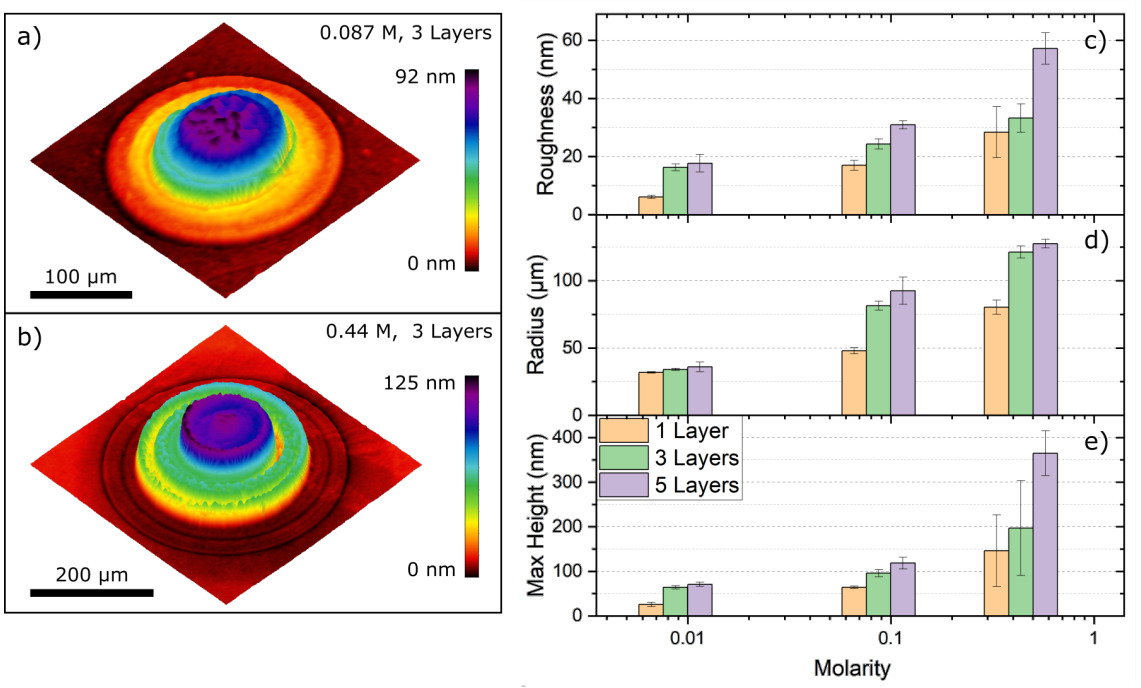

Figure 4.28: a), b) Exemplary phase shift interferometry images of fabricated Cu_xS structures on a Cu-covered wafer. c), d), e) Quantitative analysis for structures with different molarities and layers for roughness, radius, and maximum height, respectively. [111] © 2022 IOP Publishing

for the single layer is 50 pl. Such a drop takes ca. 1 s to evaporate [127], which is the same timescale as the printing duration per layer. So, the subsequent drops will be added to a lingering or partially evaporated drop. The evaporation process of pure water can be described in two phases: first, the contact line is pinned while the ink evaporates, leading to a lower contact angle and a constant contact area. During full evaporation, the contact line recedes, and the contact angle stays constant, keeping the contact angle constant [127]. However, rough surfaces can delay this depinning phenomenon. Hence, the transformation from smooth Cu to rough Cu_xS surfaces affects this process, as it extends the lifetime of the constant contact area phase. In the evaporation process, the coffee-stain effect plays a pivotal role, as a particle-containing liquid leads to enhanced deposition of material at the fringes [130]. The faster evaporation rate promotes this at the pinning outline that ensues particle transport and further deposition. These considerations emphasize the complex interplay between droplets and surface and help to explain the observed experimental trend. Higher molarities lead to rougher surfaces, which changes the surface energy and hence the wettability for further deposition. Additional layers follow this trend, and the overall results display larger radii and a pronounced coffee-stain effect (Fig. 4.28 a), b)). The maximum height (Fig. 4.28 e)) exhibits that higher molarities and more layers lead to taller structures but also to more irregularity, as can be seen from the larger error bars.

The fabrication of a fully inkjet-printed temperature sensor starts with inkjet printing and sintering a 10 mm Cu-NP line. Next, defined areas are covered with Na_2S_{aq} (0.087 M) via inkjet printing (s. Fig. 4.29 a)) and rinsed off with DI water. Profilometry along the printing direction in steps of 35 µm provides structural information to evaluate changes in the surface (s. Fig. 4.29 b)). This approach has the advantage over non-contact analysis methods such as confocal microscopy due to the matt black surface of Cu_xS. A possible drawback is the damaging of the surface through the probing tip. The topography is corrected for the curvature of the substrate warping by subtracting a polynomial background while excluding the printed structure. The in-

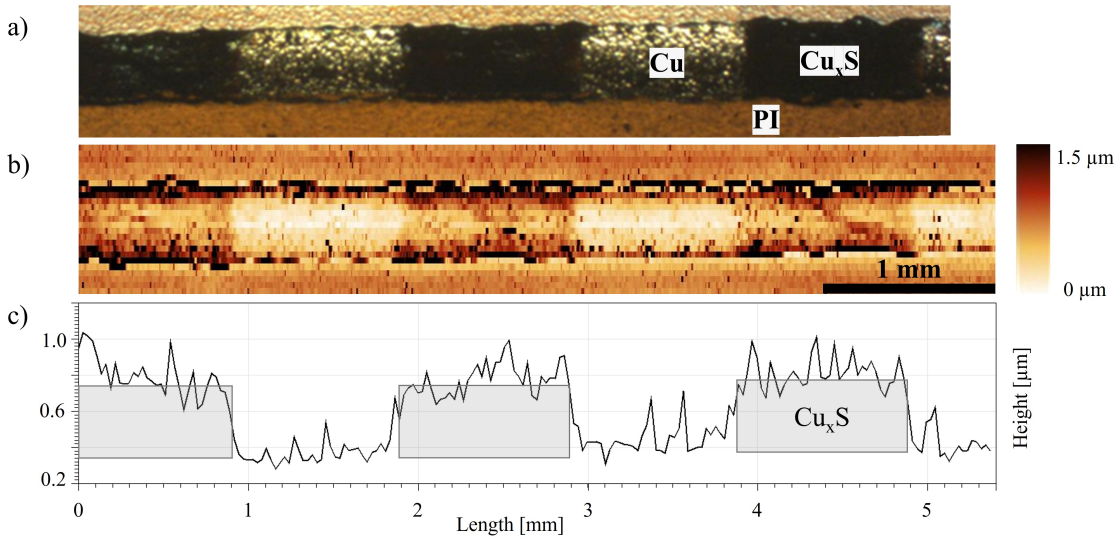

Figure 4.29: a) Optical image of an inkjet-printed and sintered Cu line (golden) on polyimide (PI) with 1 mm long transformed Cu_xS areas (dark). b) Topographic profilometry scan consisting of 25 horizontal line scans with spacing of 35 µm. c) Horizontal profile averaged over ten central profiles, showing that the transformed Cu_xS extend ca. 400 nm above the Cu line.

dentation or sinking-in of the Cu line into the substrate is preserved, visible from the lower height compared to the PI substrate and the elevated features along the edges of the Cu line due to the coffee-stain effect. Figure 4.29 c) depicts the averaged profile over ten scans along the center of the sensor and reveals that Cu_xS is elevated by 400 nm relative to the plateau of the Cu line.

4.5.2 Temperature Response

Figure 4.30 a) shows the final fully printed Cu/Cu_xS structure used to characterize the temperature response. The 10 mm long inkjet-printed and sintered Cu line on polyimide is partially converted (1 mm) to Cu_xS in the center, and manually applied Ag paste facilitates contacting. Figure 4.30 b) exhibits the negative resistive response to rising temperatures after sulfurization. An exponential beta fit (s. Sec. 2.1.2) for heating up and cooling down yields $\beta_{25,80} = (656 \pm 5)\,\mathrm{K}$ and $\beta'_{25,80} = (681 \pm 8)\,\mathrm{K}$, respectively. The indices '25,80' indicate the temperature range 25–80°C, and R_0 and T_0 are taken at 25 °C according to Equation 2.6. The 5 % offset for the resistance at rising and falling temperatures can be explained by the influence of humidity, contact issues, or chemical reactions. The impact of different contributions will be subject to further investigations, but a systematic development towards higher resistances with lower humidity is assumed. One hypothesis is that the porous structure of Cu_xS shrinks during heating as humidity evaporates, which improves the connectivity within Cu_xS. During cooling, humidity re-adsorbs, and the sensor returns to a slightly higher resistance. The reported value is similar to commercial applications (1500–2000 K) [33], thus evidently demonstrating the potential for sensor applications.

4.6 Resistive Memory Cells

The following section presents the resistive switching characteristics of two different combinations of active electrode (AE) and insulating material. First, screen-printed Ag acts as the AE, covered by inkjet-printed Spin-on-Glass (SoG), and the Ag counter electrode is manually applied. Then, thermally evaporated or inkjet-printed Cu is the AE which is partly transformed into Cu_xS and

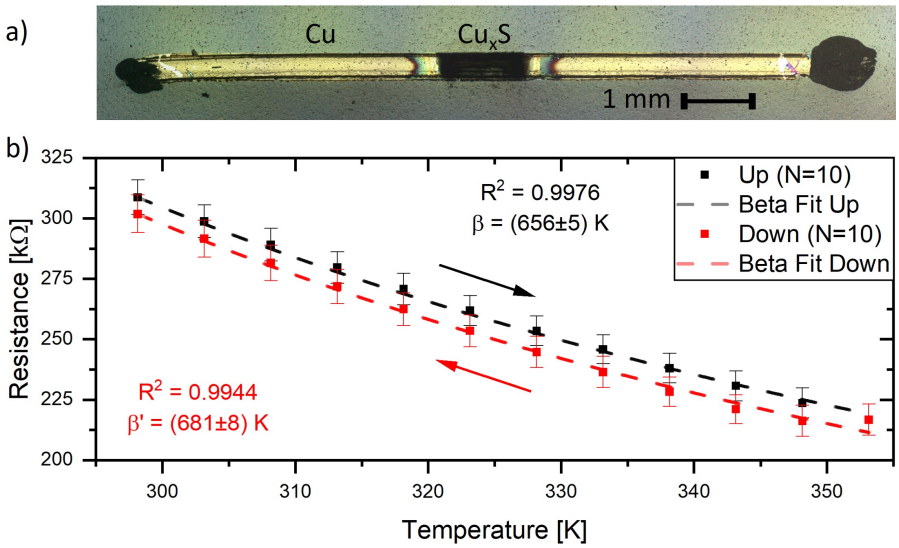

Figure 4.30: a) Optical image of thermal sensor based on a 10 mm long inkjet-printed and sintered Cu line. The Cu_xS structure is visible as the dark structure in the center is the line. Conductive Ag paste is manually applied to the edges of the line to facilitate contacting. b) Thermoresistive behavior of Cu_xS sensor for heating up and cooling down. Fitting yields $\beta_{25,80} = (656 \pm 5)\,\mathrm{K}$ for heating up and $\beta'_{25,80} = (681 \pm 8)\,\mathrm{K}$ for cooling down. The indices '25,80', indicate the temperature range 25–80°C and R_0 and T_0 taken at 25°C according to Equation 2.6. [111] © 2022 IOP Publishing

contacted either by a W-tip or conductive carbon tape. Quasi-static voltage sweeps provide the switching voltage characteristics. The voltage is applied with respect to the grounded top electrode from 0 V, to positive V_{max}, to negative V_{min}, returning to 0 V while the current is measured. A compliance current is set to stop a hard dielectric breakdown that short circuits the cell and prevents the RESET process. These information are essential for applications where switching is done via pulses instead.

4.6.1 Ag/SoG/Ag

Figure 4.31 a) shows a switching curve for the symmetric Ag/SoG/Ag setup. The slope of the $I-V$-curve is shown in Figure 4.31 b) as the resistance R. Starting from the preconditioned low resistive ON state, the RESET process can be seen as the sudden halt in current and the corresponding rise in resistance at ca. 0.1 V (Fig. 4.31 a) and b)). The cell remains in the OFF state until it switches again to the ON state at ca. -0.15 V where it goes into compliance mode at $I_{cc} = -0.5\,\mathrm{mA}$. For an ideal symmetric cell setup (Ag/SoG/Ag), symmetric switching behavior should be observed at the same absolute voltage values. The sample preparation procedure can explain the asymmetry in the switching curve. The bottom, screen-printed electrode contains ca. 62 % solid contents with organic contamination that might still be present after evaporation of the solvents during curing. Similarly, the top electrode possesses a Ag content of 58 % in the uncured material. Organic compounds and oxidation lead to different chemical environments of the Ag electrodes. This results in electrochemical redox potentials different from the pure element (s. Sec. 2.3.2), influencing the formation of the conductive filament. Hence, deviations from the symmetric, unipolar switching properties of an ideal Ag/SoG/Ag cell must be expected. The stability of the filament is investigated in Section 4.7.1.

Several alternative designs and materials were investigated for their adequacy to realize the counter electrode for a fully printed setup where lamination is only part of the post-processing.

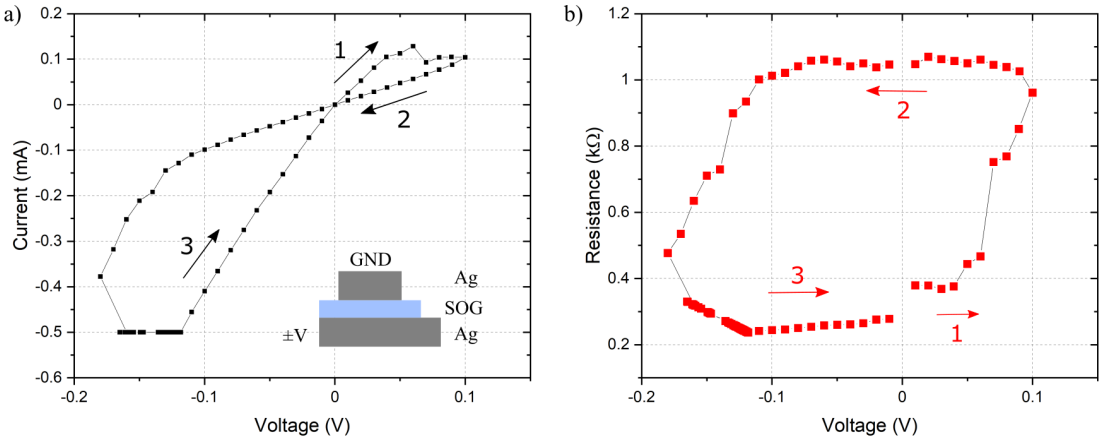

Figure 4.31: a) Current and b) resistance characteristic of a Ag/SoG/Ag cell with a compliance current of 0.5 mA. Numbered arrows indicate the sweep direction. Starting from low resistance, it jumps to a high resistive state at ca. 0.1 V. For the opposite polarity, the switching to the low resistive state occurs at ca. -0.15 V. The inset shows cell setup and polarity. Adapted from [109].

This has proven challenging as most setups exhibited short circuits that were deduced to occur at the edges of the screen-printed Ag electrode. The investigated approaches are given as starting points for further research. One attempt is printing a varying number of insulating SoG layers. Then, an intermediate sintering step after a few printed layers of SoG is performed, followed by a second printing procedure to fill cracks occurring during the curing process. Next, the coffee-stain effect of the printed SoG line was tried to be utilized for coverage. Aligning the coffee-stain effect with the edges of the Ag line was successful; however, the short circuit remains. Finally, the idea of an SoG railing was tested: first, narrow lines of SoG were printed and cured on the substrate parallel to the edges formed by the Ag electrode. The structure exhibiting a pronounced coffee-stain effect was used as a boundary for the following SoG print to minimize the spreading and thinning of the material resulting in a thicker insulating layer (s. Fig. 4.32).

A possible alternative for the counter electrode is PEDOT:PSS (poly(3,4-ethylenedioxythiophene)poly(styrenesulfonate)), a conductive and highly transparent polymer. The substrate is heated to 60°C during the printing process for optimized printing quality and does not require additional sintering. Still, the steep flanks of several micrometers are not sufficiently covered by an insulating material to prevent the short circuits. Furthermore, different top electrode materials were investigated, such as more viscous PEDOT:PSS for screen printing, Al strips, and adhesive, conductive carbon tape. Unfortunately, none of these attempts provide a stable CE.

4.6.2 Cu/Cu$_x$S/W

In the following, the microscopic structure as well as elemental composition of Cu$_x$S on a Cu-covered wafer through surface transformation by Na_2S is presented. Then, the resistive switching properties for this setup are investigated using a W-tip or adhesive C-based tape. Towards fully printed memory cells, switching is also reported for a fully printed Cu/Cu$_x$S setup, contacted via W-tip.

4.6.2.1 Structure

Scanning electron microscopy (SEM) examines the cross section of the lithographically structured and transformed Si/SiO_2(100 nm)/Cu(250 nm)/PR/Cu$_x$S cross section. After resistive switching

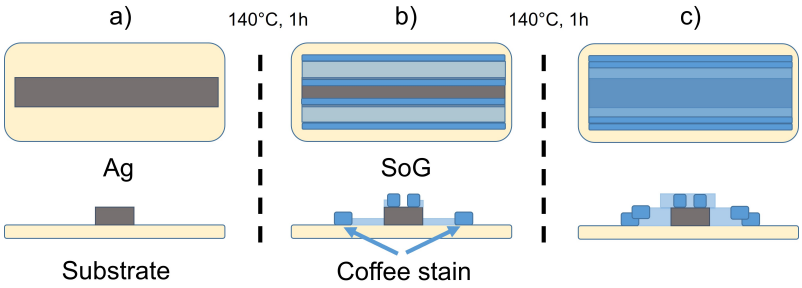

Figure 4.32: Design of Spin-on-Glass (SoG) railing to cover steep flanks of the screen-printed Ag electrode (a). Two parallel lines of SoG are printed along the edge of the Ag electrode (b). The coffee-stain effect causes taller features which could provide a railing for the next printing step of SoG to cover the steep flank of the Ag electrode (c).

is observed for the sample, the wafer is manually broken along a crystal axis. The resulting sharp edge makes the layers accessible via SEM (s. Fig. 4.33). SEM images are acquired using in-beam secondary electrons (SE) and in-beam backscattered electrons (BSE). Advantages of the respective modes are that SE displays more surface features, and BSE is more sensitive to elements with higher Z-numbers. The stage tilt is relative to the 60° sample holder.

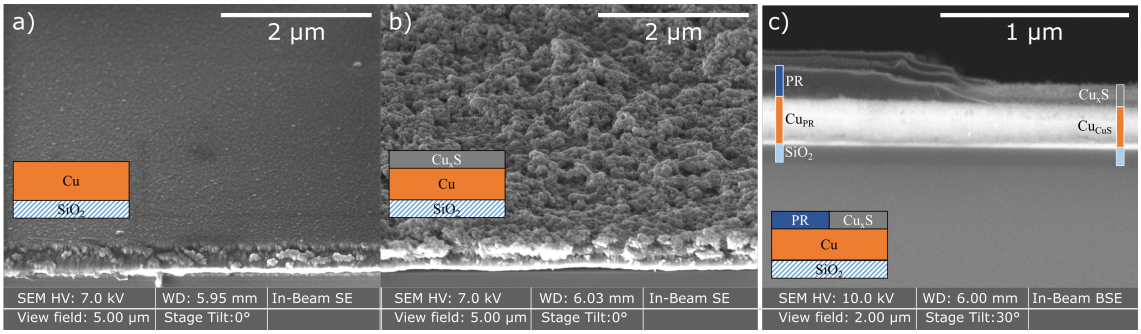

Figure 4.33: SEM images of pristine (a) $Si/SiO_2/Cu$) and transformed (b) $Si/SiO_2/Cu/Cu_xS$) cross section and surface (in-beam secondary electrons (SE)). c) $Si/SiO_2/Cu/PR/Cu_xS$ cross section (in-beam back scattered electrons (BSE)). The stage tilt is relative to the 60° sample holder. The vertical lines indicate the measurement position of the layer thickness d: $d(SiO_2) = 92\,nm$, $d(Cu_{PR}) = 252\,nm$, $d(PR) = 178\,nm$; $d(Cu_{CuS}) = 213\,nm$, $d(Cu_xS) = 123\,nm$. [111] © 2022 IOP Publishing

Figure 4.33 compares two areas of the same $Si/SiO_2/Cu$ edge: in a) the pristine surface is untreated, and the edge exposes the Cu profile. It reveals the different layers starting with the slightly darker SiO_2 on top of Si, covered with ca. 250 nm of Cu. Two separate phases of Cu are present due to imperfect two-step deposition conditions. Small particles on the surface could originate from the handling in normal atmosphere during sample preparation. In contrast to the smooth surface, b) exhibits rough and porous surface structures around several 100 nm which covers the whole area where Na_2S_{aq} has been applied. The porosity must be considerable since only the transformation of the Cu-layer is only superficial. Only little Cu is transformed into Cu_xS, as can be seen from in Figure 4.33 c) for the almost constant thickness of Cu under the PR ($d(Cu_{PR}) = 252\,nm$) compared to the Cu_xS layer ($d(Cu_{CuS}) = 213\,nm$). The thickness of the rough Cu_xS structure ranges from 120–380 nm across the edge (not shown). Thus, the growth of Cu_xS compared to the reduction of Cu implies that the transformed structure is very porous. The volume change of 300 % is significantly larger than the range of growth for dense structures. In that scenario it would range from 161–188 % due to the lower density of Cu_2S or CuS compared to

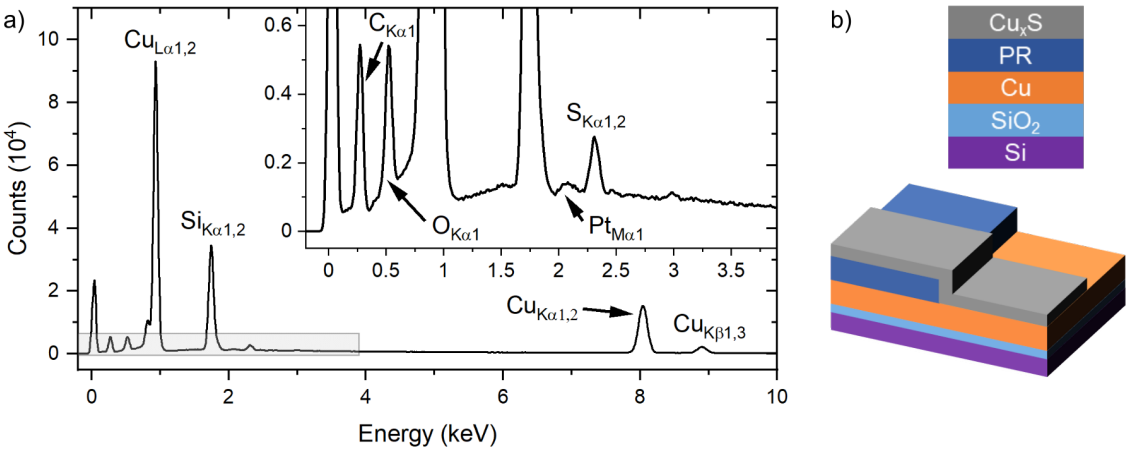

Figure 4.34: a) Integrated energy-dispersive X-ray (EDX) spectrum for the area shown in Fig. 4.35. The elemental X-ray emission lines are labelled. Inset: Zoomed-in section of spectra to highlight individual peaks. b) Cross section of sample, also probed in Fig. 4.35.

Cu ($\rho_{Cu} = 9.0\,\mathrm{g/cm^3}$, $\rho_{CuS} = 4.8\,\mathrm{g/cm^3}$, $\rho_{Cu_2S} = 5.6\,\mathrm{g/cm^3}$) [237]. The fabricated Cu_xS structure shows good mechanical adhesion through its robustness to rinsing with DI water.

In Figure 4.34 energy-dispersive X-ray spectroscopy (EDX) provides information on the chemical composition to validate the presence of Cu_xS. As the spatial resolution of EDX is in the micrometer range, the 100 nm cross section cannot be probed directly. EDX spectra are taken at every pixel, thus mapping the elemental distribution of the different layers. The area of transition between pristine and transformed is divided into four quadrants (s. Fig. 4.35). In the first quadrant (I), the evaporated Cu layer is the only additional layer on the Si/SiO2 substrate. In the second one (II), Cu is additionally covered with photoresist (PR). The $Na_2S_{(aq)}$ drop covered the lower half of the depicted section, thus, the third quadrant (III) is similar to (II) but with precipitated Cu_xS on top. The fourth quadrant (IV) is made of transformed Cu_xS on top of Cu as in (I). White, dashed lines visually separate the different quadrants, and the profile of layers in each quadrant is shown in the respective inset. Due to the information depth of 1–3 µm and layer thickness of a few 100 nm, information also originates from the Si/SiO_2 substrate.

The elemental distribution is analyzed for the K-series of the relevant components Cu, Si, S, C, and O. The elements that all quadrants have in common are Si, O, and Cu, thus, the EDX signal for C and S are most relevant to distinguish different compositions. The counts are integrated over the entire width (upper profile) and total height (right profile), resulting in a noisy distribution. Smoothening via a 1 Hz low pass filter (LPF) allows distinguishing trends and features. Differences can clearly be seen in (II) and (III) for C as it is the main element occurring in the PR, exhibiting increased intensity on the left side (s. Fig. 4.35). Thus, the C-signal originates mainly from the PR and in part from the overall noise due to organic contaminations on the surface. In the lower half of the probed area, an elevated signal is detected for S, i.e. Cu_xS covered areas in III and IV, suggesting that the precipitated material is indeed Cu_xS. Additionally, the spectrum exhibits no significant signal from Na, which could have originated from residual Na_2S.

The formation of Cu_xS on top of the PR suggests that the transformation occurs via a precipitation reaction. The basic Na_2S_{aq} drop spreads across the Cu as well as the PR area and contains Na^+ cations and HS^- anions (s. Sec. 3.3). The solution dissolves Cu^+ cations that combine with the present anions to form Cu_2S and precipitates within the remaining drop [176]. Molecular movement leads to a uniform coverage of the wetted area by Na_2S_{aq}. A deviation from homogeneous

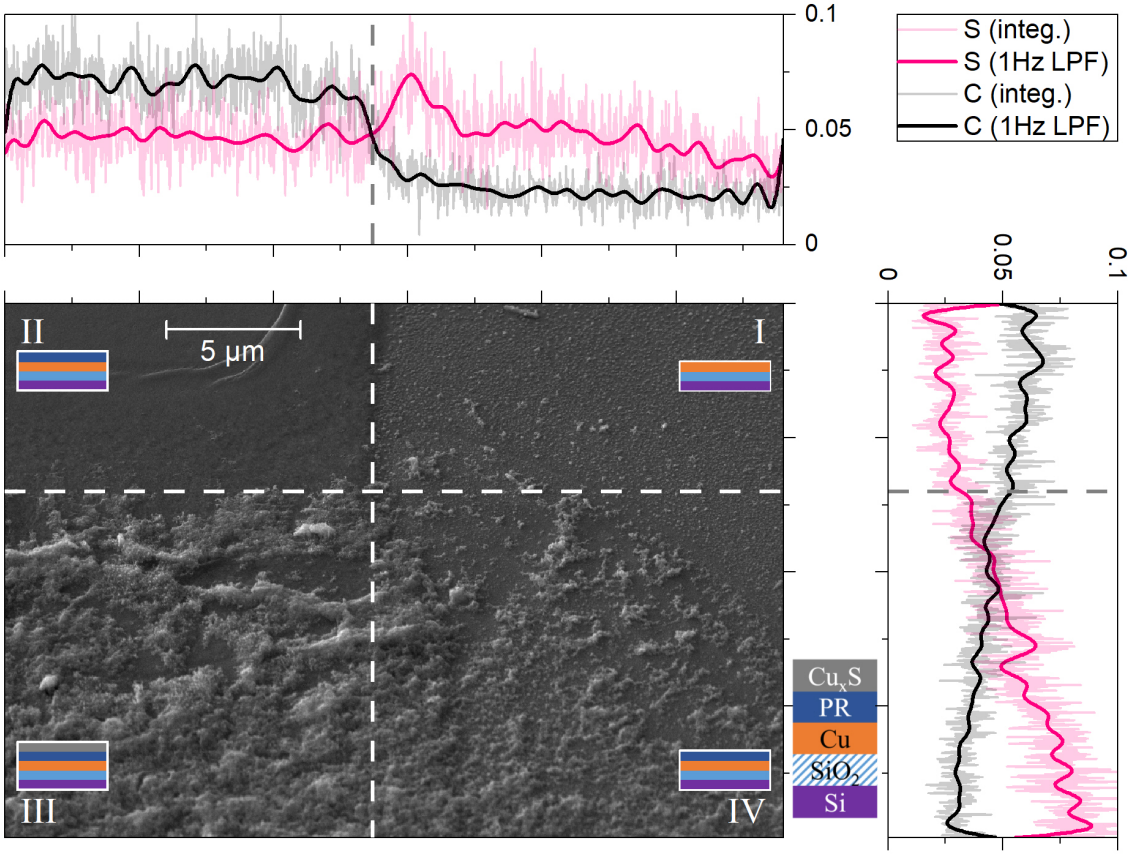

Figure 4.35: Secondary electron SEM image of an area partly covered with PR (left half) and partly covered with Cu_xS (lower half) that can be divided into four quadrants (I–IV). The profile of layers in each quadrant is shown in the respective inset. The profiles are taken for C and S from individual EDX profiles at every pixel (s. Fig. 4.34). The counts are integrated over the full width (upper profile) and full height (right profile) and smoothened via a 1 Hz low pass filter (LPF). [111]

coverage is visible on the right side of the PR boundary (s. Fig. 4.35, upper profile). The enhanced precipitation can explain this at this boundary and the subsequent accumulation along this edge.

Precipitation occurs for concentrations $c(Cu_xS)$ higher than the solubility product K_L. For the main possible compound Cu_2S, the value for $pK_L = -log(K_L) > 10^{-30}$ is vanishingly small, i.e. the chemical equilibrium is almost exclusively shifted to the product side [238]. Therefore, any dissolved Cu^+ ion from the surface reacts with hydrosulfide (HS^-) from the solution and precipitates (s. Eq. 3.16). A systemic uncertainty is the evaporation-driven rise of c, which could contribute in addition to the coffee-stain effect to the concentric ring-shaped structures depicted in Figure 4.28 or in the appendix (Fig. A.5). As this behavior affects the entire drop-sulfurization series, the relative changes for roughness, radius, and height stay consistent. However, this dynamic will require consideration for larger applied volumes.

4.6.2.2 Switching

Cu/Cu_x - Wafer

Figure 4.36 presents typical resistive switching curves for different scenarios. They show voltage-current measurements with different compliance currents for cells with directing contacting (Cu/Cu_xS/W) and with carbon tape (Cu/Cu_xS/C), respectively. In Figure 4.36 a) I_{cc} is set to 50 µA and 250 µA to demonstrate the controllability of the filament strength. In addition, it

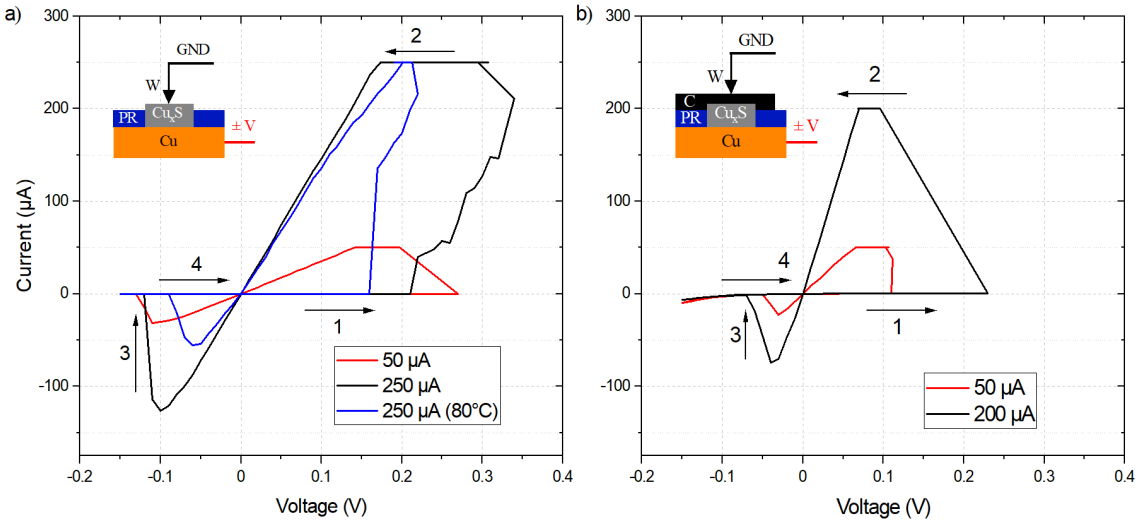

Figure 4.36: Resistive switching characteristic of a) Cu/Cu_xS/W and b) Cu/Cu_xS/C memory cells with different compliance currents. The numbered arrows indicate the sweep directions (ΔV = 10 mV). In a) and b), the SET process occurs at ca. 0.15 – 0.25 V and 0.10 – 0.25 V, respectively. The RESET happens abruptly at -0.05 – -0.1 V and the memory cells return to their initial state. Curves are taken at room temperature if not noted otherwise. [111] © 2022 IOP Publishing

displays a measurement at 80°C for $I_{cc} = 250\,\mu A$ to validate the functionality at elevated temperatures. A sharp increase in current occurs at a voltage of 0.15 – 0.25 V. This represents the SET process from OFF to ON, i.e. change in resistance from HRS $> 10^7\,\Omega$ to LRS = 1.5 kΩ and 600 Ω, for $I_{cc} = 50\,\mu A$ and $I_{cc} = 250\,\mu A$, respectively. The RESET occurs at ca. -0.1 V, where the state returns to the previous HRS.

For the Cu/Cu_xS/C setup in Figure 4.36 b), the ON state exhibits similar resistive values of 1.2 kΩ and 350 Ω, for $I_{cc} = 50\,\mu A$ and $I_{cc} = 200\,\mu A$, respectively, the OFF state is significantly reduced from $10^9\,\Omega$ to $10^5 - 10^6\,\Omega$ (not shown). The maximum reset current for both setups is smaller than I_{cc}, indicating electrochemical rather than thermal filament dissolution [77]. Furthermore, differences in the RESET dynamics are known to be mostly independent of temperature, current compliance, as well as ON resistance [239]. Thus, variations in switching characteristics such as different values for ON resistance reflect device-to-device variability rather than the influence of the inert electrode. Demonstrating comparable switching curves for direct and indirect contacting through the conductive carbon tape is essential towards the goal of a laminated top electrode for roll-to-roll fabrication.

Varying I_{cc} can be used to confirm the underlying mechanism of filamentary resistive switching. As described above, the dielectric layer determines the OFF resistance, while the metallic filament gives the ON state. Allowing more current forms a thicker filament, resulting in a distinct decrease in R_{ON} (s. Sec. 2.3.1). This correlation is confirmed for Cu/Cu_xS/W in Figure 4.37. The log-log plot emphasizes the stark change of R_{ON} with I_{cc}. However, for the largest currents ($I_{cc} > 500\,\mu A$), the slope becomes flatter. Here, the minimum resistance is no longer determined by the conductive filament alone, but contributions stem from contact resistances. Hence, by controlling I_{cc}, different values for the ON state can be programmed, leading to the possibility of storing more than one bit of information in each cell or allowing for neuromorphic computing, as discussed above. The programmed ON resistance follows the empirical law $R \propto 1/I_{cc}$ and has been observed for a wide range of resistive switching cells, making it a universal switching characteristic [77]. The OFF state is around $10^6 - 10^8\,\Omega$, and therefore the OFF/ON-ratio is up to 10^5.

Cu_xS, as well as the closely related Ag_xS, are known to exhibit metallic filament formation.

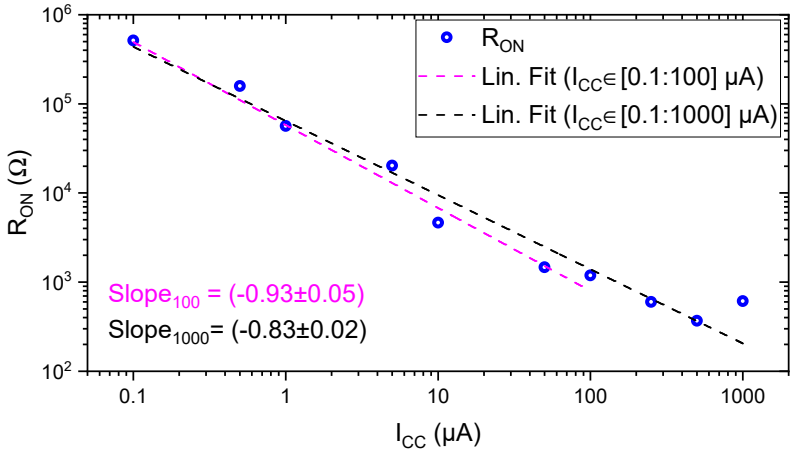

Figure 4.37: Minimum values for R_{ON} at $V = 50\,\text{mV}$ for different compliance currents I_{cc} of Cu/Cu$_x$S/W memory cells in log-log plot. Linear fits for the regions from 0.1 – 100 µA and 0.1 – 1000 µA exhibit slopes of -0.93 and -0.83, respectively. Adapted from [111].

Sakamoto *et al.* showed that for Cu/Cu$_2$S/Au cells, electrochemically sulfurized Cu films exhibit switching at similar SET and RESET voltages ($< 0.3\,\text{V}$ and -0.1 V, respectively). The formation and dissolving of conducting Cu paths are given as the origin of RS [143]. Atomic switches based on Ag and Cu filament formation within Ag$_2$S and Cu$_2$S were also investigated, where metallic filaments are described as the switching mechanism [145, 240]. Further, multi-level switching (s. Fig. 4.37) is a strong indicator that the compliance current controls the thickness of the filament, in agreement with simulations of multilevel switching in ECMs [241]. The programmed ON state follows the relation $R_{ON} = V_C/I_{cc}$, where V_C is a material-dependent constant, and the slope should be around $m = -1$. Two different ranges are used for linear fitting, as the trend flattens for $I_{cc} > 500\,\mu\text{A}$. For the reduced range $I_{cc,100} \in [0.1; 100]\,\mu\text{A}$ the fit yields $m_{100} = (-0.93 \pm 0.05)$, while the full range $I_{cc,1000} \in [0.1; 1000]\,\mu\text{A}$ yields $m_{1000} = (-0.83 \pm 0.02)$. This quantifies the observation for larger compliance currents that can be attributed to contact resistances. These results agree with other printed memory cells and insulating layers in ECMs such as Spin-on-Glass or WO$_3$, as they exhibit slopes of -0.84 and -0.70, respectively [139]. The discrepancy to $m = -1$ can be explained as additional leakage currents, leading to lower overall resistances and flatter slopes. For the Cu/Cu$_x$S/W cell, the semiconducting Cu$_x$S is expected to significantly contribute in this way.

Cu/Cu$_x$ - Inkjet

As an outlook towards fully printed memory, Cu/Cu$_x$ cells are investigated based on inkjet-printed and photonically sintered Cu-NPs on a microscope glass slide. For the surface transformation to Cu$_x$S, $Na_2S_{(aq)}(0.1\,\text{M})$ is precisely applied via inkjet printing. Contacting is done by manually contacting with the W-tip of the micromanipulator. Figure 4.38 presents the electrical characterization for a Cu/Cu$_x$/W resistive memory cell on glass. Eleven consecutive sweeps demonstrate the repeatability and continuity of the SET and RESET processes. In Figure 4.38 a) and b), SET is observed at 0.2–0.3 V with a sharp increase in current. A metallic filament can be assumed from the linear slope of the $I - V$-curve for lowering the voltage. The early onset for RESET around 0 V indicates that the filament is easily dissolved. However, the drop in resistance over four orders of magnitude from 10^7 to $10^3\,\Omega$ highlights the potential for memory applications.

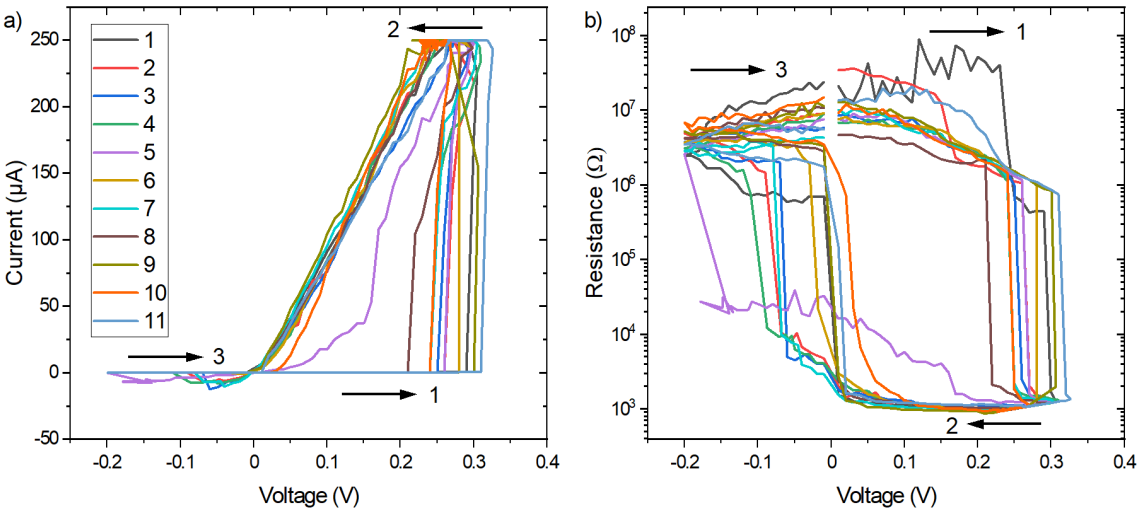

Figure 4.38: Electrical characterization of fully inkjet-printed Cu/Cu_xS contacted by W-tip on glass substrate with $I_{cc} = 250\,\mu A$. a) Ten consecutive sweeps exhibit a sharp increase in current (SET) at 0.2–0.3 V and decrease around 0 V (RESET). b) The drop in resistance over four orders of magnitude from 10^7 to $10^3\,\Omega$. The low RESET voltage suggests a weak filament and early dissolution onset. The marked arrows indicate the sweep direction.

4.7 Integration of Components

In this section, the integration of different printed components is presented. First, Ag/SoG/Ag memory cell is switched by a screen-printed Zn/MnO_2 battery, where the Ag-based current collector of the battery also serves as the active electrode for the memory. Figure 4.39 shows a schematic realization by connecting the battery to the memory and forming a non-volatile metallic filament. Then, the same type of battery switches a Cu/Cu_xS/W memory cell where the ON state is controlled through a fully inkjet-printed Cu_xS-based temperature sensor.

4.7.1 Battery and Ag/SoG/Ag memory cell

A first step towards integrating multiple printed components, a memory cell is to be switched by a battery, and the retention is determined. The Ag/SoG/Ag memory cell is sharing the active bottom electrode with the current collector from the Zn/MnO_2 battery. The sampling interval is chosen to exclude measurement-induced switching (Fig. 4.40 a)). Here, for the sampling interval $\Delta t_{read} = 1.2\,s$, the resistance stays constant around $5.5\,k\Omega$, but gradually decreases with several measurements at $\Delta t_{read} = 0.2\,s$ and settles at $3.0\,k\Omega$. The combination of both printed components with a pristine cell is investigated in Figure 4.40 b). Retention measurement over 2 minutes characterizes the initial state of the memory. The sampling interval of 1 s at 0.1 V yields a constant, high resistance of $R_{OFF} \approx 3.0 - 3.2\,k\Omega$.

Next, a memory cell is manually connected (<1 s) to the battery with an open circuit (OC) voltage of $V_{OC} = 1.4\,V$, where the positive bias is applied to the screen-printed bottom electrode. This triggers the SET process of the memory cell, and the retention measurement reveals a drop to ca. $50\,\Omega$. Such a low resistance indicates the formation of a metallic filament through the porous, insulating SoG layer of the ECM. For the first 30 s the sampling interval remains at 1 s to observe immediate changes but is then increased to 5 s to minimize the influence of the measurement on the resistance. The creeping rise of resistance over time can be explained by a slowly dissolving filament where temperature-assisted ad-atom diffusion leads to Ostwald ripening [64, p. 698]. This phenomenon was described in Section 2.3.1 as the dissolution of small crystals and the redeposition

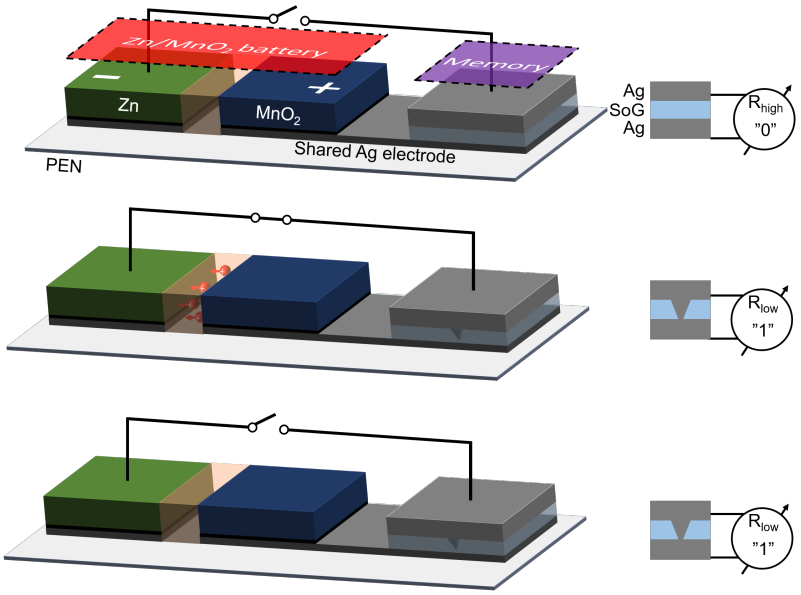

Figure 4.39: Visualization of the desired integration of a printed Zn/MnO_2 battery with a Ag/SoG/Ag memory cell, sharing the Ag electrode. The initial OFF state is changed to ON by connecting both components. The altered state is non-volatile, i.e. maintained without application of voltage. [109]

of the dissolved species on the surfaces of larger crystals. The retention starts with the continued measurement after switching in the ON state ($R_{ON} < 200\,\Omega$) and surpasses it only after $t_{ON} > 2.5\,h$ and ends up in the initial OFF state ($R_{OFF} > 3.0\,k\Omega$). After the return, this procedure can be repeated by connecting the cell to the battery again. Switching also occurs for applying the voltage with inverted polarity to the ECM, yielding similar results.

To probe the stability of the ON state after switching, repeated voltage sweeps from -0.1 V to 0.5 V and $I_{cc} = 0.5\,mA$ are applied (s. Fig. 4.41). The sweeps directly go into compliance (Fig. 4.41 b)); hence not sufficient energy is applied to actively dissolve the filament. Repeated sweeps from -0.1 V to 0.5 V but with $I_{cc} = 1.0\,mA$ show partial dissolvement of the filament, as the resistance rises from ca. $40\,\Omega$ to $600\,\Omega$. These results confirm that the formed filament is robust and partial dissolution requires either relatively large currents above 1 mA or thermally assisted diffusion over hours.

In conclusion, a retention of 2.5 h qualifies as non-volatile and demonstrates that the printed integration works. However, for practical applications in logistics, retention times of weeks to months are required. This goal should be achievable through investigations focusing on advanced methods and improved materials. Further progress is expected by increasing the OFF/ON ratio through better insulation and implementing a series resistor to define a current compliance. Still, the goal is not to realize infinite retention as this would be equal to a dielectric breakdown, which has already been demonstrated in the form of a printed write-once-read-many (WORM) memories [242]. Hence, fine-tuning of the switching properties to eventually enable reusability is desired.

4.7.2 Cu/Cu_xS/W memory cell and Cu_xS temperature sensor

For a potential application, the NTC temperature sensor (s. Sec. 4.5.2) may serve as a current limiter for the memory cell to define the ON state. Here, the sensor and the memory will experience similar thermal conditions, therefore, the performance of the memory at 80 °C was also verified (Fig. 4.36 a)). Higher temperatures will lead to a lower resistance of the sensor, which needs to

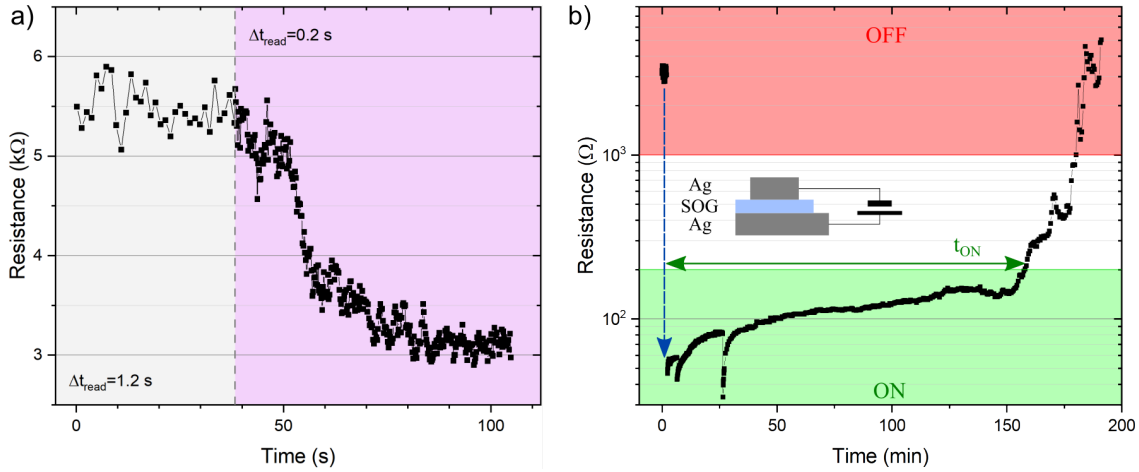

Figure 4.40: a) Retention measurement for two different sampling intervals Δt_{read}. For Δt_{read} = 1.2 s, the resistance stays constant around 5.5 kΩ but changes to 3.0 kΩ after several measurements at Δt_{read} = 0.2 s. b) Retention measurement (V_{read} = 0.1 V) before and after switching the cell by the battery. The initial resistance measurement of the ECM over 2 minutes exhibits a high resistance of ca. R_{OFF} = 3 kΩ before it drops to ca. 50 Ω after the battery is connected. A retention of the ON state (R_{ON} < 200 Ω) for t_{ON} >2.5 h is observed before returning to the OFF state (R_{OFF} > 1.0 kΩ) [109].

be in the same order of magnitude as the ON state of the ECM. The observed resistance range of the sensor (ca. 10 – 100 kΩ) is compatible with the memory cell due to the control of its ON resistance by an appropriate compliance current. Hence, for switching events for the ECM at high temperatures with the sensor in series, more current is allowed for the cell, resulting in an ON state with a lower resistance. In this way, the information about the sensor's temperature at the moment of the programming of the memory could be stored in the value of its resistance.

The temperature influence on the resistance in the ON state is negligible as the filament consists of Cu which changes according to $R(T) = R(T_0)(1 + \alpha\Delta T)$, with α_{Cu} = 0.00393 (°C)$^{-1}$ [243]. This leads to a 22 % increase in R for the change in temperature ΔT from T_0 = 25 °C to T= 80 °C. The change for a typical ON state of R(25 °C)= 1.0 kΩ to R(80 °C)= 1.2 kΩ is vanishing compared to the response for the same temperature change of the sensor from 80 kΩ to 45 kΩ (s. Fig. 4.30). This device would enable the non-volatile storage of the system's temperature at a specific time. Applications are found in the field of smart logistics, where e.g. excessive temperatures in a container during shipment can lead to damaged goods.

A conceptual scheme to integrate different printed components is shown in Figure 4.42 a). The anode of the printed battery is connected to the active electrode of the ECM cell, which is connected further in series with the temperature-dependent resistor. In the initial state, the circuit is open, and the ECM is in the high resistive OFF state, with $R(\text{HRS}) \gg R(Sens)$. When the switch is closed, the ECM sets to the LRS, which is in the same order of magnitude as the sensor. In Section 4.1, it was demonstrated that the battery provides $V > 0.9$ V for 50 h with a constant current drain of 0.2 mA, thus surpassing the necessary SET voltage of ca 0.25 V for Cu/Cu$_x$S-based memory cells (s. Sec. 4.6.2.2). From Section 4.5.2, it is known that the thermoresistive response of Cu$_x$S-based is in the range of 40 – 100 kΩ. Therefore, the higher (lower) resistance of the sensor at lower (higher) temperatures leads to a thinner (thicker) conductive filament within the ECM cell (Fig. 4.42 a)). At a later point in time, the resistance of the non-volatile state can be used to determine the temperature of the sensor at the time of the SET process. Figure 4.42 b) depicts the experimental values for $R(I_{cc}$, Cu/Cu$_x$S) from Figure 4.37 over a summary of other empirical

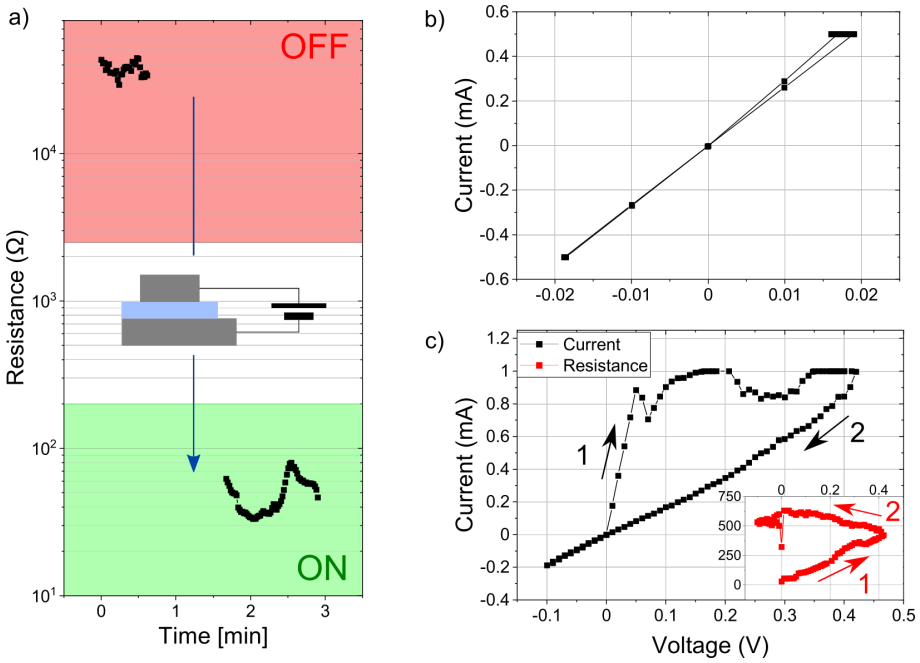

Figure 4.41: Investigation of stability of ON state. a) The initial OFF state with $R_{OFF} \approx 35\,\mathrm{k\Omega}$ switches to the ON state $R_{ON} \approx 50\,\Omega$ after connection to the screen-printed battery. b) A voltage sweep from -0.1 V to 0.5 V and $I_{cc} = 0.5\,\mathrm{mA}$ is not sufficient to reset the state as it directly reaches the compliance and remains at ca. $R = 40\,\Omega$. c) Repeated sweep from -0.1 V to 0.5 V but with $I_{cc} = 1.0\,\mathrm{mA}$ suffices to partly reset the state by increasing the resistance by an order of magnitude to ca. $R = 600\,\Omega$.

findings from the literature [244]. This agreement of different materials and switching concepts to the empirical law $R \propto I_{cc}^{-1}$ is called universal switching behavior (Sec. 2.5). The width of the distribution along the linear trend will be used to validate and attribute the ON state after the SET process to the influence of the sensor series resistor.

The parameters and results for the realization of this setup are given in Table 4.10. It is demonstrated with the same devices and configuration at two different temperatures. At a temperature of 20 °C, the sensor exhibits $R_{sens} = 40\,\mathrm{k\Omega}$. First, it is confirmed that the ECM is working by performing a successful quasi-static voltage sweep with $I_{cc} = 10\,\mu\mathrm{A}$, showing $R_{OFF} > 10^7\Omega$, $R_{ON} \approx 10^4\,\Omega$, and $V_{set} = 0.29\,\mathrm{V}$. After closing the circuit for one second, the memory cell has switched from HRS to LRS with $R_{ON} = 425\,\mathrm{k\Omega}$. The compliance current is given by $I_{cc} = V_{bat}/(R_{sens} + R_{ON})$ and R_{ON} is compared to the expected range from Figure 4.42 b). With the given values, $I_{cc} = 2.8\,\mu\mathrm{A}$ can be attributed to the range of $50-500\,\mathrm{k\Omega}$, thus the experimentally obtained value for R_{ON} is in accordance with other experiments with active current compliance. It also means on a more profound level that the series resistor prevented the ECM from forming an irreversible short circuit.

In the subsequent step, only the temperature sensor is heated on a hot plate to 100 °C to confine the thermal influence on the sensor part but not to the battery or memory. Due to the negative temperature coefficient, the resistance drops to $R_{sens} = 30\,\mathrm{k\Omega}$, and after the battery-induced switching, the memory is in the ON state with $R_{ON} = 50\,\mathrm{k\Omega}$. This corresponds to $I_{cc} = 16.3\,\mu\mathrm{A}$ and agrees with the range of $5-50\,\mathrm{k\Omega}$ from Figure 4.42 b). Hence, the decrease of R_{sens} by 25 % from 40 to 30 kΩ, leads to an order of magnitude difference in R_{ON}. The strong non-linearity of the universal switching curve enables vast changes in R_{ON} with relatively small changes in R_{sens} or I_{cc}, respectively.

In summary, capabilities for thin dielectric Cu_xS layers were demonstrated: to fabricate nanometer-scale structures on a Cu surface and for potential applications. The ability to con-

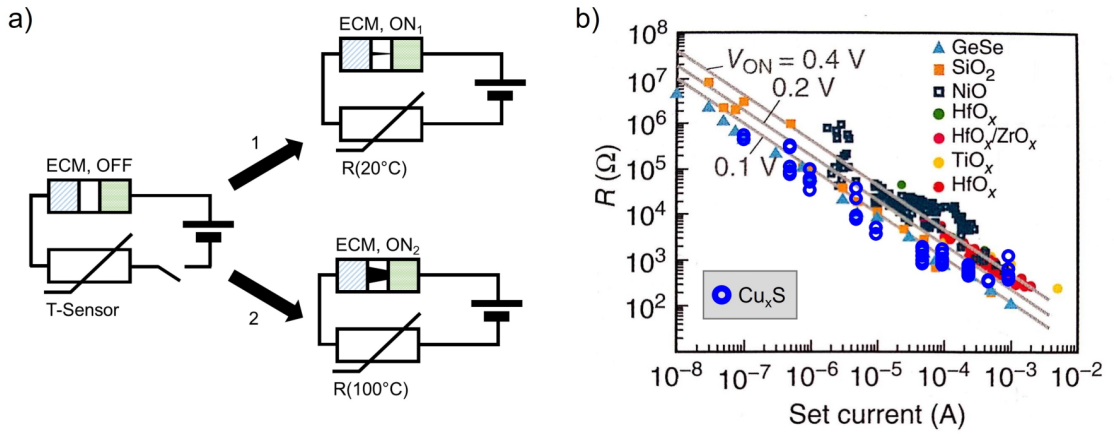

Figure 4.42: a) Conceptual scheme to integrate printed battery, memory, and sensor, storing information about the temperature of scenario 1 or 2 in the ON state of the ECM. b) Measured $R(I_{cc})$ from Figure 4.37 and from other materials and switching concepts (adapted from [244]).

Table 4.10: Parameters for the setup depicted in Figure 4.42 a). The temperature is locally applied only to the sensor and its resistance is measured. After switching the Cu/Cu$_x$S to the ON state, R_{ON} is measured and compared to the expected range for I_{cc} from Figure 4.42 b).

	Temperature [°C]	R$_{sens}$ [kΩ]	R_{ON} [kΩ]	I_{cc} [µA]	Range [kΩ]
1	20	40	425	3	50–500
	100	30	50	16	5–50

trol the feature size of small structures as well as the roughness and height of Cu$_x$S structures via molarity and layer count provides first insights into possible applications. Further investigations on the behavior of large-scale implementations with higher quantities will be essential for future developments. Homogeneous deposition and stability of thin layers in the range of 100 nm, and compatibility with existing processes are technical challenges worth exploring. The proof-of-concept for a fully printed setup with a screen-printed battery and sensor, as well as a memory cell consisting of the same components (Cu/Cu$_x$S), demonstrated a practical application where the information about the temperature of the sensor is stored as the resistive state of the memory.

Local application and transformation via inkjet printing already allow further research to design ideas. Using Cu instead of Ag will also reduce the material costs for any application. Additionally, the relatively low-tech approach of inkjet printing can enable hybrid electronics. Here, conventional semiconductor fabrication processes are used to produce established, high-volume structures customized by printing technology. Applications for other sensors such as humidity or as a sacrificial layer are plausible due to the porous structure.

Also, additive manufacturing provides options for using chemicals such as Sulfur that are incompatible with classical semiconductor processing. Here, after completing the micro-structuring and packaging of sensitive parts, inkjet printing offers the possibility to create Cu$_x$S in a backend-of-the-line step.

Chapter 5

Summary and Outlook

This research has investigated and identified methods and materials for printed autonomous systems of memory, battery, and sensors. It has realized a novel design to operate a memory cell by a printed battery through a shared electrode. Semiconducting Cu_xS structures have been fabricated using inkjet printing and characterized for sensor and memory applications as well as their integration into a single device for temperature monitoring. Furthermore, fully inkjet-printed sensors have been presented for strain and humidity measurements on flexible substrates. Printing processes and designs have been developed, minimizing the number of different inks and accelerating fabrication.

The different sensors have provided new opportunities for custom designs. Their individual characterizations have addressed application-related questions such as long-term stability or cross-sensitivity through electrical and microscopic investigations. The CNT/PDMS-based strain sensor has provided a quasi-linear piezoresistive response with vanishing hysteresis to tensile strain. The gauge factor of 1.4 is comparable to commercial metal-based strain gauges, and long-term development over thousands of bending cycles has been evaluated.

Further, photonic sintering of inkjet-printed Cu electrodes has been investigated to provide a cost-effective alternative to Ag-based structures. Microscopic analysis has revealed the porous structure of sintered Cu-NPs, resulting in good conductivity in agreement with physical models. Inkjet-printed Cu electrodes have been used for WO_3-based humidity sensors with highly reproducible sensitivity, where a 100 nm thick WO_3 layer has exhibited exponential resistive response over three orders of magnitude for relative humidity levels between 40–90 %. The sensor has mapped changes in humidity within seconds and has shown no indications for temperature cross-sensitivity. This very sensor has been used to demonstrate the suitability of a vapor barrier created from a metalized composite foil. It has protected the sensor not only from dust particles and mechanical damage but has allowed to verify the humidity barrier and make it suitable for other components.

To extend the potential for utilizing cost-effective Cu for printing techniques, a novel method has been presented for a precise surface transformation into Cu_xS by local application of $Na_2S_{(aq)}$ via inkjet printing. The nanometer-scaled structural changes have shown the surface sensitivity of the transformation, and elemental analysis results have been combined to formulate an accurate description of the process. Semiconducting Cu_xS has exhibited a negative temperature coefficient, and its potential as a fully inkjet-printed temperature sensor has been demonstrated. Additionally, Cu_xS has been used for resistive switching applications as an electrolyte, where the logical state has been tuned by controlling the compliance current to store more than one bit of data in it. Low power consumption, temperature stability, and the first steps towards a lamination process

for roll-to-roll fabrication have contributed to the development of fully printed memory cells.

One key aspect of autonomous systems is that they either harvest energy for operation from the environment or are powered through a battery. The capabilities for screen-printed Zn/MnO_2 batteries have been demonstrated by providing sufficient energy to ideally switch a memory cell 10^{13} times and enough to power small IoT devices such as smart tags. It has been examined by utilizing the Ag current collector of the battery to function as a shared active electrode for a resistive memory cell. This has highlighted the potential to take advantage of combining different printing technologies to maintain their benefits without compromising them due to complexity by compatibility problems or a plethora of inks. The battery has induced the logical switching of an inkjet-printed ECM with an insulating layer of Spin-on-Glass, and the information about this event has been stored for more than 2.5 h. As a final step, an ECM and thermal sensor based on printed Cu_xS has been powered by the screen-printed battery to store the information about the temperature as the resistive state in the memory. This has been achieved by limiting the current in the system through the temperature-dependent resistance of the sensor.

In conclusion, various materials and methods have been used to investigate multiple components for printed autonomous electronic devices. Practical questions regarding fabrication, processing, and protection have been addressed, and underlying mechanisms for long-time development, interaction with the environment, and microscopic structures have been clarified. However, the presented research also provides questions for the future, such as:

- How is the CNT/PDMS-based strain sensor affected by humidity, and could the inert PDMS layer be used to package other sensitive components?
- Can the resistance of the WO_3-based humidity sensor be reduced to make it compatible with low voltage read-outs?
- What is the cross-sensitivity of the porous Cu_xS temperature sensor to humidity?
- Could emerging Cu-based screen-printing inks replace the Ag current collector for the battery?
- Do device-to-device variations limit the field of applications?
- Can the fabrication be transferred from lab-scale to roll-to-roll?

Upcoming investigations should adhere to the fundamental idea of preserving facile fabrication for any advances in this field. Printed solutions will be found in applications with more available space and adjusted technological demands. One example is utilizing printed memory cells in a smart tag for logistics, where a limited amount of information is required, such as shipping instructions or event detection logs. Here, printed solutions provide ample opportunities to enable new and custom implementations. Scaling printed electronics to roll-to-roll applications and using Cu-based circuits will make these solutions also more cost-effective and a serious alternative to traditional solutions. As presented in this thesis, reducing the number of required inks and fabrication steps is possible. The presented low-temperature processes could lead to the establishment of printed electronics for numerous applications. The key benefits of this approach have been illustrated in the form of customizable designs and reduced material and energy consumption. The presented results have proven that established micro- and nanoscale integrated circuits can be enriched and complemented through additive printing processes with memories, sensors, and batteries.

Appendices

Appendix A

Experimental Addendum

A.1 Rheological Properties of Water

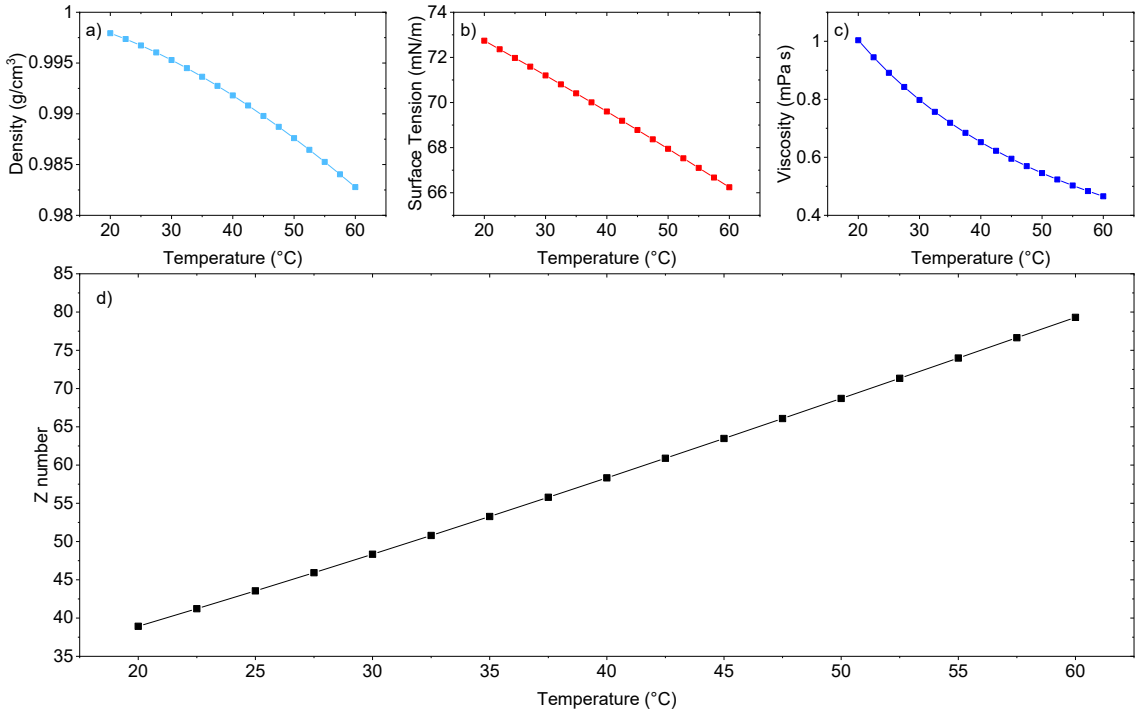

Figure A.1: Rheological properties of water (H_2O) with temperature: a) density ρ [245], b) surface tension γ [246], c) viscosity η [247], and d) Z number according to Equation 3.4: $Z = \sqrt{\gamma\rho L}/\eta$, with $L = 25\,\mu m$.

A.2 Waveforms for Inkjet Inks

The ejection for drop-on-demand inkjet printing with piezoelectric actuators requires individual waveforms for different inks (s. Sec. 3.1.3). Figure A.2 presents these waveforms for different materials (s. Tab. 3.2) using the printer Dimatix DMP2831 in combination with DMC-11610 cartridges, which provide 10 pl droplets from a nozzle of 21 µm diameter. It gives the firing voltage for ejection and non-firing voltage to prevent clogging by keeping the ink in motion during idle or when not printing.

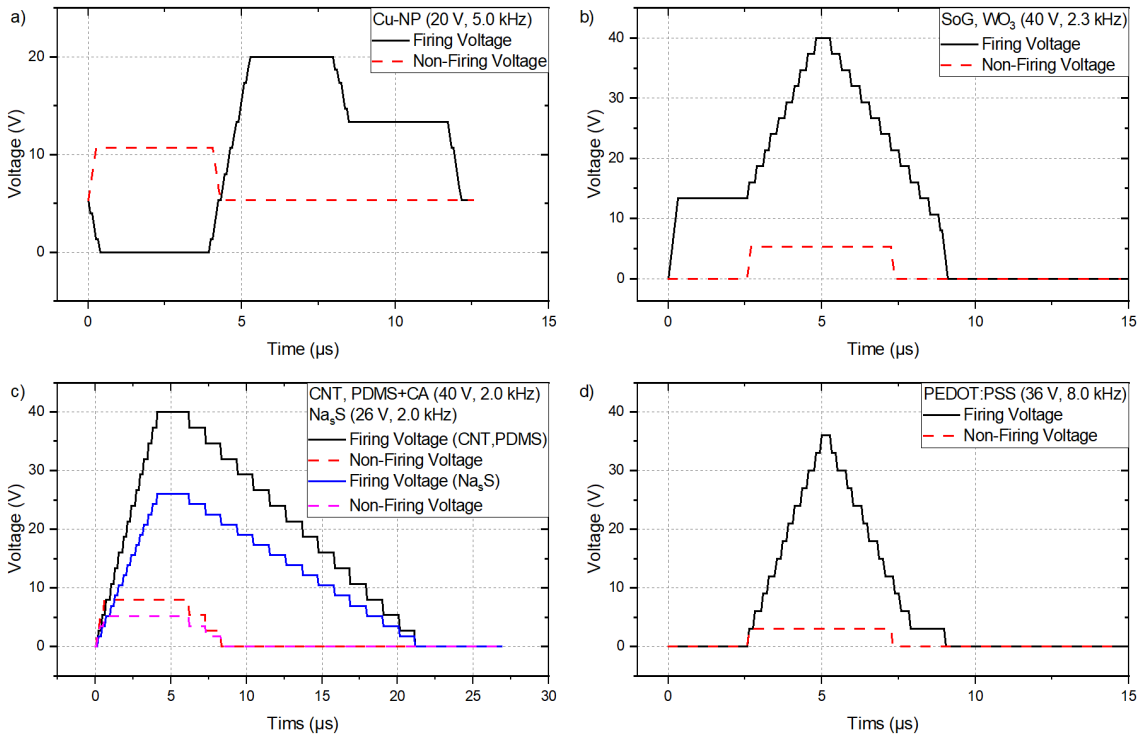

Figure A.2: Waveform (firing and non-firing), maximum voltage V_{max}, and jetting frequency f for different inkjet inks. a) Cu-NP (Metalon CI-004) with $V_{max} = 20\,\mathrm{V}$ and $f = 5.0\,\mathrm{kHz}$; b) Spin-on-Glass (SoG, Honeywell Accuglass) and WO_3 (Avantama P-10) with $V_{max} = 40\,\mathrm{V}$ and $f = 2.3\,\mathrm{kHz}$; c) Multi-walled carbon nanotubes (CNT) and PDMS+Curing Agent (CA) with $V_{max} = 40\,\mathrm{V}$ and $f = 2.0\,\mathrm{kHz}$; $Na_2S_{(aq)}$ with $V_{max} = 26\,\mathrm{V}$ and $f = 2.0\,\mathrm{kHz}$; d) PEDOT:PSS (Clevios P Jet N V2) with $V_{max} = 36\,\mathrm{V}$ and $f = 8.0\,\mathrm{kHz}$.

A.3 $Na_2S_{(aq)}$ on Si/SiO_2 Wafer

To find appropriate printing parameters for the application of Na_2S_{aq} on a Cu wafer, different drop spaces and layer counts are printed on an IPA-cleaned Si/SiO_2 wafer. It possesses a hydrophobic surface, thus, water-based Na_2S is prone to form distinct drops instead of continuous lines. Figure A.3 shows the schematic layout for the application of single drops with increasing distance (a)) and that merging occurs at a distance of ca. 35 µm.

Figure A.4 shows the schematic layout for the application of lines of length 10–100 µm (a) and that no splitting occurs for line lengths up to 100 µm. The splitting starts for line lengths larger than 200 µm for a single layer and larger than 300 µm for five layers (not shown).

In Figure A.5 a) a confocal microscopy image shows the transformed Cu_xS structure of ten inkjet-printed layers with each layer containing 50 pl of Na_2S_{aq} (0.087 M) after depositing on a $Si/SiO_2/Cu(250\,\mathrm{nm})$ wafer via inkjet printing. The radial profile in b) shows ten individual ripples of ca. 100 nm height. The horizontal feature occurs due to a microscopic scratch on the Cu surface.

A.4 Volume from Profile Measurement

To determine the thickness of the WO_3 layer for the humidity sensor (s. Sec. 4.4), single drops are deposited manually or via inkjet printing on a glass slide. In Table A.1, the geometrical properties of inkjet-printed WO_3 drops are presented, as well as the fraction of dry to wet ink. The dry volume is determined via confocal microscopy, and the ink volume is given by the number of 10 pl drops applied by the inkjet printer. The volume of 2000 pl corresponds to overlapping lines, resulting in

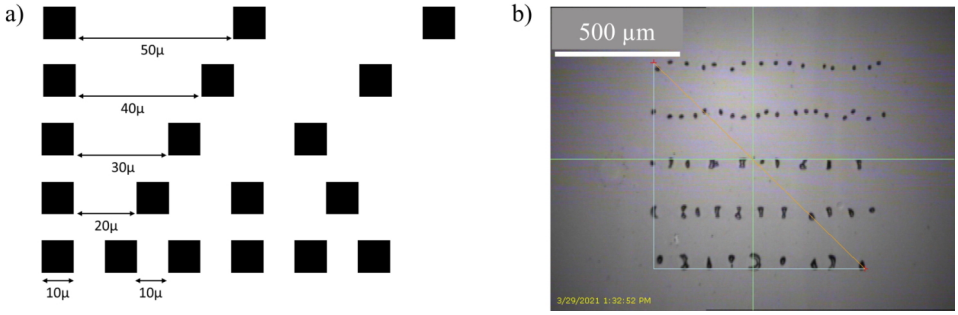

Figure A.3: a) Schematic layout for a dropspace (DS) of 10 µm to investigate the merging behavior of Na_2S_{aq} on a Si/SiO_2 wafer. Each $(10\times10)\,\mu m^2$ pixel represents the application of a single 10 pl drop. The horizontal dropspace DS is increased to observe when individual drops merge. b) Optical image from the print camera showing single drops for $DS \geq 40$ and merged drops for $DS \leq 30$, thus the merging for a single layer occurs around a spacing of 35 µm.

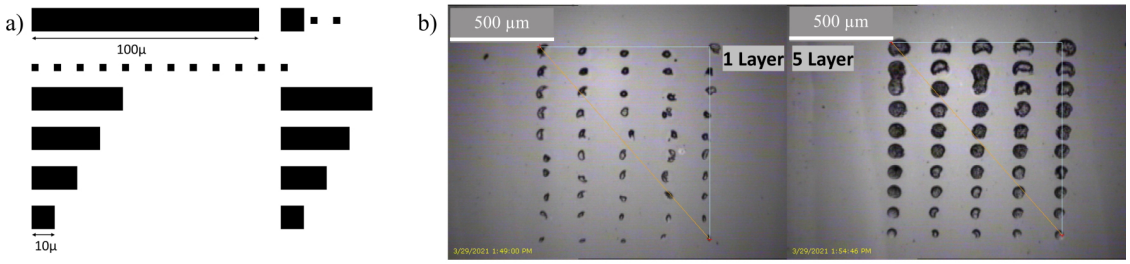

Figure A.4: a) Schematic layout for a dropspace (DS) of 10 µm to investigate the splitting behavior of Na_2S_{aq} on a Si/SiO_2 wafer. Each $(10\times10)\,\mu m^2$ pixel represents the application of a single 10 pl drop. The horizontal lengths are increased in steps of the DS to observe when printed lines split due to surface tension. b) Optical image from the print camera showing no splitting for line lengths up to 100 µm.

higher structures of ca. 100 nm compared to single drops with ca 50 nm. The largest volumes of $4.68{\cdot}10^5$ pl and $23.48{\cdot}10^5$ pl, respectively, are one and five layers of the WO_3 layer for the humidity sensor. The fraction dry/wet ink is for all measurements in the range 0.8–1.0 %.

A single profilometry profile can be sufficient to obtain information about the volume of a rotationally symmetric structure. First, an appropriate fitting function $y = f(x)$ must be found. Then, for rotating a curve about the y-axis, it is solved for the quadratic inverse function $x^2 = g(y)$. The limits must be given in terms of y as well, as $y_1 = c$ and $y_2 = d$. Finally, the volume V is

Table A.1: Geometrical properties of inkjet-printed WO_3 drops on glass slide. The fraction dry/ink is calculated from the ratio of remaining particle volume to the applied ink volume.

Volume ink [pl]	Radius Drop [µm]	Fraction dry/wet ink [%]	Avg. Height [nm]
25	69±2	1.51±0.25	51±6
50	92±5	1.16±0.01	44±5
100	112±3	0.91±0.14	47±6
2000	361±1	1.02±0.03	100±2
$4.68{\cdot}10^5$	-	0.80	109
$2.35{\cdot}10^6$	-	0.71	485
$4.12{\cdot}10^6$ [s. A.6]	$3.01{\cdot}10^3$	0.78	$1.12{\cdot}10^3$

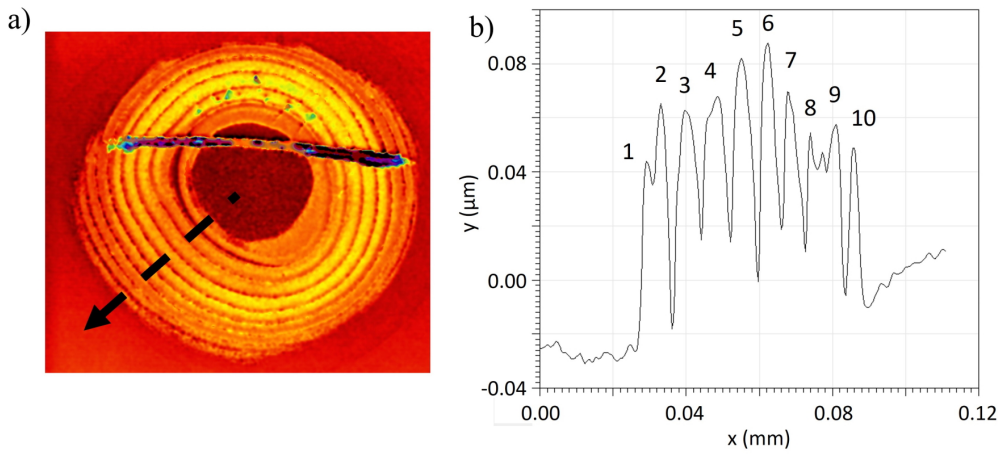

Figure A.5: a) Confocal microscopy image showing the transformed Cu_xS structure of ten inkjet-printed layers with each layer containing 50 pl of Na_2S_{aq} after depositing on a $Si/SiO_2/Cu(250\,nm)$ wafer via inkjet printing. The radial profile in b) shows ten individual ripples of ca. 100 nm height.

given by

$$V = \int_c^d \pi g(y) dy = \pi \int_c^d x^2 dy. \tag{A.1}$$

The profilometry data for a manually applied WO_3 drop on the glass slide is shown in Figure A.6. It is fitted using the area version of the Gaussian function

$$y(x) = \frac{A}{w\sqrt{\pi/2}} \cdot \exp\left[-2\left(\frac{x - x_c}{w}\right)^2\right], \tag{A.2}$$

where A is the area, x_c is the center of the curve, and w is the width. Parameters which can be derived are $\sigma = w/2$, Full Width at Half Maximum $FWHM = \sqrt{2ln(2)} \cdot w$, and the height at the centre is given as $y(x_c) = A/(w\sqrt{\pi/2})$. The discrete integral of the profilometric data and the analytic integral of the Gauss profile yield an area of $7.5{\cdot}10^3$ and $7.7{\cdot}10^3\,\mu m^2$, respectively.

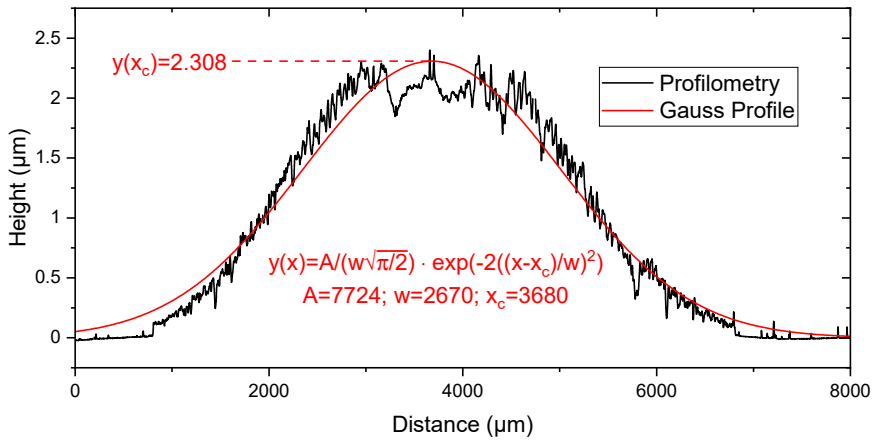

Figure A.6: Profilometry of manually applied WO_3 drop on a glass slide. The Gauss curve and fitting parameters are given. The discrete integral of the profilometric data and the analytic integral of the Gauss profile yield an area of $7.5{\cdot}10^3$ and $7.7{\cdot}10^3\,\mu m^3$, respectively. The volume of the drop can be calculated from the profile to be $3.20 \cdot 10^7\,\mu m^3$. The base diameter is 6.02 mm, yielding an average height of 1.12 µm for a cylindrical approximation.

The inverse function is shifted and centered around $x = 0$ by setting $x_c = 0$ and given by

$$g(y) = x^2 = -\frac{w^2}{2} ln\left(y \cdot \frac{w\sqrt{\pi/2}}{A}\right), \tag{A.3}$$

The limits are set to $c = 0$ and $d = y(x_c = 0)$, and thus Equation A.1 becomes

$$V = -\frac{w^2\pi}{2} \cdot y(0)\left[ln\left(\frac{w\sqrt{\pi/2}}{A}\right) + ln(y(0)) - 1\right] = 3.20 \cdot 10^7\,\mu m^3, \tag{A.4}$$

with $w = 2889$, $A = 8826$, and $y(0) = 2.438$. The fraction of dried to wet ink is calculated to be 0.78 % from the drop mass of 3.3 mg and a density of ca. 0.8 g/cm^3.

A.5 Sintering Simulation

The simulation results shown in Section 4.3.1 are performed with the proprietary software SimPulse (v. 3.0.0.3008), which assumes a translation-invariant surface. This neglects effects at the transition of the narrow Cu line to the polyimide substrate and the coffee stain effect. Comsol (v. 5.6) simulates the temperature development for the boundary region and a non-uniform profile. It models the absorption of the Cu and polyimide layer and heat conduction over time. The absorption coefficients α for the respective materials are taken as described in Subsection 4.3.1. Figure A.7 a) shows the series of 8 sintering pulses, approximated from the experimental results in Figure 4.14 b). The simulation considers a 2D cross section through the printed line. The right half of the symmetric profile is 200 µm wide and 200 nm high, with a coffee stain effect superelevation up to 900 nm over the outer 50 µm (Fig. A.7 b)). Figure A.7 c) presents the temperature profile at the boundary between the Cu line and substrate for different times. The first profile, after 1.56 ms reaches over 400 °C and shows with the following profiles an elevated temperature of ca. 50 °C compared to the plateau. The temperature distribution smoothens after the pulse ends at 9.38 ms (black curve). In Figure A.7 d), the maximum temperature at the edge is compared to the center, where it becomes ca. 50 °C hotter. Thus, the coffee stain effect leads to more energy absorption and temperature rise.

Figure A.8 shows the heat map for the cross section of the layers. The Cu line is treated as a one-dimensional object at $0 < x < 2 \cdot 10^{-4}$ m since its height is small compared to the thermal diffusion length of relevant time scales. In the simulation, air is above Cu ($y > 0$) and Kapton ($-125\,\mu m < y < 0$) below it. The color scales are adapted to the respective temperature range, and the relation to the pulse timing needs to be considered. After 1.56 ms (c) the maximum temperature is higher than at 4.69 ms (d) because at 1.56 ms the pulse is active while at 4.69 ms it is not.

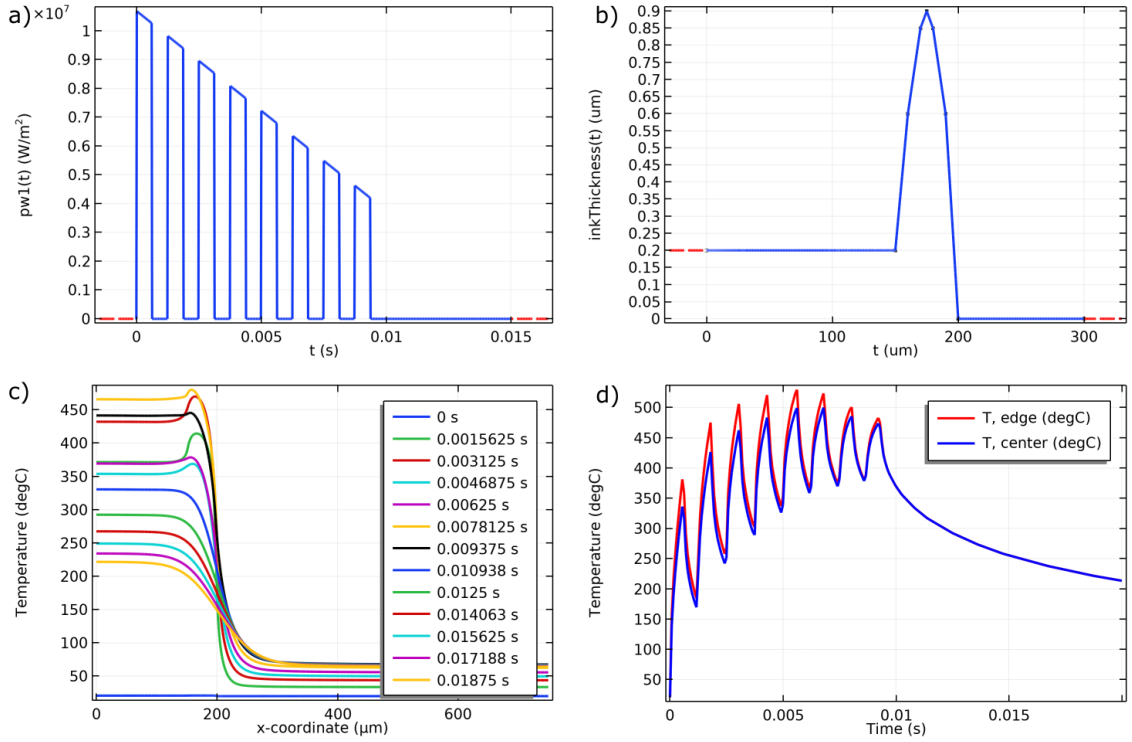

Figure A.7: a) Series of sintering pulses for the simulation, approximated to Figure 4.14 b) with 8 pulses of equal length in an envelope of 10 ms. b) Right half of symmetric Cu profile is 200 µm wide with plateau height of 200 nm and coffee stain elevation up to 900 nm. c) Temperature profile at the boundary between Cu line and substrate for different times. d) Maximum temperatures at the center and the edge of the Cu line over time.

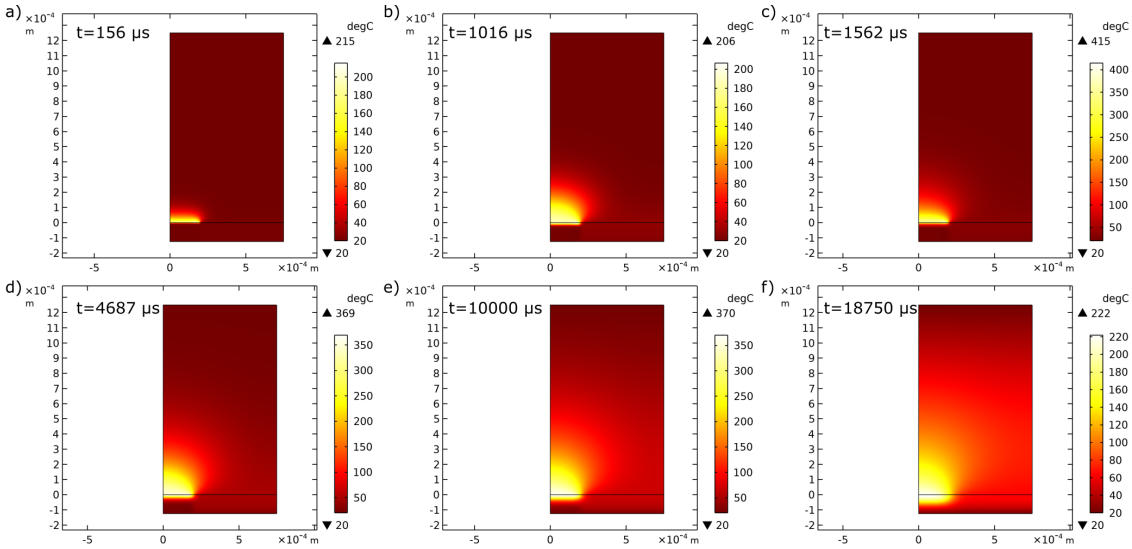

Figure A.8: Development of temperature over times a) 156 µs, b) 1 ms, c) 1.5 ms, d) 4.7 ms, e) 10 ms, f) 18.8 ms for the cross section with the symmetry axis of the two-dimensional Cu line ($0 < x < 2 \cdot 10^{-4}$ m) in the origin. Above Cu ($y > 0$) is air and below is Kapton ($y < 0$). Peak temperatures rise and fall during the process due to the pulsed heat source, while the region around the profile steadily heats up.

A.6 Climate Chamber (SH-242) T-RH Control Range

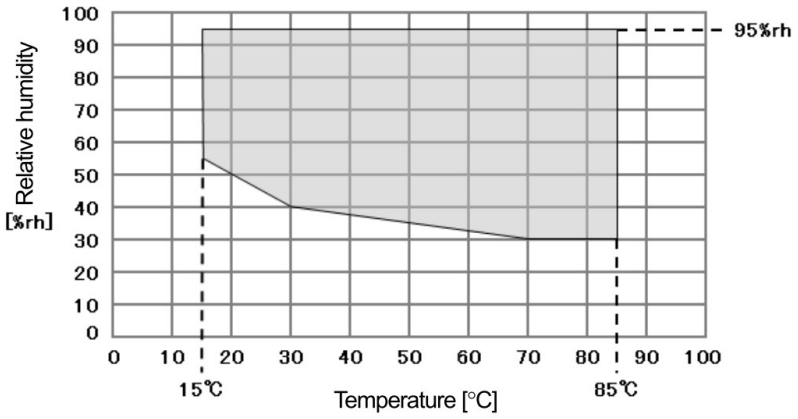

Figure A.9: Temperature-humidity control range for the climate chamber ESPEC SH-242. In the humidity control mode, the standard temperature and relative humidity range is 15–85 °C and 30–95 %rh, respectively. Without humidity control, the temperature range spans from -40 °C to +150 °C [205].

A.7 Reverse Titration

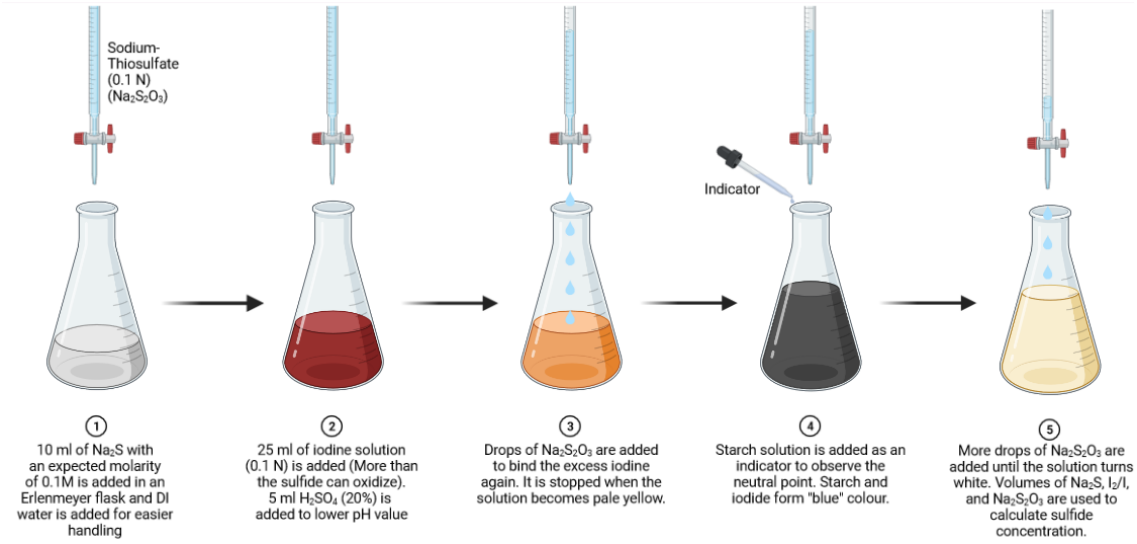

Figure A.10: Steps for reverse titration to determine the concentration of Na_2S-based ink. The image was created in BioRender.com.

The preparation of Na_2S-based ink occurs by dissolving the weighed nonahydrated compound ($Na_2S{\cdot}9H_2O$) in deionized H_2O. The molarity for samples of different ages is determined via reverse titration. First (Fig. A.10, 1), 10 ml of $Na_2S_{(aq)}$ (0.1 M) is added in an Erlenmeyer flask and DI water is added for easier handling. The additional water does not affect the measurement, as only sulfide ions are used to determine the molarity. The burette is placed above the flask and filled with a defined volume of sodium-thiosulfate ($Na_2S_2O_3$, 0.1 N). Next (Fig. A.10, 2), 25 ml of iodine solution (0.1 N) is added, providing more iod than sulfide can oxidize, resulting in a brown or reddish color. Excess iodine remains in the solution and will be titrated back in the following steps, hence the name. A pH value lower than 9 is required to prevent dissociation from triiodide

[248, p. 402], thus 5 ml of sulfuric acid (H_2SO_4, 20 %) is added. Then (Fig. A.10, 3), drops of $Na_2S_2O_3$ are added via the burette to bind excess iodine. The solution turns pale yellow as more iodine is oxidized. At this point (Fig. A.10, 4), a starch solution is added as an indicator, turning the solution dark blue or grey. In principle, no indicator is required as the color change from pale yellow to colorless could also be observed. However, the distinct change from dark grey to colorless facilitates the experimental observation. In the final step (Fig. A.10, 5), additional drops of $Na_2S_2O_3$ are added until the solution turns white. The initial concentration of $Na_2S_{(aq)}$ is calculated from its volume as well as from I_2/I, and $Na_2S_2O_3$.

The results for fresh, 4 months, and 8 months old $Na_2S_{(aq)}$ solutions are shown in Figure A.11. The older samples were stored in closed containers in a refrigerator.

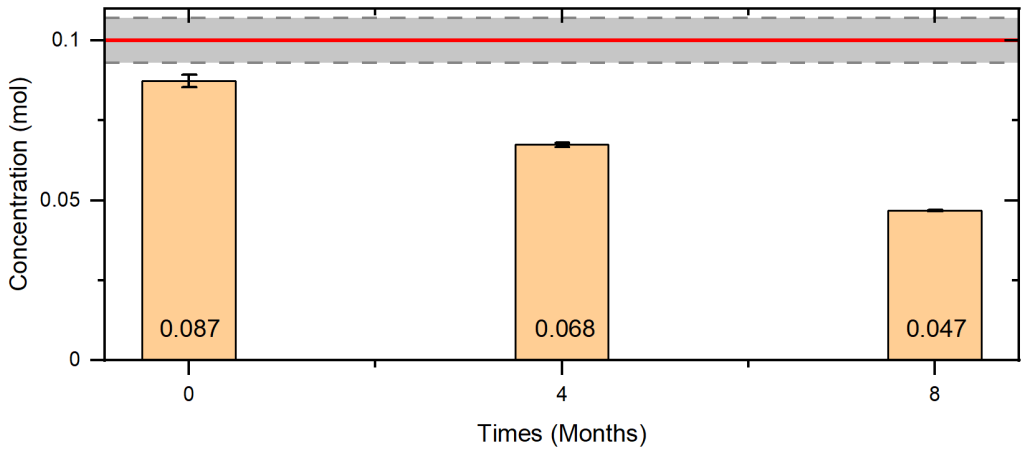

Figure A.11: Molar concentration obtained from iodometry of 0.1 M Na_2S-solutions of different age. The error bars are obtained from three distinct measurements. The concentration of the fresh sample is 13 % lower than 0.1 M (red line), even under considerations of preparation uncertainties (grey bands).

The fresh sample was prepared only two hours before the titration but shows a 13 % lower concentration (0.087 M) than expected from the weighed components (0.1 M). After four months, the concentration decreased to 0.068 M, and it fell to 0.047 M after eight months. This trend constitutes a significantly lower initial concentration and a 20-percentage point reduction in concentration during four months. The deviation cannot be explained by weighing inaccuracies, resulting in ca. ±7 %, and thus probably originating from the wet starting compound Na_2S. The volatility of aqueous H_2S causes a decreasing concentration in non-ideal storage conditions. It is equilibrated between the gas phase and the aqueous phase [178] and thus can escape from the non-ideally closed container. Furthermore, the older samples were handled for sample preparation at room temperature and repeated opening and closing of the bottle cap.

Appendix B

Publications and Supervised Works

B.1 Peer-Reviewed Journal Articles

[1] J. Jehn; M. Kaiser; C. Eulenkamp; U. Moosheimer; A. Ruediger; C. Schindler: "Cu_xS thin films for printed memory cells and temperature sensors". In *Flexible and Printed Electronics*. DOI: 10.1088/2058-8585/ac6783 (2022).

[2] J. Jehn; P. Oser; M. Courrau; M. Kaiser; D. Wu; C. Grosse; U. Moosheimer; A. Ruediger; C. Schindler: "Fully Inkjet-Printed Carbon Nanotube-PDMS-based Strain Sensor: Temperature Response, Compressive and Tensile Bending Properties, and Fatigue Investigations," in *IEEE Access*. DOI: 10.1109/ACCESS.2021.3078799 (2021).

[3] J. Jehn; M. Kaiser; U. Moosheimer; A. Ruediger; C. Schindler: "Printed resistive switching memory operated by screen-printed microbattery via shared electrode". In *Microelectronic Engineering*. DOI: 10.1016/j.mee.2021.111524 (2021).

[4] M. Delfag; G. Rachovitis; A. H. Youssef; Y. Gonzalez; J. Jehn; C. Schindler; A. Ruediger: "ZnO-based Printable Memories for Flexible and Transparent Applications". *In Writing*. (2022).

[5] M. Delfag; R. Katoch; J. Jehn; Y. Gonzalez; C. Schindler; A. Ruediger: "Sinter-free inkjet-printed PEDOT:PSS/WO_3/PEDOT:PSS flexible valency change memory". In *Flexible and Printed Electronics*. DOI: 10.1088/2058-8585/ac1fd7 (2021).

[6] P. Oser; J. Jehn; M. Kaiser; O. Düttmann; F. Schmid; L. Schulte-Spechtel et al.: Fiber-Optic Photoacoustic Generator Realized by Inkjet-Printing of CNT-PDMS Composites on Fiber End Faces. In *Macromolecular Materials and Engineering*. DOI: 10.1002/mame.202000563 (2020).

B.2 Presentations at Conferences

[1] J. Jehn, U. Moosheimer, M. Kaiser, A. Ruediger, C. Schindler; "Inkjet-Gedruckter Resistiver Feuchtesensor auf Basis von WO_3 (Inkjet-printed resistive humidity sensor based on WO_3)", *3. Symposium Elektronik und Systemintegration*, Landshut 2022.

[2] J. Jehn, U. Moosheimer, M. Kaiser, A. Ruediger, C. Schindler; "Printed Integration of a Memory Device with a Temperature Sensor based on Cu_xS", *LOPEC*, München 2022.

[3] J. Jehn, S. Heeg, U. Moosheimer, C. Eulenkamp, M. Kaiser, A. Ruediger, C. Schindler; "Integration and Operation of Printed Memory With Screen-Printed Micro-Battery Electrode", *LOPEC*, München 2021.

[4] J. Jehn, S. Heeg, U. Moosheimer, C. Eulenkamp, M. Kaiser, A. Ruediger, C. Schindler; "Elektrische und mechanische Charakterisierung gedruckter Zink-Kohle Batterien (Electrical and Mechanical Characterization of printed Zn/MnO_2 batteries)", *2. Symposium Elektronik und Systemintegration*, Landshut 2020 (cancelled, Corona).

[5] J. Jehn, B. Mittermeier, E. Linkerhaegner, M. Kaiser, A. Ruediger, U. Moosheimer, C. Schindler; "Fully inkjet-printed transparent resistive memory cells based on a Ag nanowire mesh", *Memrisys*, Dresden 2019.

B.3 Master Thesis

[1] S. Heeg, "Characterization of CuS-Based Resistive Random Access Memory Cells in Combination with Screen Printed Batteries", Master Thesis, January 2021.

[2] S. Preiwisch, "Fabrication and Electrical Characterization on the Micro- and Nanoscale for Printed Memory Devices", Master Thesis, February 2021.

B.4 Bachelor Thesis

[1] F. Bandle, "Fabrication and Characterization of Inkjet-Printed Copper-Based Memory Cells with Oxide Dielectrics", Bachelor Thesis, August 2022.

B.5 Project Studies

A project study is a supervised research topic within a laboratory for ca. two months in full-time.

[1] A. Dirndorfer, "Microwave Sintering of Inkjet-Printed Copper Nanoparticles", Project Study, July 2019.

[2] S. Heeg, "Material- and electrical characterization of screen printed $Zn\text{-}MnO_2$ batteries", Project Study, January 2020.

[3] M. Werber, "Untersuchung von Gedruckten Silber-Nanowire Elektroden für Resistive Datenspeicherzellen (Investigations of Printed Silver-Nanowire Electrodes for Resistive Memory Cells)", Project Study, March 2020.

[4] D.V. Kumar, "Characterization of Zn/MnO_2 Printed Batteries," Project Study, May 2020.

[5] P. Schildwächter, "Gedruckte Sensoren Basierend auf der Widerstandsänderung bei Temperatur- und Feuchtigkeitsänderung (Printed Sensors Based on Resistance Change with Temperature and Humidity Change)", Project Study, May 2020.

[6] B. T. Duong, "Preliminary Investigation of the Fabrication and Electrical Characterization of Printed Temperature and Humidity Sensors", Project Study, June 2020.

[7] S. Preiwisch, "Herstellung und Charakterisierung von Gedruckten, Resistiven Datenspeicherzellen mit Isolator-Schichten aus Wolframoxid (Fabrication and Characterization of Printed, Resistive Memory Cells with Tungsten-Trioxid as Insulating Material)", Project Study, August 2020.

[8] S. Marxen, "Alternative Aufbau- und Verbindungstechnik Mittels Inkjet-Druck von Flussmittel (Alternative for Integrated Circuit Packaging via Inkjet Printing of Fluxing Agent)", Project Study, November 2020.

[9] M. Eder, "Herstellung von Cu_2S Schichten für Resistive Speicherzellen (Fabrication of Cu_2S Layers for Resistive Memory Cells)", Project Study, December 2020.

[10] M.A. Maz Courrau, "Characterization of Strain and Temperature Sensors Based on Inkjet-Printed Carbon Nanotubes (CNTs)", Project Study, March 2021.

[11] P.G. Saad Naguib, "Fabrication and Characterization of Copper Sulfide Temperature and Humidity Sensor", Project Study, May 2021.

[12] J. Stoib, "Gedruckte Sensoren Basierend auf Widerstandsänderung in Regulierter Klimatischer Umgebung (Printed Sensors Based on Resistance Change in Regulated Climate Environment)", Project Study, September 2021.

[13] L. Huber, "Sensitivität gedruckter, resistiver Feuchtesensoren unter Berücksichtigung einer Feuchteisolation (Sensitivity of printed resistive humidity sensors considering humidity isolation)", Project Study, January 2022.

B.6 Laboratory Classes

[1] Supervision of Lab Class Microtechnology, "Fabrication of a Surface Acoustic Wave Filter (SAW Filter), Including Thermal Evaporation and Lithography Within a Clean Room", 2019–2021.

[2] Supervision of Lab Class Nanotechnology, "Fabrication and Characterization of a Dielectric Mirror out of Porous Silicon Using Anodic Etching with Hydrofluoric Acid (HF) Within a Clean Room", 2019–2022.

[3] S. Marxen, "Entwicklung Eines Sinterprozesses für Gedruckte Cu-Nanopartikel (Delevopment of a Sinter Process for Printed Cu-Nanoparticles)," Laboratory Class, July 2020.

Sommaire récapitulatif en français: 'Mémoire, Batterie et Capteurs Imprimés pour Systèmes Autonomes'

Motivation

Au cours des dernières décennies, la numérisation a profondément transformé notre société à de nombreux niveaux. Avec l'émergence et la découverte d'Internet, les objets physiques connectés permettent la prochaine étape de ce développement - la réalisation de l'Internet des objets (IoT). Un modèle architectural le décrit comme un réseau faiblement couplé composé d'objets intelligents décentralisés. Il s'agit d'objets physiques ou numériques autonomes dotés de capacités de détection, de traitement et de réseau (voir [7]).

L'IdO est déjà présent dans de nombreux domaines de notre vie quotidienne, de la maison intelligente aux applications telles que la logistique et les soins de santé, où l'IdO peut contribuer à améliorer la qualité de notre vie. Les éléments cruciaux pour son développement futur sont la détection, la communication et le modélisation (voir [8]). Sur ce marché en pleine croissance, il est essentiel d'adopter des nouvelles approches innovantes pour répondre à l'évolution des besoins mondiaux. L'approche traditionnelle "plus rapide, plus petite et plus complexe" ne permet pas de répondre aux questions concernant les conceptions personnalisées et les processus de fabrication rapides, décentralisés et moins sophistiqués.

L'électronique imprimée s'est avérée être un candidat sérieux pour répondre à ces demandes. Notre approche comprend des batteries et des capteurs sérigraphiés ainsi que des cellules de mémoire qui peuvent être entièrement imprimées par jet d'encre (voir [25]). Dans ce cas, les avantages de la fabrication additive incluent l'utilisation de conceptions numériques, de faibles coûts et la possibilité d'une production décentralisée. En effet, les étapes de lithographie, coûteuses et gourmandes en matériaux, peuvent être éliminées et les processus ne nécessitent plus un environnement de salle blanche.

En outre, l'extension des substrats et donc des applications possibles constitue un avantage considérable. Contrairement aux plaquettes de semi-conducteurs, les circuits et les dispositifs peuvent être imprimés pratiquement sur toutes les surfaces (papier, tissu, feuille). Cela élargit le choix des matériaux possibles, car ils n'ont plus besoin d'être compatibles avec la technologie CMOS. Mais le principal avantage est que les structures minces (sub-µm à µm) conservent les propriétés flexibles de substrats comme le PET (polyéthylène téréphtalate), le PEN (polyéthylène naphtalate) ou le polyimide (nom de marque : Kapton). L'ensemble du secteur de l'électronique flexible repose

sur ces avantages et, par conséquent, nos recherches sur les fonctionnalités et les mécanismes des dispositifs imprimés facilitent les perspectives de ce domaine et ouvrent de nouvelles voies pour les applications.

Pour un maillage étendu des composants IoT, l'indépendance vis-à-vis du réseau électrique est essentielle. Les systèmes sensoriels autonomes se caractérisent par le fait qu'ils obtiennent l'énergie nécessaire à leur fonctionnement à partir de l'environnement ou qu'ils sont alimentés par une batterie pendant une période limitée. Dans le cadre de cette thèse, la technologie d'impression à faible coût doit être étudiée et utilisée pour imprimer des cellules de mémoire, des batteries et des capteurs sur des substrats flexibles dans le but de les combiner pour former un système autonome de contrôle de la température, de l'humidité ou de la contrainte pour le secteur de la logistique intelligente. Il s'agit de l'utilisation de réseaux de systèmes numérisés aux nœuds pour la production des réseaux, tels que les lieux de stockage et les points de manutention. Ici, des informations sont collectées via des capteurs, grâce auxquels un autocontrôle partiel ou complet peut être créé via des règles et des algorithmes. Les processus peuvent ainsi être ajustés dynamiquement ou les stocks peuvent être surveillés en permanence [28].

Jusqu'à présent, les processus classiques de salle blanche et les techniques sous vide ont été principalement utilisés pour fabriquer les cellules de stockage de données. Tant l'environnement de laboratoire que les équipements utilisés entraînent une augmentation des coûts de fabrication et de la consommation d'énergie. Pour l'intégration de puces à l'échelle nanométrique, ces processus sont inévitables en raison de la pureté et de la taille de la structure réalisables. Cependant, il existe des applications qui ne présentent pas ces exigences élevées. Un domaine relativement nouveau de la fabrication électronique est l'électronique flexible imprimée [9]. L'objectif ici est d'imprimer des circuits complets dans des processus de rouleau à rouleau, idéalement avec une utilisation nulle ou minimale de puces. Les principales techniques d'impression présentées dans ce travail sont la sérigraphie et l'impression à jet d'encre et sont choisies pour l'application respective. La sérigraphie offre une impression à grande échelle avec des épaisseurs de couche de 5 à 100 µm, idéale pour les batteries imprimées, tandis que la seconde offre une taille de caractéristique plus petite et des couches minces de 0,1 à 1 µm, permettant des couches minces pour les composants flexibles. En plus de scalabilité, l'accent est mis sur une production rapide et flexible avec des matériaux peu coûteux et donc de faibles coûts de fabrication. Ceci est rendu possible par des matériaux de substrat industriellement établis tels que le PET, le PEN ou le Kapton. Les exemples d'électronique imprimée sont nombreux. Le recâblage imprimé permet l'intégration de circuits électriques sur des surfaces complexes [12, 9], les panneaux de commande dans l'industrie automobile sont désormais imprimés avec des composants électroniques [50], et des étiquettes intelligentes sont imprimées pour le contrôle de la chaîne du froid dans l'industrie alimentaire [51] ou pour le suivi des patients [52].

Objectifs de la Recherche

L'objectif de ce projet de doctorat sera d'étudier les mécanismes de commutation des cellules de mémoire à métallisation électrochimique imprimées (ECM) et d'examiner la possibilité de les combiner avec différents composants électroniques imprimés tels que des capteurs ou des batteries. Les différents choix de matériaux offrent les possibilités d'élargir les applications futures. Cependant, les implications de ces matériaux sur le comportement de commutation ou même sur le mécanisme de commutation ne sont pas encore bien comprises. Les nanoparticules (NPs) de Cu imprimées par jet d'encre devraient être utilisées comme électrode active pour les cellules de mémoire ainsi que pour les pistes conductrices en général. Le frittage photonique est la technique pivot pour

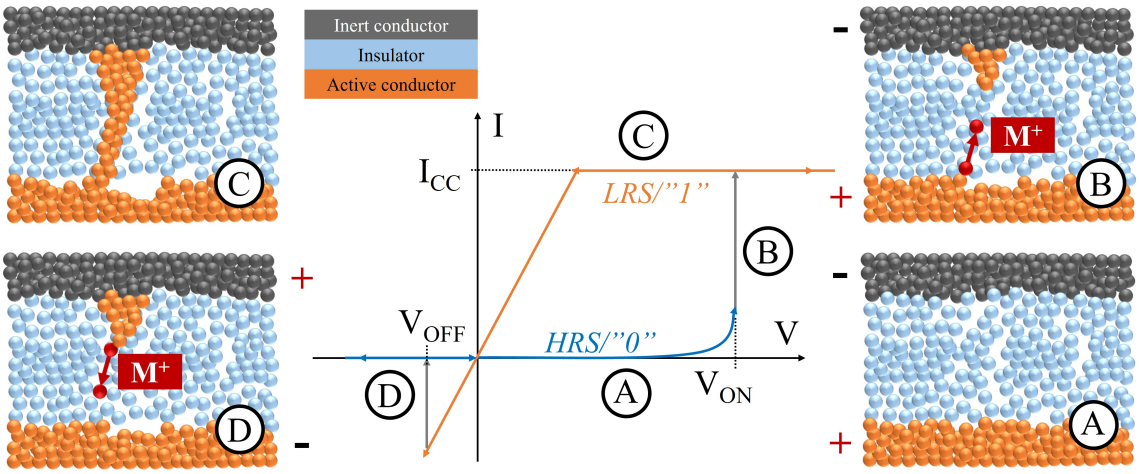

Figure 5.1: Mécanisme de commutation d'un ECM. A) État de haute résistance (HRS) ; B) Les ions migrent vers la contre-électrode (processus SET) ; C) Un filament se forme et l'état de basse résistance (LRS) est établi par le courant de conformité (I_{cc}) ; D) Le filament est dissous pour revenir à l'état HRS sous tension inversée. Adapté de [78].

créer des structures conductrices à partir des NPs initialement oxydées. De nouveaux matériaux seront étudiés pour fonctionner comme matériaux diélectriques ou composants sensoriels qui peuvent idéalement être utilisés pour différents dispositifs. Les candidats sont les matériaux WO3 et CuxS qui peuvent être utilisés pour des applications de capteur ou de mémoire ou les nanotubes de carbone multi-parois qui fournissent une maille conductrice pour surveiller les dommages induits par la déformation. Un autre objectif est de fabriquer une batterie entièrement sérigraphiée qui peut, par exemple, alimenter une cellule de mémoire.

Théorie

Dans ce chapitre, les principes fondamentaux de la technologie des mémoires à accès aléatoire résistives (RRAM), des batteries et des différents capteurs sont expliqués.

Cellules de mémoire résistives

L'idée fondamentale des cellules de mémoire résistive, est que les informations sont stockées sous forme d'états logiques "0" et "1" en état résistif haut (HRS) ou bas (LRS). Les cellules de stockage de données résistives se caractérisent par leur structure simple, dans laquelle deux électrodes sont séparées par un diélectrique. On peut en distinguer deux types [77] : Dans le premier cas, on utilise une modification de la conductivité de l'isolant, par exemple en disposant des lacunes d'oxygène conductrices et des réactions aux électrodes lorsqu'une tension externe est appliquée. Dans le second cas, lorsqu'une tension externe est appliquée, un filament métallique de matériau d'électrode est généré dans l'isolant en raison d'une réaction redox au niveau des électrodes [79]. Lorsque la polarité de la tension externe est inversée, ce filament peut à nouveau être dissous. Le deuxième type est appelé mémoire de métallisation électrochimique (ECM) et sera étudié dans le cadre de cette thèse.

Le mécanisme de commutation est décrit comme la formation (LRS) et la rupture (HRS) d'un filament métallique traversant la couche isolante (s. Fig. 5.1, A–D). Ces états résistifs distincts peuvent être utilisés pour stocker des informations sous la forme d'états logiques : 0 pour le HRS

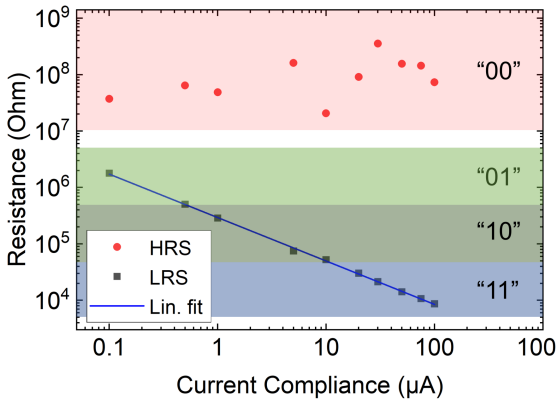

Figure 5.2: Valeurs de résistance pour le HRS et le LRS avec différentes conformations de courant. L'attribution de plusieurs états logiques à la plage accessible permet le stockage de plus d'un bit par cellule de mémoire. Les plages sont d'au moins une décennie dans l'échelle logarithmique, ce qui permet une lecture facile et tolère les variations du dispositif. (Cf. [74])

ou 1 pour le LRS. Le filament est créé en appliquant une polarisation positive V à l'électrode active (AE), généralement constituée d'Ag ou de Cu, tandis que la contre-électrode inerte (CE) est mise à la terre. Cette polarisation oxyde le métal (M) et entraîne la formation d'ions. Un champ électrique local $E = V/d$ est induit comme dans un condensateur par V sur la couche isolante d'épaisseur d. Les ions sont accélérés le long du champ électrique E vers la CE, où ils sont à nouveau réduits. Pendant la croissance du filament de l'EC vers l'AE, E est encore augmenté, en raison de la réduction de la distance de séparation d. On suppose que différents filaments parallèles commencent à se former pendant ce processus. Cependant, la croissance dynamique conduit à un processus auto-accéléré et aboutit à un scénario du type "le gagnant prend tout". La plus petite fente subit le champ électrique le plus élevé et donc la croissance la plus rapide jusqu'à ce que le processus SET s'arrête, car elle ponte la couche isolante et le champ électrique s'effondre.

Pendant cette opération, l'état de marche peut être réglé par la conformité du courant. Le diamètre du filament créé peut être contrôlé en limitant le courant autorisé comme $R(LRS) \propto 1/I$. C'est une condition préalable au processus RESET, où le filament se dissout partiellement. Cette formation contrôlable permet le stockage de plus de deux états logiques par cellule. La division de la plage OFF/ON en quatre états distincts, à savoir l'état OFF et trois états ON différents, permet un stockage multi-bits ("00", "01", "10", "11") qui augmente la densité de stockage potentielle [74]. Les données de la figure 5.2 illustrent cela de manière plus graphique. Dans le HRS, pour des valeurs supérieures à $10^7\,\Omega$, l'état logique "00" est attribué. En choisissant une conformité du courant inférieure à 0,5 µA, le LRS se situe dans la plage comprise entre $5 \cdot 10^5\,\Omega$ – $5 \cdot 10^6\,\Omega$, c'est-à-dire l'état logique "10". La modification de I_{cc} conduit à un LRS différent et donc aux autres états logiques. Une décade de résistance par état facilite la lecture et permet une certaine variation du comportement de commutation. La lecture elle-même se fait avec une tension bien inférieure au seuil de commutation pour préserver l'état. Le mûrissement d'Ostwald et l'auto-diffusion peuvent conduire à la rupture spontanée des filaments, ce qui limite potentiellement le temps de rétention de l'état non-volatile [85].

Batterie

Une batterie est une cellule électrochimique constituée d'une électrode positive et d'une électrode négative séparées par un électrolyte qui peut conduire les ions entre les électrodes mais agit comme un isolant électrique [53]. Notre approche consiste à utiliser une batterie zinc-carbone, où la masse

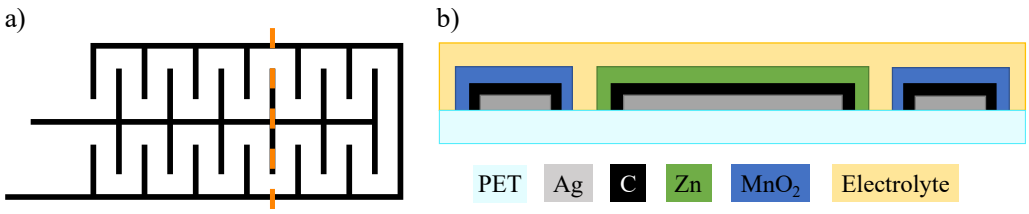

Figure 5.3: a) Disposition planaire de la batterie sérigraphiée ; b) Coupe transversale de la batterie le long de la ligne pointillée en a) ; le collecteur de courant (Ag) est protégé par une pâte conductrice (C) pour l'empêcher de réagir avec les électrodes électrochimiques (Zn, MnO_2) qui sont reliées par un électrolyte.

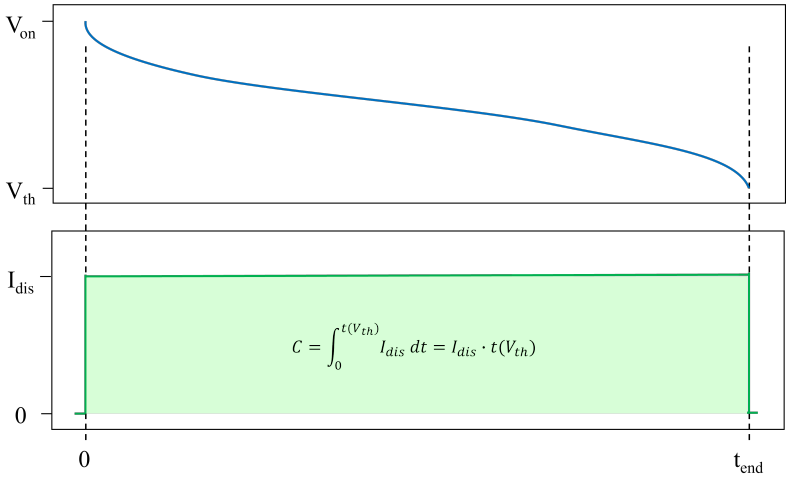

Figure 5.4: Courbe schématique de décharge galvanostatique d'une batterie. La courbe supérieure montre la diminution de la tension au cours du temps avec un courant de décharge constant I_{dis}. La mesure s'arrête à la tension de seuil V_{th} et la capacité est calculée par la formule donnée.

positive est constituée de MnO2 et la masse négative de Zn.

La disposition de la batterie sérigraphiée est illustrée à la Figure 5.3 a). Elle est conçue de manière planaire afin de faciliter la procédure d'impression et d'obtenir des batteries plus fines, ce qui est bénéfique pour les propriétés de flexion. De plus, aucun séparateur n'est nécessaire pour minimiser l'influence des problèmes de court-circuit causés par la croissance des dendrites [59] avec des distances d'électrodes à l'échelle millimétrique. Elle optimise également la dynamique du transport des ions dans la direction bidimensionnelle, même sous contrainte de flexion [60]. L'inconvénient de cette approche est que la zone active est limitée par rapport à une configuration empilée. Pour surmonter ce problème, la conception planaire contient plusieurs doigts pour maximiser la zone où les matériaux actifs se font face. Le nombre de ces doigts peut être augmenté pour obtenir une plus grande capacité. La Figure 5.3 b) montre la coupe transversale d'une pile le long de la ligne orange en pointillés en a).

La cellule fournit une tension initiale en circuit ouvert VOC d'environ 1,35 V (voir [57]). Cette valeur est prise aux bornes lorsqu'aucun courant externe ne circule. La réaction à l'anode (-) a généralement lieu à des potentiels d'électrode plus faibles qu'à la cathode (+). Pour la décharge dans une batterie Zn-MnO_2, le Zn joue le rôle d'anode, où la réaction chimique d'oxydation libère des électrons ; le MnO_2 est la cathode, où les réactions de réduction gagnent des électrons du circuit [56].

La valeur de la capacité C'est la plus pertinente pour concevoir la taille et la géométrie de la batterie afin de garantir un courant suffisant. Idéalement, elle est obtenue à partir d'une batterie

neuve, conditionnée et soumise à une décharge à courant constant à température ambiante. La tension qui diminue progressivement au cours de ce processus est mesurée et une tension de seuil V_{th} est définie où la batterie est considérée comme vide (Fig. 5.4). Lorsque Vth est atteinte, C'est calculé pour un courant de décharge constant I_{dis} comme suit

$$C = \int_0^{t(V_{th})} I_{dis} dt \overset{I=const.}{=} I_{dis} \cdot t(V_{th}). \tag{5.1}$$

Capteurs

Les capteurs sont utilisés pour détecter et accéder à un changement physique dans un système. Voici quelques exemples de catégories de capteurs : environnementaux (température, humidité relative, gaz), physiques (déformation, vibration, magnétique), de contrôle (fuites, débit, position). Le changement est mesuré par la modification d'une propriété électrique telle que la tension, la résistance ou l'impédance. Pour surveiller l'état d'un système autonome, les exemples les plus pertinents de capteurs sont la contrainte, la température et l'humidité. En général, un capteur doit être choisi en fonction de l'ensemble de la configuration. Une faible résistance initiale est bénéfique pour les applications dont la consommation d'énergie est minimale. En même temps, elle facilite la lecture si la résistance est plus élevée. Une sensibilité relative de 1 % se traduit par une variation absolue plus importante pour une valeur initiale plus grande.

Expérimentation

Ce chapitre présente les résultats et la discussion des composants électroniques imprimés individuels ainsi que les premières étapes vers leur intégration.

Batterie

La batterie Zn/MnO_2 sérigraphiée sera caractérisée par profilométrie et pulvérisation par faisceau ionique focalisé (FIB) - microscopie électronique à balayage (SEM) pour les dimensions géométriques et les propriétés structurelles. Ensuite, la capacité de la batterie activée est présentée.

Pour l'examen microscopique, une batterie imprimée complète sans électrolyte est étudiée par FIB-SEM. La Figure 5.5 montre les surfaces de l'électrode de MnO_2 (a) et de l'électrode de Zn (b), respectivement. L'électrode de MnO2 possède une structure microcristalline poreuse, tandis que l'électrode de Zn présente des caractéristiques sphériques qui sont couvertes par un matériau continu. En c), la section transversale de la zone en b) est pulvérisée et polie par FIB pour exposer les différentes couches. En bas, le collecteur de courant en Ag à base de paillettes d'une épaisseur de 3 µm est suivi de 6 µm de carbone conducteur. La partie principale de la section transversale est l'électrode de Zn de 17 µm d'épaisseur, constituée de particules de Zn allant de 1,0 à 6,8 µm noyées dans du carbone conducteur. La limite entre la couche de carbone protectrice et l'électrode de Zn peut être déterminée à partir de la structure granulaire du fond jusqu'à la structure plus lisse avec de grands pores. En d), la zone centrale de la couche d'Ag en c) est agrandie pour montrer la structure microscopique et le substrat dense et lisse. Ces images SEM montrent clairement que les électrodes actives sont soit très poreuses (MnO_2), soit principalement remplies de carbone conducteur (Zn).

Les paramètres clés pour la caractérisation des batteries sont la capacité C, car elle détermine les objectifs et les domaines d'application. Pour la détermination de C, un programme Labview communique avec le SMU Keithley pour une décharge galvanostatique de la batterie. Pour la

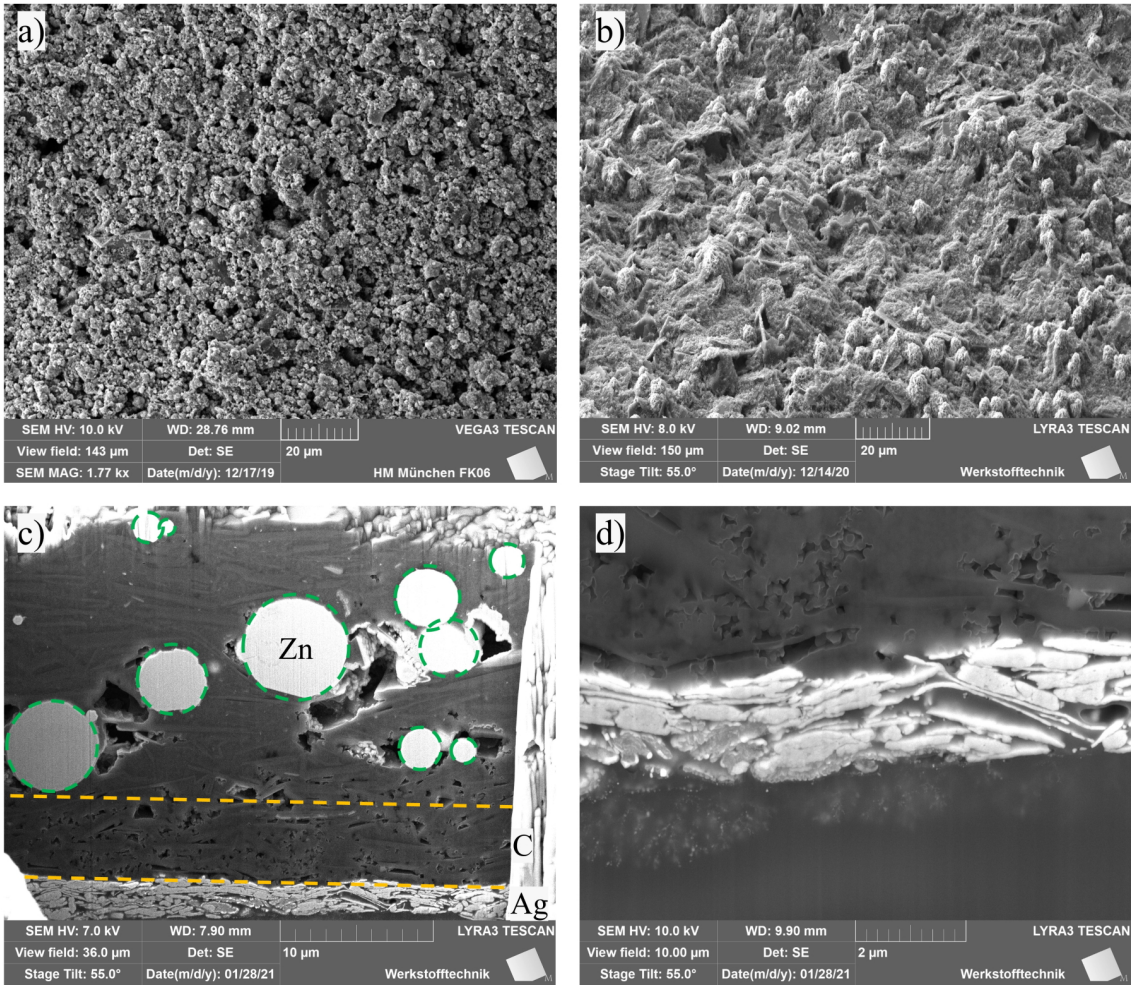

Figure 5.5: Images par microscopie électronique à balayage (MEB) de a) la surface de l'électrode de MnO_2, b) l'électrode de Zn, c) la section transversale découverte par pulvérisation in situ par faisceau d'ions focalisé (FIB), avec la couche d'Ag en paillettes (3 µm), le carbone conducteur (6 µm) et les particules de Zn (cercles pointillés verts) de 1,0–6,8 µm noyées dans le carbone conducteur (17 µm). En d), la zone centrale de la couche d'Ag est agrandie.

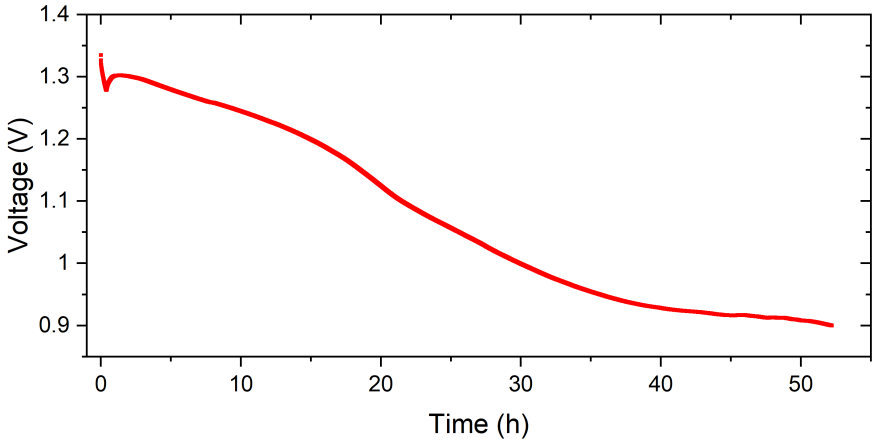

Figure 5.6: Courbe de décharge sous un courant constant de 200 µA sur une durée de 52,2 h. La capacité et l'énergie sont calculées à 10,4 mAh et 40,4 J, respectivement.

mesure de la capacité, la batterie activée est scellée dans une pochette en polyéthylène (PE) pour maintenir l'humidité dans l'électrolyte aqueux. La Figure 5.6 montre une courbe de décharge sous un courant constant de 200 µA sur une durée de 52,2 h jusqu'à atteindre $V_{th} = 0,90$ V. Cela donne une capacité de 10,4 mAh et une énergie de 40,4 J pour l'intégration de la tension sur cette période.

L'information isolée sur la capacité n'est pas adaptée à la comparaison des performances des batteries. Pour ce faire, la capacité gravimétrique est calculée en rapportant C au poids des couches imprimées de la batterie. Pour décrire les couches individuelles de la pile, on imprime des feuilles individuelles avec les matériaux respectifs. Chaque couche est imprimée sur des substrats PET propres et prérétrécis, puis séchée. Cette approche permet de peser les matériaux individuels et de sonder la hauteur moyenne par profilométrie. À partir de ces mesures, la capacité gravimétrique est calculée à environ 130 mAh/g. 130 mAh/g, ce qui se situe dans la partie inférieure des dispositifs comparables mais fabriqués traditionnellement à base de Zn/Mn (100–410 mAh/g [61]). Ce résultat est remarquable car aucun effort n'a encore été fait pour réduire le poids de la batterie, ce qui augmenterait encore la capacité gravimétrique.

Dans le cadre de la thèse, il est démontré plus en détail que la batterie sérigraphiée Zn/MnO_2 n'est pas adaptée à une utilisation pour des applications rechargeables.

Capteurs

Dans les sections suivantes, les performances et les potentiels des capteurs de contrainte, d'humidité et de température seront examinés.

Déformation

Le capteur de déformation entièrement imprimé par jet d'encre est constitué de nanotubes de carbone multi-parois (MWCNT) intégrés dans du polydiméthylsiloxane (PDMS). La figure XXX montre le processus d'impression en deux étapes sur le polyimide : d'abord, l'encre MWCNT+PDMS est imprimée en forme de méandre du capteur ; ensuite, l'agent de durcissement (CA) est imprimé pour couvrir toute la surface afin de réticuler le PDMS pour la stabilité et l'adhésion. Les MWCNT individuels possèdent un diamètre extérieur de 6–9 nm et des longueurs d'environ 5 µm et la première encre contient 25 % en poids de MWCNT en suspension dans le PDMS. Des couches multiples sont obtenues en répétant le processus d'impression pour atteindre une résistance dans la

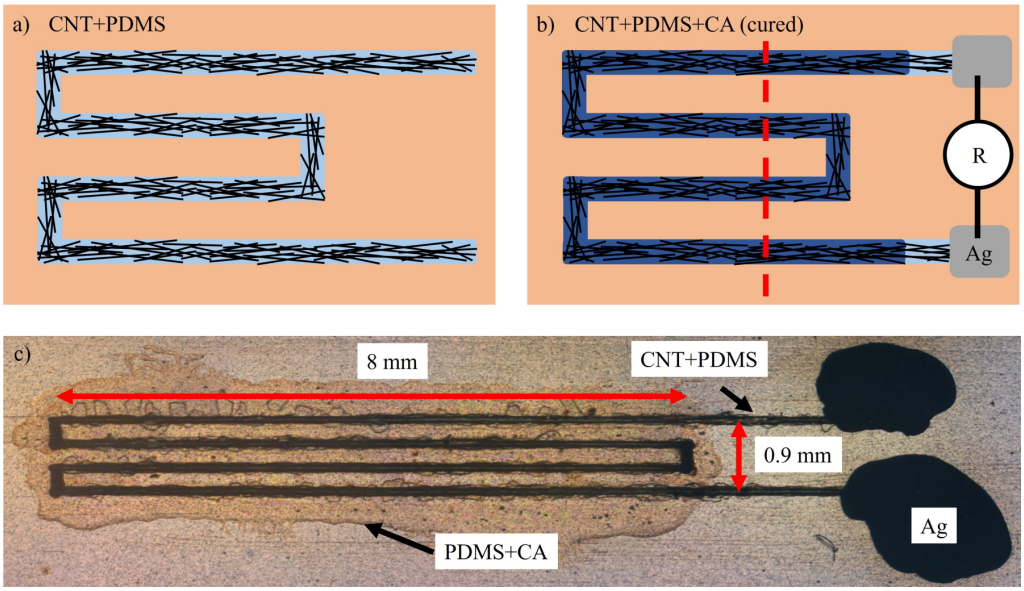

Figure 5.7: Le processus d'impression sur le substrat polyimide comprend a) l'application de la structure CNT/PDMS et après le séchage (100 °C, 10 minutes) suit b) l'impression de l'agent de durcissement (CA) et l'étape de durcissement (250 °C, 30 minutes) et la pâte d'Ag pour le contact. La résistance est mesurée entre les deux contacts pour la caractérisation et la ligne rouge en pointillés indique l'axe de flexion. c) Image prise au microscope optique de la structure finale. ©[110]

rage désirée de 100 kΩ à 10 MΩ. Après une impression réussie de la première étape avec plusieurs couches, la structure est chauffée sur une plaque chauffante à 100 °C pendant 10 minutes pour se débarrasser des solvants résiduels. À ce stade, une pâte d'Ag conductrice est appliquée manuellement aux deux extrémités du capteur pour mesurer la résistance et confirmer la conductivité électrique du réseau de CNT.

Pour la caractérisation du régime de compression, ainsi que du régime de tension, l'échantillon est plié pas à pas jusqu'à une déformation maximale de $\epsilon = \pm 1,0\,\%$ et remis dans sa position initiale. Cette opération est répétée plusieurs fois pour le même régime de déformation avant de passer au côté opposé. Sur la Figure 5.8 a), la déformation en tension présente une réponse quasi-linéaire avec une hystérésis disparaissant après le troisième cycle. Cela démontre que ce capteur peut être utilisé sans problème pour mesurer la déformation en traction après quelques cycles de flexion initiaux. Les changements relatifs de la figure XX c) sont calculés par rapport à la résistance initiale de la première mesure pour R0 et pour chaque courbe individuelle pour la valeur initiale correspondante de R_0 pour R_1 et R_2. Il apparaît qu'une certaine relaxation se produit après chaque mesure car la résistance finale $R_{1,2}$ est toujours plus grande que la résistance initiale de la mesure suivante R_0. Pour la Figure 5.8 b), les cycles de flexion compressive suivants présentent une tendance similaire pour un effet d'hystérésis qui s'estompe, visible comme le déclin de la variation relative de R_2 dans la Figure 5.8 c). Cependant, la hausse caractéristique à un certain niveau de déformation est toujours présente, décalant seulement son début de $\epsilon \approx -0,3\,\%$ pour le premier passage, à $\epsilon \approx -0,6\,\%$ pour le quatrième passage. Par la présente, nous pouvons conclure que ce comportement général n'est pas causé par une flexion de traction antérieure mais qu'il s'agit d'une propriété intrinsèque de l'échantillon CNT/PDMS.

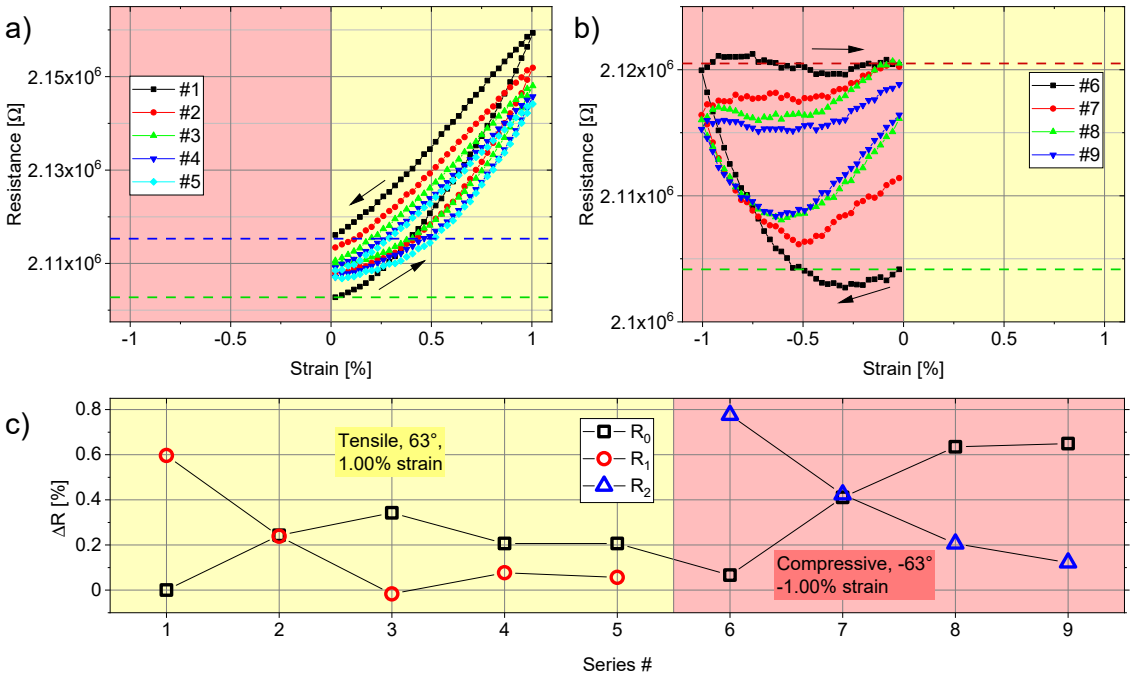

Figure 5.8: Comportement piézorésistif du capteur durci pour une déformation de tension répétée (a), une déformation de compression (b) et la variation relative (c) de la résistance après déformation de tension et de compression (R_1 et R_2) par rapport à la résistance initiale de chaque mesure R_0. Les flèches en a) et b) indiquent la direction de la variation et les lignes pointillées correspondent aux valeurs utilisées en c).

Humidié

Le capteur d'humidité imprimé par jet d'encre est constitué de transducteurs interdigités en cuivre (IDT) recouverts de WO_3-NPs. Le frittage photonique des structures en cuivre imprimées par jet d'encre a été étudié au préalable. Le résultat de l'impression est d'abord caractérisé géométriquement par profilométrie et microscopie confocale. La Figure 5.9 présente les étapes de fabrication des structures en Cu en général, et des IDTs en Cu recouverts de NPs WO_3 pour un capteur d'humidité en particulier.

Les IDTs présentent une structure bien définie avec des largeurs de doigts de 450–520 µm, laissant des espaces de 300–230 µm entre eux. Après l'application de WO_3 (b), d)), la zone couverte devient plus diffuse, indiquant qu'elle couvre toutes les zones et lissant partiellement la surface. L'épaisseur de la couche de WO3 sensible à l'humidité pour le capteur est calculée à partir des mesures de microscopie confocale pour être égale à 120 nm pour un volume appliqué de 0,468 µL sur une surface de $(6{,}5\times5{,}3)\,\mathrm{mm}^2$.

La réponse à l'humidité est étudiée dans une chambre climatique afin de distinguer les influences de la température et de l'humidité. La Figure 5.10 a) montre l'évolution de la résistance du capteur avec différents paliers d'humidité dans la chambre climatique à 30 °C. La plage d'humidité est choisie en fonction de la sensibilité du capteur et l'humidité maximale tient compte de la température du point de rosée Td. Pour 85 % d'humidité à 30 °C, Td est d'environ 27 °C, la température ne doit donc pas descendre en dessous pour éviter la condensation. Pour la gamme 50–85 %rh, la résistance du capteur s'étend entre $R = 2 \cdot 10^7 - 5 \cdot 10^9\,\Omega$. La résistance présente une diminution (augmentation) exponentielle avec l'humidité croissante (décroissante). Il apparaît également que l'humidité contrôlée varie jusqu'à ±5 %, ce qui peut être observé pour RH(Actual) = 80 % et ce bruit se traduit directement par des variations de R également. Un autre développement

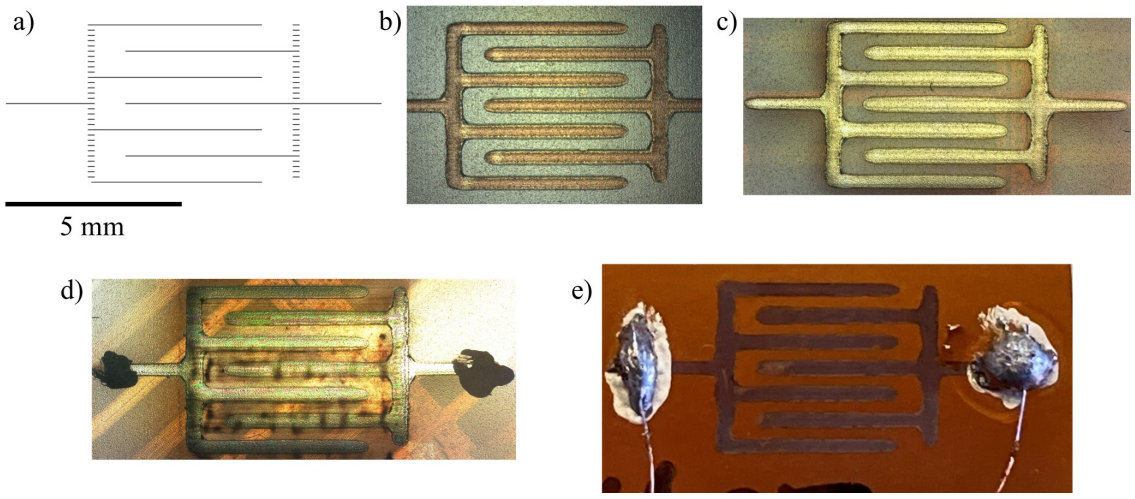

Figure 5.9: a) Mise en page numérique pour l'impression par jet d'encre d'un IDT en Cu sur Kapton d'une surface effective de $(6.0\times4.5)\,\mathrm{mm}^2$ et de lignes supplémentaires pour le contact. Images microscopiques de b) l'IDT en Cu séché après impression, c) la structure après frittage photonique, et d) après application de la couche de WO_3 sensible à l'humidité et de la pâte d'Ag pour faciliter le contact. e) Image optique de la structure finale avec fils de cuivre soudés pour les mesures dans la chambre climatique. La barre d'échelle s'applique à toutes les images.

systématique est la montée lente mais régulière de R pour la plupart des plateaux d'humidité qui ne peut pas être expliquée par les déviations oscillatoires mentionnées ci-dessus. Cette augmentation est indépendante de la direction précédente du changement d'humidité et pourrait suggérer que l'humidité se désorbe lentement du matériau du capteur au fil du temps. Une autre explication pourrait être trouvée dans l'absorption et le gonflement du substrat de polyimide et donc le changement de la configuration géométrique et des distances entre les doigts de l'IDT. Cependant, cela est peu probable car l'augmentation de R se produit pour une augmentation à long terme, ainsi que pour une diminution de l'humidité. La Figure 5.10 b) donne la relation $R(RH)$, où l'échelle de couleur indique l'évolution dans le temps. Les points de données uniques situés entre les plateaux d'humidité relative tracent la réponse du capteur. Les points de données qui se chevauchent sont étalés horizontalement pour les rendre visibles, ainsi les valeurs d'humidité sont présentes au-delà du maximum de 86 %. La visualisation permet de constater que le passage à des niveaux d'humidité plus élevés (50–85 %) se produit plus rapidement, ce qui se voit au nombre réduit de points de données et au fait que R se situe systématiquement sous la tendance. Pour les changements vers des conditions plus sèches (85–50 %), cette tendance est inversée et cela prend plus de temps et présente des valeurs plus grandes pour R. Ce comportement peut être interprété comme une réponse plus rapide aux niveaux d'humidité croissants par rapport aux niveaux décroissants. L'ajustement linéaire dans le tracé semi-logarithmique donne $R(RH) = 1.6\,10^{13}\cdot\exp\left(-0.16\,RH\right)\Omega$, où $k = -0,16\,1/\%$ décrit la sensibilité à l'humidité. Il est également montré que le coefficient observé n'est pas significativement affecté par une augmentation de la température à 60 °C.

Ensuite, le capteur d'humidité imprimé par jet d'encre est scellé dans une feuille composite qui sert de barrière à la vapeur. La barrière est constituée d'un substrat en PET de 12 µm, métallisé avec 9 µm d'Al, et d'une couche supérieure scellable en PE-LD (polyéthylène basse densité) de 40 µm. La Figure 5.11 examine la caractéristique du capteur pour les capteurs ouverts et protégés à 30 °C et 60 °C, respectivement. En a), la réponse résistive à 30 °C du capteur ouvert suit de près l'HR, tandis que le capteur protégé ne répond que pour une $HR > 80\,\%$rh. Par conséquent, toute la plage d'humidité est prise en compte pour l'ajustement du capteur ouvert, tandis que

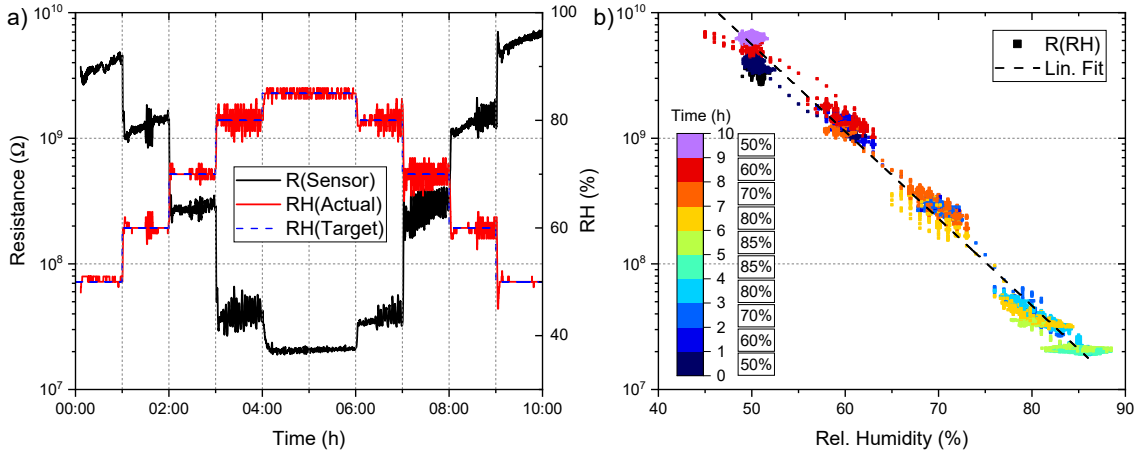

Figure 5.10: Réponse résistive sur une échelle semi-logarithmique pour le capteur d'humidité à base de WO_3 en fonction du temps, ainsi que les valeurs réelles et cibles pour l'HR à 30 °C. L'humidité est balayée par étapes d'au moins une heure entre 50 et 85 %rh. b) Résistance en fonction de l'humidité relative (RH) pour les données de a). L'échelle de couleurs représente l'évolution dans le temps et les différentes valeurs cibles pour l'HR. Les points de données qui se chevauchent sont disposés horizontalement pour les rendre visibles. L'ajustement linéaire donne $R(RH) = 1.6\,10^{13} \cdot \exp(-0.16\,RH)\,\Omega$.

seule $l'HR > 77\,\%\text{rh}$ est considérée pour le capteur protégé. Le coefficient d'humidité résistif k est de $-0.12\,\%\text{rh}^{-1}$ et $-0.08\,\%\text{rh}^{-1}$, respectivement, ce qui montre une sensibilité plus faible pour le capteur protégé. En b), les réponses à 60 °C montrent que les deux capteurs répondent à toute la gamme d'humidité mais avec des valeurs significativement différentes pour $k_{\text{open}} = -0.11\,\%\text{rh}^{-1}$ et $k_{\text{barrier}} = -0.03\,\%\text{rh}^{-1}$, respectivement. De plus, aux deux températures, l'ajustement pour le capteur protégé a une valeur R^2 inférieure à 0,7, alors que le capteur ouvert montre un R^2 ¿ 0,97. Par conséquent, les deux scénarios ne peuvent être comparés que partiellement. La sensibilité plus faible pourrait également être causée par le temps de latence à travers la barrière.

Les origines de la perméation de l'humidité pourraient être des défauts ou des pores dans la couche d'aluminium, des mécanismes de diffusion activés thermiquement, ou une étanchéité imparfaite due à des particules ou aux fils de cuivre intégrés. Une feuille d'aluminium sans trou de quelques microns à une transmission de vapeur d'eau négligeable (voir [233]). Cela s'applique également à la perméation de gaz activée thermiquement à travers les solides, lorsqu'une augmentation de température de 30 °C entraîne un facteur de 10 dans le taux de transmission de la vapeur d'eau (voir [234]). Ainsi, le joint est la raison la plus probable de la déficience de l'isolation contre l'humidité, qui est fabriquée manuellement.

Température

Le composé Cu_xS est utilisé pour le capteur de température ainsi que pour la cellule de mémoire. La transformation localisée de la surface par impression à jet d'encre de $Na_2S_{(aq)}$ et rinçage avec de l'eau DI sur des surfaces Cu est illustrée dans la Figure 5.12. Cette méthode permet une application précise et définie de 50 pl avec différentes concentrations molaires (0,0087, 0,087, 0,44) M. La variabilité d'une structure à l'autre donne l'écart type dans les barres d'erreur de la Figure 5.12 c–e). La microscopie confocale fournit des informations sur l'influence de la concentration molaire de la solution de Na_2S sur la mouillabilité, la rugosité et le volume de la structure transformée. Les résultats de l'analyse des grains pour les mesures exemplaires de la Figure 5.12 a) et b) sont réalisés dans Gwyddion [235]. Ils montrent que la rugosité quadratique moyenne (RMS) augmente

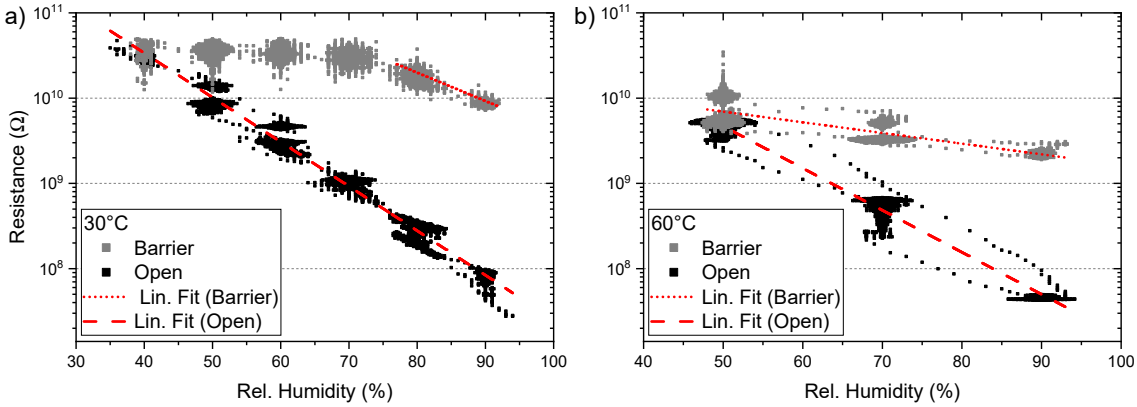

Figure 5.11: Résistance en fonction de l'humidité relative pour un capteur ouvert et à l'intérieur d'un pare-vapeur. a) Les différentes tendances à 30 °C, où le capteur ouvert présente une tendance linéaire tandis que celui protégé par un pare-vapeur ne répond que pour une $HR > 80\,\%$rh. b) À 60 °C, les deux capteurs présentent des tendances continues mais avec des pentes différentes. Les points de données qui se chevauchent sont disposés horizontalement pour les rendre visibles.

avec la molarité et le nombre de couches. On sait, d'après l'interaction entre l'Ag et les solutions de Na_2S, que la vitesse de corrosion augmente de façon logarithmique avec la concentration et de façon linéaire avec la valeur du pH [236]. Comme le Cu présente un comportement électrochimique similaire à celui de l'Ag, on peut considérer que cela explique les tendances observées.

La fabrication d'un capteur de température entièrement imprimé par jet d'encre commence par l'impression et le frittage d'une ligne de NP de Cu de 10 mm. Ensuite, des zones de 1 mm sont recouvertes par impression à jet d'encre avec du Na2Saq (0,087 M) et rincées avec de l'eau DI. La structure finale Cu/Cu_xS entièrement imprimée sur polyimide utilisée pour caractériser la réponse à la température est présentée sur la Figure 5.13 a). La ligne de Cu imprimée par jet d'encre et frittée de 10 mm de long est partiellement convertie en Cu_xS au centre et la pâte d'Ag conductrice facilite le contact. La Figure 5.13 b) montre une réponse résistive négative claire à l'augmentation des températures après la sulfuration. Un ajustement bêta exponentiel donne $\beta_{25,80} = (659 \pm 2)\,\mathrm{K}$. Les indices '25,80', indiquent la plage de température 25–80 °C et R_0 et T_0 pris à 25 °C selon le modèle bêta. Bien que ces valeurs soient inférieures à celles des applications commerciales (1500–2000 K) [33], elles démontrent clairement la réponse semi-conductrice et le potentiel d'utilisation des capteurs.

Les cellules de mémoire et leur intégration

Deux configurations différentes pour les cellules de mémoire ECM seront discutées, où toutes deux visent à réduire le nombre d'encres nécessaires à l'intégration de différents composants électroniques imprimés. Le premier consiste en une conception symétrique de Ag/Spin-on-Glass/Ag et tire profit de l'électrode Ag sérigraphiée qui peut non seulement être utilisée comme collecteur de courant pour la batterie mais aussi comme électrode active pour la cellule ECM. Le second explore les possibilités d'utilisation des composants émergents à base de Cu dans l'électronique imprimée pour une cellule $Cu/Cu_xS/W$. Pour une détermination précise de la caractéristique de commutation des cellules ECM, la tension est balayée de manière quasi statique par rapport à l'électrode supérieure mise à la terre, de 0 V, à V_{max} positif, à V_{min} négatif, en revenant à 0 V pendant que le courant est mesuré.

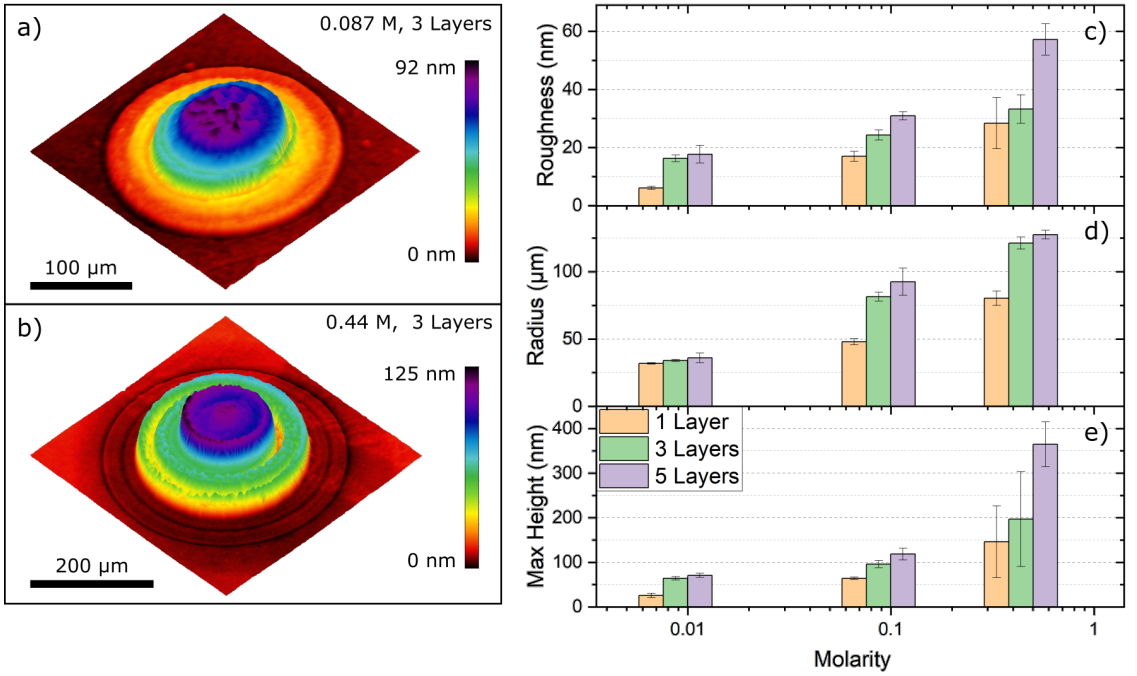

Figure 5.12: a), b) Exemples d'images d'interférométrie par déplacement de phase des structures Cu_xS fabriquées sur une plaquette recouverte de Cu. c), d), e) Analyse quantitative des structures de différentes molarités et couches pour la rugosité, le rayon et la hauteur maximale des structures, respectivement.

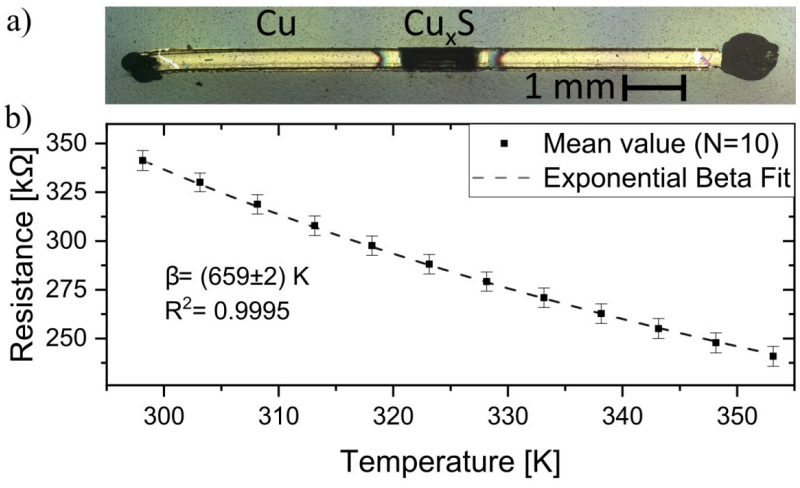

Figure 5.13: a) Image optique d'un capteur thermique basé sur une ligne de Cu de 10 mm de long imprimée par jet d'encre et frittée. La structure Cu_xS transformée est visible comme la structure sombre au centre de la ligne. Une pâte d'Ag conductrice est appliquée sur les bords de la ligne pour faciliter le contact. b) Comportement thermorésistif d'un capteur Cu_xS. Un ajustement bêta exponentiel donne $\beta_{25,80} = (659 \pm 2)$ K. Les indices '25,80', indiquent la plage de température 25–80°C et R_0 et t_0 pris à 25°C.

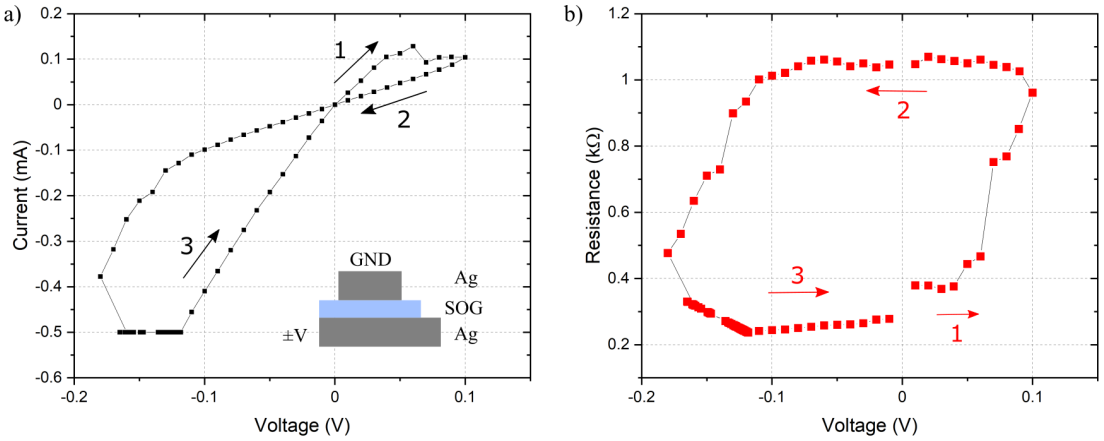

Figure 5.14: Courant (a) et résistance (b) caractéristique d'une cellule Ag/SOG/Ag avec un courant d'écriture de 0,5 mA. Les flèches numérotées indiquent la direction du balayage. Ici, en partant d'une faible résistance, on passe à un état de haute résistance à env. 0,1 V. Pour la polarité opposée, le passage à l'état de faible résistance se produit à environ -0,15 V. L'encart supérieur montre la configuration et la polarité de la cellule.

Ag/SoG

Une courbe de commutation typique est illustrée à la Figure 5.14. En partant de l'état ON à faible résistivité, le processus RESET est clairement visible comme le saut de courant à env. 0.1 V. Le système reste à l'état OFF jusqu'à ce qu'il passe à l'état ON à environ -0,15 V où il passe en mode de conformité à $I_{cc} = -0,5\,\text{mA}$. La pente de la courbe $I - V$ est indiquée dans l'encart comme la résistance R.

Dans l'étape suivante, la combinaison des deux composants imprimés est étudiée (s. Fig. 5.15). Dans un premier temps, une mesure de rétention initiale est effectuée sur 2 minutes avec un intervalle d'échantillonnage rapide de 1 s à 0,1 V afin de déterminer la résistance d'origine et d'exclure que la mesure elle-même puisse induire un événement de commutation. On obtient ainsi une résistance constante et élevée de $R_{OFF} \approx 3.0 - 3.2\,\text{k}\Omega$. Ensuite, la cellule est brièvement (<1 s) connectée à la batterie avec une tension en circuit ouvert (OC) de $V_{OC} = 1,4\,\text{V}$ avant de poursuivre immédiatement la mesure de rétention. La résistance chute à environ 50 Ω et commence à augmenter progressivement au cours des heures suivantes. Une résistance aussi faible est une indication de la formation d'un filament métallique à travers la couche SoG poreuse et isolante de l'ECM. L'augmentation rampante de la résistance au fil du temps peut s'expliquer par un filament qui se dissout lentement, où la diffusion d'ad-atomes assistée par la température entraîne une maturation d'Ostwald [64, p. 698].

En définissant deux régions clairement distinctes représentant respectivement l'état logique OFF ($R_{OFF} > 1,0\,\text{k}\Omega$) et ON ($R_{ON} < 200\,\Omega$), nous obtenons un temps de rétention tON d'environ 2,5 h. Après le retour à l'état OFF, cette procédure peut être répétée en connectant la cellule à la batterie. La commutation se produit également pour l'application de la tension avec une polarité inversée à l'ECM, ce qui donne des résultats similaires.

Cu/Cu$_x$S

Le cuivre, en tant que matériau de base pour un ECM à base de Cu/Cu$_x$S, est évaporé thermiquement sur une tranche de Si et structuré par lithographie pour observer la transformation du Cu en Cu$_x$S dans une zone définie et fournir une fine couche de séparation de 150 nm pour le contact.

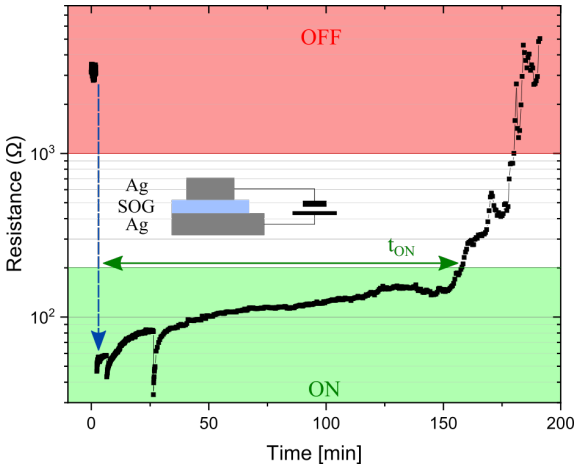

Figure 5.15: Mesure de rétention ($V_{read} = 0,1\,\mathrm{V}$) avant et après avoir connecté la cellule à la batterie. La mesure initiale sur 2 minutes montre une résistance élevée d'environ $R_{OFF} = 3\,\mathrm{k\Omega}$. Après la connexion de la pile sérigraphiée (<1 s) à l'ECM, la résistance chute à environ 50 Ω. En définissant des régions de R représentant les états logiques OFF ($R_{OFF} > 1,0\,\mathrm{k\Omega}$) et ON ($R_{ON} < 200\,\Omega$), une rétention de l'état ON t_{ON} >2.5 h est observée. L'augmentation progressive de la résistance au fil du temps est une indication de la dissolution d'un filament, par exemple causée par le mûrissement d'Ostwald.

La microscopie électronique à balayage (MEB) examine la section transversale de l'échantillon $Si/SiO_2(100\,nm)/Cu(250\,nm)/Photoresist/Cu_xS$. Les détails et la discussion sont élaborés au sein de la thèse.

Les courbes typiques de commutation résistive sont présentées à la Figure 5.16. Elles montrent les mesures tension-courant des cellules $Cu/Cu_xS/W$ et $Cu/Cu_xS/C$, respectivement, pour différents courants de conformité. Dans la Figure 5.16 a) I_{cc} est réglé sur 50 µA et 250 µA pour démontrer la contrôlabilité de la force du filament. En outre, elle affiche une mesure à 80 °C pour $I_{cc} = 250\,\mu\mathrm{A}$ afin de valider la fonctionnalité à des températures élevées. Une forte augmentation du courant se produit à une tension d'environ 0,2–0,3 kV. Cela équivaut au processus de SET de OFF à ON, c'est-à-dire à un changement de résistance de $> 10^7\,\Omega$ à 1,5 kΩ et 600 Ω, pour $I_{cc} = 50\,\mu\mathrm{A}$ et $I_{cc} = 250\,\mu\mathrm{A}$, respectivement. Le RESET se produit à environ -0,1 V, où l'état revient à l'état OFF précédent. Le SET se produit à environ 0,1–0,25 V et le RESET à environ -0,05 V. Alors que l'état ON présente des valeurs résistives similaires de 1,2 kΩ et 350 Ω, pour $I_{cc} = 50\,\mu\mathrm{A}$ et $I_{cc} = 200\,\mu\mathrm{A}$, respectivement, l'état OFF est considérablement réduit à $10^5 - -10^6\,\Omega$. La démonstration de courbes de commutation comparables dans b) où l'électrode inerte est un ruban de carbone conducteur est essentielle pour atteindre l'objectif d'une électrode supérieure laminée. Le courant de réinitialisation pour les deux configurations est plus petit que l'ICC, indiquant une dissolution électrochimique plutôt que thermique du filament [77]. En outre, les différences dans la dynamique de RESET sont principalement indépendantes de la température, de la conformité du courant, ainsi que de la résistance ON [239]. Ainsi, les variations dans les caractéristiques de commutation telles que les différentes valeurs pour la résistance ON reflètent la variabilité de la configuration plutôt que l'électrode inerte.

Un schéma conceptuel permettant d'intégrer différents composants imprimés est présenté à la Figure 5.17 a). L'anode de la batterie imprimée est connectée à l'électrode active de la cellule ECM, qui est ensuite connectée en série avec la résistance dépendant de la température. Dans l'état initial, le circuit est ouvert, et l'ECM est dans l'état OFF à haute résistance, avec $R(OFF) \gg R(Sens)$. Lorsque l'interrupteur est fermé, l'ECM passe à l'état ON à faible résistivité, qui est du même ordre de grandeur que le capteur. Précédemment, nous avons démontré que la batterie fournit

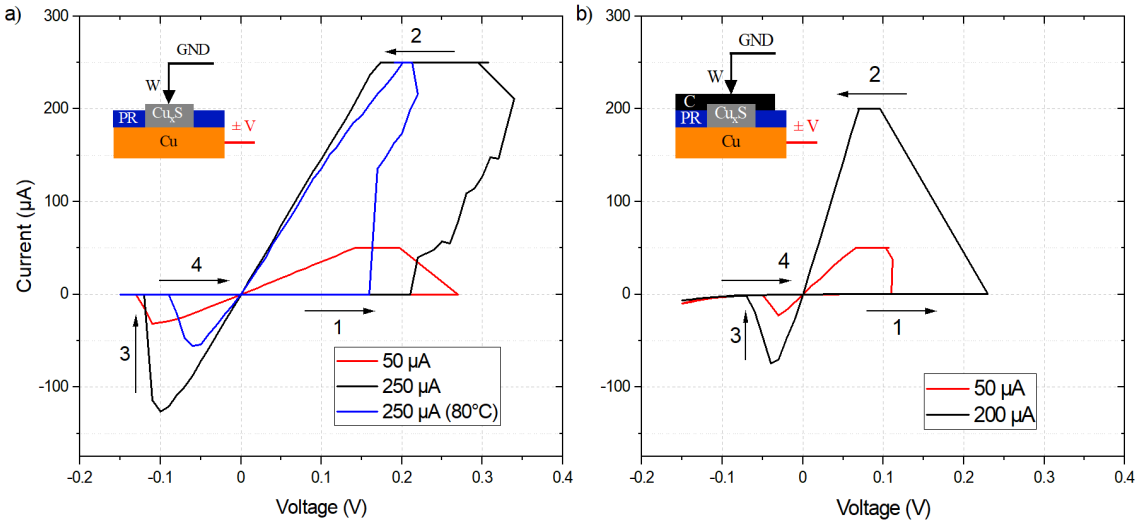

Figure 5.16: Courbe de commutation résistive représentée comme la caractéristique de courant d'une cellule de mémoire a) Cu/Cu_xS/W et b) Cu/Cu_xS/C avec différents courants de conformité. Les flèches numérotées indiquent les directions de balayage (ΔV=10 mV). Dans a) et b), le processus SET se produit à env. 0,15–0,25 V et 0,10–0,25 V, respectivement. Le RESET se produit brusquement à environ -0,1 V et -0,05 V pour revenir à l'état initial, respectivement. Les courbes sont prises à température ambiante, sauf indication contraire.

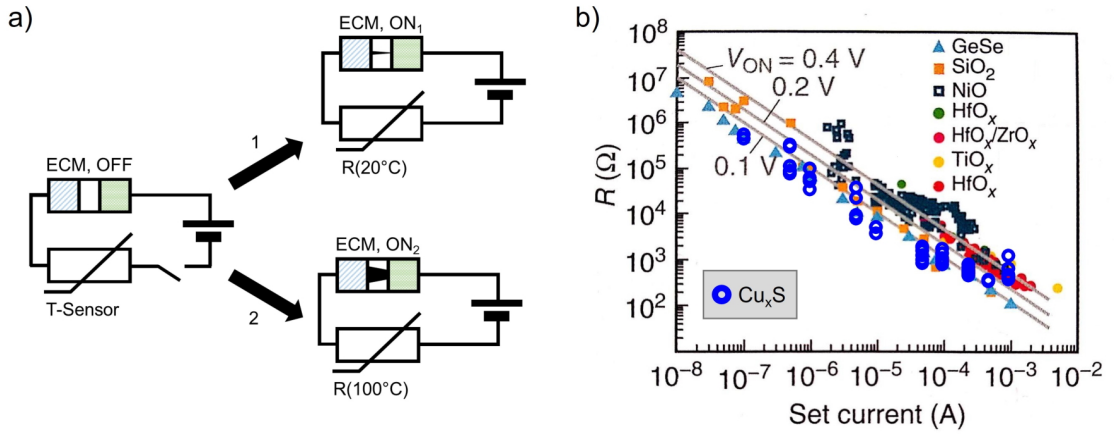

Figure 5.17: a) Schéma conceptuel pour intégrer une batterie imprimée, une mémoire et un capteur, stockant des informations sur la température du scénario 1 ou 2 dans l'état ON de l'ECM. b) $R(I_{cc})$ mesuré à partir de cellules Cu/Cu_xS et d'autres matériaux et concepts de commutation (adapté de [244]).

$V > 0,9\,\mathrm{V}$ pendant 50 h avec un drain de courant constant de 0,2 mA, dépassant ainsi la tension SET nécessaire d'environ 0,25 V pour les cellules de mémoire à base de Cu/Cu_xS. En outre, nous savons que la réponse thermorésistive des cellules à base de Cu_xS est comprise entre 40 et 100 kΩ. Par conséquent, la résistance plus élevée (plus faible) du capteur à des températures plus basses (plus élevées) conduit à un filament conducteur plus fin (plus épais) au sein de la cellule ECM (Fig. 5.17 a)). À un moment ultérieur, la résistance de l'état non volatile peut être utilisée pour déterminer la température du capteur au moment du processus de SET. La Figure 5.17 b) représente les valeurs expérimentales supplémentaires pour $R(I_{cc}, Cu/Cu_xS)$) de Figure 5.16 sur un résumé d'autres résultats empiriques de la littérature [244]. Cet accord de différents matériaux et concepts de commutation avec la loi empirique $R \propto 1/I_{cc}$ est appelé comportement de commutation universel. La largeur de la distribution le long de la tendance linéaire sera utilisée pour valider et attribuer l'état ON après le processus SET à l'influence de la résistance série du capteur.

Il est démontré avec les mêmes dispositifs et la même configuration à deux températures différentes. À une température de 20 °C, le capteur présente $R_{sens} = 40\,k\Omega$. Tout d'abord, il est confirmé que l'ECM fonctionne en effectuant avec succès un balayage de tension quasi-statique avec I_{cc}=10 µA, montrant $R_{OFF} > 10^7\Omega$, $R_{ON} \approx 10^4\,\Omega$, et $V_{set} = 0,29\,\mathrm{V}$. Après avoir fermé le circuit pendant une seconde, la cellule de mémoire est passée du HRS au LRS avec $R_{ON} = 425\,\mathrm{k}\Omega$. Le courant de conformité est donné par $I_{cc} = V_{bat}/(R_{sens} + R_{ON})$ et R_{on} est comparé à la plage attendue de la Figure 5.17 b). Avec les valeurs données, I_{cc}=2,8 µA peut être attribué à la plage de 50–500 kΩ, ainsi la valeur obtenue expérimentalement pour R_{ON} est en accord avec d'autres expériences avec un courant de conformité actif. Cela signifie également, à un niveau plus profond, que la résistance série a empêché l'ECM de former un court-circuit irréversible. Dans l'étape suivante, seul le capteur de température est chauffé sur une plaque chauffante à 100 °C pour confiner l'influence thermique à la partie capteur mais pas à la batterie ou à la mémoire. En raison du coefficient de température négatif, la résistance chute à $R_{sens} = 30\,\mathrm{k}\Omega$ et après la commutation induite par la batterie, la mémoire est à l'état ON avec $R_{ON} = 50\,\mathrm{k}\Omega$. Cela correspond à $I_{cc} = 16,3\,\mu\mathrm{A}$ et correspond à la plage de 5–50 kΩ de la Figure 5.17 b). Par conséquent, la diminution de Rsens de 25 % de 40 à 30 kΩ, conduit à une différence d'ordre de grandeur dans R_{ON}. La forte non-linéarité de la courbe de commutation universelle permet de vastes changements de RON avec des changements relativement faibles de R_{sens} ou I_{cc}, respectivement.

Résumé et perspectives

Ce projet de doctorat avait pour but d'étudier et d'identifier les méthodes et les matériaux adéquats pour un la conception d'un système autonome et imprimé de mémoire, de batterie et de capteur. Dans le cadre de cette thèse, différents capteurs entièrement imprimés par jet d'encre sur des substrats flexibles ont été présentés et étudiés pour surveiller ou détecter les changements de contrainte, d'humidité ou de température. Le processus d'impression a été conçu pour nécessiter qu'un nombre limité d'encres différentes et aucune méthode de fabrication sophistiquée. Cette approche maintient la possibilité de conceptions personnalisées, la rentabilité et la fabrication décentralisée, c'est-à-dire les avantages de l'électronique imprimée.

Les prochains efforts de recherche en ce sujet devraient approfondir la sensibilité croisée de la température et de l'humidité pour les éléments sensoriels. Les complications éventuelles pourraient être résolues par un emballage amélioré. Il convient également de souligner que l'objectif n'est pas de remplacer les circuits intégrés établis à l'échelle micro et nanométrique, mais de les compléter en tirant parti d'un espace disponible plus important et d'applications moins exigeantes. Une cellule de mémoire imprimée dans une étiquette intelligente pour la logistique ne stocke que des informa-

tions limitées telles que les instructions d'expédition ou les journaux de détection d'événements, mais n'a pas besoin d'être commutée autant de fois que les cellules de mémoire conventionnelles. Un défi important pour les applications à grande échelle est la transition des dispositifs à l'échelle du laboratoire vers des processus de rouleau à rouleau. L'imprimante à jet d'encre industrielle combinée au frittage photonique pourrait maintenir des conceptions personnalisées avec un rendement suffisant pour la rendre plus viable.

Bibliography

[1] IEEE: "The International Roadmap for Devices and Systems: 2020: Executive Summary". 2020 (page 1).

[2] K. Petherbridge, P. Evans, and D. Harrison: "The origins and evolution of the PCB: a review". *Circuit World* **31**, 41–45. ISSN: 0305-6120. DOI: 10.1108/03056120510553211 (2005) (pages 1, 20).

[3] R. Das, X. He, and K. Ghaffarzadeh: "Flexible, Printed and Organic Electronics 2020-2030: Forecasts, Technologies, Markets: Market data and technology and application appraisal: providing the complete picture". 2020 (page 1).

[4] LG Electronics: "31.5" 4K OLED Display with Pixel Dimming and 1M:1 Contrast Ratio: 32EP950-B". 2022. URL: https://www.lg.com/ca_en/desktop-monitors/lg-32ep950-b (visited on 04/14/2022) (page 1).

[5] J. Strutwolf, Y. Chen, J. Ullrich, et al.: "Memristive devices based on mass printed organic resistive switching layers". *Applied Physics A* **127**. ISSN: 0947-8396. DOI: 10.1007/s00339-021-04851-9 (2021) (pages 1, 14).

[6] T. Syrový, T. Kazda, J. Akrman, et al.: "Towards roll-to-roll printed batteries based on organic electrodes for printed electronics applications". *Journal of Energy Storage* **40**, 102680. ISSN: 2352152X. DOI: 10.1016/j.est.2021.102680 (2021) (page 1).

[7] G. Kortuem, F. Kawsar, V. Sundramoorthy, et al.: "Smart objects as building blocks for the Internet of things". *IEEE Internet Computing* **14**, 44–51. ISSN: 1089-7801. DOI: 10.1109/MIC.2009.143 (2010) (pages 1, 107).

[8] A. Al-Fuqaha, M. Guizani, M. Mohammadi, et al.: "Internet of Things: A Survey on Enabling Technologies, Protocols, and Applications". *IEEE Communications Surveys & Tutorials* **17**, 2347–2376. DOI: 10.1109/COMST.2015.2444095 (2015) (pages 1, 107).

[9] Y. Bonnassieux, C. J. Brabec, Y. Cao, et al.: "The 2021 Flexible and Printed Electronics Roadmap". *Flexible and Printed Electronics*. DOI: 10.1088/2058-8585/abf986 (2021) (pages 1, 108).

[10] J. A. Rogers, X. Chen, and X. Feng: "Flexible Hybrid Electronics". *Advanced Materials* **32**, e1905590. ISSN: 0935-9648. DOI: 10.1002/adma.201905590 (2020) (page 1).

[11] S. Park, H. Kim, J.-H. Kim, et al.: "Advanced Nanomaterials, Printing Processes, and Applications for Flexible Hybrid Electronics". *Materials (Basel, Switzerland)* **13**. ISSN: 1996-1944. DOI: 10.3390/ma13163587 (2020) (page 1).

[12] E. Sowade, M. Polomoshnov, A. Willert, et al.: "Toward 3D–Printed Electronics: Inkjet–Printed Vertical Metal Wire Interconnects and Screen–Printed Batteries". *Advanced Engineering Materials* **45**, 1900568. ISSN: 1438-1656. DOI: 10.1002/adem.201900568 (2019) (pages 2, 108).

[13] Z. Chen, U. Gengenbach, X. Liu, et al.: "An Automated Room Temperature Flip-Chip Mounting Process for Hybrid Printed Electronics". *Micromachines* **13**, 583. DOI: 10.3390/mi13040583 (2022) (page 2).

[14] C. L. Baumbauer, M. G. Anderson, J. Ting, et al.: "Printed, flexible, compact UHF-RFID sensor tags enabled by hybrid electronics". *Scientific reports* **10**, 16543. DOI: 10.1038/s41598-020-73471-9 (2020) (page 2).

[15] L. Yin, J. Scharf, J. Ma, et al.: "High Performance Printed AgO-Zn Rechargeable Battery for Flexible Electronics". *Joule* **5**, 228–248. ISSN: 25424351. DOI: 10.1016/j.joule.2020.11.008 (2021) (page 2).

[16] Y. Chu, C. Qian, P. Chahal, et al.: "Printed Diodes: Materials Processing, Fabrication, and Applications". *Advanced science (Weinheim, Baden-Wurttemberg, Germany)* **6**, 1801653. ISSN: 2198-3844. DOI: 10.1002/advs.201801653 (2019) (page 2).

[17] D. H. Kim, H. E. Lee, B. K. You, et al.: "Flexible Crossbar–Structured Phase Change Memory Array via Mo–Based Interfacial Physical Lift–Off". *Advanced Functional Materials* **29**, 1806338. ISSN: 1616301X. DOI: 10.1002/adfm.201806338 (2019) (page 2).

[18] P. Mahato, E. Puyoo, D. Deleruyelle, et al.: "CBRAM devices with a water casted solid polymer electrolyte for flexible electronic applications". *2019 IEEE 14th Nanotechnology Materials and Devices Conference (NMDC)*. IEEE (102019), pp. 1–5. ISBN: 978-1-7281-2637-1. DOI: 10.1109/NMDC47361.2019.9083996 (page 2).

[19] C. Dias, D. C. Leitao, C. S. R. Freire, et al.: "Resistive switching of silicon-silver thin film devices in flexible substrates". *Nanotechnology* **31**, 135702. ISSN: 0957-4484. DOI: 10.1088/1361-6528/ab5eb7 (2020) (page 2).

[20] M. Delfag, R. Katoch, J. Jehn, et al.: "Sinter-free inkjet-printed PEDOT:PSS/WO_3/PEDOT:PSS flexible valency change memory". *Flexible and Printed Electronics* **6**, 035011. DOI: 10.1088/2058-8585/ac1fd7 (2021) (pages 2, 25).

[21] M. H. Malik, G. Grosso, H. Zangl, et al.: "Flip Chip integration of ultra-thinned dies in low-cost flexible printed electronics; the effects of die thickness, encapsulation and conductive adhesives". *Microelectronics Reliability* **123**, 114204. ISSN: 00262714. DOI: 10.1016/j.microrel.2021.114204 (2021) (page 2).

[22] A. Mei, X. Li, L. Liu, et al.: "A hole-conductor-free, fully printable mesoscopic perovskite solar cell with high stability". *Science (New York, N.Y.)* **345**, 295–298. DOI: 10.1126/science.1254763 (2014) (page 2).

[23] P. M. Grubb, H. Subbaraman, S. Park, et al.: "Inkjet Printing of High Performance Transistors with Micron Order Chemically Set Gaps". *Scientific reports* **7**, 1202. DOI: 10.1038/s41598-017-01391-2 (2017) (page 2).

[24] J. Kwon, Y. Takeda, R. Shiwaku, et al.: "Three-dimensional monolithic integration in flexible printed organic transistors". *Nature communications* **10**, 54. DOI: 10.1038/s41467-018-07904-5 (2019) (page 2).

[25] B. Huber, P. B. Popp, M. Kaiser, et al.: "Fully inkjet printed flexible resistive memory". *Applied Physics Letters* **110**, 143503. ISSN: 0003-6951. DOI: 10.1063/1.4978664 (2017) (pages 2, 25, 38, 39, 107).

[26] A. Albrecht: "Printed Sensors for the Internet of Things". Dissertation. München: Technische Universität München (2018) (page 2).

[27] X. Wang, S. Zheng, F. Zhou, et al.: "Scalable fabrication of printed Zn//MnO_2 planar micro-batteries with high volumetric energy density and exceptional safety". *National Science Review* **30**, 1803181. ISSN: 2095-5138. DOI: 10.1093/nsr/nwz070 (2019) (pages 2, 7, 17).

[28] Y. Ding, M. Jin, S. Li, et al.: "Smart logistics based on the internet of things technology: an overview". *International Journal of Logistics Research and Applications* **24**, 323–345. ISSN: 1367-5567. DOI: 10.1080/13675567.2020.1757053 (2021) (pages 2, 108).

[29] Omega Engineering Inc.: "Omega KFH Series: Pre-Wired Strain Gages (Data Sheet)". https://assets.omega.com/pdf/test-and-measurement-equipment/strain-gauges/KFH.pdf 2022. (Visited on 04/14/2022) (pages 4, 31, 54).

[30] H. Farahani, R. Wagiran, and M. N. Hamidon: "Humidity sensors principle, mechanism, and fabrication technologies: a comprehensive review". *Sensors (Basel, Switzerland)* **14**, 7881–7939. DOI: 10.3390/s140507881 (2014) (pages 5, 6, 33).

[31] K.-S. Chou, T.-K. Lee, and F.-J. Liu: "Sensing mechanism of a porous ceramic as humidity sensor". *Sensors and Actuators B: Chemical* **56**, 106–111. ISSN: 09254005. DOI: 10.1016/S0925-4005(99)00187-2 (1999) (page 5).

[32] M. Faraday: "Experimental Researches In Electricity - Volume 1". Read Books Limited (2016). ISBN: 9781473383326 (page 5).

[33] TDK Group Company: "NTC Termistors: General Technical Information". 2018. URL: https://www.tdk-electronics.tdk.com/download/531116/19643b7ea798d7c4670141a88cd993f9/pdf-general-technical-information.pdf (visited on 04/14/2022) (pages 5, 75, 119).

[34] J. S. Steinhart and S. R. Hart: "Calibration curves for thermistors". *Deep Sea Research and Oceanographic Abstracts* **15**, 497–503. ISSN: 00117471. DOI: 10.1016/0011-7471(68)90057-0 (1968) (page 5).

[35] M. Matus: "Temperature measurement in dimensional metrology – Why the Steinhart-Hart equation works so well". *Proceedings of MacroScale 2011*. DOI: 10.7795/810.20130620D (2011) (page 6).

[36] S. Khan, S. Ali, A. Khan, et al.: "Wearable Printed Temperature Sensors: Short Review on Latest Advances for Biomedical Applications". *IEEE reviews in biomedical engineering* **PP**. DOI: 10.1109/RBME.2021.3121480 (2021) (page 6).

[37] Y.-F. Wang, T. Sekine, Y. Takeda, et al.: "Fully Printed PEDOT:PSS-based Temperature Sensor with High Humidity Stability for Wireless Healthcare Monitoring". *Scientific reports* **10**, 2467. DOI: 10.1038/s41598-020-59432-2 (2020) (page 6).

[38] V. S. Turkani, D. Maddipatla, B. B. Narakathu, et al.: "A carbon nanotube based NTC thermistor using additive print manufacturing processes". *Sensors and Actuators A: Physical* **279**, 1–9. ISSN: 09244247. DOI: 10.1016/j.sna.2018.05.042 (2018) (pages 6, 54).

[39] D. Barmpakos, C. Tsamis, and G. Kaltsas: "A Multi-parameter paper sensor fabricated by inkjet-printed silver nanoparticle ink and PEDOT:PSS". *Microelectronic Engineering*, 111266. ISSN: 01679317. DOI: 10.1016/j.mee.2020.111266 (2020) (pages 6, 33).

[40] Y. Li, Y. Liu, S. R. A. Bhuiyan, et al.: "Printed Strain Sensors for On–Skin Electronics". *Small Structures*. ISSN: 2688-4062. DOI: 10.1002/sstr.202100131 (2021) (page 6).

[41] L. Duan, D. R. D'hooge, and L. Cardon: "Recent progress on flexible and stretchable piezoresistive strain sensors: From design to application". *Progress in Materials Science* **114**. DOI: 10.1016/j.pmatsci.2019.100617 (2019) (pages 6, 31, 51).

[42] X. Xu, G. Han, H. Yu, et al.: "Resistance change of stretchable composite based on inkjet printed silver nanowire". *Journal of Physics D: Applied Physics*. ISSN: 0022-3727. DOI: 10.1088/1361-6463/ab524d (2019) (page 6).

[43] L.-.-W. Lo, H. Shi, H. Wan, et al.: "Inkjet–Printed Soft Resistive Pressure Sensor Patch for Wearable Electronics Applications". *Advanced Materials Technologies* **6**, 1900717. ISSN: 2365-709X. DOI: 10.1002/admt.201900717 (2019) (page 6).

[44] X. Fu, M. Ramos, A. M. Al-Jumaily, et al.: "Stretchable strain sensor facilely fabricated based on multi-wall carbon nanotube composites with excellent performance". *Journal of Materials Science* **54**, 2170–2180. ISSN: 0022-2461. DOI: 10.1007/s10853-018-2954-4 (2019) (pages 6, 31).

[45] J. Shintake, Y. Piskarev, S. H. Jeong, et al.: "Ultrastretchable Strain Sensors Using Carbon Black–Filled Elastomer Composites and Comparison of Capacitive Versus Resistive Sensors". *Advanced Materials Technologies* **3**, 1700284. ISSN: 2365-709X. DOI: 10.1002/admt.201700284 (2018) (pages 6, 31).

[46] Y. Cheng, K. Wang, H. Xu, et al.: "Recent developments in sensors for wearable device applications". *Analytical and bioanalytical chemistry* **413**, 6037–6057. DOI: 10.1007/s00216-021-03602-2 (2021) (page 6).

[47] G. Mattana, T. Kinkeldei, D. Leuenberger, et al.: "Woven Temperature and Humidity Sensors on Flexible Plastic Substrates for E-Textile Applications". *IEEE Sensors Journal* **13**, 3901–3909. ISSN: 1530-437X. DOI: 10.1109/JSEN.2013.2257167 (2013) (page 6).

[48] G. Dubourg, J. Katona, M. Rodović, et al.: "Flexible and highly sensitive humidity sensors using screen-printed TiO_2 nanoparticles as sensitive layer". *Journal of Physics: Conference Series* **939**, 012008. ISSN: 1742-6588. DOI: 10.1088/1742-6596/939/1/012008 (2017) (pages 6, 33).

[49] X. Zhang, D. Maddipatla, A. K. Bose, et al.: "Printed Carbon Nanotubes-Based Flexible Resistive Humidity Sensor". *IEEE Sensors Journal* **20**, 12592–12601. ISSN: 1530-437X. DOI: 10.1109/JSEN.2020.3002951 (2020) (page 6).

[50] Jakajima B.V.: "Automotive 3D Printing Conference". 2021. URL: https://www.automotive3dprintingconference.com/ (visited on 04/14/2022) (pages 6, 108).

[51] Quad Industries: "Printed Sensors". 2021. URL: https://www.quad-ind.com/printed-electronics/printed-sensors/ (visited on 04/14/2022) (pages 6, 108).

[52] Holst Centre: "Disposable Health Patch". URL: https://holstcentre.com/expertise/components-devices-systems/health-patch/ (visited on 04/14/2022) (pages 7, 108).

[53] P. Connor, R. D. Bailey, R. M. Dell, et al.: "Understanding Batteries". Cambridge: Royal Society of Chemistry (2007). ISBN: 978-0-85404-605-8. DOI: 10.1039/9781847552228 (pages 7, 110).

[54] G. Leclanché: "Quelques observations sur l'emploi des piles électriques: Pile constante au peroxyde de manganese a un seul liquide". **16** (1867) (page 7).

[55] M. Song, H. Tan, D. Chao, et al.: "Recent Advances in Zn-Ion Batteries". *Advanced Functional Materials* **28**, 1802564. ISSN: 1616301X. DOI: 10.1002/adfm.201802564 (2018) (page 7).

[56] M. Winter and R. J. Brodd: "What are batteries, fuel cells, and supercapacitors?". *Chemical reviews* **104**, 4245–4269. ISSN: 0009-2665. DOI: 10.1021/cr020730k (2004) (pages 7, 8, 14, 35, 111).

[57] N. Zhang, F. Cheng, J. Liu, et al.: "Rechargeable aqueous zinc-manganese dioxide batteries with high energy and power densities". *Nature Communications* **8**, 652. DOI: 10.1038/s41467-017-00467-x (2017) (pages 7, 47, 111).

[58] W. Sun, F. Wang, S. Hou, et al.: "Zn/MnO_2 Battery Chemistry With H^+ and Zn^{2+} Coinsertion". *Journal of the American Chemical Society* **139**, 9775–9778. DOI: 10.1021/jacs.7b04471 (2017) (pages 7, 47).

[59] W. Lu, C. Xie, H. Zhang, et al.: "Inhibition of Zinc Dendrite Growth in Zinc-Based Batteries". *ChemSusChem* **11**, 3996–4006. DOI: 10.1002/cssc.201801657 (2018) (pages 7, 46, 47, 111).

[60] Y. Ren, F. Meng, S. Zhang, et al.: "CNT@MnO_2 composite ink toward a flexible 3D printed micro–zinc–ion battery". *Carbon Energy*. ISSN: 2637-9368. DOI: 10.1002/cey2.177 (2022) (pages 7, 111).

[61] D. Chao, W. Zhou, C. Ye, et al.: "An Electrolytic Zn-MnO_2 Battery for High-Voltage and Scalable Energy Storage". *Angewandte Chemie (International ed. in English)* **58**, 7823–7828. DOI: 10.1002/anie.201904174 (2019) (pages 7, 14, 17, 48, 114).

[62] C. H. Hamann and W. Vielstich: "Elektrochemie". 4., vollständig überarbeitete und aktualisierte Auflage. Weinheim: Wiley-VCH-Verlag GmbJ &Co. KGaA (2005). ISBN: 978-3-527-31068-5 (pages 8, 30).

[63] M. B. Lim, T. N. Lambert, and B. R. Chalamala: "Rechargeable alkaline zinc–manganese oxide batteries for grid storage: Mechanisms, challenges and developments". *Materials Science and Engineering: R: Reports* **143**, 100593. ISSN: 0927796X. DOI: 10.1016/j.mser.2020.100593 (2021) (pages 8, 46).

[64] R. Waser, ed.: "Nanoelectronics and information technology: Advanced electronic materials and novel devices". 3., completely rev. and enl. ed. Weinheim: Wiley-VCH (2012). ISBN: 978-3-527-40927-3 (pages 8, 38, 83, 121).

[65] T. W. Hickmott: "Low–Frequency Negative Resistance in Thin Anodic Oxide Films". *Journal of Applied Physics* **33**, 2669–2682. ISSN: 0021-8979. DOI: 10.1063/1.1702530 (1962) (page 9).

[66] J. G. Simmons and R. R. Verderber: "New conduction and reversible memory phenomena in thin insulating films". *Proceedings of the Royal Society of London. Series A. Mathematical and Physical Sciences* **301**, 77–102. ISSN: 0080-4630. DOI: 10.1098/rspa.1967.0191 (1967) (page 9).

[67] M. N. Kozicki, C. Gopalan, M. Balakrishnan, et al.: "Non-Volatile memory based on solid electrolytes". *Non-Volatile Memory Technology Symposium, 2004*. Piscataway, NJ: IEEE Operations Center (2004), pp. 10–17. ISBN: 0-7803-8726-0. DOI: 10.1109/NVMT.2004.1380792 (page 9).

[68] K. Terabe, T. Hasegawa, T. Nakayama, et al.: "Quantized conductance atomic switch". *Nature* **433**, 47–50. ISSN: 0028-0836. DOI: 10.1038/nature03190 (2005) (pages 9, 25).

[69] R. Yang, K. Terabe, G. Liu, et al.: "On-demand nanodevice with electrical and neuromorphic multifunction realized by local ion migration". *ACS nano* **6**, 9515–9521. DOI: 10.1021/nn302510e (2012) (page 9).

[70] F. M. Bayat, M. Prezioso, B. Chakrabarti, et al.: "Implementation of multilayer perceptron network with highly uniform passive memristive crossbar circuits". *Nature Communications* **9**, 2331. DOI: 10.1038/s41467-018-04482-4 (2018) (page 9).

[71] S. Goswami, R. Pramanick, A. Patra, et al.: "Decision trees within a molecular memristor". *Nature* **597**, 51–56. ISSN: 0028-0836. DOI: 10.1038/s41586-021-03748-0 (2021) (page 9).

[72] TIA: "Low-power FPGA based on NanoBridge technology". 2017. URL: https://www.tia-nano.jp/data/doc/1515026501_doc_13_1.pdf (visited on 04/14/2022) (page 9).

[73] NEC: "Spinning off from NEC with the world's one-and-only technology". 2021. URL: https://www.nec.com/en/global/rd/special/202101/index.html (visited on 04/14/2022) (page 9).

[74] S. Menzel and R. Waser: "Analytical analysis of the generic SET and RESET characteristics of electrochemical metallization memory cells". *Nanoscale* **5**, 11003–11010. DOI: 10.1039/c3nr03387b (2013) (pages 9–11, 110).

[75] D. Ielmini: "Resistive switching memories based on metal oxides: mechanisms, reliability and scaling". *Semiconductor Science and Technology* **31**, 063002. ISSN: 0268-1242. DOI: 10.1088/0268-1242/31/6/063002 (2016) (page 9).

[76] S. Menzel, S. Tappertzhofen, R. Waser, et al.: "Switching kinetics of electrochemical metallization memory cells". *Physical chemistry chemical physics : PCCP* **15**, 6945–6952. DOI: 10.1039/c3cp50738f (2013) (page 9).

[77] D. Ielmini and R. Waser: "Resistive switching: From fundamentals of nanionic redox processes to memristive device applications / edited by Daniele Ielmini and Rainer Waser". Weinheim, Germany: Wiley-VCH (2016). ISBN: 978-3-527-33417-9 (pages 9, 11, 35, 81, 109, 122).

[78] I. Valov, R. Waser, J. R. Jameson, et al.: "Electrochemical metallization memories—fundamentals, applications, prospects". *Nanotechnology* **22**, 289502. ISSN: 0957-4484. DOI: 10.1088/0957-4484/22/28/289502 (2011) (pages 10, 12, 109).

[79] C. Schindler, I. Valov, and R. Waser: "Faradaic currents during electroforming of resistively switching Ag-Ge-Se type electrochemical metallization memory cells". *Physical chemistry chemical physics : PCCP* **11**, 5974–5979. DOI: 10.1039/b901026b (2009) (pages 9, 109).

[80] S. Dirkmann and T. Mussenbrock: "Resistive switching in memristive electrochemical metallization devices". *AIP Advances* **7**, 065006. DOI: 10.1063/1.4985443 (2017) (page 10).

[81] C. M. Osburn and D. W. Ormond: "Dielectric Breakdown in Silicon Dioxide Films on Silicon". *Journal of The Electrochemical Society* **119**, 597. ISSN: 00134651. DOI: 10.1149/1.2404269 (1972) (pages 10, 38).

[82] S. Choi, S. H. Tan, Z. Li, et al.: "SiGe epitaxial memory for neuromorphic computing with reproducible high performance based on engineered dislocations". *Nature materials* **17**, 335–340. ISSN: 1476-1122. DOI: 10.1038/s41563-017-0001-5 (2018) (page 10).

[83] I. Valov and R. Waser: "Comment on real-time observation on dynamic growth/dissolution of conductive filaments in oxide-electrolyte- based ReRAM". *Advanced materials (Deerfield Beach, Fla.)* **25**, 162–164. DOI: 10.1002/adma.201202592 (2013) (page 11).

[84] W. Wang, E. Covi, Y.-H. Lin, et al.: "Switching Dynamics of Ag-Based Filamentary Volatile Resistive Switching Devices–Part II: Mechanism and Modeling". *IEEE Transactions on Electron Devices*, 1–8. ISSN: 0018-9383. DOI: 10.1109/TED.2021.3095033 (2021) (page 11).

[85] W. Wang, M. Wang, E. Ambrosi, et al.: "Surface diffusion-limited lifetime of silver and copper nanofilaments in resistive switching devices". *Nature communications* **10**. DOI: 10.1038/s41467-018-07979-0 (2019) (pages 11, 12, 110).

[86] P. W. Voorhees: "The theory of Ostwald ripening". *Journal of Statistical Physics* **38**, 231–252. ISSN: 0022-4715. DOI: 10.1007/BF01017860 (1985) (page 12).

[87] J. V. Alemán, A. V. Chadwick, J. He, et al.: "Definitions of terms relating to the structure and processing of sols, gels, networks, and inorganic-organic hybrid materials (IUPAC Recommendations 2007)". *Pure and Applied Chemistry* **79**, 1801–1829. ISSN: 0033-4545. DOI: 10.1351/pac200779101801 (2007) (page 12).

[88] X. Wang, J. Sparkman, and J. Gou: "Strain sensing of printed carbon nanotube sensors on polyurethane substrate with spray deposition modeling". *Composites Communications* **3**, 1–6. ISSN: 24522139. DOI: 10.1016/j.coco.2016.10.003 (2017) (page 12).

[89] K. J. Yoon, J.-W. Han, D.-I. Moon, et al.: "Electrically-generated memristor based on inkjet printed silver nanoparticles". *Nanoscale Advances* **18**, 507. DOI: 10.1039/C9NA00329K (2019) (page 12).

[90] K. Black, J. Singh, D. Mehta, et al.: "Silver Ink Formulations for Sinter-free Printing of Conductive Films". *Scientific reports* **6**, 20814. DOI: 10.1038/srep20814 (2016) (page 12).

[91] E. Covi, W. Wang, Y.-H. Lin, et al.: "Switching Dynamics of Ag Based Filamentary Volatile Resistive Switching Devices–Part I: Experimental Characterization". *IEEE Transactions on Electron Devices*, 1–7. ISSN: 0018-9383. DOI: 10.1109/TED.2021.3076029 (2021) (page 12).

[92] N. A. Lange: "Lange's handbook of chemistry". 15. ed. McGraw-Hill handbooks. New York, NY: McGraw-Hill (1999). ISBN: 0-07-016384-7 (pages 12, 25, 29, 46).

[93] A. Roy and P.-R. Cha: "Electric field induced charge migration and formation of conducting filament during resistive switching in electrochemical metallization (ECM) memory cells". *Journal of Applied Physics* **128**, 205102. ISSN: 0021-8979. DOI: 10.1063/5.0026350 (2020) (page 12).

[94] Y. Yang, P. Gao, S. Gaba, et al.: "Observation of conducting filament growth in nanoscale resistive memories". *Nature communications* **3**, 732. DOI: 10.1038/ncomms1737 (2012) (page 12).

[95] F. Pan, S. Gao, C. Chen, et al.: "Recent progress in resistive random access memories: Materials, switching mechanisms, and performance". *Materials Science and Engineering: R: Reports* **83**, 1–59. ISSN: 0927796X. DOI: 10.1016/j.mser.2014.06.002 (2014) (page 12).

[96] L. Goux, J. Radhakrishnan, A. Belmonte, et al.: "Key material parameters driving CBRAM device performances". *Faraday discussions* **213**, 67–85. DOI: 10.1039/C8FD00115D (2019) (page 12).

[97] S. Slesazeck and T. Mikolajick: "Nanoscale resistive switching memory devices: a review". *Nanotechnology* **30**, 352003. ISSN: 0957-4484. DOI: 10.1088/1361-6528/ab2084 (2019) (page 13).

[98] E. Carlos, R. Branquinho, R. Martins, et al.: "Recent Progress in Solution-Based Metal Oxide Resistive Switching Devices". *Advanced Materials* **33**, e2004328. ISSN: 0935-9648. DOI: 10.1002/adma.202004328 (2021) (page 13).

[99] K. Rahman, M. Mustafa, N. M. Muhammad, et al.: "Electrohydrodynamic printed TiO_2 flexible memory device – fabrication and characterisation". *Electronics Letters* **48**, 1261. ISSN: 0013-5194. DOI: 10.1049/el.2012.1003 (2012) (page 13).

[100] S. Nau, C. Wolf, K. Popovic, et al.: "Inkjet-Printed Resistive Switching Memory Based on Organic Dielectric Materials: From Single Elements to Array Technology". *Advanced Electronic Materials* **1**, 1400003. ISSN: 2199160X. DOI: 10.1002/aelm.201400003 (2015) (page 13).

[101] H. Hu, A. Scholz, S. A. Singaraju, et al.: "Inkjet-printed bipolar resistive switching device based on Ag/ZnO/Au structure". *Applied Physics Letters* **119**, 112103. ISSN: 0003-6951. DOI: 10.1063/5.0058526 (2021) (page 14).

[102] L. Wu, J. Li, C. Liu, et al.: "Inkjet printed $BiFeO_3$ thin films with non-volatile resistive switching behaviors". *Physics Letters A* **404**, 127406. ISSN: 03759601. DOI: 10.1016/j.physleta.2021.127406 (2021) (page 14).

[103] E. Ramon, E. Sowade, C. Martinez Domingo, et al.: "Large-scale fabrication of all-inkjet-printed resistors and WORM memories on flexible polymer films with high yield and stability". *Flexible and Printed Electronics*. DOI: 10.1088/2058-8585/abdb40 (2021) (page 14).

[104] M. Lanza, H.-S. P. Wong, E. Pop, et al.: "Recommended Methods to Study Resistive Switching Devices". *Advanced Electronic Materials* **5**, 1800143. ISSN: 2199160X. DOI: 10.1002/aelm.201800143 (2019) (pages 14, 17).

[105] M. Lanza, R. Waser, D. Ielmini, et al.: "Standards for the Characterization of Endurance in Resistive Switching Devices". *ACS nano*. DOI: 10.1021/acsnano.1c06980 (2021) (page 14).

[106] VARTA Microbattery GmbH: "Rechargeable Button Cells NiMH". 2018. URL: https://www.varta-ag.com/fileadmin/varta_microbattery/downloads/service/battery-documentation/nickel-metal-hydride/Sales-Literature-201810_HANDBOOK_Rechargeable_Button_Cells_NiMH_en.pdf (visited on 04/14/2022) (page 14).

[107] G. A. Ghiurcan, C.-C. Liu, A. Webber, et al.: "Development and Characterization of a Thick-Film Printed Zinc-Alkaline Battery". *Journal of The Electrochemical Society* **150**, A922. ISSN: 00134651. DOI: 10.1149/1.1578478 (2003) (page 14).

[108] A. Gambhir, P. Sandwell, and J. Nelson: "The future costs of OPV – A bottom-up model of material and manufacturing costs with uncertainty analysis". *Solar Energy Materials and Solar Cells* **156**, 49–58. ISSN: 09270248. DOI: 10.1016/j.solmat.2016.05.056 (2016) (page 16).

[109] J. Jehn, M. Kaiser, U. Moosheimer, et al.: "Printed resistive switching memory operated by screen-printed microbattery via shared electrode". *Microelectronic Engineering* **239-240**, 111524. ISSN: 01679317. DOI: 10.1016/j.mee.2021.111524 (2021) (pages 19, 45, 49, 77, 84, 85).

[110] J. Jehn, P. Oser, M. A. M. Courrau, et al.: "Fully Inkjet-Printed Carbon Nanotube-PDMS-Based Strain Sensor: Temperature Response, Compressive and Tensile Bending Properties, and Fatigue Investigations". *IEEE Access* **9**, 72207–72216. DOI: 10.1109/ACCESS.2021.3078799 (2021) (pages 19, 32, 45, 50, 53, 55, 56, 58, 115).

[111] J. Jehn, M. Kaiser, C. Eulenkamp, et al.: "Cu_xS Thin Films for Printed Memory Cells and Temperature Sensors". *Flexible and Printed Electronics*. DOI: 10.1088/2058-8585/ac6783 (2022) (pages 19, 39, 45, 74, 76, 78, 80–82).

[112] W. J. Hyun, S. Lim, B. Y. Ahn, et al.: "Screen Printing of Highly Loaded Silver Inks on Plastic Substrates Using Silicon Stencils". *ACS applied materials & interfaces* **7**, 12619–12624. DOI: 10.1021/acsami.5b02487 (2015) (page 20).

[113] L. Liu, Y. Pei, S. Ma, et al.: "Inkjet Printing Controllable Polydopamine Nanoparticle Line Array for Transparent and Flexible Touch–Sensing Application". *Advanced Engineering Materials* **22**, 1901351. ISSN: 1438-1656. DOI: 10.1002/adem.201901351 (2020) (page 20).

[114] Y. Khan, A. Thielens, S. Muin, et al.: "A New Frontier of Printed Electronics: Flexible Hybrid Electronics". *Advanced Materials* **32**, e1905279. ISSN: 0935-9648. DOI: 10.1002/adma.201905279 (2020) (page 20).

[115] H.-W. Lin, C.-P. Chang, W.-H. Hwu, et al.: "The rheological behaviors of screen-printing pastes". *Journal of Materials Processing Technology* **197**, 284–291. ISSN: 09240136. DOI: 10.1016/j.jmatprotec.2007.06.067 (2008) (page 20).

[116] D. Novaković, N. Kašiković, G. Vladić, et al.: "Screen Printing". *Printing on Polymers*. Elsevier (2016), pp. 247–261. ISBN: 9780323374682. DOI: 10.1016/B978-0-323-37468-2.00015-4 (page 20).

[117] Q. Li, J. Zhang, Q. Li, et al.: "Review of Printed Electrodes for Flexible Devices". *Frontiers in Materials* **5**. DOI: 10.3389/fmats.2018.00077 (2019) (page 20).

[118] S. Yanniotis, S. Skaltsi, and S. Karaburnioti: "Effect of moisture content on the viscosity of honey at different temperatures". *Journal of Food Engineering* **72**, 372–377. ISSN: 02608774. DOI: 10.1016/j.jfoodeng.2004.12.017 (2006) (page 20).

[119] A. Lorenz, M. Klawitter, M. Linse, et al.: "The project 'Rock-Star': The evolution of rotary printing for solar cell metallization". *Proceedings of the 9th Workshop on Metallization and Interconnection for Crystalline Silicon Solar Cells*. AIP Conference Proceedings. AIP Publishing (2021), p. 020008. DOI: 10.1063/5.0056060 (page 21).

[120] G. D. Martin, S. D. Hoath, and I. M. Hutchings: "Inkjet printing - the physics of manipulating liquid jets and drops". *Journal of Physics: Conference Series* **105**, 012001. ISSN: 1742-6588. DOI: 10.1088/1742-6596/105/1/012001 (2008) (page 21).

[121] I. Gibson, D. Rosen, and B. Stucker: "Material Jetting". *Additive Manufacturing Technologies*. Ed. by I. Gibson, D. Rosen, and B. Stucker. New York, NY: Springer New York (2015), pp. 175–203. ISBN: 978-1-4939-2112-6. DOI: 10.1007/978-1-4939-2113-3_7 (page 21).

[122] Dimatix Fujifilm: "Dimatix Materials Printer DMP-2800 series User Manual". 2010 (page 21).

[123] B. Derby: "Inkjet Printing of Functional and Structural Materials: Fluid Property Requirements, Feature Stability, and Resolution". *Annual Review of Materials Research* **40**, 395–414. ISSN: 1531-7331. DOI: 10.1146/annurev-matsci-070909-104502 (2010) (pages 22, 23).

[124] P. C. Duineveld, M. M. de Kok, M. Buechel, et al.: "Ink-jet printing of polymer light-emitting devices". *Organic Light-Emitting Materials and Devices V*. Ed. by Z. H. Kafafi. SPIE Proceedings. SPIE (2001), p. 59. DOI: 10.1117/12.457460 (page 22).

[125] R. Bhola and S. Chandra: "Parameters controlling solidification of molten wax droplets falling on a solid surface". *Journal of Materials Science* **34**, 4883–4894. ISSN: 0022-2461. DOI: 10.1023/A:1004680315199 (1999) (page 22).

[126] B. Derby: "Additive Manufacture of Ceramics Components by Inkjet Printing". *Engineering* **1**, 113–123. ISSN: 20958099. DOI: 10.15302/J-ENG-2015014 (2015) (page 22).

[127] T. Lim, S. Han, J. Chung, et al.: "Experimental study on spreading and evaporation of inkjet printed pico-liter droplet on a heated substrate". *International Journal of Heat and Mass Transfer* **52**, 431–441. ISSN: 00179310. DOI: 10.1016/j.ijheatmasstransfer.2008.05.028 (2009) (pages 22, 73, 74).

[128] A. Lee, K. Sudau, K. H. Ahn, et al.: "Optimization of Experimental Parameters to Suppress Nozzle Clogging in Inkjet Printing". *Industrial & Engineering Chemistry Research* **51**, 13195–13204. ISSN: 0888-5885. DOI: 10.1021/ie301403g (2012) (pages 22, 24).

[129] S. Krainer, C. Smit, and U. Hirn: "The effect of viscosity and surface tension on inkjet printed picoliter dots". *RSC Advances* **9**, 31708–31719. DOI: 10.1039/C9RA04993B (2019) (page 22).

[130] R. D. Deegan, O. Bakajin, T. F. Dupont, et al.: "Capillary flow as the cause of ring stains from dried liquid drops". *Nature* **389**, 827–829. ISSN: 0028-0836. DOI: 10.1038/39827 (1997) (pages 23, 74).

[131] E. Tekin, P. J. Smith, and U. S. Schubert: "Inkjet printing as a deposition and patterning tool for polymers and inorganic particles". *Soft matter* **4**, 703–713. DOI: 10.1039/b711984d (2008) (page 23).

[132] D. Mampallil and H. B. Eral: "A review on suppression and utilization of the coffee-ring effect". *Advances in colloid and interface science* **252**, 38–54. DOI: 10.1016/j.cis.2017.12.008 (2018) (page 23).

[133] Y. Li, Q. Yang, M. Li, et al.: "Rate-dependent interface capture beyond the coffee-ring effect". *Scientific reports* **6**, 24628. DOI: 10.1038/srep24628 (2016) (page 24).

[134] S. M. Song and S. M. Cho: "Copper Ion Inks Capable of Screen Printing and Intense Pulsed-Light Sintering on PET Substrates". *ACS Applied Electronic Materials*. ISSN: 2637-6113. DOI: 10.1021/acsaelm.2c00098 (2022) (pages 24, 37).

[135] Copprint: "Rapid Self-Sintering Nano Copper Inks". 2022. URL: https://www.copprint.com/ (visited on 04/14/2022) (pages 24, 37).

[136] T. Stubhan, N. Li, N. A. Luechinger, et al.: "High Fill Factor Polymer Solar Cells Incorporating a Low Temperature Solution Processed WO_3 Hole Extraction Layer". *Advanced Energy Materials* **2**, 1433–1438. ISSN: 16146832. DOI: 10.1002/aenm.201200330 (2012) (page 25).

[137] J. Solis, S. Saukko, L. Kish, et al.: "Semiconductor gas sensors based on nanostructured tungsten oxide". *Thin Solid Films* **391**, 255–260. ISSN: 00406090. DOI: 10.1016/s0040-6090(01)00991-9 (2001) (page 25).

[138] M. N. Kozicki, C. Gopalan, M. Balakrishnan, et al.: "A Low-Power Nonvolatile Switching Element Based on Copper-Tungsten Oxide Solid Electrolyte". *IEEE Transactions On Nanotechnology* **5**, 535–544. ISSN: 1536-125X. DOI: 10.1109/TNANO.2006.880407 (2006) (page 25).

[139] B. Mittermeier, A. Bednar, M. Kaiser, et al.: "Comparison of spin-on-glass and WO_3 as an insulating layer for printed resistive memory devices". *Materials Technology* **34**, 350–355. ISSN: 1066-7857. DOI: 10.1080/10667857.2019.1567896 (2019) (pages 25, 82).

[140] C.-C. Hsu, H. Chuang, and W.-C. Jhang: "Annealing effect on forming-free bipolar resistive switching characteristics of sol-gel WO_x resistive memories with Al conductive bridges". *Journal of Alloys and Compounds* **882**, 160758. ISSN: 09258388. DOI: 10.1016/j.jallcom.2021.160758 (2021) (page 25).

[141] O. A. Shilova: "'Spin-on glass' films for semiconductor technology". *Surface Coatings International Part B: Coatings Transactions* **86**, 195–202. ISSN: 1476-4865. DOI: 10.1007/BF02699653 (2003) (page 25).

[142] N. Yamada and T. Takahashi: "Methylsiloxane Spin-on-Glass Films for Low Dielectric Constant Interlayer Dielectrics". *Journal of The Electrochemical Society* **147**, 1477. ISSN: 00134651. DOI: 10.1149/1.1393381 (2000) (page 25).

[143] T. Sakamoto, H. Sunamura, H. Kawaura, et al.: "Nanometer-scale switches using copper sulfide". *Applied Physics Letters* **82**, 3032–3034. ISSN: 0003-6951. DOI: 10.1063/1.1572964 (2003) (pages 25, 29, 82).

[144] M. Morales-Masis, S. J. van der Molen, W. T. Fu, et al.: "Conductance switching in Ag_2S devices fabricated by in situ sulfurization". *Nanotechnology* **20**, 095710. ISSN: 0957-4484. DOI: 10.1088/0957-4484/20/9/095710 (2009) (page 25).

[145] A. Aiba, R. Koizumi, T. Tsuruoka, et al.: "Investigation of Ag and Cu Filament Formation Inside the Metal Sulfide Layer of an Atomic Switch Based on Point-Contact Spectroscopy". *ACS applied materials & interfaces* **11**, 27178–27182. DOI: 10.1021/acsami.9b05523 (2019) (pages 25, 29, 82).

[146] S. Iijima: "Helical microtubules of graphitic carbon". *Nature* **354**, 56–58. ISSN: 0028-0836. DOI: 10.1038/354056a0 (1991) (page 25).

[147] P. Oser, O. Düttmann, F. Schmid, et al.: "Synthesis and Characterization of CNT Composites for Laser–Generated Ultrasonic Waves". *Macromolecular Materials and Engineering* **305**, 1900852. ISSN: 1438-7492. DOI: 10.1002/mame.201900852 (2020) (pages 26, 31, 32).

[148] P. Oser, J. Jehn, M. Kaiser, et al.: "Fiber–Optic Photoacoustic Generator Realized by Inkjet–Printing of CNT–PDMS Composites on Fiber End Faces". *Macromolecular Materials and Engineering*, 2000563. ISSN: 1438-7492. DOI: 10.1002/mame.202000563 (2020) (pages 26, 31, 32).

[149] S. Abbasi, P. J. Carreau, and A. Derdouri: "Flow induced orientation of multiwalled carbon nanotubes in polycarbonate nanocomposites: Rheology, conductivity and mechanical properties". *Polymer* **51**, 922–935. ISSN: 00323861. DOI: 10.1016/j.polymer.2009.12.041 (2010) (pages 26, 50, 54).

[150] I. Gibson, D. Rosen, and B. Stucker, eds.: "Additive Manufacturing Technologies". New York, NY: Springer New York (2015). ISBN: 978-1-4939-2112-6. DOI: 10.1007/978-1-4939-2113-3 (pages 26, 27).

[151] P. Pawlow: "Ober die Abhängigkeit des Schmelzpunktes von der Oberflächenenergie eines festen Körpers (Zusatz.)". *Zeitschrift für Physikalische Chemie* **65U**, 545–548. ISSN: 0942-9352. DOI: 10.1515/zpch-1909-6532 (1909) (page 27).

[152] O. A. Yeshchenko, I. M. Dmitruk, A. A. Alexeenko, et al.: "Size-dependent melting of spherical copper nanoparticles embedded in a silica matrix". *Physical Review B* **75**, 461. ISSN: 1050-2947. DOI: 10.1103/PhysRevB.75.085434 (2007) (pages 27, 62).

[153] L. Somlyai-Sipos, D. Janovszky, A. Sycheva, et al.: "Investigation of the Melting Point Depression of Copper Nanoparticles". *IOP Conference Series: Materials Science and Engineering* **903**, 012002. ISSN: 1757-8981. DOI: 10.1088/1757-899X/903/1/012002 (2020) (pages 27, 62).

[154] S. A. Little, T. Begou, R. W. Collins, et al.: "Optical detection of melting point depression for silver nanoparticles via in situ real time spectroscopic ellipsometry". *Applied Physics Letters* **100**, 051107. ISSN: 0003-6951. DOI: 10.1063/1.3681367 (2012) (page 27).

[155] K. A. Schroder, S. McCool, D. Hamill, et al.: "Electrical, plating and catalytic uses of metal nanomaterial compositions". 2005 (page 27).

[156] K. A. Schroder: "Mechanisms of Photonic Curing™: Processing High Temperature Films on Low Temperature Substrates". *Nanotechnology*, 220–223. ISSN: 0957-4484 (2011) (page 27).

[157] Y.-R. Jang, S.-J. Joo, J.-H. Chu, et al.: "A Review on Intense Pulsed Light Sintering Technologies for Conductive Electrodes in Printed Electronics". *International Journal of Precision Engineering and Manufacturing-Green Technology*. ISSN: 2288-6206. DOI: 10.1007/s40684-020-00193-8 (2020) (page 27).

[158] E.-K. Yu, L. Piao, and S.-H. Kim: "Sintering Behavior of Copper Nanoparticles". *Bull. Korean Chem. Soc.* **32**, 4099–4102. DOI: 10.5012/BKCS.2011.32.11.4099 (2011) (page 28).

[159] J. Ryu, H.-S. Kim, and H. T. Hahn: "Reactive Sintering of Copper Nanoparticles Using Intense Pulsed Light for Printed Electronics". *Journal of Electronic Materials* **40**, 42–50. ISSN: 0361-5235. DOI: 10.1007/s11664-010-1384-0 (2011) (pages 28, 63, 64).

[160] C.-H. Ryu, S.-J. Joo, and H.-S. Kim: "Two-step flash light sintering of copper nanoparticle ink to remove substrate warping". *Applied Surface Science* **384**, 182–191. ISSN: 01694332. DOI: 10.1016/j.apsusc.2016.05.025 (2016) (page 28).

[161] H.-J. Chan, B.-C. Huang, L.-W. Wang, et al.: "Porosity reduction in inkjet-printed copper film by progressive sintering on nanoparticles". *Thin Solid Films* **627**, 33–38. ISSN: 00406090. DOI: 10.1016/j.tsf.2017.02.062 (2017) (pages 28, 63, 64).

[162] W.-S. Han, J.-M. Hong, H.-S. Kim, et al.: "Multi-pulsed white light sintering of printed Cu nanoinks". *Nanotechnology* **22**, 395705. ISSN: 0957-4484. DOI: 10.1088/0957-4484/22/39/395705 (2011) (page 28).

[163] F. Ternero, L. G. Rosa, P. Urban, et al.: "Influence of the Total Porosity on the Properties of Sintered Materials—A Review". *Metals* **11**, 730. DOI: 10.3390/met11050730 (2021) (pages 28, 29).

[164] A. Donev, I. Cisse, D. Sachs, et al.: "Improving the density of jammed disordered packings using ellipsoids". *Science (New York, N.Y.)* **303**, 990–993. DOI: 10.1126/science.1093010 (2004) (page 28).

[165] J. M. Montes, F. G. Cuevas, and J. Cintas: "Porosity effect on the electrical conductivity of sintered powder compacts". *Applied Physics A* **92**, 375–380. ISSN: 0947-8396. DOI: 10.1007/s00339-008-4534-y (2008) (pages 28, 29).

[166] R. E. Parkin: "A note on the extinction coefficient and absorptivity of glass". *Solar Energy* **114**, 196–197. ISSN: 0038092X. DOI: 10.1016/j.solener.2015.01.004 (2015) (pages 29, 60, 61).

[167] L. Selwyn: "Understanding how silver objects tarnish". URL: https://www.canada.ca/en/conservation-institute/services/training-learning/in-person-workshops/understanding-silver-tarnish.html#shr-pg0 (visited on 04/14/2022) (page 29).

[168] T. E. Graedel: "Corrosion Mechanisms for Silver Exposed to the Atmosphere". *Journal of The Electrochemical Society* **139**, 1963–1970. ISSN: 00134651. DOI: 10.1149/1.2221162 (1992) (page 29).

[169] P. Mazurkiewicz: "Accelerated Corrosion of Printed Circuit Boards Due to High Levels of Reduced Sulfur Gasses in Industrial Environments". *Proceedings of the 32nd International Symposium for Testing and Failure Analysis* (2006) (page 29).

[170] S. Jacobs, S. Reiber, and M. Edwards: "Sulfide–induced copper corrosion". *Journal AWWA* **90**, 62–73. ISSN: 0003-150X. DOI: 10.1002/j.1551-8833.1998.tb08469.x (1998) (page 29).

[171] J. Ortíz-Corona and F. J. Rodríguez-Gómez: "Role of copper in tarnishing process of silver alloys in sulphide media". *Transactions of Nonferrous Metals Society of China* **29**, 2646–2657. ISSN: 10036326. DOI: 10.1016/S1003-6326(19)65171-X (2019) (pages 29, 30).

[172] D. Simon, J. Bardolle, and M. Bujor: "Study of the Reactivity of Silver, Copper, Silver-Copper, and Silver-Palladium Alloys used in Telephone Relay Contacts". *IEEE Transactions on Components, Hybrids, and Manufacturing Technology* **3**, 13–16. ISSN: 0148-6411. DOI: 10.1109/tchmt.1980.1135595 (1980) (page 29).

[173] C. Coughlan, M. Ibáñez, O. Dobrozhan, et al.: "Compound Copper Chalcogenide Nanocrystals". *Chemical reviews* **117**, 5865–6109. ISSN: 0009-2665. DOI: 10.1021/acs.chemrev.6b00376 (2017) (page 29).

[174] L. Liu, R. Chen, W. Liu, et al.: "Fabrication of superhydrophobic copper sulfide film for corrosion protection of copper". *Surface and Coatings Technology* **272**, 221–228. ISSN: 02578972. DOI: 10.1016/j.surfcoat.2015.04.003 (2015) (page 29).

[175] J.-S. Chung and H.-J. Sohn: "Electrochemical behaviors of CuS as a cathode material for lithium secondary batteries". *Journal of Power Sources* **108**, 226–231. ISSN: 03787753. DOI: 10.1016/S0378-7753(02)00024-1 (2002) (page 29).

[176] K. Rahmouni, M. Keddam, A. Srhiri, et al.: "Corrosion of copper in 3% NaCl solution polluted by sulphide ions". *Corrosion Science* **47**, 3249–3266. ISSN: 0010938X. DOI: 10.1016/j.corsci.2005.06.017 (2005) (pages 30, 79).

[177] P. M. May, D. Batka, G. Hefter, et al.: "Goodbye to S^{2-} in aqueous solution". *Chemical communications (Cambridge, England)* **54**, 1980–1983. DOI: 10.1039/C8CC00187A (2018) (page 30).

[178] Q. Li and J. R. Lancaster: "Chemical foundations of hydrogen sulfide biology". *Nitric oxide : biology and chemistry* **35**, 21–34. DOI: 10.1016/j.niox.2013.07.001 (2013) (pages 30, 102).

[179] H. Kaesche: "Die Korrosion der Metalle". Berlin, Heidelberg: Springer Berlin Heidelberg (2011). ISBN: 978-3-642-18427-7. DOI: 10.1007/978-3-642-18428-4 (page 30).

[180] D. S. Adams: "Making solutions from hydrated compounds". *CSH protocols*. DOI: 10.1101/pdb.ip54 (2008) (page 30).

[181] J. C. Costa, F. Spina, P. Lugoda, et al.: "Flexible Sensors—From Materials to Applications". *Technologies* **7**, 35. DOI: 10.3390/technologies7020035 (2019) (pages 31, 33).

[182] M. Amjadi, K.-U. Kyung, I. Park, et al.: "Stretchable, Skin-Mountable, and Wearable Strain Sensors and Their Potential Applications: A Review". *Advanced Functional Materials* **26**, 1678–1698. ISSN: 1616301X. DOI: 10.1002/adfm.201504755 (2016) (page 31).

[183] J. M. Wu, C.-Y. Chen, Y. Zhang, et al.: "Ultrahigh sensitive piezotronic strain sensors based on a $ZnSnO_3$ nanowire/microwire". *ACS nano* **6**, 4369–4374. DOI: 10.1021/nn3010558 (2012) (page 31).

[184] K. S. Karimov, F. A. Khalid, M. Tariq Saeed Chani, et al.: "Carbon nanotubes based flexible temperature sensors". *Optoelectronics and Advanced Materials - Rapid Communications* **6**, 194–196 (2012) (page 31).

[185] A. Di Bartolomeo, M. Sarno, F. Giubileo, et al.: "Multiwalled carbon nanotube films as small-sized temperature sensors". *Journal of Applied Physics* **105**, 064518. ISSN: 0021-8979. DOI: 10.1063/1.3093680 (2009) (page 31).

[186] X. Song, S. Liu, Z. Gan, et al.: "Controllable fabrication of carbon nanotube-polymer hybrid thin film for strain sensing". *Microelectronic Engineering* **86**, 2330–2333. ISSN: 01679317. DOI: 10.1016/j.mee.2009.04.012 (2009) (page 31).

[187] S. Walczak and M. Sibiński: "Flexible, textronic temperature sensors, based on carbon nanostructures". *Bulletin of the Polish Academy of Sciences Technical Sciences* **62**, 759–763. DOI: 10.2478/bpasts-2014-0082 (2014) (page 31).

[188] K. Kanao, S. Harada, Y. Yamamoto, et al.: "Highly selective flexible tactile strain and temperature sensors against substrate bending for an artificial skin". *RSC Advances* **5**, 30170–30174. DOI: 10.1039/c5ra03110a (2015) (page 31).

[189] F. Michelis, L. Bodelot, Y. Bonnassieux, et al.: "Highly reproducible, hysteresis-free, flexible strain sensors by inkjet printing of carbon nanotubes". *Carbon* **95**, 1020–1026. ISSN: 00086223. DOI: 10.1016/j.carbon.2015.08.103 (2015) (page 31).

[190] N. X. Williams, G. Bullard, N. Brooke, et al.: "Printable and recyclable carbon electronics using crystalline nanocellulose dielectrics". *Nature Electronics* **4**, 261–268. DOI: 10.1038/s41928-021-00574-0 (2021) (page 31).

[191] C. Gerlach, D. Krumm, M. Illing, et al.: "Printed MWCNT-PDMS-Composite Pressure Sensor System for Plantar Pressure Monitoring in Ulcer Prevention". *IEEE Sensors Journal* **15**, 3647–3656. ISSN: 1530-437X. DOI: 10.1109/JSEN.2015.2392084 (2015) (page 31).

[192] N. Naserifar, S. S. Yerneni, L. E. Weiss, et al.: "Inkjet Printing of Curing Agent on Thin PDMS for Local Tailoring of Mechanical Properties". *Macromolecular rapid communications* **41**, e1900569. DOI: 10.1002/marc.201900569 (2020) (page 32).

[193] B. Huber, J. Schober, M. Kaiser, et al.: "Rotate-to-bend setup for fatigue bending tests on inkjet-printed silver lines". *Flexible and Printed Electronics* **3**, 035005. DOI: 10.1088/2058-8585/aad5a4 (2018) (pages 32, 40, 41).

[194] H. Park, S. Lee, S. H. Jeong, et al.: "Enhanced Moisture-Reactive Hydrophilic-PTFE-Based Flexible Humidity Sensor for Real-Time Monitoring". *Sensors (Basel, Switzerland)* **18**. DOI: 10.3390/s18030921 (2018) (page 33).

[195] C.-L. Hsu, I.-L. Su, and T.-J. Hsueh: "Tunable Schottky contact humidity sensor based on S-doped ZnO nanowires on flexible PET substrate with piezotronic effect". *Journal of Alloys and Compounds* **705**, 722–733. ISSN: 09258388. DOI: 10.1016/j.jallcom.2017.02.136 (2017) (page 33).

[196] I. Valov and T. Tsuruoka: "Effects of moisture and redox reactions in VCM and ECM resistive switching memories". *Journal of Physics D: Applied Physics* **51**, 413001. ISSN: 0022-3727. DOI: 10.1088/1361-6463/aad581 (2018) (page 35).

[197] Z. Guo and Y. Fan: "Heat seal properties of polymer–aluminum–polymer composite films for application in pouch lithium-ion battery". *RSC Advances* **6**, 8971–8979. DOI: 10.1039/c5ra27097a (2016) (page 35).

[198] Wendler M., Hübner G., and Krebs M.: "Development of Printed Thin and Flexible Batteries". *Int. Circ. Graph. Educ. Res.* **4**, 32–41 (2011) (page 35).

[199] H.-D. Kim, M. J. Yun, S. M. Hong, et al.: "Impact of roughness of bottom electrodes on the resistive switching properties of platinum/nickel nitride/nickel 1×1 crossbar array resistive random access memory cells". *Microelectronic Engineering* **126**, 169–172. ISSN: 01679317. DOI: 10.1016/j.mee.2014.07.018 (2014) (page 37).

[200] J. Guy, G. Molas, P. Blaise, et al.: "Experimental and theoretical understanding of Forming, SET and RESET operations in Conductive Bridge RAM (CBRAM) for memory stack optimization". *2014 IEEE International Electron Devices Meeting*. IEEE (122014), pp. 6.5.1–6.5.4. ISBN: 978-1-4799-8001-7. DOI: 10.1109/IEDM.2014.7046997 (page 39).

[201] S. Menzel, U. Böttger, M. Wimmer, et al.: "Physics of the Switching Kinetics in Resistive Memories". *Advanced Functional Materials* **25**, 6306–6325. ISSN: 1616301X. DOI: 10.1002/adfm.201500825 (2015) (page 39).

[202] J. Park, W. Lee, M. Choe, et al.: "Quantized conductive filament formed by limited Cu source in sub-5nm era". *2011 International Electron Devices Meeting*. IEEE (122011), pp. 3.7.1–3.7.4. ISBN: 978-1-4577-0505-2. DOI: 10.1109/IEDM.2011.6131484 (page 39).

[203] Tektronix, Inc.: "Series 2400 SourceMeter SMU Instruments: Datasheet". 2021. URL: https://www.tek.com/en/sitewide-content/datasheets/s/e/r/series-2400-sourcemeter-instruments (visited on 04/14/2022) (page 40).

[204] J. Lewis: "Material challenge for flexible organic devices". *Materials Today* **9**, 38–45. ISSN: 13697021. DOI: 10.1016/S1369-7021(06)71446-8 (2006) (page 41).

[205] Espec Corp.: "Operation Manual: Bench-top type temperature (and humidty) chamber". 2014 (pages 42, 101).

[206] Veeco Instruments Inc.: "Dektak 150 Surface Profiler". 2009 (page 42).

[207] ATOS: "PLμ 300: Optical Imaging Profiler". 2004 (pages 42, 73).

[208] I. Utke, S. Moshkalev, and P. Russell: "Nanofabrication using focused ion and electron beams: principles and applications". Oxford University Press (2012) (page 43).

[209] M. Simon-Najasek, S. Huebner, F. Altmann, et al.: "Advanced FIB sample preparation techniques for high resolution TEM investigations of HEMT structures". *Microelectronics Reliability* **54**, 1785–1789. ISSN: 00262714. DOI: 10.1016/j.microrel.2014.07.101 (2014) (page 43).

[210] Tescan: "LYRA3: Technical Specifications". 2018 (page 43).

[211] Y. Li, J. Fu, C. Zhong, et al.: "Recent Advances in Flexible Zinc-Based Rechargeable Batteries". *Advanced Energy Materials* **9**, 1802605. ISSN: 16146832. DOI: 10.1002/aenm.201802605 (2019) (page 46).

[212] N. T. Dinh, E. Sowade, T. Blaudeck, et al.: "High-resolution inkjet printing of conductive carbon nanotube twin lines utilizing evaporation-driven self-assembly". *Carbon* **96**, 382–393. ISSN: 00086223. DOI: 10.1016/j.carbon.2015.09.072 (2016) (pages 49, 50, 59).

[213] K. Parmar, M. Mahmoodi, C. Park, et al.: "Effect of CNT alignment on the strain sensing capability of carbon nanotube composites". *Smart Materials and Structures* **22**, 075006. ISSN: 0964-1726. DOI: 10.1088/0964-1726/22/7/075006 (2013) (page 50).

[214] H.-L. Kao, C.-L. Cho, L.-C. Chang, et al.: "A Fully Inkjet-Printed Strain Sensor Based on Carbon Nanotubes". *Coatings* **10**, 792. DOI: 10.3390/coatings10080792 (2020) (pages 50, 53, 59).

[215] B. Earp, J. Simpson, J. Phillips, et al.: "Electrically Conductive CNT Composites at Loadings below Theoretical Percolation Values". *Nanomaterials (Basel, Switzerland)* **9**. ISSN: 2079-4991. DOI: 10.3390/nano9040491 (2019) (page 51).

[216] N. Selvan, S. B. Eshwaran, A. Das, et al.: "Piezoresistive natural rubber-multiwall carbon nanotube nanocomposite for sensor applications". *Sensors and Actuators A: Physical* **239**, 102–113. ISSN: 09244247. DOI: 10.1016/j.sna.2016.01.004 (2016) (page 51).

[217] W. Obitayo and T. Liu: "A Review: Carbon Nanotube-Based Piezoresistive Strain Sensors". *Journal of Sensors* **2012**, 1–15. ISSN: 1687-725X. DOI: 10.1155/2012/652438 (2012) (pages 52, 54).

[218] J. Canet-Ferrer, E. Coronado, A. Forment-Aliaga, et al.: "Correction of the tip convolution effects in the imaging of nanostructures studied through scanning force microscopy". *Nanotechnology* **25**, 395703. ISSN: 0957-4484. DOI: 10.1088/0957-4484/25/39/395703 (2014) (page 52).

[219] A. Bouhamed, C. Müller, S. Choura, et al.: "Processing and characterization of MWCNTs/epoxy nanocomposites thin films for strain sensing applications". *Sensors and Actuators A: Physical* **257**, 65–72. ISSN: 09244247. DOI: 10.1016/j.sna.2017.01.022 (2017) (page 52).

[220] J. Yan and Y. G. Jeong: "Multiwalled carbon nanotube/polydimethylsiloxane composite films as high performance flexible electric heating elements". *Applied Physics Letters* **105**, 051907. ISSN: 0003-6951. DOI: 10.1063/1.4892545 (2014) (page 52).

[221] H. C. Neitzert, L. Vertuccio, and A. Sorrentino: "Epoxy/MWCNT Composite as Temperature Sensor and Electrical Heating Element". *IEEE Transactions On Nanotechnology* **10**, 688–693. ISSN: 1536-125X. DOI: 10.1109/TNANO.2010.2068307 (2011) (page 53).

[222] R. Zhang, H. Deng, R. Valenca, et al.: "Strain sensing behaviour of elastomeric composite films containing carbon nanotubes under cyclic loading". *Composites Science and Technology* **74**, 1–5. ISSN: 02663538. DOI: 10.1016/j.compscitech.2012.09.016 (2013) (page 55).

[223] J. Chen, Y. Zhu, and W. Jiang: "A stretchable and transparent strain sensor based on sandwich-like PDMS/CNTs/PDMS composite containing an ultrathin conductive CNT layer". *Composites Science and Technology* **186**, 107938. ISSN: 02663538. DOI: 10.1016/j.compscitech.2019.107938 (2020) (page 55).

[224] J. Schijve: "Fatigue of structures and materials in the 20th century and the state of the art". *International Journal of Fatigue* **25**, 679–702. ISSN: 01421123. DOI: 10.1016/S0142-1123(03)00051-3 (2003) (page 55).

[225] A. Fatemi and L. Yang: "Cumulative fatigue damage and life prediction theories: a survey of the state of the art for homogeneous materials". *International Journal of Fatigue* **20**, 9–34. ISSN: 01421123. DOI: 10.1016/S0142-1123(97)00081-9 (1998) (page 57).

[226] PulseForge: "High-Intensity Light Curing Manual". 2021 (pages 60, 61).

[227] R. H. French, J. M. Rodriguez-Parada, M. K. Yang, et al.: "Optical properties of materials for concentrator photovoltaic systems". *2009 34th IEEE Photovoltaic Specialists Conference (PVSC)*. IEEE (2009), pp. 000394–000399. ISBN: 978-1-4244-2949-3. DOI: 10.1109/PVSC.2009.5411657 (pages 60, 61).

[228] P. B. Johnson and R. W. Christy: "Optical Constants of the Noble Metals". *Physical Review B* **6**, 4370–4379. ISSN: 1050-2947. DOI: 10.1103/PhysRevB.6.4370 (1972) (pages 60, 61).

[229] A. Parretta, M. K. Jayaraj, A. Di Nocera, et al.: "Electrical and Optical Properties of Copper Oxide Films Prepared by Reactive RF Magnetron Sputtering". *physica status solidi (a)* **155**, 399–404. ISSN: 18626300. DOI: 10.1002/pssa.2211550213 (1996) (page 60).

[230] P. S. Liu, T. F. Li, and C. Fu: "Relationship between electrical resistivity and porosity for porous metals". *Materials Science and Engineering: A* **268**, 208–215. ISSN: 09215093. DOI: 10.1016/S0921-5093(99)00073-8 (1999) (page 64).

[231] M. G. Lawrence: "The Relationship between Relative Humidity and the Dewpoint Temperature in Moist Air: A Simple Conversion and Applications". *Bulletin of the American Meteorological Society* **86**, 225–234. ISSN: 0003-0007. DOI: 10.1175/BAMS-86-2-225 (2005) (page 68).

[232] G. L. Graff, R. E. Williford, and P. E. Burrows: "Mechanisms of vapor permeation through multilayer barrier films: Lag time versus equilibrium permeation". *Journal of Applied Physics* **96**, 1840–1849. ISSN: 0021-8979. DOI: 10.1063/1.1768610 (2004) (page 72).

[233] DuPont Teijin Films: "Oxygen and Water Vapour Barrier Properties of Flexible Packaging Films". 2017. URL: http://usa.dupontteijinfilms.com/wp-content/uploads/2017/01/Oxygen_And_Walter_Vapour_Barrier_Properties_of_Flex_Pack_Films.pdf (visited on 04/14/2022) (pages 72, 118).

[234] J. Fahlteich, M. Fahland, W. Schönberger, et al.: "Permeation barrier properties of thin oxide films on flexible polymer substrates". *Thin Solid Films* **517**, 3075–3080. ISSN: 00406090. DOI: 10.1016/j.tsf.2008.11.089 (2009) (pages 72, 118).

[235] D. Nečas and P. Klapetek: "Gwyddion: an open-source software for SPM data analysis". *Open Physics* **10**. DOI: 10.2478/s11534-011-0096-2 (2012) (pages 73, 118).

[236] J. I. Lee, S. M. Howard, J. J. Kellar, et al.: "Electrochemical interaction between silver and sulfur in sodium sulfide solutions". *Metallurgical and Materials Transactions B* **32**, 895–901. ISSN: 1073-5615. DOI: 10.1007/s11663-001-0075-x (2001) (pages 73, 119).

[237] D. R. Lide: "Handbook of Chemistry and Physics: Internet Version 2005". Boca Raton, FL: CRC Press (2005) (page 79).

[238] E. Schweda: "Anorganische Chemie". 17., völlig neu bearb. Aufl. Stuttgart: Hirzel (2012). ISBN: 9783777621340 (page 80).

[239] J. van den Hurk, S. Menzel, R. Waser, et al.: "Processes and Limitations during Filament Formation and Dissolution in GeS_x-based ReRAM Memory Cells". *The Journal of Physical Chemistry C* **119**, 18678–18685. ISSN: 1932-7447. DOI: 10.1021/acs.jpcc.5b03622 (2015) (pages 81, 122).

[240] A. Nayak, T. Tsuruoka, K. Terabe, et al.: "Switching kinetics of a Cu_2S-based gap-type atomic switch". *Nanotechnology* **22**, 235201. ISSN: 0957-4484. DOI: 10.1088/0957-4484/22/23/235201 (2011) (page 82).

[241] S. Menzel, U. Böttger, and R. Waser: "Simulation of multilevel switching in electrochemical metallization memory cells". *Journal of Applied Physics* **111**, 014501. ISSN: 0021-8979. DOI: 10.1063/1.3673239 (2012) (page 82).

[242] J. Leppäniemi, T. Mattila, T. Kololuoma, et al.: "Roll-to-roll printed resistive WORM memory on a flexible substrate". *Nanotechnology* **23**, 305204. ISSN: 0957-4484. DOI: 10.1088/0957-4484/23/30/305204 (2012) (page 84).

[243] J. M. Eargle, ed.: "Electroacoustical Reference Data". Boston, MA: Springer US (2002). ISBN: 978-1-4613-5839-8. DOI: 10.1007/978-1-4615-2027-6 (page 85).

[244] D. Ielmini and S. Menzel: "Universal Switching Behavior". *Resistive Switching*. Ed. by D. Ielmini and R. Waser. Weinheim, Germany: Wiley-VCH Verlag GmbH & Co. KGaA (2016), pp. 317–340. ISBN: 9783527680870. DOI: 10.1002/9783527680870.ch11 (pages 86, 87, 123, 124).

[245] F. E. Jones and G. L. Harris: "ITS-90 Density of Water Formulation for Volumetric Standards Calibration". *Journal of research of the National Institute of Standards and Technology* **97**, 335–340. ISSN: 1044-677X. DOI: 10.6028/jres.097.013 (1992) (page 95).

[246] N. B. Vargaftik, B. N. Volkov, and L. D. Voljak: "International Tables of the Surface Tension of Water". *Journal of Physical and Chemical Reference Data* **12**, 817–820. ISSN: 0047-2689. DOI: 10.1063/1.555688 (1983) (page 95).

[247] D. S. Viswanath and G. Natarajan: "Data book on the viscosity of liquids". New York: Hemisphere Publ. Corp (1989). ISBN: 0891167781 (page 95).

[248] D. C. Harris: "Lehrbuch der quantitativen Analyse". 8. Auflage. Lehrbuch. Berlin and Heidelberg: Springer Spektrum (2014). ISBN: 978-3-642-37788-4 (page 102).